JOURNAL OF RESEARCH

OF THE U.S. GEOLOGICAL SURVEY

MAY–JUNE 1977
VOLUME 5, NUMBER 3

Scientific notes and summaries of investigations in geology, hydrology, and related fields

U.S. DEPARTMENT OF THE INTERIOR

UNITED STATES DEPARTMENT OF THE INTERIOR
CECIL D. ANDRUS, Secretary
GEOLOGICAL SURVEY
V. E. McKelvey, Director

For sale by Superintendent of Documents, U.S. Government Printing Office, Washington, DC 20402. Annual subscription rate, $18.90 (plus $4.75 for foreign mailing). Make check or money order payable to Superintendent of Documents. Send all subscription inquiries and address changes to Superintendent of Documents at above address.

Purchase single copy ($3.15) from Branch of Distribution, U.S. Geological Survey, 1200 South Eads Street, Arlington, VA 22202. Make check or money order payable to U.S. Geological Survey.

Library of Congress Catalog-card No. 72-600241.

The Journal of Research is published every 2 months by the U.S. Geological Survey. It contains papers by members of the Geological Survey and their professional colleagues on geologic, hydrologic, topographic, and other scientific and technical subjects.

Correspondence and inquiries concerning the Journal (other than subscription inquiries and address changes) should be directed to Anna M. Orellana, Managing Editor, Journal of Research, Publications Division, U.S. Geological Survey, 321 National Center, Reston, VA 22092.

Papers for the Journal should be submitted through regular Division publication channels.

The Secretary of the Interior has determined that the publication of this periodical is necessary in the transaction of the public business required by law of this Department. Use of funds for printing this periodical has been approved by the Director of the Office of Management and Budget through June 30, 1980.

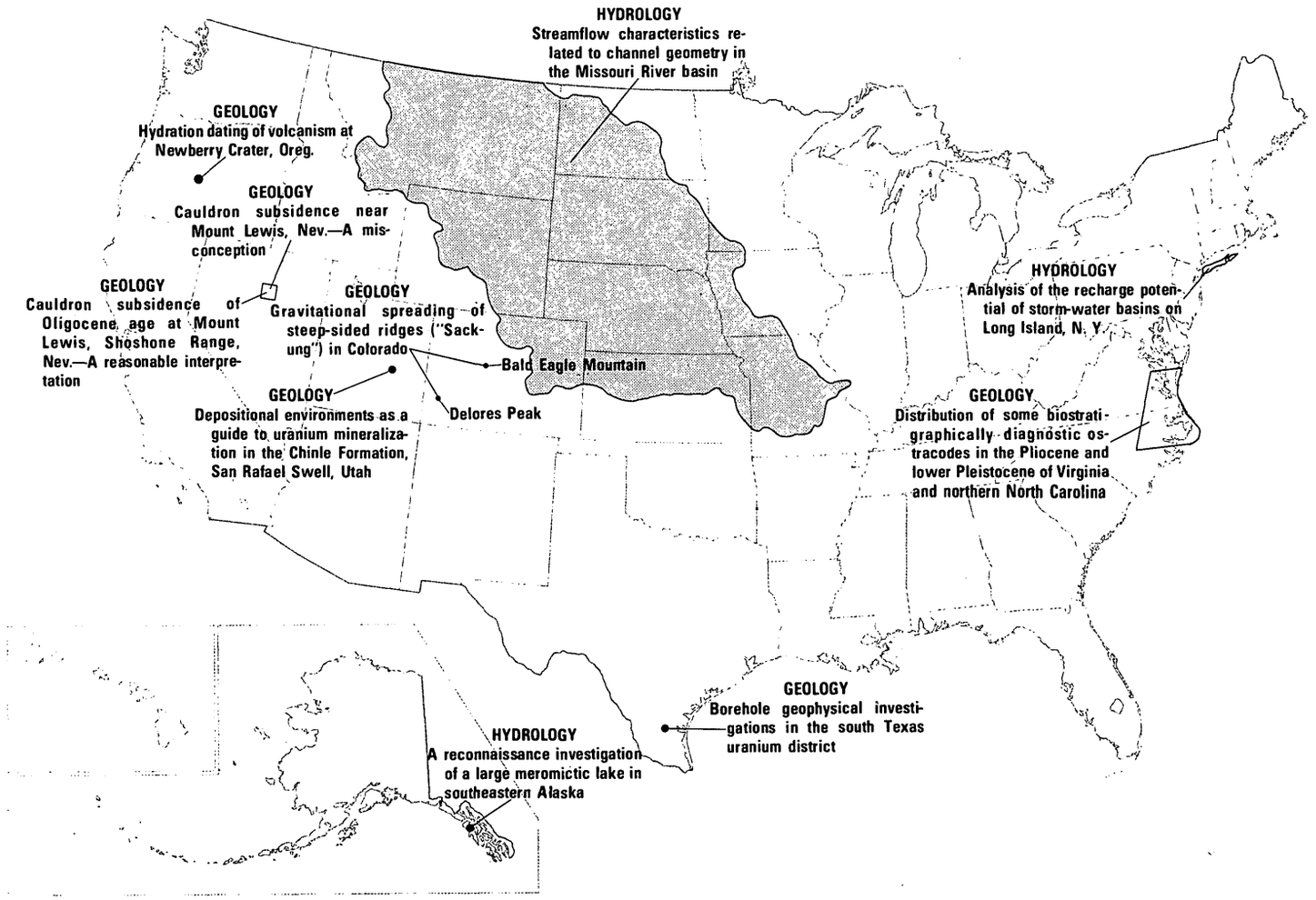

GEOGRAPHIC INDEX TO ARTICLES

See "Contents" for articles concerning areas outside the United States and articles without geographic orientation.

JOURNAL OF RESEARCH

of the

U.S. Geological Survey

Vol. 5 No. 3 May–June 1977

CONTENTS

SI units and U.S. customary equivalents ---------- II

HYDROLOGIC STUDIES

Derivation of solute-transport equations for a turbulent natural-channel flow--*Nobuhiro Yotsukura* 277
Streamflow characteristics related to channel geometry in the Missouri River basin ---------- *E. R. Hedman and W. M. Kastner* 285
Routing of stormwater flows through storm drains ---------- *M. E. Jennings and T. N. Keefer* 301
Analysis of the recharge potential of storm-water basins on Long Island, N.Y ---------- *D. A. Aronson and R. C. Prill* 307
A reconnaissance investigation of a large meromictic lake in southeastern Alaska ---- *G. A. McCoy* 319

GEOLOGIC STUDIES

Cauldron subsidence near Mount Lewis, Nev—A misconception ---------- *James Gilluly* 325
Cauldron subsidence of Oligocene age at Mount Lewis, Shoshone Range, Nev—A reasonable interpretation ---------- *C. T. Wrucke and M. L. Silberman* 331
Hydration dating of volcanism at Newberry Crater, Oreg ---------- *Irving Friedman* 337
Borehole geophysical investigations in the south Texas uranium district ---------- *J. J. Daniels, J. H. Scott, P. D. Blackmon, and H. C. Starkey* 343
Gravitational spreading of steep-sided ridges ("Sackung") in Colorado ---------- *D. H. Radbruch-Hall, D. J. Varnes, and R. B. Colton* 359
Depositional environments as a guide to uranium mineralization in the Chinle Formation, San Rafael Swell, Utah ---------- *Robert Lupe* 365
Distribution of some biostratigraphically diagnostic ostracodes in the Pliocene and lower Pleistocene of Virginia and northern North Carolina ---------- *J. E. Hazel* 373
A new method for determining the solubility of salts in aqueous solutions at elevated temperatures ---------- *R. W. Potter II, R. S. Babcock, and D. L. Brown* 389
Determination of 22 minor and trace elements in 8 new USGS standard rocks by instrumental activation analysis with epithermal neutrons ---------- *J. J. Rowe and Eiliv Steinnes* 397

Recent publications of the U.S. Geological Survey ---------- Inside of back cover

SI UNITS AND U.S. CUSTOMARY EQUIVALENTS

[SI, International System of Units, a modernized metric system of measurement. All values have been rounded to four significant digits except 0.01 bar, which is the exact equivalent of 1 kPa. Use of hectare (ha) as as alternative name for square hectometer (hm^2) is restricted to measurement of land or water areas. Use of liter (L) as a special name for cubic decimeter (dm^3) is restricted to the measurement of liquids and gases; no prefix other than milli should be used with liter. Metric ton (t) as a name for megagram (Mg) should be restricted to commercial usage, and no prefixes should be used with it. Note that the style of meter² rather than square meter has been used for convenience in finding units in this table. Where the units are spelled out in text, Survey style is to use square meter]

SI unit		U.S. customary equivalent	
Length			
millimeter (mm)	=	0.039 37	inch (in)
meter (m)	=	3.281	feet (ft)
	=	1.094	yards (yd)
kilometer (km)	=	0.621 4	mile (mi)
	=	0.540 0	mile, nautical (nmi)
Area			
centimeter² (cm^2)	=	0.155 0	inch² (in^2)
meter² (m^2)	=	10.76	feet² (ft^2)
	=	1.196	yards² (yd^2)
	=	0.000 247 1	acre
hectometer² (hm^2)	=	2.471	acres
	=	0.003 861	section (640 acres or 1 mi²)
kilometer² (km^2)	=	0.386 1	mile² (mi^2)
Volume			
centimeter³ (cm^3)	=	0.061 02	inch³ (in^3)
decimeter³ (dm^3)	=	61.02	inches³ (in^3)
	=	2.113	pints (pt)
	=	1.057	quarts (qt)
	=	0.264 2	gallon (gal)
	=	0.035 31	foot³ (ft^3)
meter³ (m^3)	=	35.31	feet³ (ft^3)
	=	1.308	yards³ (yd^3)
	=	264.2	gallons (gal)
	=	6.290	barrels (bbl) (petroleum, 1 bbl=42 gal)
	=	0.000 810 7	acre-foot (acre-ft)
hectometer³ (hm^3)	=	810.7	acre-feet (acre-ft)
kilometer³ (km^3)	=	0.239 9	mile³ (mi^3)
Volume per unit time (includes flow)			
decimeter³ per second (dm^3/s)	=	0.035 31	foot³ per second (ft^3/s)
	=	2.119	feet³ per minute (ft^3/min)
Volume per unit time (includes flow)—Continued			
decimeter³ per second (dm^3/s)	=	15.85	gallons per minute (gal/min)
	=	543.4	barrels per day (bbl/d) (petroleum, 1 bbl=42 gal)
meter³ per second (m^3/s)	=	35.31	feet³ per second (ft^3/s)
	=	15 850	gallons per minute (gal/min)
Mass			
gram (g)	=	0.035 27	ounce avoirdupois (oz avdp)
kilogram (kg)	=	2.205	pounds avoirdupois (lb avdp)
megagram (Mg)	=	1.102	tons, short (2 000 lb)
	=	0.984 2	ton, long (2 240 lb)
Mass per unit volume (includes density)			
kilogram per meter³ (kg/m^3)	=	0.062 43	pound per foot³ (lb/ft^3)
Pressure			
kilopascal (kPa)	=	0.145 0	pound-force per inch² (lbf/in^2)
	=	0.009 869	atmosphere, standard (atm)
	=	0.01	bar
	=	0.296 1	inch of mercury at 60°F (in Hg)
Temperature			
temp kelvin (K)	=	[temp deg Fahrenheit (°F) + 459.67]/1.8	
temp deg Celsius (°C)	=	[temp deg Fahrenheit (°F) − 32]/1.8	

CORRECTION

In volume 5, number 2, of the "Journal of Research of the U.S. Geological Survey," the explanation for figure 4 on page 151 was omitted and is as follows:

Land use change, 1970-72

Commercial and services 0-0
Industry 1-1
Transportation 2-2
Multifamily residence 3-3
Single-family residence 4-4
Strip and cluster development 5-5
Agriculture, with residence 6-6
Improved open space 7-7
Unimproved open space 8-8
Water 9-9

Change polygons are identified by numbers separated by a hyphen; the first digit indicates the land use in 1970, and the second digit indicates the land use in 1972. For example, a change polygon coded 6-4 means that the land use changed from Agriculture (6) in 1970 to Single-family residence (4) in 1972. Land use in transition is shown by an asterisk (*) following the use code.

Any use of trade names and trademarks in this publication is for descriptive purposes only and does not constitute endorsement by the U.S. Geological Survey.

Jour. Research U.S. Geol. Survey
Vol. 5, No. 3, May–June 1977, p. 277–284

DERIVATION OF SOLUTE-TRANSPORT EQUATIONS FOR A TURBULENT NATURAL-CHANNEL FLOW

By NOBUHIRO YOTSUKURA, Reston, Va.

Abstract.—The continuity equation of water and the convection-diffusion equation for a solute are derived by use of an orthogonal curvilinear (natural) coordinate system, which follows the meandering and irregular pattern of natural channel geometry. The solute is assumed to be neutrally buoyant, conservative, and passive. The three-, two-, and one-dimensional equations derived herein represent one of the most satisfactory descriptions of solute transport by turbulent flow in a natural channel.

A description of solute transport in natural channels often requires both the continuity equation of water and the convection-diffusion equation for a solute in turbulent open-channel flows (Holley, 1971; Chang, 1971). This report documents the procedure for deriving these equations for incompressible water and for a conservative, neutrally buoyant, and passive solute. Use is made of an orthogonal curvilinear (natural) coordinate system, in which the longitudinal coordinate axis approximately follows the meandering longitudinal direction of a channel flow (Chang, 1971; Fukuoka and Sayre, 1973). This coordinate system is adopted in order to define quantities such as velocity and discharge in a manner consistent with the characteristics of a nonuniform flow, but, more importantly, in order to utilize the scalar diffusivity concept properly in such a flow (Hinze, 1959; Dagan, 1969; Fischer, 1973).

The three-, two-, and one-dimensional equations for turbulent-flow transport will be derived in sequence, starting from the three-dimensional equations for instantaneous mass balance of water and a solute. Time- and space-averagings are performed rigorously utilizing Leibnitz's rule for reversing the order of integration and differentiation, Reynolds' averaging rules, and necessary boundary conditions (Leendertse, 1970; Holley, 1971). The procedure is devoid of such assumptions as uniform distribution of solute concentration, stationary flow boundaries, and steadiness or uniformity of flow, which are often required in conventional derivations of transport equations. On the other hand, each averaging process produces a covariance between the deviations of concentration and velocity from their averaged values. It is shown that an aggregate expression for the covariance, variously called mixing, dispersion, and diffusion, is where major assumptions and approximations are introduced into the convection-diffusion equation, which is otherwise exact. These covariances are expressed in gradient-type flux forms following Boussinesq's and Taylor's phenomenological models (Hinze, 1959; Taylor, 1954).

Various phases of the derivation have been reported in some of the above references as well as in other recent papers (Sayre and Yeh, 1973; Yotsukura and Sayre, 1976). The only new aspect of the present report is concerned with the one-dimensional equations. The entire derivation, however, is documented in the present report as it should prove useful and as it appears nowhere else in the literature.

NATURAL COORDINATE SYSTEM

An orthogonal curvilinear coordinate system, hereinafter called the natural coordinate system, is illustrated in figure 1 (Chang, 1971; Fukuoka and Sayre, 1973). The system is composed of three mutually orthogonal sets of coordinate surfaces, which may be called longitudinal, transverse, and horizontal coordinate surfaces. The longitudinal and transverse coordinate surfaces are vertical, typically curved, and nonparallel. The horizontal coordinate surfaces are all parallel, horizontal planes. For reasons that will become clear later, it is best to aline the longitudinal coordinate surfaces, at least approximately, in the direction of depth-averaged total velocity vectors.

The origin, 0, is located at the intersection point of three specially selected coordinate surfaces, as shown in figure 1. The x axis is defined as the intersection of the longitudinal and horizontal coordinate surfaces (positive in the downstream direction), the z axis as

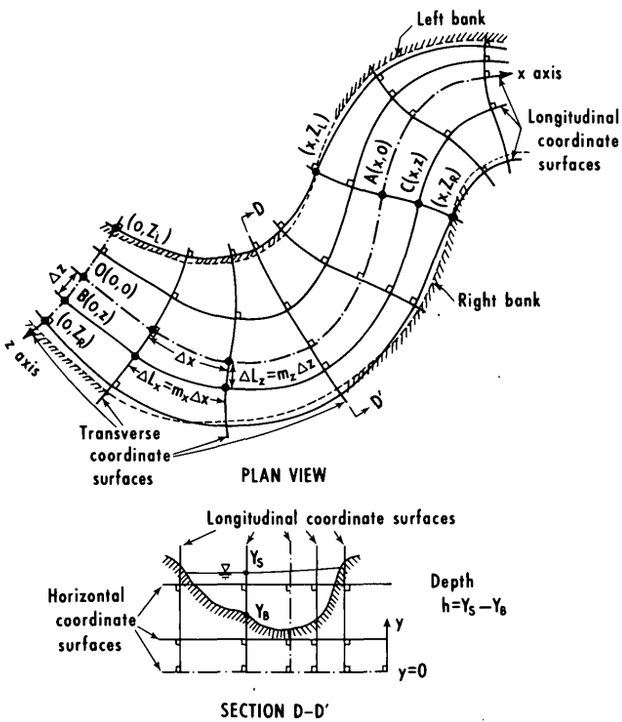

FIGURE 1.—Orthogonal curvilinear coordinate system for a natural channel.

the intersection of the transverse and horizontal surfaces (positive to the right), and the y axis as the intersection of the longitudinal and transverse surfaces (positive in the upward direction). Again for reasons to be explained later, it is best to locate the x axis in the midstream region of the channel. The x and z coordinates of a point, C, in figure 1, are defined respectively as the horizontal distance, L_{OA} along the x axis and L_{OB} along the z axis. Therefore, all points on a transverse coordinate surface have a common coordinate value, x, and, similarly, all points on a longitudinal coordinate surface have a common coordinate value, z. Coordinate values for y are measured vertically upward from the x–z plane.

Due to curvature in channel alinement and (or) variations in width along the channel, horizontal distances, measured along different longitudinal (or transverse) coordinate surfaces from one transverse (or longitudinal) coordinate surface to another, are generally not equal. To take care of this, the metric coefficients, m_x and m_z, are introduced to correct for differences between distances along curved coordinate surfaces and those measured along the respective axes. As illustrated in figure 1, the horizontal distance along the longitudinal coordinate surface from B to C is given by $L_{BC}=\int_0^x m_x\,dx$ and that along the transverse coordinate surface from A to C by $L_{AC}=\int_0^z m_z\,dz$. The values of m_x and m_z may vary from point to point and are functions of both x and z, except that $m_x=1$ on the x axis and $m_z=1$ on the z axis. Because all horizontal coordinate surfaces are parallel, the metric coefficient m_y is unity. The present natural coordinate system is thus based on the assumption that the total velocity vector everywhere in the channel is predominantly oriented in the horizontal direction. This is reasonable in most natural channels. Note also that, if $m_x=m_z=1$ everywhere, the coordinate system reduces to a rectangular Cartesian system.

Differential and integral operations in the natural coordinate system follow those for a general orthogonal curvilinear coordinate system (Kaplan, 1953). For present purposes, it suffices to remember that integration or differentiation of a function along a curved coordinate surface is always related to an infinitesimal distance, such as $dL_x=m_x\,dx$ or $dL_z=m_z\,dz$. Notations dL_x and dL_z, however, will not be used in the following development.

INSTANTEOUS MASS BALANCE EQUATIONS

The principle of mass conservation for incompressible water and a conservative solute, which is neutrally buoyant and passive, can be described by the following equations (Daily and Harleman, 1966):

$$\nabla\cdot\vec{\omega} = 0, \tag{1}$$

$$\frac{\partial\theta}{\partial t} + \nabla\cdot(\theta\vec{\omega}) = \varepsilon\nabla^2\theta. \tag{2}$$

The notation $\vec{\omega}$ is the velocity vector, Θ the solute concentration, ε the molecular diffusion coefficient, and t the time. The symbol ∇ designates the divergence operator and ∇^2 the divergence gradient operator. These equations represent instantaneous mass balance for water and a solute, respectively.

Equations 1 and 2 may be expanded in the present natural coordinate system (Kaplan, 1953; Chang, 1971) as follows:

$$\frac{1}{m_x m_z}\left[\frac{\partial}{\partial x}(m_z\omega_x) + \frac{\partial}{\partial y}(m_x m_z\omega_y) + \frac{\partial}{\partial z}(m_x\omega_z)\right] = 0, \tag{3}$$

$$\frac{\partial\Theta}{\partial t} + \frac{1}{m_x m_z}\left[\frac{\partial}{\partial x}(m_z\theta\omega_x) + \frac{\partial}{\partial y}(m_x m_z\theta\omega_y) + \frac{\partial}{\partial z}(m_x\theta\omega_z)\right]$$
$$= \frac{\varepsilon}{m_x m_z}\left[\frac{\partial}{\partial x}\left(\frac{m_z}{m_x}\frac{\partial\theta}{\partial x}\right) + \frac{\partial}{\partial y}\left(m_x m_z\frac{\partial\theta}{\partial y}\right) + \frac{\partial}{\partial z}\left(\frac{m_x}{m_z}\frac{\partial\theta}{\partial z}\right)\right]. \tag{4}$$

When $m_x=m_z=1$, equations 3 and 4 reduce to the familiar three-dimensional continuity and convection-diffusion equations in a rectangular Cartesian system. Equation 4 is given in the so-called conservation form but may be simplified to the advection form by substituting equation 3 into the left-hand side (Crowley,

1968). The following operation, however, will be performed throughout by use of the conservation form.

LEIBNITZ'S RULE AND REYNOLDS' RULES

In carrying out the integration of equations with respect to time or space, Leibnitz's rule for reversing the order of integration and differential is frequently used. If ϕ is a function of independent variables p and q, and α and β are parameters depending on q, this rule is written (Korn and Korn, 1961) as follows:

$$\int_{\alpha(q)}^{\beta(q)} \frac{\partial}{\partial q}\phi(p,q)dp = \frac{\partial}{\partial q}\int_{\alpha(q)}^{\beta(q)} \phi(p,q)dp - \phi(\beta,q)\frac{\partial\beta}{\partial q} + \phi(\alpha,q)\frac{\partial\alpha}{\partial q}. \quad (5)$$

In handling time or space averages of a quantity and its deviations from the averages, Reynolds' operational rules will be used frequently. For a function ϕ, the average is denoted by $\bar{\phi}$ and a deviation from the average by ϕ', so that $\phi=\bar{\phi}+\phi'$. The following operational rules are generally valid for turbulent-flow analysis (Monin and Yaglom, 1973):

$$\overline{\phi'} = 0, \quad (6)$$

$$\overline{\phi+\psi} = \bar{\phi}+\bar{\psi}, \quad (7)$$

$$\overline{\phi\cdot\psi} = \bar{\phi}\cdot\bar{\psi}, \quad (8)$$

$$\overline{\phi\cdot\psi} = \bar{\phi}\cdot\bar{\psi} + \overline{\phi'\cdot\psi'}, \quad (9)$$

$$\overline{\frac{\partial\phi}{\partial x}} = \frac{\partial\bar{\phi}}{\partial x}. \quad (10)$$

In the following development, overlined and prime notations will be specified independently in each section to indicate whether they pertain to time-averaged, depth-averaged, or cross-section-averaged quantities. Since each section involves only one mode of averaging, notational conflicts are thereby averted.

THREE-DIMENSIONAL EQUATIONS BY TIME INTEGRATION

As most natural channel flow regimes are turbulent, instantaneous mass balance equations (eqs. 3 and 4) need to be integrated and averaged over an appropriate time interval. Such a time interval should be long enough to damp out turbulent fluctuations and, more realistically, be defined for a specific problem based on the scales of flow and channel geometry under investigation. In this section, the overlined symbol will be used to denote these time-averaged quantities. For a function ϕ, $\bar{\phi}$ is defined by

$$\bar{\phi} = \frac{1}{T}\int_{t_1}^{t_2}\phi dt \quad , \quad (11)$$

where T is the time interval, t_2-t_1. An instantaneous value, ϕ, is the sum of $\bar{\phi}$ and ϕ', where ϕ' is an instantaneous deviation from the time-averaged $\bar{\phi}$.

The integration of equations 3 and 4 over a time interval, T, is carried out for each term by applying Leibnitz's rule or equation 5. Note that m_x and m_z are independent of time and thus are treated as constants in the integration. For an illustration, the first term of equation 3 is integrated as

$$\int_{t_1}^{t_2}\frac{\partial}{\partial x}(m_z\omega_x)dt = \frac{\partial}{\partial x}(m_z\int_{t_1}^{t_2}\omega_x dt) = \frac{\partial}{\partial x}(m_z\, T\,\bar{\omega}_x). \quad (12)$$

The other two terms of equation 3 may be integrated in the manner similar to that of equation 12.

Integration of the first term of equation 4 requires the mean theorem of integration for a continuous function (Kaplan, 1953) so that

$$\int_{t_1}^{t_2}\frac{\partial\theta}{\partial t}dt = \theta(t_2) - \theta(t_1) = T\frac{\partial\bar{\theta}}{\partial t}. \quad (13)$$

Integration of the convection terms on the left side of equation 4 requires use of some of Reynolds' rules, in particular, equation 9. For example, the first convection term may be integrated to a form

$$\int_{t_1}^{t_2}\frac{\partial}{\partial x}(m_z\theta\omega_x)dt = \frac{\partial}{\partial x}(m_z\int_{t_1}^{t_2}\theta\omega_x dt) = \frac{\partial}{\partial x}\left[m_z T(\bar{\theta}\cdot\bar{\omega}_x + \overline{\theta'\cdot\omega'_x})\right]. \quad (14)$$

where $\bar{\Theta}$ and $\bar{\omega}_x$ are the time-averaged values of concentration and longitudinal velocity and Θ' and ω'_x are instantaneous deviations from the averaged values. Even though $\overline{\Theta'}$ and $\overline{\omega'_x}$ are zero, the mean of the product of the deviations or the covariance, $\overline{\Theta'\cdot\omega'_x}$, is not zero, and this effect is commonly expressed in analogy to molecular diffusions as

$$\overline{\theta'\cdot\omega'_x} = -\frac{e_x}{m_x}\frac{\partial\bar{\theta}}{\partial x}. \quad (15)$$

The symbol e_x is the longitudinal turbulent diffusion coefficient first introduced by Boussinesq (Hinze, 1959). Integration of the other two convection terms of equation 4 produces covariances, $\overline{\Theta'\cdot\omega'_y}$ and $\overline{\Theta'\cdot\omega'_z}$, which are handled in the manner similar to that of equation 15.

The newly defined turbulent diffusion terms may be combined with the molecular diffusion terms on the right-hand side of the integrated form of equation 4. The remaining terms on the left-hand side of the equation are the time-derivative term (eq. 13) and the three terms containing $\bar{\Theta}\cdot\bar{\omega}_x$, $\bar{\Theta}\cdot\bar{\omega}_y$, and $\bar{\Theta}\cdot\bar{\omega}_z$, which may be called the time-averaged convection terms.

Introducing new symbols $s=\bar{\Theta}$, $u_x=\bar{\omega}_x$, $u_y=\bar{\omega}_y$, $u_z=\bar{\omega}_z$, the three-dimensional continuity and convection-diffusion equations averaged over the time interval, T, become independent of T and are written as (Chang, 1971) follows:

$$\frac{1}{m_x m_z}\left[\frac{\partial}{\partial x}(m_z u_x) + \frac{\partial}{\partial y}(m_x m_z u_y) + \frac{\partial}{\partial z}(m_x u_z)\right] = 0, \tag{16}$$

$$\frac{\partial s}{\partial t} + \frac{1}{m_x m_z}\left[\frac{\partial}{\partial x}(m_z s u_x) + \frac{\partial}{\partial y}(m_x m_z s u_y) + \frac{\partial}{\partial z}(m_x s u_z)\right]$$
$$= \frac{1}{m_x m_z}\left[\frac{\partial}{\partial x}\left(\frac{m_z}{m_x}(e_x + \epsilon)\frac{\partial s}{\partial x}\right) + \frac{\partial}{\partial y}\left(m_x m_z (e_y + \epsilon)\frac{\partial s}{\partial y}\right) + \frac{\partial}{\partial z}\left(\frac{m_x}{m_z}(e_z + \epsilon)\frac{\partial s}{\partial z}\right)\right]. \tag{17}$$

Equations 16 and 17 reduce to familiar forms in a Cartesian system, when m_x and m_z are made unity and symbols are defined for the overall mixing coefficients, $e_x+\epsilon$, $e_y+\epsilon$, and $e_z+\epsilon$. It is worth noting that the turbulent diffusion coefficients, e_x, e_y, and e_z, have been shown to contain many theoretical deficiencies from the mechanics of turbulence (Hinze, 1959). Nevertheless, these coefficients have been empirically established as satisfactory working models in most natural channel flows (Fischer, 1973). The molecular diffusion coefficient, ϵ, assumed to be constant, is normally an order smaller than the turbulent diffusion coefficients.

No assumptions are introduced in developing equations 16 and 17 except for those related to the covariance terms, $\overline{\Theta' \cdot \omega'}$. In utilizing the three principal (scalar) diffusion coefficients for approximation of $\overline{\Theta' \cdot \omega'}$, however, a justification is that the principal axes of the diffusion tensor can be alined approximately with the three coordinate directions when one adopts the natural coordinate system (Hinze, 1959; Dagan, 1969). If a stationary rectangular Cartesian coordinate system were used instead, it would be very difficult to satisfy the above alinement requirement in a generally meandering nonuniform channel, and it would thus be difficult to justify simple scalar expressions, as given in equation 17. Overcoming these difficulties is a major advantage of utilizing the natural coordinate system over a Cartesian system. If one wants to use a Cartesian system and only the principal diffusion coefficients, one must necessarily imply that the coordinate system is continuously readjusted in the downstream direction, so that the main flow direction is in agreement with the longitudinal coordinate direction.

TWO-DIMENSIONAL EQUATIONS BY DEPTH INTEGRATION

The three-dimensional continuity and convection-diffusion equations (eqs. 16 and 17) are now integrated over a local depth to obtain depth-averaged two-dimensional equations. This process, requiring the use of Leibnitz's rule and boundary conditions at the water surface and the bed, can best be illustrated by an example. In equations 16 and 17, m_x and m_z are independent of y and can be treated as constants in integration. Designate values of y at flow boundaries as Y, so that Y_B and Y_S represent the channel bed and water surface, respectively. Note that Y_S and Y_B are functions of x, z, and t, whereas y is an independent variable. Each term of equation 16 is now integrated with respect to y from Y_B to Y_S, as follows:

$$\int_{Y_B}^{Y_S}\frac{\partial}{\partial x}(m_z u_x)dy = \frac{\partial}{\partial x}\int_{Y_B}^{Y_S} m_z u_x dy - \overset{①}{m_z u_x\Big|_{Y_S}\frac{\partial Y_S}{\partial x}} + \overset{④}{m_z u_x\Big|_{Y_B}\frac{\partial Y_B}{\partial x}}, \tag{18}$$

$$\int_{Y_B}^{Y_S}\frac{\partial}{\partial z}(m_x u_z)dy = \frac{\partial}{\partial z}\int_{Y_B}^{Y_S} m_x u_z dy - \overset{②}{m_x u_z\Big|_{Y_S}\frac{\partial Y_S}{\partial z}} + \overset{⑤}{m_x u_z\Big|_{Y_B}\frac{\partial Y_B}{\partial z}}, \tag{19}$$

$$\int_{Y_B}^{Y_S}\frac{\partial}{\partial y}(m_x m_z u_y)dy = \overset{③}{m_x m_z u_y\Big|_{Y_S}} - \overset{⑥}{m_x m_z u_y\Big|_{Y_B}}. \tag{20}$$

The kinematical boundary condition at Y_S (x, z, t) requires that

$$dy = \frac{\partial Y_S}{\partial t}dt + \frac{\partial Y_S}{m_x \partial x}m_x dx + \frac{\partial Y_S}{m_z \partial z}m_z dz \tag{21}$$

or, by dividing equation 21 by dt, velocities at Y_S are related by

$$u_y = \frac{\partial Y_S}{\partial t} + \frac{u_x}{m_x}\frac{\partial Y_S}{\partial x} + \frac{u_z}{m_z}\frac{\partial Y_S}{\partial z}. \tag{22}$$

Multiplying equation 22 by $m_x\ m_z$, the sum of the terms ①, ②, and ③ in equations 18, 19, and 20 is equal to $m_x\ m_z\ \dfrac{\partial Y_S}{\partial t}$. A similar boundary equation can be derived at the bed, and the sum of the terms ④, ⑤, and ⑥ can be shown to be equal to $-m_x\ m_z\ \dfrac{\partial Y_B}{\partial t}$. The depth-integrated form of equation 16 thus reduces to

$$\frac{1}{m_x m_z}\left[\frac{\partial}{\partial x}\int_{Y_B}^{Y_S} m_z u_x\, dy + \frac{\partial}{\partial z}\int_{Y_B}^{Y_S} m_x u_z\, dy + m_x m_z\frac{\partial(Y_S - Y_B)}{\partial t}\right] = 0. \tag{23}$$

In integrating the left side of equation 17, the above kinematical boundary conditions are again used to cancel eight terms arising from application of Leibnitz's rule, so that the depth-integrated left side of equation 17 is

$$\frac{\partial}{\partial t}\int_{Y_B}^{Y_S} s\,dy + \frac{1}{m_x m_z}\left[\frac{\partial}{\partial x}\left(m_z\int_{Y_B}^{Y_S} s u_x dy\right) + \frac{\partial}{\partial z}\left(m_x\int_{Y_B}^{Y_S} s u_z dy\right)\right]. \tag{24}$$

Integration of the right side of equation 17 requires use of another boundary condition which specifies that no diffusive flux is allowed across the water surface and the bed. Designating the flux vector as $\vec{f}$ and the unit normal vector at a boundary as $\vec{n}$, this condition is given

by $$\vec{f}\cdot\vec{n} = 0, \tag{25}$$

where $$\vec{f} = \frac{(e_x + \epsilon)}{m_x}\frac{\partial s}{\partial x}\vec{i} + (e_y + \epsilon)\frac{\partial s}{\partial y}\vec{j} + \frac{(e_z + \epsilon)}{m_z}\frac{\partial s}{\partial z}\vec{k} \tag{26}$$

and $$\vec{n} = \left[\left(\frac{1}{m_x}\frac{\partial Y}{\partial x}\right)^2 + 1 + \left(\frac{1}{m_z}\frac{\partial Y}{\partial z}\right)^2\right]^{-\frac{1}{2}}\cdot\left[-\frac{1}{m_x}\frac{\partial Y}{\partial x}\vec{i} + \vec{j} - \frac{1}{m_z}\frac{\partial Y}{\partial z}\vec{k}\right] \tag{27}$$

at $Y=Y_S$ and $Y=Y_B$. The symbols $\vec{i}$, $\vec{j}$, and $\vec{k}$ are unit vectors in the respective coordinate directions. Because of equation 25, some boundary terms arising from application of Leibnitz's rule to the integrated right side of equation 17 are canceled out; this cancellation leaves only

$$\frac{1}{m_x m_z}\left[\frac{\partial}{\partial x}\left(\frac{m_z}{m_x}\int_{Y_B}^{Y_S}(e_x+\varepsilon)\frac{\partial s}{\partial x}dy\right)+\frac{\partial}{\partial z}\left(\frac{m_x}{m_z}\int_{Y_B}^{Y_S}(e_z+\varepsilon)\frac{\partial s}{\partial z}dy\right)\right]. \quad (28)$$

Before equating expressions 24 and 28 for the depth-integrated convection-diffusion equation, integrals in expression 24, such as $\int s u_x dy$, will be considered further. In this section, overlined and prime notations pertain only to depth-averaging, so that

$$\bar{\phi}=\frac{1}{h}\int_{Y_B}^{Y_S}\phi dy, \quad (29)$$

where $h=Y_S-Y_B$ and ϕ represents a function whose time-averaging was completed in the preceding section. The function, $\phi\ (x,y,z,t)$, is the sum of $\bar{\phi}\ (x,z,t)$ and $\phi'\ (x,y,z,t)$, where ϕ' is a local deviation from the depth-averaged $\bar{\phi}$.

The integral in the second term of expression 24 may be written as

$$\int_{Y_B}^{Y_S} s u_x dy = h\,\overline{s u_x} = h\left[\bar{s}\cdot\bar{u}_x+\overline{s'\cdot u'_x}\right]. \quad (30)$$

Note that the bracketed part of equation 30 is analogous to the last parenthesized part of equation 14. The difference is that equation 30 refers to depth-averaging, whereas equation 14 refers to time-averaging. It is due to Taylor's (1954) longitudinal dispersion theory that this spatial covariance term, $\overline{s'u'_x}$, may also be equated to a gradient-type flux form

$$\overline{s'u'_x}=-\frac{k_x}{m_x}\frac{\partial\bar{s}}{\partial x}, \quad (31)$$

which is analagous to equation 15. The symbol k_x is the longitudinal convective dispersion coefficient induced by the depthwise variation of u_x and s. The other covariance, $\overline{s'u'_z}$ from expression 24, may be handled in the manner similar to that of equation 31.

The first integral of expression 28 may be written as

$$\int_{Y_B}^{Y_S}(e_x+\varepsilon)\frac{\partial s}{\partial x}dy = h\,\overline{(e_x+\varepsilon)\frac{\partial s}{\partial x}} = h\left[(\bar{e}_x+\varepsilon)\frac{\partial\bar{s}}{\partial x}+\overline{e'_x\frac{\partial s'}{\partial x}}\right]. \quad (32)$$

The covariance term is usually related to the product-of-averages term, but small relative to it, so that it is conveniently absorbed into the latter term. Similar approximations will be applied to the second term of expression 28.

Utilizing the notations defined by equation 29, the depth-averaged form of the continuity equation is obtained from equation 23, as

$$\frac{\partial h}{\partial t}+\frac{1}{m_x m_z}\left[\frac{\partial}{\partial x}(m_z h\,\bar{u}_x)+\frac{\partial}{\partial z}(m_x h\,\bar{u}_z)\right]=0. \quad (33)$$

The depth-averaged convection-diffusion equation is obtained by equating expressions 24 and 28, substituting approximating expressions, such as equations 31 and 32, and moving all diffusive flux terms to the right-hand side of the equation, so that

$$\frac{\partial}{\partial t}(h\bar{s})+\frac{1}{m_x m_z}\left[\frac{\partial}{\partial x}(m_z h\,\bar{u}_x\,\bar{s})+\frac{\partial}{\partial z}(m_x h\,\bar{u}_z\,\bar{s})\right]$$

$$=\frac{1}{m_x m_z}\left[\frac{\partial}{\partial x}\left(\frac{m_z}{m_x}h\,(k_x+\bar{e}_x+\varepsilon)\frac{\partial\bar{s}}{\partial x}\right)+\frac{\partial}{\partial z}\left(\frac{m_x}{m_z}h\,(k_z+\bar{e}_z+\varepsilon)\frac{\partial\bar{s}}{\partial z}\right)\right]. \quad (34)$$

Introducing new notations

$c=\bar{s}$, $v_x=\bar{u}_x$, $v_z=\bar{u}_z$, and $d_x=k_x+\bar{e}_x+\varepsilon$, and $d_z=k_z+\bar{e}_z+\varepsilon$, where d_x and d_z are the overall mixing coefficients in the respective coordinate directions, the two-dimensional continuity and convection-diffusion equations are finally written (Yotsukura and Sayre, 1976) as follows:

$$\frac{\partial h}{\partial t}+\frac{1}{m_x m_z}\left[\frac{\partial}{\partial x}(m_z h\,v_x)+\frac{\partial}{\partial z}(m_x h\,v_z)\right]=0, \quad (35)$$

$$\frac{\partial}{\partial t}(hc)+\frac{1}{m_x m_z}\left[\frac{\partial}{\partial x}(m_z h\,v_x\,c)+\frac{\partial}{\partial z}(m_x h\,v_z\,c)\right]$$

$$=\frac{1}{m_x m_z}\left[\frac{\partial}{\partial x}\left(\frac{m_z}{m_x}hd_x\frac{\partial c}{\partial x}\right)+\frac{\partial}{\partial z}\left(\frac{m_x}{m_z}hd_z\frac{\partial c}{\partial z}\right)\right]. \quad (36)$$

In going from the three-dimensional equations 16 and 17 to the two-dimensional equations 35 and 36, no assumptions were introduced except for those related to spatial covariance terms, such as equations 31 and 32. One must remember that the convective dispersion coefficient, as defined by equation 31, is an asymptotic approximation and thus applies only when solute concentration is well distributed over the depth of flow (Fischer, 1973). For a steady uniform flow, Taylor's longitudinal dispersion theory has been verified by Aris (1956), Elder (1959), Fischer (1966), and Sayre (1967), among many others. Note that the mixing coefficient, d, is the sum of the convective dispersion coefficient, k, the depth-averaged turbulent diffusion coefficient, $\bar{e}$, and the molecular diffusion coefficient, ϵ, where $k \gg \bar{e} \gg \epsilon$.

ONE-DIMENSIONAL EQUATIONS BY WIDTH INTEGRATION

The two-dimensional continuity and convection-diffusion equations (eqs. 35 and 36) are now integrated over the top width of a channel to obtain cross-section-averaged one-dimensional equations. Equations 35 and 36 are first multiplied by m_x. Each term of the equations is then integrated with respect to $m_z dz$ along a transverse coordinate from the left bank to the right bank (fig. 1). Designate boundary values of z as Z, so that Z_L and Z_R represent the left bank and the right bank, respectively. Note that Z_L and Z_R are functions of x and t, whereas z is an independent variable.

The kinematical boundary condition at $Z_L\ (x,t)$ may

be derived as follows. Define a function $F(x,z,t) = Z_L(x,t) - z$, so that $F = 0$ at the left bank. The total differential of F is, therefore, zero, or

$$dF = \frac{\partial Z_L}{\partial t}\, dt + \frac{\partial Z_L}{\partial x}\, dx - dz = 0. \tag{37}$$

Noting that $v_x = m_x dx/dt$ and $v_z = m_z dz/dt$ in the natural coordinate system, equation 37 can be reduced to

$$\frac{v_z}{m_z} = \frac{\partial Z_L}{\partial t} + \frac{v_x}{m_x}\frac{\partial Z_L}{\partial x}, \tag{38}$$

where v_z and v_x are velocity components at Z_L. The boundary condition at Z_R can be derived in the manner similar to that of equation 38.

When the continuity equation (eq. 35) is integrated with respect to $m_z dz$, some terms arising from application of Leibnitz's rule are canceled because of equation 38 and its counterpart at Z_R. This is analogous to the treatment given to equations 18, 19, and 20 in the depth-integration process. The width-integrated form of equation 35 then reduces to

$$\frac{\partial}{\partial t}\int_{Z_L}^{Z_R} m_x\, h\, m_z\, dz + \frac{\partial}{\partial x}\int_{Z_L}^{Z_R} v_x\, h\, m_z\, dz = 0. \tag{39}$$

Integration of the left side of the convection-diffusion equation (eq. 36) also utilizes the kinematical boundary conditions to cancel several boundary terms. The width-integrated left side of equation 36 then reduces to

$$\frac{\partial}{\partial t}\int_{Z_L}^{Z_R} c\, m_x\, h\, m_z\, dz + \frac{\partial}{\partial x}\int_{Z_L}^{Z_R} c\, v_x\, h\, m_z\, dz. \tag{40}$$

Integration of the right side of equation 36 requires another boundary condition similar to equation 25. The solute flux vector, $\vec{f}$, and the unit normal vector, $\vec{n}$, at Z_L may be written as

$$\vec{f} = \frac{hd_x}{m_x}\frac{\partial c}{\partial x}\vec{i} + \frac{hd_z}{m_z}\frac{\partial c}{\partial z}\vec{k}, \tag{41}$$

and

$$\vec{n} = \left[\left(\frac{1}{m_x}\frac{\partial Z_L}{\partial x}\right)^2 + \left(\frac{1}{m_z}\right)^2\right]^{-\frac{1}{2}} \cdot \left[-\frac{1}{m_x}\frac{\partial Z_L}{\partial x}\vec{i} + \frac{1}{m_z}\vec{k}\right]. \tag{42}$$

The condition of no diffusive flux through the left bank is that the scalar product, $\vec{f}\cdot\vec{n}$, is zero, or

$$-\frac{hd_x}{m_x^2}\frac{\partial c}{\partial x}\frac{\partial Z_L}{\partial x} + \frac{hd_z}{m_z^2}\frac{\partial c}{\partial z} = 0. \tag{43}$$

Equation 43 and its counterpart at Z_R may be used to cancel some boundary terms arising from the integration of the right side of equation 36; this cancellation leaves only

$$\frac{\partial}{\partial x}\int_{Z_L}^{Z_R} \frac{d_x}{m_x}\frac{\partial c}{\partial x}\, h\, m_z\, dz. \tag{44}$$

Before equating expressions 40 and 44 for the width-integrated convection-diffusion equation, integrals in expression 40, such as $\int c v_x h m_z dz$, will be considered further. In this section overlined and prime notations pertain only to cross-section-averaging, and the average is defined by

$$\bar{\phi} = \frac{1}{A}\int_{Z_L}^{Z_R} \phi h\, m_z dz, \tag{45}$$

where A is the cross-sectional area given by

$$A = \int_{Z_L}^{Z_R} h m_z dz, \tag{46}$$

and ϕ represents a function whose time-averaging and depth-averaging were completed in the preceding two sections. The function $\phi\ (x,z,t)$ is the sum of $\bar{\phi}\ (x,t)$ and $\phi'\ (x,z,t)$, a widthwise local deviation from the cross-section-averaged $\bar{\phi}$. That equation 45 defines a customary cross-section-averaged value can be shown easily by substituting equation 29 into equation 45, with overlined notations modified. By virtue of equation 45, each width-integrated term in equation 39 and expressions 40 and 44 can be expressed in terms of a cross-section-averaged value.

The integral in the first term of expression 40 may be written as

$$\int_{Z_L}^{Z_R} c\, m_x\, h\, m_z\, dz = A\,\overline{c\, m_x} = A\left[\bar{c}\cdot\bar{m}_x + \overline{c'\cdot m_x'}\right]. \tag{47}$$

The covariance term in equation 47 is a peculiar term resulting from the use of the natural coordinate system. The term will be kept in the present form for later comments.

The integral in the second term of expression 40 is written as

$$\int_{Z_L}^{Z_R} c\, v_x\, h\, m_z\, dz = A\,\overline{c\, v_x} = A\left[\bar{c}\cdot\bar{v}_x + \overline{c'\cdot v_x'}\right]. \tag{48}$$

The covariance term of equation 48 is analogous to those of equations 14 and 30. In extending Taylor's longitudinal dispersion theory to natural streams, Fischer (1966) showed that this covariance can also be expressed in a gradient-type flux form. In the natural coordinate system, the flux form may be written as

$$\overline{c'\cdot v_x'} = -\frac{K_x}{\bar{m}_x}\frac{\partial \bar{c}}{\partial x}, \tag{49}$$

which is analogous to equations 15 and 31. The symbol K_x is the longitudinal convective dispersion coefficient induced by the widthwise variation of v_x and c.

The integral in expression 44 is written as

$$\int_{Z_L}^{Z_R} \frac{d_x}{m_x}\frac{\partial c}{\partial x}\, h\, m_z dz = A\,\overline{\frac{d_x}{m_x}\cdot\frac{\partial c}{\partial x}} = A\left[\left(\frac{\bar{d}_x}{\bar{m}_x}\right)\cdot\frac{\partial \bar{c}}{\partial x} + \overline{\left(\frac{d_x}{m_x}\right)'\cdot\frac{\partial c'}{\partial x}}\right]. \tag{50}$$

The covariance term of equation 50 is small relative to the product-of-averages term, so that it is conveniently absorbed into the latter term as was done in equation 32.

Utilizing the notations defined by equation 45, the cross-section-averaged form of the continuity equation is obtained from equation 39 as

$$\frac{\partial}{\partial t}(A\,\bar{m}_x) + \frac{\partial}{\partial x}(A\,\bar{v}_x) = 0. \tag{51}$$

The cross-section-averaged convection-diffusion equation is obtained by equating expressions 40 and 44, substituting 45, 47, and 48, and moving all diffusive flux terms to the right-hand side of the equation. It is

$$\frac{\partial}{\partial t}\left[A\,\bar{c}\,\bar{m}_x + A\,\overline{c'm'_x}\right] + \frac{\partial}{\partial x}\left(A\,\bar{c}\,\bar{v}_x\right) = \frac{\partial}{\partial x}\left[A\left(\frac{K_x}{\bar{m}_x} + \frac{\overline{d_x}}{\overline{m_x}}\right)\cdot\frac{\partial\bar{c}}{\partial x}\right]. \quad (52)$$

Introducing new notations $C=\bar{c}$, $V=\bar{v}_x$, $M=\bar{m}_x$, and

$$D = K_x + M\left(\frac{\overline{d_x}}{\overline{m_x}}\right), \quad (53)$$

the one-dimensional continuity and convection-diffusion equations are finally written as

$$\frac{\partial A}{\partial t} + \frac{1}{M}\frac{\partial}{\partial x}(AV) = 0, \quad (54)$$

and $$\frac{\partial}{\partial t}(AC) + \frac{\partial}{\partial t}\left[\frac{A\,\overline{c'm'_x}}{M}\right] + \frac{1}{M}\frac{\partial}{\partial x}(AVC) = \frac{1}{M}\frac{\partial}{\partial x}\left[\frac{AD}{M}\frac{\partial C}{\partial x}\right]. \quad (55)$$

In going from the depth-averaged equations 35 and 36 to the cross-section-averaged equations 54 and 55, no assumptions were introduced except for those related to the spatial covariance terms, such as equations 49 and 50. As was the case with k_x, the convective dispersion coefficient, K_x, induced by the widthwise variation of v_x and c, is an asymptotic approximation. Thus, its application assumes that solute concentration is well distributed over the channel width (Fischer, 1973). The overall mixing coefficient, D, as defined by equation 53, is more complicated than that for a rectangular Cartesian coordinate system, which may be obtained by letting $M=m_x=1$ in equation 53. Nevertheless, equation 53 clearly shows that contributions to the mixing coefficient are additive if one recalls that d_x, the two-dimensional mixing coefficient, is the sum of the convective dispersion coefficient induced by depth integration, k_x, a depth-averaged value of the turbulent diffusion coefficient, e_x, and the constant molecular diffusion coefficient, ε. According to Fischer's (1966) and other studies, the contribution of K_x to D is by far the most significant of all other contributions. Fischer's theory, as an extension of Taylor's, has been satisfactorily verified in a steady uniform open-channel flow.

The covariance $\overline{c'm'_x}$ in equation 55 is a term unique to the natural coordinate system, since it will be 0 in a rectangular Cartesian system, wherein $m'_x=0$. Noting that m'_x is determined predominantly by the geometry of the coordinate system, whereas c' is dependent on the widthwise distribution of solute concentration, which in turn depends on time, the covariance is probably of insignificant magnitude except at a sharp bend.

DISCUSSION AND SUMMARY

As outlined in the introduction, merits of the transport equation derived herein are drawn mostly from analytical considerations. By use of the natural coordinate system, one can define a stationary coordinate system for an entire flow field, in which the channel axis meanders and the width and depth vary from point to point. As no assumptions are introduced in the derivation process except those related to covariance terms between solute concentration and convective velocities, the transport equations thus derived apply to unsteady or nonuniform natural channel flows with moving boundaries.

On the other hand, in order to apply gradient-type diffusive flux models to various covariance terms, solute concentration must be well distributed over the depth and (or) the channel width. Another restriction is that, because of the present configuration of the natural coordinate systems, the predominant flow direction must be horizontal.

Gradient-type diffusive flux models were introduced into convection-diffusion equations with only cursory references to the mechanics of turbulent flows. Understanding the mechanics, however, is an essential prerequisite to applying the equations properly to a real turbulent flow. The reader is referred to Fischer's (1973) comprehensive review of the mechanics of mixing. Briefly, the gradient-type flux models for dispersion and diffusion have been verified as asymptotic approximations only in a steady uniform flow. Their applicability in an unsteady flow is less certain theoretically and experimentally. The convection-diffusion equations are workable models in most natural rivers and estuaries, where the average velocity is high and well defined and the scale of turbulence is small.

Transport equations in the natural coordinate system have two additional parameters, m_x and m_z, compared with those in a rectangular Cartesian coordinate system. Significance of these parameters beyond their analytical utility is not well known currently. Sayre and Yeh (1973) found that the range of m_x is from 0.84 to 1.14 for the Aspinwall Bend in the Missouri River near Cooper Nuclear Station, which probably represents one of the sharpest bends in a large river. It is thus apparent that, for one-dimensional equations, the metric coefficient, M, will tend to unity if one locates the x axis in the central part of a channel as Sayre and Yeh did in their Missouri study.

Despite some uncertainties and limitations arising from the current knowledge on the mechanics of turbulent mixing, equations 16 and 17 for three (space) dimensions, equations 35 and 36 for two dimensions, and equations 54 and 55 for one dimension represent one of the most workable forms of equations for solute transport by turbulent flow in a natural channel.

NOTATIONS

A	cross-sectional area along a transverse coordinate
C	cross-sectional-averaged solute concentration
c	depth-averaged solute concentration
D	cross-section-averaged mixing coefficient
d_x, d_z	depth-averaged mixing coefficients
e_x, e_y, e_z	turbulent diffusion coefficients
F	function
$\vec{f}$	diffusive solute flux vector at flow boundary
h	local flow depth, $= Y_S - Y_B$
$\vec{i}$	unit vector in the longitudinal direction
$\vec{j}$	unit vector in the vertical direction
$\vec{k}$	unit vector in the transverse direction
k_x, k_z	convective dispersion coefficient induced by depthwise variation of s and u_x (u_z)
K_x	convective dispersion coefficient induced by widthwise variation of c and v_x
L_x, ΔL_x, L_{OA}, L_{BC}	distance along a longitudinal coordinate
L_z, ΔL_z, L_{OB}, L_{AC}	distance along a transverse coordinate
m_x, m_z	metric coefficients
M	cross-section-averaged longitudinal metric coefficient
$\vec{n}$	unit normal vector at flow boundary
p	function
q	function
s	time-averaged solute concentration
t, t_2, t_1	time
T	time interval, $= t_2 - t_1$
u_x, u_y, u_z	time-averaged velocities
v_x, v_z	depth-averaged velocities
V	cross-section-averaged longitudinal velocity
x	distance along the longitudinal axis from origin
y	distance along the vertical axis from origin
Y, Y_S, Y_B	values of y at flow boundaries
z	distance along the transverse axis from origin
Z, Z_L, Z_R	values of z at flow boundaries
α	parameter
β	parameter
ε	molecular diffusion coefficient
θ	instantaneous solute concentration
ϕ	function
ψ	function
$\vec{\omega}$, ω_x, ω_y, ω_z	instantaneous velocity vector and components
∇	divergence operator
∇^2	divergent gradient operator

REFERENCES CITED

Aris, R., 1956, On the dispersion of a solute in a fluid flowing through a tube: Royal Soc. [London] Proc., v. 235A, p. 67–77.

Chang, Y. C., 1971, Lateral mixing in meandering channels: Iowa City, Iowa Univ., Ph. D. dissert., 195 p.

Crowley, W. P., 1968, Numerical advection experiments: Monthly Weather Rev., v. 96, no. 1, p. 1–11.

Dagan, G., 1969, Dispersivity tensor for turbulent uniform channel flow: Am. Soc. Civil Engineers Proc., Hydraulics Div. Jour., v. 95, no. HY5, p. 1699–1712.

Daily, J. W., and Harleman, D. R. F., 1966, Fluid dynamics: Cambridge, Mass., Addison-Wesley Publishing Co., Inc.

Elder, J. W., 1959, The dispersion of marked fluid in turbulent shear flow: Jour. Fluid Mechanics, v. 5, pt. 4, p. 544–560.

Fischer, H. B., 1966, Longitudinal dispersion in laboratory and natural streams: Calif. Inst. Technology, W. M. Keck Lab. Hydraulics and Water Resources Rept. KH–R–12, 250 p.

——— 1973, Longitudinal dispersion and turbulent mixing in open-channel flow, *in* Volume 5, Annual review of fluid mechanics: Palo Alto, Calif., Annual Reviews, Inc., p. 59–78.

Fukuoka, S., and Sayre, W. W., 1973, Longitudinal dispersion in sinuous channels: Am. Soc., Civil Engineers Proc., Hydraulics Div. Jour., v. 99, no. HY1, p. 195–217.

Hinze, J. O., 1959, Turbulence: New York, McGraw-Hill Book Co., p. 275–375.

Holley, E. R., 1971, Transverse mixing in Rivers: Delft, Netherlands, Delft Hydraulics Lab. Rept. S132, 92 p.

Kaplan, W., 1953, Advanced calculus: Cambridge, Mass., Addison-Wesley Publishing Co., Inc., p. 151–158.

Korn, G. A., and Korn, T. M., 1961, Mathematical handbook for scientists and engineers: New York, McGraw-Hill Book Co., Inc., p. 100.

Leendertse, J. J., 1970, A water-quality simulation model for well-mixed estuaries and coastal seas; Volume 1, Principles of Computation: Santa Monica, Calif., Rand Corp. Memo. Rm–6230–RC., 71 p.

Monin, A. S., and Yaglom, A. M., 1973, Statistical fluid mechanics; mechanics of turbulence: Cambridge, Mass., Massachusetts Inst. Technology Press, p. 205–218.

Sayre, W. W., 1967, Dispersion of mass in open-channel flow: Fort Collins, Colorado State Univ., Ph. D. dissert., 192 p.

Sayre, W. W., and Yeh, T. P., 1973, Transverse mixing characteristics of the Missouri River downstream from the Cooper Nuclear Station : Iowa Univ., Iowa Inst. Hydraulic Research, IIHR Rept. 145, 46 p.

Taylor, G. I., 1954, The dispersion of matter in turbulent flow through a pipe: Royal Soc. [London], Proc., ser. A, v. 223, p. 446–468.

Yotsukura, N., and Sayre, W. W., 1976, Transverse mixing in natural channels: Water Resources Research, v. 12, no. 4, p. 695–704.

Jour. Research U.S. Geol. Survey
Vol. 5, No. 3, May–June 1977, p. 285–300

STREAMFLOW CHARACTERISTICS RELATED TO CHANNEL GEOMETRY IN THE MISSOURI RIVER BASIN

By E. R. HEDMAN and W. M. KASTNER, Lawrence, Kans.

Abstract.—The relation of flood-frequency characteristics and mean annual runoff values to active-channel and depositional-bar geometry are presented for six regions in the Missouri River basin. Equations were derived by regression analyses based on the correlation of flow characteristics with the dimensions of the channel geometry. The flow characteristics also were related to the drainage area and a precipitation parameter for comparison. Data for continuous-record gaging stations were used in the derivation. The standard errors for the equations relating either active-channel or depositional-bar widths to mean annual runoff ranged from 26 to 53 percent. The equations relating either active-channel or depositional-bar widths to the flood-frequency discharges of 2, 5, 10, 25, 50, and 100 years had standard errors ranging from 29 to 84 percent.

The purpose of this study was to develop and improve reconnaissance techniques based on measurable channel geometry that would provide indirect determinations of streamflow characteristics at ungaged sites in the Missouri River basin. Previous investigations by Moore (1968) in Nevada, by Hedman (1970) in California, and by Hedman and Kastner (1972) in Kansas have shown the feasibility of estimating the mean annual runoff from the width and average depth measured at cross sections between depositional bars in the stream channel. A study by Hedman, Moore, and Livingston (1972) in Colorado showed the feasibility of estimating mean annual runoff and flood-frequency discharges using depositional-bar geometry. A study by Hedman, Kastner, and Hejl (1974) showed the feasibility of estimating flood-frequency discharges from the width and average depth measured at cross sections of the active channel. The study presented here investigated the use of the depositional-bar and active-channel methods. The width and the average depth of both cross sections were measured when possible and were related to the mean annual runoff and flood-frequency discharges.

Planners and designers would benefit from quick, reliable techniques for estimating flow characteristics. The data from a stream-gaging program produce reliable estimates of flow characteristics only after records have been collected for several years. Relations have been defined for quickly estimating flow characteristics at ungaged sites from drainage-basin indices measured on available maps. However, such estimates are sometimes of low reliability, and a technique using field measurements to improve the reliability of the estimates is needed.

Analyses for this study were made for the purpose of establishing a relation of flood-frequency and mean annual runoff values to the channel geometry of streams in the Missouri River basin.

CHANNEL-GEOMETRY FEATURES

Several channel-geometry features have been investigated as reference levels for estimating streamflow characteristics. The depositional bar and the active channel were selected for this study. The geometry of these two features was measured, and their measurements were related to the mean annual runoff and the flood-frequency discharges.

Depositional-bar geometry

The depositional bars used in this study were the same channel bars used and described in previous studies by Hedman (1970), Hedman and Kastner (1972), and Hedman, Moore, and Livingston (1972). These bars are synonymous with those described by R. F. Hadley (written commun., 1972) as follows:

> A longitudinal, in-channel depositional feature formed along the borders of a stream channel at a stage of the flow regime when the local competence of the stream is incapable of moving the sediment particles on the submerged surface of the bar. Emerged channel bars are generally free of perennial vegetation. A channel bar may extend for a considerable distance along the channel or it may be one of a series of bars that occupy similar relative positions in the channel. These features previously have been termed berms in the literature (Moore, D. O., 1968, p. 34, and Hedman, E. R., 1970, p. E5).

Methods for selecting the bars and for measuring the cross sections have been fairly well standardized. The reference point used to measure the geometry of the depositional bars is selected at the streamward shoulder of the bar. It is very important not to use isolated bars caused by scour and deposition resulting from obstructions in a channel, such as boulders, logs, or bridge piers. Bars that are used to determine the reference levels should continue or reappear along the stream, and the reference levels should be consistently at approximately the same elevation.

Active-channel geometry

The active channel is a geomorphic expression of recent discharges. Depositional features within the active channel are altered and shifted regularly during the normal fluctuation of streamflow. Beyond the boundaries of the active channel the geomorphic features are generally permanent and vegetated. The sides of the active channel, which contain the discharge at normal stages, are formed by relatively steep sloped banks.

The reference level used to measure the geometry of the active channel is selected where the banks abruptly change to a more gently sloping surface. This level is associated with the stabilizing influence of riparian vegetation. Hence, the break in slope identifying the active-channel reference level is generally coincident with the lower limit of permanent vegetation. However, caution is necessary in using the vegetation line. If high flows are infrequent, some grasses and sedges may grow down the banks into the water, and in arid regions banks may not support vegetation. The active-channel reference points are above and shoreward from the reference level defined by the more temporary depositional bars, and the width and average depth of the active-channel cross sections are about 30 and 130 percent greater, respectively, for the stations that have been measured.

Sculpturing of the active channel occurs at all discharges. Floodflows tend to enlarge the channels by caving and cutting the banks. If the width of the channel is larger than necessary for quasi-equilibrium, the unused parts of the wide channel are healed by vegetation which stabilizes these areas and induces deposition. The action of healing or reducing the channel is a slow but effective way of reducing a width that has been enlarged by high floodflows. The active-channel width represents a balance between the narrowing forces and the general regime of the stream. Reduction of the channel width toward an equilibrium width occurs much faster in humid regions that have ample vegetation. In some regions where vegetation is sparse the material in the channel is mostly sand, floods are frequent, and the channels may never heal except in reaches where the bank caving is restricted by extremely large bed material or a rock outcrop.

COLLECTION OF FIELD DATA

The channel surveys were made at continuous-record stations in the Missouri River basin where relatively stable depositional-bar and active-channel cross sections could be identified and where the streamflow records provided good estimates of streamflow characteristics.

At cross sections where the reference points for the depositional-bar or the active-channel width were adequately defined, a tape or graduated tag line was stretched tightly across and perpendicular to the low-water channel as shown in figure 1. The width, in feet, was measured between the reference points (A–A' or B–B' in fig. 1). The depths, in feet, were measured from the line to the streambed at 10 to 15 equidistant points, and the mean depth was computed by the mid-section method. Because the channel dimensions of width and average depth may have varied along the channel, two or three cross sections were surveyed at

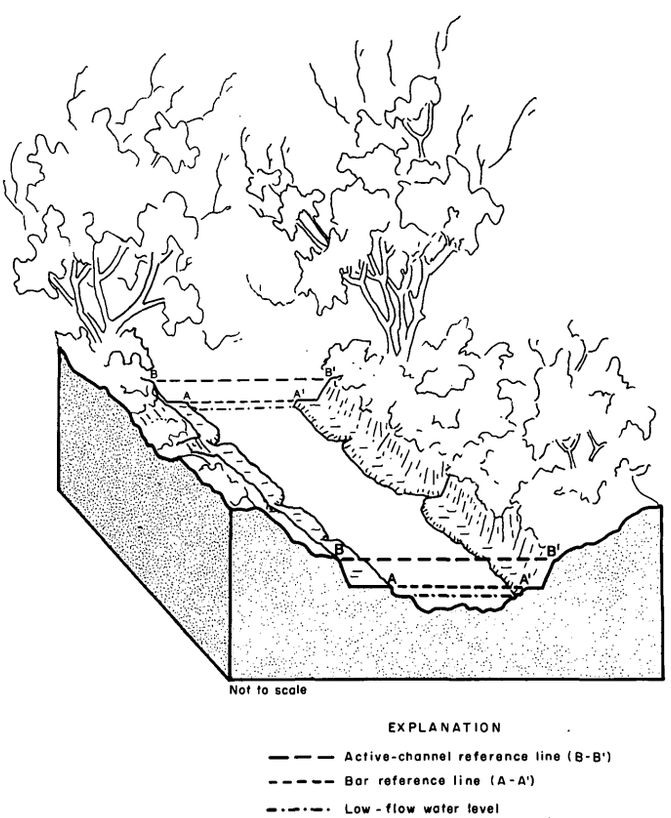

FIGURE 1.—Typical stream cross section.

each of the gaging sites. Cross sections were located one or more stream widths apart.

Field training and experience are necessary for effective selection of depositional bars and the active channel used to establish the reference levels. Unusually shaped channel cross sections should not be used. Bars of approximately the same shape and width should continue or reappear along the stream, and the reference points on opposite banks should be consistently about the same elevation in the same general reach of channel.

Cross sections that have the reference points defined by the depositional-bars (A–A') and active-channel geometry (B–B') are shown in the photographs in figures 2–5.

In this study relatively straight or stabilized reaches of meandering channels were selected where active bank cutting or deposition was not in the process of altering the channel width. Braided reaches were avoided as were reaches in the channel that indicated the channel had been widened or realined by an extreme flood or by construction work and had not had time to heal. Likewise, reaches having banks that could not be rapidly sculptured by the water (that is, banks composed of resistant material such as bedrock and reaches lined with riprap or concrete and having abnormally narrow widths) were not used. Reaches with large pools or steep inclines also were avoided.

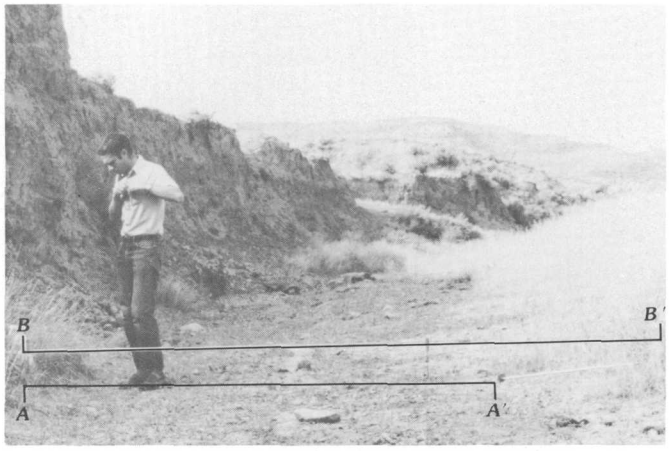

FIGURE 4.—Reference points for depositional bars (A –A') and the active channel (B –B') in a reach of a stream in region 1 and region A (Wyoming).

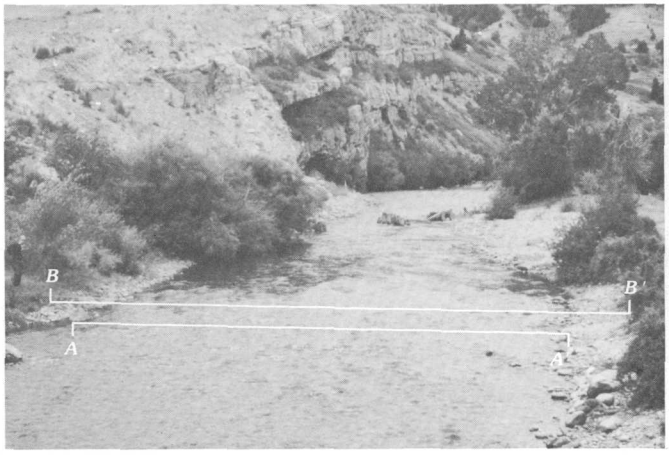

FIGURE 2.—Reference points for depositional bars (A –A') and the active channel (B –B') in a reach of a stream in the mountain region (Montana).

FIGURE 5.—Reference points for depositional bars (A –A') and the active channel (B –B') in a reach of a stream in region 4 and region C (Kansas).

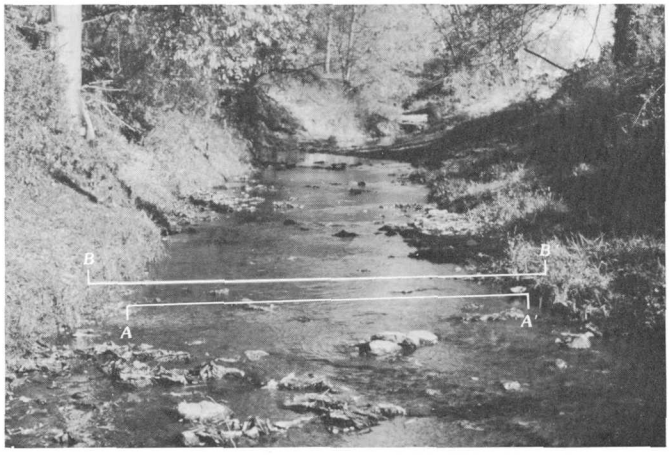

FIGURE 3.—Reference points for depositional bars (A –A') and the active channel (B –B') in a reach of a stream in region 3 and region D (Missouri).

GAGING-STATION DATA

The streamflow records in this study are from the Missouri River basin streams. The data from continuous-record stations having 20 or more years of record were used in the analyses and are listed in table 1. The

TABLE 1.—*Basin and streamflow characteristics at selected gaging stations*

Gaging station			Basin characteristics								Streamflow characteristics					
No.	Name	Length of record (years)	Active channel geometry width (ft)	Active channel geometry depth (ft)	Depositional bar width (ft)	Depositional bar depth (ft)	Total drainage area (mi^2)	Mean annual precipitation (in)	2-yr 24-hr precipitation (in)	Mean annual runoff (acre-foot)	2-yr flood discharge (ft^3/s)	5-yr flood discharge (ft^3/s)	10-yr flood discharge (ft^3/s)	25-yr flood discharge (ft^3/s)	50-yr flood discharge (ft^3/s)	100-yr flood discharge (ft^3/s)
060195	Ruby R. ab Res. nr Alder, Mt.	35	44	2.62	38	2.39	538.0	13.0	1.3	125300	915	1180	1340	1530	1660	1790
060330	Boulder R. nr Boulder, Mt.	43	44	2.02	35	0.87	381.0	12.0	1.5	87660	1100	1690	2100	2640	3040	3460
060350	Willow Cr. nr Harrison, Mt.	36	23	1.51	18	0.56	83.8	12.0	1.5	28260	235	364	454	571	661	752
060485	Bridger Cr. nr Bozeman, Mt.	25	22	1.86	19	0.81	62.5	14.0	1.9	26520	295	462	580	735	854	975
060615	Prickly Pear Cr. nr Clancy, Mt.	40	24	1.43	19	0.71	192.0	12.0	1.3	34990	265	415	520	658	763	871
060625	Tenmile Cr. nr Rimini, Mt.	59	19	0.85	13	0.42	32.7	12.0	1.3	12610	218	352	449	578	678	781
060770	Sheep Cr. nr White Sulphur Springs, Mt.	31	25	1.54	22	0.44	54.4	24.0	1.9	23110	211	300	359	433	487	541
060905	Belt Cr. nr Monarch, Mt.	22	62	1.76	52	0.58	368.0	20.0	2.1	129000	1590	2810	3750	5090	6190	7360
061100	Judith R. nr Utica, Mt.	53	38	1.22	33	0.72	328.0	17.0	2.0	38470	441	775	1030	1400	1700	2020
061155	N. Fk. Musselshell R. nr Delpine, Mt.	33	17	1.52	13	0.56	31.4	17.0	1.7	8690	87	162	224	314	389	471
061185	S. Fk. Musselshell R. ab Martinsdale, Mt.	32	47	1.84	35	0.47	287.0	14.0	1.7	59700	696	1010	1210	1480	1680	1880
061910	Gardner R., Yellowstone National Park	34	55	2.05	49	0.97	202.0	19.0	1.4	159400	1250	1580	1790	2020	2190	2350
061975	Boulder R. nr Contact, Mt.	30	86	2.46	70	1.35	226.0	23.0	2.3	275300	3650	4260	4620	5030	5300	5560
062065	Sunlight Cr. nr Painter, Wy.	29	49	2.04	-	-	135.0	17.5	1.7	91290	1170	1410	1550	1710	1830	1930
062685	Fifteen Mile Cr. nr Worland, Wy.	23	22	1.80	-	-	518.0	7.2	1.2	7900	1180	1870	2380	3070	3620	4200
062710	Ten Sleep Cr. nr Ten Sleep Wy.	41	51	2.19	44	1.40	247.0	16.7	1.7	105800	1630	2170	2520	2950	3280	3590
062890	Little Bighorn R. nr Wyola, Mt.	35	49	1.93	45	0.93	193.0	20.0	2.3	109400	1050	1460	1740	2100	2370	2640
062915	Lodgegrass Cr. nr Wyola, Mt.	35	24	1.58	24	0.70	80.7	15.0	2.2	35860	434	617	744	909	1040	1160
062980	Tongue R. nr Dayton, Wy.	44	52	2.60	50	1.60	204.0	25.5	2.4	135500	1630	2210	2600	3090	3460	3830
062985	Little Tongue R. nr Dayton, Wy.	22	16	0.71	16	0.50	25.1	18.5	1.5	9350	125	240	338	489	622	772
063110	N. Fk. Powder R. nr Hazelton, Wy.	26	16	1.60	14	0.60	24.5	20.0	2.1	10360	324	456	548	667	760	855
063145	N. Fk. Crazy Woman Cr. nr Grueb, Wy.	24	20	1.42	16	0.91	51.7	15.6	1.9	13400	270	591	897	1410	1900	2480
063155	Middle Fk. Crazy Woman Cr. nr Grueb, Wy.	31	25	1.20	-	-	82.7	15.6	1.9	16160	316	659	975	1490	1970	2530
063170	Powder River at Arvada, Wy.	54	145	2.29	98	1.20	6050.0	11.9	1.6	198500	7800	15000	21300	31300	40300	50700
063175	N. Fk. Clear Cr. nr Buffalo, Wy.	20	18	1.55	16	0.60	29.0	17.0	1.5	10060	191	345	472	664	829	1020
063185	Clear Cr. nr Buffalo, Wy.	52	35	1.77	31	0.90	120.0	17.0	1.5	45280	683	1070	1370	1780	2110	2460
063255	Little Powder R. nr Broadus, Mt.	24	30	2.03	15	0.15	1974.0	15.0	1.7	28690	1070	1730	2240	2970	3570	4230
063340	Little Missouri R. nr Alzada, Mt.	53	40	4.63	36	-	904.0	16.0	1.8	55930	1730	3300	4660	6780	8660	10800
063350	Little Beaver Cr. nr Marmath, ND	34	42	2.40	-	-	587.0	13.5	1.3	32170	3290	5930	8040	11100	13700	16500
063360	Little Missouri R. at Medora, ND	47	160	2.90	115	0.60	6190.0	14.1	1.4	343400	9760	20200	29400	43800	56500	71000
063365	Beaver Cr. at Wibaux, Mt.	29	18	1.20	14	0.70	351.0	14.0	1.6	16140	704	2430	4610	9080	14000	20700
063395	Knife R. nr Golden Valley, ND	29	38	3.30	34	0.70	1230.0	15.8	1.6	70200	3050	7150	11100	17700	23900	31300

TABLE 1.—*Basin and streamflow characteristics at selected gaging stations*—Continued

Gaging station			Basin characteristics								Streamflow characteristics					
No.	Name	Length of record (years)	Active channel geometry width (ft)	Active channel geometry depth (ft)	Depositional bar width (ft)	Depositional bar depth (ft)	Total drainage area (mi^2)	Mean annual precipitation (in)	2-yr 24-hr precipitation (in)	Mean annual runoff (acre-foot)	2-yr flood discharge (ft^3/s)	5-yr flood discharge (ft^3/s)	10-yr flood discharge (ft^3/s)	25-yr flood discharge (ft^3/s)	50-yr flood discharge (ft^3/s)	100-yr flood discharge (ft^3/s)
063400	Spring Cr. at Zap, ND	28	21	2.00	18	0.30	549.0	15.7	1.6	31730	1730	3520	5090	7520	9660	12100
063405	Knife R. at Hazen, ND	40	48	3.00	45	0.60	2240.0	15.8	1.6	131100	4820	10600	16000	24700	32600	41800
063430	Heart R. nr South Heart, ND	26	18	2.60	12	0.30	315.0	15.5	1.5	20210	1470	3640	5800	9500	13000	17300
063450	Green R. nr Gladstone, ND	28	22	2.00	17	0.30	356.0	15.5	1.6	25940	1370	3360	5320	8610	11700	15400
063470	Antelope Cr. nr Carson, ND	25	12	1.40	8.0	0.10	221.0	16.2	1.6	11660	1040	2870	4810	8290	11700	15900
063495	Apple Cr. nr Menoken, ND	27	21	2.60	16	0.40	1180.0	16.2	1.7	25790	580	1750	3090	5590	8160	11400
063500	Cannonball R. at Regent, ND	24	30	1.80	24	0.80	580.0	15.7	1.5	32670	1910	5050	8290	14000	19500	26200
063510	Cannonball R. below Bentley, ND	31	54	1.80	52	0.20	1140.0	15.7	1.5	64190	2800	7890	13400	23400	33300	45700
063520	Cedar Cr. nr Haynes, ND	24	19	1.80	17	0.30	553.0	15.1	1.5	24340	1050	3440	6310	11900	17900	25700
063525	Cedar Cr. nr Pretty Rock, ND	31	46	1.10	-	-	1340.0	15.2	1.5	53760	1680	5590	10300	19700	29700	42900
063540	Cannonball R. at Breien, ND	58	75	1.80	54	0.80	4100.0	15.6	1.6	178200	4700	11900	19200	31700	43600	57900
063545	Beaver Cr. at Linton, ND	24	28	2.60	17	0.20	617.0	16.6	1.7	30720	1030	3000	5180	9200	13300	18400
063555	N. Fk. Grand R. nr White Butte, SD	28	33	2.80	31	1.20	1190.0	14.0	1.9	42310	1230	4840	9900	21300	34900	54400
063565	S. Fk. Grand R. nr Cash, SD	28	26	2.30	22	0.43	1350.0	12.7	1.9	40720	1820	4330	6810	11100	15100	20000
063595	Moreau R. nr Faith, SD	30	36	1.58	-	-	2660.0	13.2	1.9	99980	3790	8840	13800	22000	29900	39300
063940	Beaver Cr. nr Newcastle, Wy.	29	24	3.16	20	1.20	1320.0	13.9	1.6	23690	1160	2190	3100	4530	5830	7340
063950	Cheyenne R. at Edgemont, SD	31	105	1.50	-	-	7143.0	14.3	1.8	76800	3410	6810	9930	15000	19700	25400
064000	Hat Cr. nr Edgemont, SD	24	20	1.00	16	0.90	1044.0	14.0	2.0	16810	1160	3300	5830	10900	16500	24000
064090	Castle Cr. ab Deerfield Res., nr Hill City, SD	25	13	1.18	11	1.00	83.0	19.5	2.0	7240	64	149	236	393	550	749
064105	Rapid Cr. ab Pactola Res., at Silver City, SD	20	24	1.08	21	0.35	292.0	21.0	2.0	29920	272	616	961	1560	2160	2900
064255	Elk Cr. nr Elm Springs, SD	23	26	2.05	-	-	540.0	16.9	2.0	18260	1150	4200	8390	17800	29000	45300
064265	Belle Fourche R. below Moorcroft, Wy.	27	26	3.63	22	1.60	1670.0	14.0	1.7	15210	755	1620	2450	3870	5240	6900
064305	Redwater Cr. at Wyoming-South Dakota State Line	24	22	3.21	-	-	471.0	20.0	1.8	25940	276	797	1420	2670	4060	5960
064315	Spearfish Cr. at Spearfish, SD	27	34	1.20	32	0.60	168.0	22.0	1.9	36320	296	730	1210	2110	3070	4330
064330	Redwater R. ab Belle Fourche, SD	28	49	1.62	38	0.80	920.0	20.0	1.8	95630	842	2070	3380	5790	8260	11400
064335	Hay Cr. at Belle Fourche, SD	20	5.0	0.74	-	-	121.0	18.5	1.8	942	53	183	360	756	1230	1930
064390	Cherry Cr. nr Plainview, SD	27	54	1.27	-	-	1190.0	13.3	2.0	34270	1580	3960	6460	11000	15600	21300
064410	Bad R. nr Midland, SD	28	36.0	0.95	14	-	1460.0	15.9	2.2	49410	2900	5680	8080	11800	15000	18600
064415	Bad R. nr Fort Pierre, SD	44	63	2.94	-	-	3107.0	16.3	2.2	112300	6030	12900	19100	29100	38200	48800
064420	Medicine Knoll Cr. nr Blunt, SD	24	13	0.62	6.0	0.20	455.0	17.4	2.3	3850	93	491	1170	2950	5360	9180
064440	White R. at Crawford, Nb.	39	13	1.67	9.9	0.48	313.0	17.6	1.9	14630	368	870	1400	2390	3410	4740
064460	White R. nr Oglala, SD	30	32	6.00	19	5.00	2200.0	15.9	2.0	41660	941	1830	2660	4050	5370	6970
064470	White R. nr Kadoka, SD	32	90.0	0.40	-	-	5000.0	15.9	2.1	209400	9890	15900	20700	27800	33900	40600
064495	Little White R. nr Rosebud, SD	30	52	3.01	48	-	1020.0	16.2	2.1	81140	821	1740	2630	4180	5700	7580
064505	Little White R. below White River, SD	28	55	0.80	46	0.33	1570.0	16.3	2.1	94910	2010	4460	6950	11400	15800	21400

TABLE 1.—*Basin and streamflow characteristics at selected gaging stations*—Continued

Gaging station			Basin characteristics								Streamflow characteristics					
No.	Name	Length of record (years)	Active channel teo-metry width (ft)	Active channel geo-metry depth (ft)	Deposi-tional bar width (ft)	Deposi-tional bar depth (ft)	Total drain-age area (mi^2)	Mean annual pre-cipi-tation (in)	2-yr 24-hr pre-cipi-tation (in)	Mean annual runoff (acre-foot)	2-yr flood dis-charge (ft^3/s)	5-yr flood dis-charge (ft^3/s)	10-yr flood dis-charge (ft^3/s)	25-yr flood dis-charge (ft^3/s)	50-yr flood dis-charge (ft^3/s)	100-yr flood dis-charge (ft^3/s)
064545	Niobrara R. ab Box Butte Res., Nb.	27	16	2.25	15	1.60	1400.0	16.2	1.9	22530	225	530	862	1490	2160	3040
064610	Minnechaduza Cr. at Valentine, Nb.	26	24	1.69	19	0.51	390.0	17.7	2.2	25100	224	380	514	721	907	1120
064625	Plum Cr. at Meadville, Nb.	26	52	2.06	44	0.32	600.0	21.0	2.3	77520	451	760	1020	1430	1790	2200
064635	Long Pine Cr. nr Riverview, Nb.	24	48	1.55	32	0.65	390.0	22.3	2.4	96360	1210	2520	3820	6110	8380	11300
064715	Elm R. at Westport, SD	27	31	1.30	-	-	1680.0	18.0	2.2	34120	678	2790	5750	12300	20000	30700
064730	James R. at Ashton, SD	28	60	4.20	-	-	11000.0	17.0	2.4	111600	564	1570	2640	4570	6480	8840
064735	S. Fk. Snake Cr. nr Athol, SD	29	14	1.02	10	0.36	1820.0	17.4	2.3	8110	99	569	1390	3570	6490	11100
064745	Turtle Cr. at Redfield, SD	27	18	1.74	-	-	1540.0	17.5	2.3	17940	219	1180	2800	6920	12300	20600
064785	James R. nr Scotland, SD	45	105	6.30	-	-	21550.0	19.3	2.3	279700	2080	4770	7300	11400	15200	19500
064790	Vermillion R. nr Wakonda, SD	28	39	2.00	30	0.50	1680.0	23.2	2.6	86940	1520	3710	5850	9440	12800	16800
064800	Big Sioux R. nr Brookings, SD	20	63	1.80	53	0.50	4420.0	21.4	2.5	122400	2200	6730	11900	21800	31900	44900
064810	Big Sioux R. nr Dell Rapids, SD	25	75	6.10	69	2.00	5060.0	21.7	2.6	199200	3150	8960	15300	26800	38300	52700
064815	Skunk Cr. nr Sious Falls, SD	25	30	1.20	23	0.40	570.0	23.9	2.6	36510	1620	4500	7590	13100	18600	25400
066000	Perry Cr. at 38th Street, Sioux City, Ia.	31	22	0.73	-	-	65.1	25.7	2.8	10940	2440	4970	7150	10500	13300	16600
066005	Floyd R. at James, Ia.	39	80	3.45	-	-	882.0	26.7	2.8	130400	3720	8910	13800	21600	28700	36900
060100	Omaha Cr. at Homer, Nb.	28	21	1.62	15	0.78	168.0	26.7	2.8	26520	3930	7620	10600	15000	18600	22500
066066	Little Sioux R. at Correctionville, Ia.	48	115	3.50	-	-	2500.0	27.7	2.9	500600	6560	12700	17700	25000	31000	37400
066072	Maple R. at Mapleton, Ia.	36	115	0.63	-	-	669.0	27.3	3.0	165900	6140	11200	15000	20500	24900	29500
066080	Tekamah Cr. at Tekamah, Nb.	24	15	0.90	11	0.43	23.0	29.4	2.9	4650	1630	3530	5200	7760	9980	12500
066085	Soldier R. at Pisgah, Ia.	34	88	2.38	-	-	407.0	27.5	3.0	90560	9240	15300	19600	25400	29900	34500
066090	New York Cr. at Herman, Nb.	24	22	1.20	12	0.20	25.4	19.0	3.0	4940	1220	3360	5560	9360	13000	17300
066160	N. Fk. Michigan R. nr Gould, Co.	23	18	1.28	15	0.51	21.2	26.0	1.4	12820	184	243	281	328	362	396
066210	Douglas Cr. nr Foxpark, Wy.	26	43	1.15	28	0.62	120.0	26.0	1.3	57020	910	1290	1550	1890	2140	2400
066675	N. Laramie R. nr Wheatland, Wy.	39	38	1.78	-	-	370.0	15.5	1.5	29780	646	1800	3140	5790	8680	12600
066710	Rawhide Cr. nr Lingle, Wy.	45	15	2.52	12	-	522.0	13.0	1.6	15580	225	548	892	1520	2170	2990
066775	Horse Cr. nr Lyman, Nb.	43	42	2.53	34	-	1570.0	15.0	1.7	46370	707	1330	1880	2750	3550	4490
066850	Pumpkin Cr. nr Bridgeport, Nb.	42	22	1.15	17	1.00	1020.0	15.7	1.9	22680	168	425	717	1290	1910	2740
066870	Blue Cr. nr Lewellen, Nb.	43	37	1.44	-	-	1120.0	16.6	2.1	50640	227	343	434	564	674	795
066920	Birdwood Cr. nr Hershey, Nb.	42	37	1.90	33	1.40	1000.0	18.5	2.2	110800	423	616	761	967	1140	1320
067105	Bear Cr. at Morrison, Co.	64	38	1.52	38	0.91	164.0	23.0	1.9	39270	498	1200	1910	3120	4290	5710
067165	Clear Cr. nr Lawson, Co.	28	58	2.06	41	1.70	147.0	26.0	1.3	99260	1050	1720	2230	2950	3520	4140
067195	Clear Cr. nr Golden, Co.	63	73	1.93	61	1.42	399.0	22.0	1.5	165200	1650	2630	3360	4370	5170	6020
067225	S St. Vrain Cr. nr Ward. Co.	24	21	1.29	20	0.90	14.4	23.0	1.8	20364	234	315	367	432	480	528
067240	St. Vrain Cr. at Lyons, Co.	83	63	1.65	47	1.27	212.0	22.0	2.1	93460	1130	1910	2510	3360	4050	4800
067255	Middle Boulder Cr. at Nederland, Co.	29	32	1.59	31	0.93	36.2	27.0	1.8	39270	439	607	718	859	965	1070

TABLE 1.—*Basin and streamflow characteristics at selected gaging stations*—Continued

Gaging station			Basin characteristics								Streamflow characteristics					
No.	Name	Length of record (years)	Active channel geometry width (ft)	Active channel geometry depth (ft)	Depositional bar width (ft)	Depositional bar depth (ft)	Total drainage area (mi^2)	Mean annual precipitation (in)	2-yr 24-hr precipitation (in)	Mean annual runoff (acre-foot)	2-yr flood discharge (ft^3/s)	5-yr flood discharge (ft^3/s)	10-yr flood discharge (ft^3/s)	25-yr flood discharge (ft^3/s)	50-yr flood discharge (ft^3/s)	100-yr flood discharge (ft^3/s)
067330	Big Thompson R. at Estes Park, Co.	27	50	1.65	49	0.81	137.0	31.0	1.8	92010	1010	1390	1650	1970	2220	2460
067715	Wood R. nr Gibbon, Nb.	25	17	1.02	9.2	0.12	572.0	22.9	2.4	10290	594	1400	2210	3650	5080	6860
067720	Wood R. nr Alda, Nb	20	19	0.73	11	0.13	628.0	23.0	2.5	8400	435	827	1170	1690	2160	2690
067825	S. Loup R. at Ravenna, Nb.	24	94	2.22	87	0.75	1570.0	21.3	2.4	140600	4040	8980	13800	22100	30000	39800
067835	Mud Cr. nr Sweetwater, Nb.	27	25	2.86	16	1.96	707.0	22.5	2.4	30600	1120	2700	4350	7310	10300	14000
067940	Beaver Cr. at Genoa, Nb.	33	50	2.53	41	0.91	627.0	24.6	2.7	92740	2540	5470	8180	12600	16600	21300
067955	Shell Cr. nr Columbus, Nb.	27	23	1.68	19	0.98	270.0	25.8	2.7	31810	1610	3050	4210	5900	7310	8830
067975	Elkhorn R. at Ewing, Nb.	27	89	1.70	59	0.91	1400.0	22.2	2.4	130400	1410	3340	5240	8480	11600	15300
068000	Maple Cr. nr Nickerson, Nb.	22	55	1.92	47	0.75	450.0	27.7	2.8	45000	2230	4640	6680	9750	12400	15200
068040	Wahoo Cr. at Ithaca, Nb.	24	43	2.79	27	1.78	271.0	29.0	2.9	56580	4700	12600	20700	34600	47700	63300
068060	Waubonsie Cr. nr Bartlett, Ia.	24	16	2.09	-	-	30.4	32.2	3.2	8110	2740	5960	8760	13000	16600	20600
068065	Weeping Water Cr. at Union, Nb.	24	34	3.11	23	0.70	241.0	29.8	3.1	57740	3980	10700	17500	29000	39600	52100
068090	Davids Cr. nr Hamlin, Ia.	22	22	2.73	-	-	26.0	31.0	3.2	8040	876	2470	4130	6990	9710	12900
068130	Tarkio R. at Fairfax, Mo.	51	88	6.00	72	4.00	508.0	32.0	3.3	131900	6360	11700	15600	20900	25100	29300
068140	Turkey Cr. nr Seneca, Ks.	25	34	2.76	23	0.72	276.0	30.9	3.2	89110	4640	9800	14100	20500	25700	31400
068160	Mill Cr. at Oregon, Mo.	24	12	1.24	9.5	0.46	4.9	34.0	3.4	1380	699	1560	2300	3430	4380	5420
068175	Nodaway R. nr Burlington Junction, Mo.	52	185	3.20	150	2.80	1240.0	32.0	3.3	379600	12700	23300	31300	42300	50900	59900
068200	White Cloud Cr. nr Maryville, Mo.	24	9.0	0.62	5.5	0.18	6.1	34.0	3.3	2350	727	1660	2480	3740	4820	6000
068210	Jenkins Branch at Gower, Mo.	24	8.4	0.70	4.5	0.29	2.7	34.0	3.4	1120	556	1320	2000	3040	3930	4910
068235	Buffalo Cr. nr Haigler, Nb.	33	6.0	1.12	6.0	-	260.0	17.8	2.2	5800	35	58	77	106	131	159
068240	Rock Cr. at Parks, Nb.	33	9.5	1.41	7.5	0.90	20.0	18.0	2.2	10360	47	86	120	174	223	280
068250	S. Fk. Republican R. nr Idalia, Co.	21	29	0.97	29	0.30	1300.0	16.0	2.1	23400	2850	9260	17600	35600	56800	87100
068255	Landsman Cr. nr Hale, Co.	23	11	1.28	7.5	0.40	268.0	16.0	2.1	2830	925	3990	8860	21200	37900	64400
068315	Frenchman Cr. nr Imperial, Nb.	33	29	1.73	25	1.17	880.0	18.8	2.1	50860	293	616	928	1460	1970	2600
068350	Stinking Water Cr. nr Palisade, Nb.	24	29	2.12	-	-	1500.0	19.9	2.2	31590	387	855	1330	2170	3010	4070
068410	Medicine Cr. ab Harry Strunk Lake, Nb.	24	32	2.52	25	1.19	770.0	20.7	2.3	51080	2440	5530	8770	14700	20800	28600
068450	Sappa Cr. nr Oberlin, Ks.	33	19	0.94	10	0.48	1063.0	18.3	2.2	12820	825	2470	4510	8770	13700	20500
068465	Beaver Cr. at Cedar Bluffs, Ks.	28	13	1.07	14	0.97	1618.0	17.8	2.2	16450	605	1510	2510	4390	6360	8950
068585	N. Fk.Smoky Hill R. nr McAllaster, Ks.	21	22	1.32	7.1	0.49	670.0	16.4	2.2	3550	470	2770	7300	21100	42600	81000
068595	Ladder Cr. below Chalk Cr. nr Scott City, Ks.	24	16	1.48	10	0.39	1460.0	17.8	2.3	6820	823	3460	7570	17900	31600	53100
068600	Smoky Hill R. at Elkader, Ks.	35	45	1.32	21	0.35	3555.0	17.0	2.3	27460	2080	9100	20400	49300	88400	151000
068635	Big Cr. nr Hays, Ks.	27	30	2.29	17	0.85	542.0	21.6	2.4	30570	2050	4610	7170	11600	16100	21500
068670	Saline R. nr Russell, Ks.	22	49	2.60	53	0.63	1502.0	21.6	2.4	86940	3520	8840	14500	24600	34800	47800
068710	N. Fk. Solomon R. at Glade, Ks.	21	47	1.16	45	0.41	849.0	20.0	2.4	24560	2530	7110	12400	22800	34000	49000
068715	Bow Cr. nr Stockton, Ks.	23	22	0.87	10	0.44	341.0	21.0	2.4	10720	1280	3300	5490	9570	13800	19200

TABLE 1.—*Basin and streamflow characteristics at selected gaging stations*—Continued

Gaging station			Basin characteristics								Streamflow characteristics					
No.	Name	Length of record (years)	Active channel geometry width (ft)	Active channel geometry depth (ft)	Depositional bar width (ft)	Depositional bar depth (ft)	Total drainage area (mi^2)	Mean annual precipitation (in)	2-yr 24-hr precipitation (in)	Mean annual runoff (acre-foot)	2-yr flood discharge (ft^3/s)	5-yr flood discharge (ft^3/s)	10-yr flood discharge (ft^3/s)	25-yr flood discharge (ft^3/s)	50-yr flood discharge (ft^3/s)	100-yr flood discharge (ft^3/s)
068730	S. Fk. Solomon R. ab Webster Res., Ks.	29	36	1.55	22	0.71	1035.0	20.0	2.4	53470	4450	13800	25500	49800	77200	115000
068840	Little Blue R. nr Fairbury, Nb.	53	118	3.45	82	1.27	2350.0	25.6	2.9	264400	6940	15700	23900	37700	50500	65700
068855	Black Vermillion R. nr Frankfort, Ks.	21	38	3.03	27	1.15	410.0	30.0	3.3	94910	7460	17300	26300	40300	52600	66500
068880	Vermillion Cr. nr Wamego, Ks.	31	37	3.70	25	1.38	243.0	31.4	3.3	65780	4780	10300	15000	22000	28000	34600
068915	Wakarusa R. nr Lawrence, Ks.	43	42	5.06	24	1.56	425.0	33.7	3.6	140600	6400	12400	17000	23500	28600	33900
068920	Stranger Cr. nr Tonganoxie, Ks.	45	42	4.00	20	1.58	406.0	34.4	3.7	155800	5920	11300	15500	21200	25800	30400
068935	Blue River nr Kansas City, Mo.	35	62	1.76	45	1.46	188.0	36.0	3.6	105800	9320	16200	21100	27500	32400	37400
068940	Little Blue R. nr Lake City, Mo.	26	45	4.10	27	2.10	184.0	36.0	3.6	94910	3730	6420	8310	10700	12600	14400
068950	Crooked R. nr Richmond, Mo.	25	37	3.25	29	2.05	159.0	36.0	3.4	71510	4300	8640	12100	17000	20900	25000
068960	Wakenda Cr. at Carrollton, Mo.	23	48	2.56	35	0.72	248.0	36.0	3.4	102200	4820	6620	7690	8920	9750	10500
068970	E. Fk. Big Cr. nr Bethany, Mo.	39	61	1.45	33	0.40	95.0	34.0	3.3	34990	2540	4380	5700	7430	8740	10100
068980	Thompson R. at Davis City, Ia.	42	150	5.28	132	2.28	701.0	31.5	3.3	261500	7530	11300	13700	16600	18700	20800
068990	Weldon R. at Mill Grove, Mo.	43	111	4.45	75	1.70	494.0	34.0	3.3	178200	11100	18900	24200	30900	35700	40300
069000	Medicine Cr. nr Galt, Mo.	51	57	3.30	43	1.90	225.0	36.0	3.3	100700	5710	10500	14000	18700	22200	25700
069070	Lamine R. at Clifton City, Mo.	49	90	3.50	58	1.49	598.0	40.0	3.5	331800	16100	27800	35700	45700	52900	60000
069080	Blackwater R. at Blue Lick, Mo.	47	90	6.67	-	-	1120.0	38.0	3.5	516600	10800	18600	23900	30600	35500	40200
069140	Pottawatomie Cr. nr Garnett, Ks.	34	63	4.40	43	0.96	334.0	38.0	3.8	160800	11500	21100	28200	37600	44800	52100
069165	Big Sugar Cr. at Farlinville, Ks.	24	41	2.88	33	0.88	198.0	40.0	3.8	93460	6990	13400	18200	24800	29900	35100
069175	Marmaton R. nr Fort Scott, Ks.	46	60	2.74	45	1.10	40.8	39.4	3.9	204300	11900	23700	32700	45000	54600	64300
069195	Cedar Cr. nr Pleasonton, Mo.	30	72	3.60	45	0.81	420.0	40.0	3.8	210800	8770	14700	18800	23800	27300	30800
069270	Maries R. at Westphalia, Mo.	25	72	2.07	60	0.97	257.0	40.0	3.6	152900	11500	15900	18500	21500	23500	25300
069300	Big Piney R. nr Big Piney, Mo.	51	90	5.80	85	2.80	560.0	42.0	3.7	386200	12000	20900	27100	34900	40500	46100
069315	Little Beaver Cr. nr Rolla, Mo.	26	10	0.52	7.0	0.12	6.4	42.0	3.7	3800	1420	2390	3050	3860	4440	5000
069320	Little Piney Cr. at Newburg, Mo.	44	55	2.84	-	-	200.0	42.0	317	108000	6400	12400	16900	22900	27400	31900

mean annual runoff is the average discharge for the period of record through the 1973 water year. The peak discharges are represented by discharges determined from the flood-frequency curves at recurrence intervals of 2, 5, 10, 25, 50, and 100 years. The flood-frequency curves were developed for this study by applying a Pearson type III distribution to the logarithms of annual peak discharges through the 1973 water year or for the period of record. Such a curve depends on the mean, the standard deviation, and the skew coefficient computed from the logarithms of the annual peaks. It is subject to the error inherent in estimating the population parameters from the sample statistics. The Water Resources Council (1967) recognized that the skew coefficient had greater variability between samples than the mean and the standard deviation. The

possible use of a regional value of skew coefficient was suggested in place of the value based on short records of annual peaks. Hardison (1974) presented a map of generalized skew coefficients for the conterminous United States. It presented an areal variation in generalized skew coefficients without abrupt changes. Skew coefficients were taken from Hardison's map and were used directly in the computation of the flood-frequency values in table I. Although the estimated long-term recurrence-interval values for some stations with shorter records were used collectively for this statistical analysis, these values should not be used individually.

MULTIPLE-REGRESSION ANALYSES

In this analysis all data were transformed to logarithms before defining the relation by multiple-regression techniques. Past experience has shown that this transformation allows linear relation to be approached when hydrologic variables are related. The use of antilogs causes the defined linear-regression equations to have the general form

$$Q=a(W_{DB}, W_{AC}, \text{ or } A)^{b_1}(D_{DB}, D_{AC}, \text{ or } P)^{b_2} \quad (1)$$

for the relation of discharge to channel geometry or of discharge to channel geometry, drainage area, and precipitation.

In the equations, Q is either Q_A, the mean annual runoff in acre-feet, or Q_2, Q_5, . . . Q_{100}, the peak discharge in cubic feet per second for the indicated recurrence interval in years; W_{DB} and W_{AC} are average widths, in feet, for the depositional-bar and active-channel measurements, respectively; D_{DB} and D_{AC} are average depositional-bar and active-channel depths, respectively, in feet; A is the total drainage area of the basin, in square miles; $P_{2,24}$ is the 2-year 24-hour precipitation intensity, in inches; P is the mean annual precipitation, in inches. The a is a regression constant obtained in the analysis and the b's are the regression coefficients. The equations presented in this analysis are to be used with English units.

The gaging-station number and name, the length of record, the basin characteristics (W_{AC}, D_{AC}, W_{DB}, D_{DB}, A, $P_{2,24}$ and P) to be used as independent variables, and the streamflow characteristics (Q_2, Q_5, Q_{10}, Q_{25}, Q_{50}, Q_{100}, and Q_A) to be used as dependent variables are all listed in table 1.

The regression program used is the stepwise-regression program BMD02R from the Biomedical computer programs developed by the School of Medicine at the University of California (Dixon, 1965). The program forms a sequence of linear-regression equations in a stepwise manner. In step one, a simple relation is defined using the one independent variable that most effectively explains the site-to-site variation of a selected flow characteristic. In each subsequent step, one variable is added to the equation. The variable added is the one that, by itself, causes the largest reduction in the error sum of squares and, therefore, can be considered to be the variable that will strengthen the equation more than any of the other unused available variables. This program also permits the inclusion of a specified variable in the equation regardless of its value in strengthening the equation.

The program provides regression equations, standard errors of estimate, coefficients of determination (R^2) indicating the proportion of the total variance in the dependent variable that has been explained by the equation, and F-ratios for testing the statistical significance of the equations and of each independent variable.

Most channel dimensions probably are formed by and linked to the flow regime of the stream with some of the dimensions being affected more by one part of the regime or by specific streamflow characteristics than by others. A specific streamflow characteristic is only one factor in a flow regime. The best correlation obtainable between a channel dimension and different streamflow characteristics would not be always the same channel dimension. The analyses by Hedman (1970), Hedman and Kastner (1972), and Hedman, Moore, and Livingston (1972) showed a good relation of annual runoff to the width and average depth at cross sections between depositional bars in the stream channel. The analyses by Hedman, Kastner, and Hejl (1974) showed a good relation of flood-frequency characteristics to the width of the active channel.

Both the channel and the streamflow characteristics differ markedly across the Missouri River basin. Mountain streams, which include snow melt, have different flow regimes than plains streams. The relationships between the channel geometry and the floodflow characteristics also differ.

The data for all the gaging stations listed in table 1 were included in the first analysis. The basin and climatic characteristics were introduced into the analysis in an attempt to differentiate the streamflow characteristics of the mountain and plains streams and, therefore, link the channel-geometry equations for these two stream types. This approach did not improve the results significantly.

Apparently the streambed and the bank material in the reaches of channel that were studied defined the channel shape and affected the relation of the channel geometry to the streamflow characteristics. The more

cohesive materials may limit the rate of sculpturing, whereas, the less cohesive materials may limit the rate of healing of the channels. The size of the bed material probably could be used to measure the cohesiveness, but too few data were available to accurately test this hypothesis.

Because these variations could not be explained by measurable parameters, the basin was divided into six regions on the basis of sediment availability, vegetation, climate, and topography in order to analyze the annual runoff as shown in figure 6. Six different regions, shown in figure 7, were chosen for measurement of flood discharges. The boundaries of the regions were then adjusted after the first analyses and the regressions were rerun.

For each of the regions shown in figures 6 and 7, equations are presented that express the relation of the streamflow characteristics to the width of the active channel (W_{AC}), the width of the depositional bar (W_{DB}), and the basin characteristics (A, P, or $P_{2,24}$). The depth of the active channel (D_{AC}) and depositional bar (D_{DB}) were included if they reduced the standard error.

The equations that had the lowest standard errors correlating mean annual runoff to channel-geometry parameters are given in table 2. Equations that had the lowest standard errors correlating the flood-frequency discharges to channel-geometry parameters are given in table 3. In both tables, equations that had the lowest standard errors correlating the streamflow characteristics to drainage-basin parameters, such as area and precipitation, are shown for comparison.

In the equations, Q is either Q_A, the mean annual runoff in acre-feet, or Q_2, Q_5, . . . Q_{100}, the flood-frequency discharge in cubic feet per second for the indicated recurrence interval in years; W_{DB} and W_{AC} are average widths, in feet, for the depositional-bar and active-channel measurements, respectively; D_{DB} and D_{AC} are the average depositional-bar and active-channel depths, respectively, in feet; A is total drainage area of the basin, in square miles; $P_{2,24}$ is 2-year 24-hour precipitation intensity, in inches; P is mean annual precipitation, in inches.

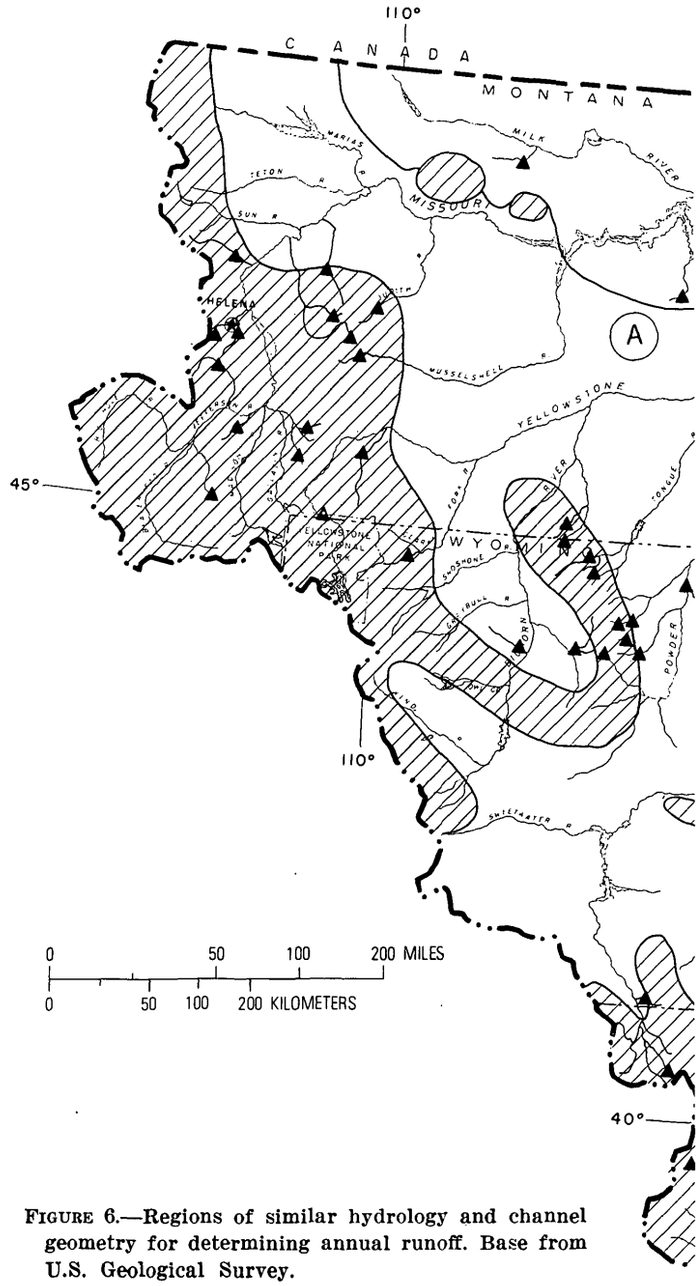

FIGURE 6.—Regions of similar hydrology and channel geometry for determining annual runoff. Base from U.S. Geological Survey.

LIMITS OF DEFINITION

The equations in this report can be considered to define relations only within the range of data used because regression analyses do not define actual physical relations. Equations were defined from data on streams having virtually natural flows. It might be expected that the equations would be valid for other conditions; however, it has not been demonstrated that the equations define relations for streams where flows are significantly affected by regulation or diversion. The equations also were defined only for measured widths between depositional bars of 4.5 to 132 feet (1.4 to 40.2 meters), average depths of 0.10 to 5.00 feet (0.03 to 1.52 m), measured active-channel widths of 5.0 to 185 feet (1.52 to 56.4 m), and average depths of 0.40 to 6.67 feet (0.12 to 2.03 m). The degree to which the equations reflect relations outside these ranges is unknown. Flows from urbanized areas would not be covered by

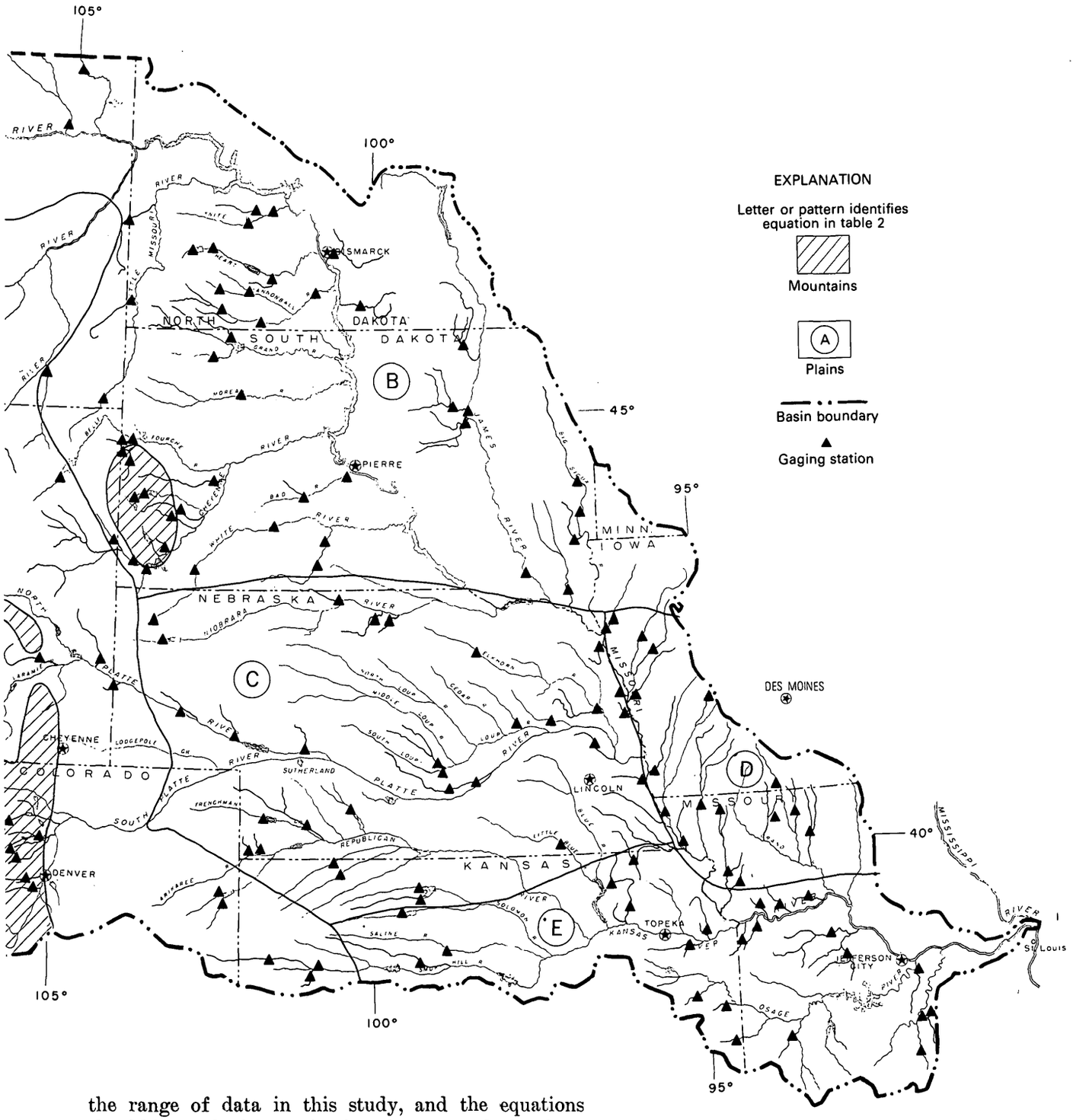

the range of data in this study, and the equations should be used with caution in urban watersheds where a high percentage of the drainage area has impervious surfaces or storm sewers.

Equations are only valid for English units. If metric values are desired, compute them with English units and then transform the answers to metric equivalents as follows:

English unit	*Multiply by*	*To obtain metric unit*
Inches (in)	2.54	Centimeters (cm)
Feet (ft)	0.3048	Meters (m)
Square miles (mi^2)	2.590	Square kilometers (km^2)
Cubic feet per second (ft^3/s)	28.32	Liters per second (L/s)
Acre-feet (acre-ft)	1,233	Cubic meters (m^3)

TABLE 2.—*Equations and standard errors of estimate for determining mean annual runoff*

Equation	Standard error of estimate in percent	Equation No.
Mountain regions		
$Q_A = 53.0\ W_{AC}^{1.907}$	27 (30, -23)	(2)
$Q_A = 87.1\ W_{AC}^{1.691}\ D_{AC}^{0.570}$	24 (27, -21)	(3)
$Q_A = 84.5\ W_{DB}^{1.863}$	30 (34, -25)	(4)
$Q_A = 37.3\ A^{0.834}\ P_A^{1.053}$	60 (76, -43)	(5)
Region A		
$Q_A = 77.0\ W_{AC}^{1.587}$	48 (58, -37)	(6)
$Q_A = 95.8\ W_{AC}^{1.455}\ D_{AC}^{0.497}$	44 (53, -34)	(7)
$Q_A = 196\ W_{DB}^{1.531}$	34 (39, -28)	(8)
$Q_A = 52.3\ A^{1.080}\ P_{2,24}^{-2.918}$	71 (94, -48)	(9)
Region B		
$Q_A = 157\ W_{AC}^{1.624}$	26 (29, -23)	(10)
$Q_A = 477\ W_{DB}^{1.411}$	30 (34, -25)	(11)
$Q_A = 66.5\ A^{0.290}\ P_A^{1.597}$	87 (120, -54)	(12)
Region C		
$Q_A = 488\ W_{AC}^{1.263}$	44 (53, -35)	(13)
$Q_A = 757\ W_{AC}^{1.008}\ D_{AC}^{0.817}$	33 (38, -28)	(14)
$Q_A = 714\ W_{DB}^{1.257}$	41 (49, -33)	(15)
$Q_A = 78.8\ A^{0.499}\ P_{2,24}^{3.374}$	87 (119, -54)	(16)
Region D		
$Q_A = 27.4\ W_{AC}^{1.842}$	37 (43, -30)	(17)
$Q_A = 73.9\ W_{DB}^{1.720}$	43 (52, -34)	(18)
$Q_A = 2.18\ A^{0.999}\ P_{2,24}^{4.202}$	14 (16, -13)	(19)
Region E		
$Q_A = 59.6\ W_{AC}^{1.935}$	33 (38, -28)	(20)
$Q_A = 197\ W_{AC}^{1.451}\ D_{AC}^{0.625}$	23 (26, -21)	(21)
$Q_A = 567\ W_{DB}^{1.483}$	53 (66, -40)	(22)
$Q_A = 1.98\ A^{0.833}\ P_{2,24}^{5.079}$	46 (56, -36)	(23)

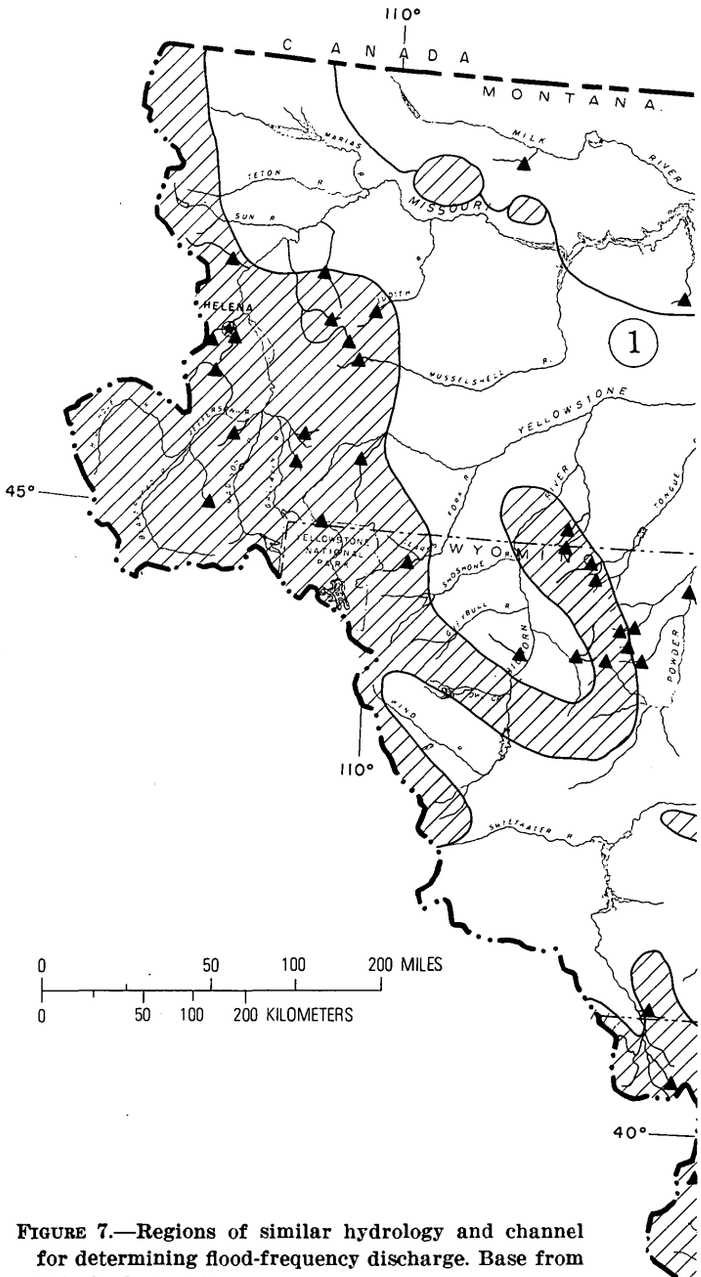

FIGURE 7.—Regions of similar hydrology and channel for determining flood-frequency discharge. Base from U.S. Geological Survey.

CONCLUSIONS

Channel-geometry measurements can be used to determine mean annual runoff and flood-frequency discharges for streams in the Missouri River basin. By use of the active-channel width, the standard error for mean annual runoff was 27 percent for mountain streams and ranged from 26 to 48 percent for plains streams. For the flood-frequency discharges of 2, 5, 10, 25, 50, and 100 years, the standard errors for regression equations using the active-channel width ranged from 27 to 50 percent for the mountains and 29 to 74 percent

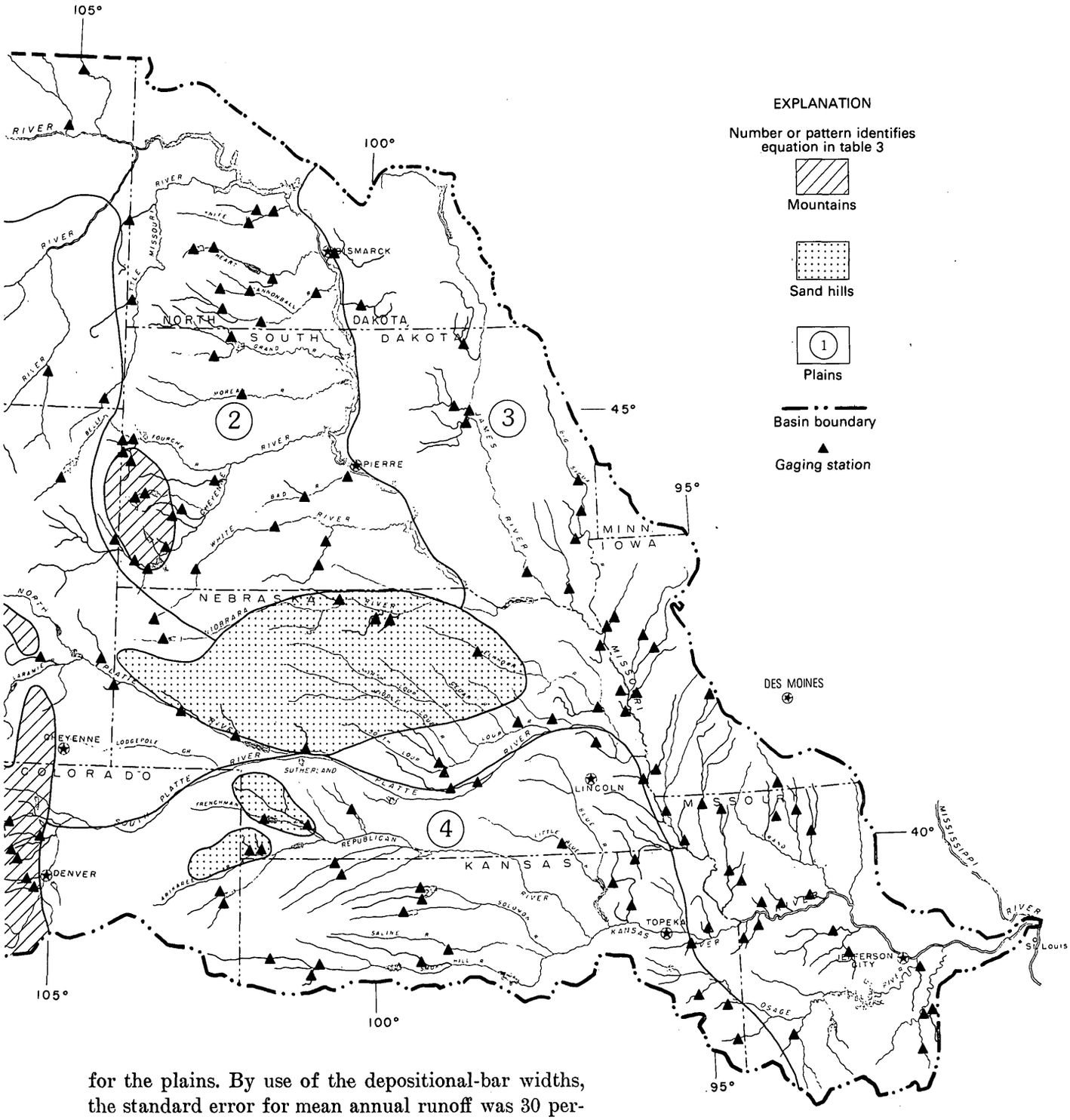

for the plains. By use of the depositional-bar widths, the standard error for mean annual runoff was 30 percent for the mountains and ranged from 30 to 53 percent for the plains. For the flood-frequency discharges of 2, 5, 10, 25, 50, and 100 years, the standard errors ranged from 31 to 50 percent for the mountains and from 31 to 84 percent for the plains. In most determinations the standard error of the regression equation was not improved with average depth of the active channel or depositional bar, and when the equation was improved the standard error was reduced an insignificant amount.

The basin characteristics, mean annual precipitation, and 2-year, 24-hour precipitation, gave a much better

TABLE 3.—*Equations and standard errors of estimate for determining flood-frequency discharge*

Equation	Standard error of estimate in percent	Equation No.
Mountains		
$Q_2 = 1.03\ W_{AC}^{1.768}$	31 (35, -26)	(24)
$Q_2 = 1.63\ W_{AC}^{1.571}\ D_{AC}^{0.521}$	29 (33, -25)	(25)
$Q_2 = 1.61\ W_{DB}^{1.720}$	36 (43, -30)	(26)
$Q_2 = 0.938\ A^{0.698}\ P_A^{1.020}$	69 (90, -47)	(27)
$Q_5 = 2.84\ W_{AC}^{1.613}$	27 (30, -23)	(28)
$Q_5 = 3.99\ W_{DB}^{1.588}$	31 (36, -26)	(29)
$Q_5 = 1.85\ A^{0.689}\ P_A^{0.963}$	54 (67, -40)	(30)
$Q_{10} = 4.87\ W_{AC}^{1.529}$	30 (34, -26)	(31)
$Q_{10} = 6.46\ W_{DB}^{1.517}$	33 (38, -28)	(32)
$Q_{10} = 2.55\ A^{0.684}\ P_A^{0.945}$	49 (60, -38)	(33)
$Q_{25} = 8.76\ W_{AC}^{1.436}$	37 (44, -30)	(34)
$Q_{25} = 10.9\ W_{DB}^{1.439}$	39 (46, -32)	(35)
$Q_{25} = 3.56\ A^{0.679}\ P_A^{0.930}$	47 (57, -36)	(36)
$Q_{50} = 12.9\ W_{AC}^{1.374}$	43 (52, -34)	(37)
$Q_{50} = 15.3\ W_{DB}^{1.388}$	44 (53, -35)	(38)
$Q_{50} = 4.37\ A^{0.675}\ P_A^{0.924}$	47 (58, -37)	(39)
$Q_{100} = 18.3\ W_{AC}^{1.318}$	50 (61, -38)	(40)
$Q_{100} = 20.9\ W_{DB}^{1.341}$	50 (62, -38)	(41)
$Q_{100} = 5.20\ A^{0.672}\ P_A^{0.921}$	49 (61, -38)	(42)
Sandhills		
$Q_2 = 2.54\ W_{AC}^{1.392}$	30 (34, -26)	(43)
$Q_2 = 2.98\ W_{AC}^{1.218}\ D_{AC}^{0.814}$	26 (29, -23)	(44)
$Q_2 = 2.50\ W_{DB}^{1.479}$	34 (40, -29)	(45)
$Q_2 = .000927\ A^{0.640}\ P_A^{2.906}$	76 (102, -50)	(46)
$Q_5 = 4.12\ W_{AC}^{1.435}$	41 (49, -33)	(47)
$Q_5 = 4.32\ W_{DB}^{1.506}$	48 (59, -37)	(48)
$Q_5 = .00826\ A^{.672}\ P_A^{3.091}$	82 (111, -53)	(49)

TABLE 3.—*Equations and standard errors of estimate for determining flood-frequency discharge*—Continued

Equation	Standard error of estimate in percent	Equation No.
Sandhills--Continued		
$Q_{10} = 5.51\ W_{AC}^{1.453}$	49 (60, -38)	(50)
$Q_{10} = 5.95\ W_{DB}^{1.515}$	58 (73, -42)	(51)
$Q_{10} = .000883\ A^{0.689}\ P_A^{3.150}$	87 (119, -54)	(52)
$Q_{25} = 7.71\ W_{AC}^{1.468}$	59 (76, -43)	(53)
$Q_{25} = 8.60\ W_{DB}^{1.521}$	69 (90, -47)	(54)
$Q_{25} = .00102\ A^{0.706}\ P_A^{3.198}$	94 (131, -57)	(55)
$Q_{50} = 9.69\ W_{AC}^{1.477}$	67 (87, -46)	(56)
$Q_{50} = 11.0\ W_{DB}^{1.524}$	77 (103, -51)	(57)
$Q_{50} = .00118\ A^{0.718}\ P_A^{3.212}$	99 (140, -58)	(58)
$Q_{100} = 12.0\ W_{AC}^{1.483}$	74 (98, -50)	(59)
$Q_{100} = 13.9\ W_{DB}^{1.525}$	84 (115, -54)	(60)
$Q_{100} = .00141\ A^{0.728}\ P_A^{3.208}$	105 (150, -60)	(61)
Region 1		
$Q_2 = 5.01\ W_{AC}^{1.497}$	57 (72, -42)	(62)
$Q_2 = 6.94\ W_{DB}^{1.518}$	52 (65, -39)	(63)
$Q_2 = 9.91\ A^{0.940}\ P_{2,24}^{-3.931}$	88 (122, -55)	(64)
$Q_5 = 21.4\ W_{AC}^{1.314}$	35 (41, -29)	(65)
$Q_5 = 34.9\ W_{DB}^{1.276}$	45 (55, -35)	(66)
$Q_5 = 31.1\ A^{0.796}\ P_{2,24}^{-2.656}$	85 (116, -54)	(67)
$Q_{10} = 47.1\ W_{AC}^{1.212}$	30 (34, -26)	(68)
$Q_{10} = 82.7\ W_{DB}^{1.137}$	49 (60, -38)	(69)
$Q_{10} = 57.4\ A^{0.718}\ P_{2,24}^{-1.969}$	84 (115, -54)	(70)
$Q_{25} = 112\ W_{AC}^{1.101}$	32 (37, -27)	(71)
$Q_{25} = 211\ W_{DB}^{0.989}$	57 (72, -42)	(72)
$Q_{25} = 61.9\ A^{0.627}$	85 (116, -54)	(73)
$Q_{25} = 112\ A^{0.634}\ P_{2,24}^{-1.216}$	85 (117, -54)	(74)
$Q_{50} = 198\ W_{AC}^{1.027}$	38 (44, -31)	(75)

TABLE 3.—*Equations and standard errors of estimate for determining flood-frequency discharge*—Continued

Equation	Standard error of estimate in percent	Equation No.
Region 1--Continued		
$Q_{50} = 390\ W_{DB}^{0.892}$	64 (83, -45)	(76)
$Q_{50} = 121\ A^{0.575}$	84 (114, -53)	(77)
$Q_{50} = 172\ A^{0.580}\ P_{2,24}^{-0.723}$	87 (118, -54)	(78)
$Q_{100} = 334\ W_{AC}^{0.959}$	44 (54, -35)	(79)
$Q_{100} = 307\ W_{AC}^{1.070}\ D_{AC}^{-0.467}$	38 (45, -31)	(80)
$Q_{100} = 683\ W_{DB}^{0.804}$	72 (95, -49)	(81)
$Q_{100} = 224\ A^{0.529}$	84 (115, -53)	(82)
$Q_{100} = 256\ A^{0.531}\ P_{2,24}^{-0.273}$	88 (122, -55)	(83)
Region 2		
$Q_2 = 48.8\ W_{AC}^{1.086}$	38 (44, -31)	(84)
$Q_2 = 55.5\ W_{AC}^{0.996}\ D_{AC}^{0.266}$	36 (42, -30)	(85)
$Q_2 = 135\ W_{DB}^{0.828}$	35 (41, -29)	(86)
$Q_2 = 68.9\ A^{0.529}\ P_{2,24}^{-0.581}$	38 (45, -31)	(87)
$Q_5 = 188\ W_{AC}^{0.966}$	29 (33, -25)	(88)
$Q_5 = 204\ W_{AC}^{0.912}\ D_{AC}^{0.162}$	29 (33, -25)	(89)
$Q_5 = 362\ W_{DB}^{0.820}$	31 (35, -26)	(90)
$Q_5 = 279\ A^{0.487}\ P_{2,24}^{-0.891}$	28 (32, -24)	(91)
$Q_{10} = 373\ W_{AC}^{0.910}$	30 (35, -26)	(92)
$Q_{10} = 592\ W_{DB}^{0.821}$	32 (37, -27)	(93)
$Q_{10} = 561\ A^{0.465}\ P_{2,24}^{-0.990}$	29 (33, -29)	(94)
$Q_{25} = 759\ W_{AC}^{0.854}$	35 (41, -29)	(95)
$Q_{25} = 990\ W_{DB}^{0.825}$	36 (42, -30)	(96)
$Q_{25} = 1150\ A^{0.440}\ P_{2,24}^{-1.038}$	34 (39, -28)	(97)
$Q_{50} = 1190\ W_{AC}^{0.820}$	40 (47, -32)	(98)
$Q_{50} = 1370\ W_{DB}^{0.828}$	40 (48, -32)	(99)
$Q_{50} = 2200\ W_{DB}^{0.731}\ D_{DB}^{0.208}$	39 (46, -32)	(100)
$Q_{50} = 1810\ A^{0.0424}\ P_{2,24}^{-1.051}$	39 (46, -32)	(101)

TABLE 3.—*Equations and standard errors of estimate for determining flood-frequency discharge*—Continued

Equation	Standard error of estimate in percent	Equation No.
Region 2--Continued		
$Q_{100} = 1870\ W_{AC}^{0.778}$	43 (52, -34)	(102)
$Q_{100} = 1980\ W_{DB}^{0.811}$	42 (50, -34)	(103)
$Q_{100} = 3480\ W_{DB}^{0.696}\ D_{DB}^{0.247}$	40 (48, -33)	(104)
$Q_{100} = 2840\ A^{0.402}\ P_{2,24}^{-1.030}$	42 (51, -34)	(105)
Region 3		
$Q_2 = 41.1\ W_{AC}^{1.049}$	70 (92, -48)	(106)
$Q_2 = 79.6\ W_{DB}^{0.952}$	65 (84, -46)	(107)
$Q_2 = 0.00125\ A^{0.262}\ P_A^{3.916}$	96 (135, -58)	(108)
$Q_5 = 185\ W_{AC}^{0.875}$	46 (56, -36)	(109)
$Q_5 = 284\ W_{DB}^{0.824}$	43 (52, -34)	(110)
$Q_5 = 0.0779\ A^{0.250}\ P_A^{2.930}$	74 (98, -50)	(111)
$Q_{10} = 398\ W_{AC}^{0.786}$	38 (44, -31)	(112)
$Q_{10} = 537\ W_{DB}^{0.759}$	36 (42, -30)	(113)
$Q_{10} = 0.704\ A^{0.245}\ P_A^{2.394}$	64 (83, -45)	(114)
$Q_{25} = 881\ W_{AC}^{0.693}$	35 (41, -29)	(115)
$Q_{25} = 1040\ W_{DB}^{0.692}$	33 (39, -28)	(116)
$Q_{25} = 7.43\ A^{0.240}\ P_A^{1.815}$	56 (71, -42)	(117)
$Q_{50} = 1450\ W_{AC}^{0.635}$	37 (44, -30)	(118)
$Q_{50} = 1590\ W_{DB}^{0.650}$	36 (42, -29)	(119)
$Q_{50} = 589\ A^{0.227}\ P_{2,24}^{1.843}$	52 (65, -40)	(120)
$Q_{100} = 2270\ W_{AC}^{0.583}$	41 (49, -33)	(121)
$Q_{100} = 2290\ W_{DB}^{0.614}$	40 (48, -32)	(122)
$Q_{100} = 1040\ A^{0.232}\ P_{2,24}^{1.501}$	49 (60, -38)	(123)
Region 4		
$Q_2 = 26.2\ W_{AC}^{1.361}$	50 (62, -38)	(124)
$Q_2 = 69.5\ W_{DB}^{1.231}$	51 (63, -38)	(125)
$Q_2 = 0.0227\ A^{0.376}\ P_A^{2.932}$	49 (60, -38)	(126)

TABLE 3.—*Equations and standard errors of estimate for determining flood-frequency discharge*—Continued

Equation	Standard error of estimate in percent	Equation No.
Region 4--Continued		
$Q_5 = 179\ W_{AC}^{1.065}$	38 (45, -31)	(127)
$Q_5 = 433\ W_{DB}^{0.926}$	44 (53, -35)	(128)
$Q_5 = 36.2\ A^{0.338}\ P_{2,24}^{3.168}$	50 (61, -38)	(129)
$Q_{10} = 531\ W_{AC}^{0.884}$	41 (49, -33)	(130)
$Q_{10} = 1210\ W_{DB}^{0.743}$	48 (59, -37)	(131)
$Q_{10} = 135\ A^{0.333}\ P_{2,24}^{2.387}$	53 (66, -40)	(132)
$Q_{25} = 1790\ W_{AC}^{0.676}$	51 (63, -39)	(133)
$Q_{25} = 3750\ W_{DB}^{0.535}$	58 (74, -43)	(134)
$Q_{25} = 589\ A^{0.328}\ P_{2,24}^{1.476}$	58 (74, -43)	(135)
$Q_{50} = 4090\ W_{AC}^{0.530}$	62 (79, -44)	(136)
$Q_{50} = 8040\ W_{DB}^{0.390}$	68 (90, -47)	(137)
$Q_{50} = 1610\ A^{0.325}\ P_{2,24}^{0.837}$	63 (81, -45)	(138)
$Q_{100} = 8720\ W_{AC}^{0.395}$	73 (97, -49)	(139)
$Q_{100} = 5750\ W_{AC}^{0.601}\ D_{AC}^{-0.055}$	73 (96, -49)	(140)
$Q_{100} = 16100\ W_{DB}^{0.256}$	80 (108, -52)	(141)
$Q_{100} = 6200\ A^{0.296}$	67 (88, -47)	(142)
$Q_{100} = 4070\ A^{0.323}\ P_{2,24}^{0.237}$	68 (89, -47)	(143)

correlation with mean annual runoff in region D (western Iowa and northwestern Missouri) than channel-geometry measurements, and their use is recommended for that region.

Both the channel and streamflow characteristics varied markedly across the Missouri River basin. The relationships between the channel geometry and flow characteristics also varied. Additional research is needed to better explain the regional differences.

REFERENCES CITED

Dixon, W. J., ed., BMD, Biomedical computer programs: Los Angeles, California Univ. School of Medicine, 620 p.

Hardison, C. H., 1974, Generalized skew coefficients of annual floods in the United States and their application: Water Resources Research v. 10, no. 4, p. 745–752.

Hedman, E. R., 1970, Mean annual runoff as related to channel geometry in selected streams in California: U.S. Geological Survey Water-Supply Paper 1999–E, 17 p.

Hedman, E. R., and Kastner, W. M., 1972, Mean annual runoff as related to channel geometry of selected streams in Kansas: Kansas Water Resources Board Tech. Rept. 9, 25 p.

Hedman, E. R., Moore, D. O., and Livingston, R. K., 1972, Selected stream-flow characteristics as related to channel geometry of perennial streams in Colorado: U.S. Geological Survey open-file rept., 14 p.

Hedman, E. R., Kastner, W. M., and Hejl, H. R., Jr., 1974, Flood-frequency characteristics as related to channel geometry of streams in Kansas: Kansas Water Resources Board Tech. Rept. 10, 21 p.

Moore, D. O., 1968, Estimating mean runoff in ungaged semiarid areas: Internat. Assoc. Sci. Hydrology Bull. 13, v. 1, p. 29–39. [Reprinted as Nevada Dept. Conserv. and Nat. Resources Water Resources Bull. 36, p. 36–39.]

Water Resources Council, 1967, A uniform technique for determining flood flow frequencies: Hydrol. Committee, Water Resources Council Bull. 15, 15 p.

Jour. Research U.S. Geol. Survey
Vol. 5, No. 3, May–June 1977, p. 301–305

ROUTING OF STORMWATER FLOWS THROUGH STORM DRAINS

By MARSHALL E. JENNINGS and THOMAS N. KEEFER, Bay Saint Louis, Miss.

Abstract.—Storm-drain flow-routing methods based on kinematic-wave routing and storage-routing methods are compared with the MLSR (multiple-linearization storm-drain routing) method for hypothetical circular pipe problems. The MLSR method, based on a diffusion-wave routing concept, is shown to give very good results without incurring the numerical solution or damping problems of other methods.

Within the last 5 years, interest in urban stormwater modeling has increased significantly. This renewed interest is, for the most part, due to the extremely large amount of money projected to be spent on storm-drainage facilities and to the growing recognition of the magnitude of urban-runoff pollution. Brandstetter (1974), in his review of 18 mathematical models for the nonsteady simulation of the urban rainfall-runoff process and for flow routing in storm drains, found a variety of methods used for storm-drain flow routing. The methods ranged from solution of the equations of open-channel flow applied to pipes to time-offset methods. Next to the estimation of runoff from catchment areas, flow routing in storm drains is perhaps the most critical process of concern in modeling urban stormwater. This report presents a storm-drain flow-routing method based on a diffusion-wave concept for the equations of open-channel flow. The technique shows considerable promise as an accurate and cost-effective method for application to urban stormwater modeling.

METHODS FOR FLOW ROUTING IN STORM DRAINS

As pointed out by Yen (1973), most methods of storm-drain flow routing use various simplifications which result in approximate solutions for the well-known equations of open-channel unsteady flow for momentum (eq 1) and continuity (eq 2),

$$\frac{\partial V_1}{\partial t}+V_1\frac{\partial V_1}{\partial x}+g\cos\theta\frac{\partial h}{\partial x}=g(S_o-S_f) \qquad (1)$$

$$\frac{\partial h}{\partial t}+Y\frac{\partial V_1}{\partial x}+V_1\frac{\partial h}{\partial x}=0, \qquad (2)$$

in which x is the longitudinal direction of the storm drain; V_1 is the cross-sectional average flow velocity in the x direction; t is time; g is the gravitational acceleration; h is the depth of flow measured perpendicular to x; θ is the angle between the storm-drain invert and a horizontal plane; S_o is sin θ, the storm-drain slope; S_f is the friction slope; and Y, the hydraulic depth, is equal to cross-sectional flow area divided by the width of the free surface.

Problems that arise in the numerical solution of equations 1 and 2, whether the complete equations or a simplified set are being solved, include difficulties in defining boundary conditions, a variety of stability problems, and relatively high computer computation costs. Yen (1973) presented an urban flow model called the Illinois Storm Sewer System Simulation Model which numerically solves equations 1 and 2 for storm-drain networks. Another example of numerical solution of the equations of flow is found in Yevjevich and Barnes (1970). Some investigators have chosen simplified versions of the momentum equation, relying on the kinematic wave solution technique. Such solutions include those of Brandstetter (1974), Leclerc and Schaake (1973), and Lager, Pyatt, and Shubinski (1971). Each of these kinematic-wave solution approaches appears to differ slightly with respect to the approach for numerical differentiation, and so forth. The solution method of Lager, Pyatt, and Shubinski (1971) requires an iteration procedure to insure oscillation-free results for storm drains on steep slopes.

Other investigators, seeking to avoid the problems of numerical solution of equations 1 and 2 have suggested methods based only on the solution of the continuity equation (eq 2). These solutions amount to storage routing where an inflow hydrograph is routed through storm-drain storage to produce an outflow hydrograph. Such methods are represented by the work of Lanyon and Jackson (1974) and Terstriep and Stall (1974) and apparently produce good results if the reach lengths are not too long. Finally, the simplest method, which avoids use of equations 1 and 2, is the time-offset method in which the inflow hydrograph is shifted in time without being changed in shape (Preul and Papadakis, 1970).

Briefly alluded to by Yen (1973) are the diffusion-wave solutions to equations 1 and 2. According to Yen, direct applications of diffusion-wave methods do not appear promising; however, the authors of the present report believe convolution methods based on the diffusion-wave concept have merit. Such methods have been found useful in natural, open-channel flow routing by Keefer and McQuivey (1974) and have been compared favorably to a numerical solution method by Keefer (1976). The method applied to storm-drain routing is called the MLSR (multiple-linearization storm-drain routing) method. Because the method promises advantages of lower computation cost and freedom from numerical solution difficulties while providing accurate solutions, test cases were set up for comparing results with those of other methods cited above.

The MLSR method

The MLSR method as applied to conduits is a straightforward extension of the multiple-linearization flow-routing model described by Keefer and McQuivey (1974) Multiple linearization simulates the nonlinear behavior of equation 1 by means of a multiple-input linear system. Each input accepts only a particular range of flow. The routing of each range is governed by a two-parameter, linear-response function characteristic for the range. Thus, the low-flow part of a hydrograph is routed with a response function suited to low flow. This flexibility is not possible in standard diffusion-wave models. The diffusion analogy response functions suggested by Hyami (1951) are used here. The two parameters required for each response function are a wave celerity, C, and wave damping (dispersion coefficient), D.

Two problems are basic to the MLSR model: First is the determination of C and D, and second is the selection of the number of ranges of flow to be represented by response functions. The first is a problem because little or no literature exists describing linear routing in conduits. Thus, it was not known beforehand how much damping to expect or to what parameters to relate it. The same was true of the celerity. The second problem is a function of the nonlinearity of equation 1 over the total range of flows considered. The nature of this function also was not known.

Both the celerity and dispersion coefficients for each response function were determined from open-channel formulas

$$C=\frac{1}{T}\frac{dQ}{dy} \tag{3}$$

and

$$D=\kappa\frac{Q}{S_oT} \tag{4}$$

where T is the top width; S_o is now the pipe slope; Q is the discharge; y is depth; and κ is a coefficient suggested by Harley (1967) to be ½. This was verified for a number of natural channels by McQuivey and Keefer (1974). A preliminary test hydrograph was routed by using a single-response function for a 6-foot(1830-millimeter)-diameter pipe using mean values of Q and T. This compared favorably with a method of characteristics solution presented by Lager, Pyatt, and Shubinski (1971). This indicated that equations 3 and 4 would be satisfactory for the purposes here. It was then possible to solve equations 3 and 4 simultaneously with Manning's equation to construct curves of C and D versus Q for a pipe. These curves indicated that the celerity did not vary a great deal from low flow to full flow but that the dispersion did. A sophisticated scheme of dividing the flow into ranges was not required because of the small celerity variation. Nine ranges were selected as a compromise between computational efficiency and accuracy. Range 1 routes flows from 0 to 0.15 full; range 2 routes flows from 0.15 to 0.25 full and so on up to range 9 that carries flows from 0.85 to 1.0 full flow. A storage scheme was developed that retains and releases that portion of flows which exceeds conduit capacity.

The overall MLSR routing scheme for a particular reach of conduit is as follows: First, the slope and diameter of the conduit are determined; second, the full-flow capacity is computed; third, a response function is computed and stored for each range of flow using the appropriate percent of full flow value (0.1 →0.9), Manning's equation and equations 3 and 4; and finally, a multiple-response function convolution technique similar to that described by Keefer (1974) is used to route the inflow hydrograph. The only change in the overall method for other shape conduits is to apply appropriate formulas for geometry (such as trapezoid or rectangle) when carrying out the third step.

The diffusion analogy response function will not, in theory, handle supercritical flow; however, Harley (1967) described a more sophisticated linear-response function that will. Unpublished work by the second author compared Harley's response function to the diffusion analogy response function for several critical conditions. In all cases the numerical integration scheme required to convert an instantaneous response function to one of finite duration converted both types (Harley and diffusion analogy) to unit-impulse functions. This indicated that for realistic cases, for example, 1- to 5-minute time intervals and reaches less than 1 mile 1.61 kilometers), a numerical routing

scheme should collapse to a time-offset method for critical flows. The model used here does this.

Testing the routing method

Ideally, the methods of storm-drain flow routing should be tested utilizing data from gaged reaches, that is, time coincident flow hydrographs available at each end of the test reach. The gaged reaches should duplicate realistic field conditions such as typical length, 500 ft (152 meters) to 3000 ft. (915 m); geometry; slope; and roughness. Unfortunately such data essentially do not exist—if a storm drain is gaged at all it is gaged at a single point. Therefore most investigators must rely on theoretical "exact" solutions for surrogate data. Two such "data" sets were available to the authors of this present report.

The transport block of the Storm Water Management Model (Lager and others, 1971), based on a kinematic-wave solution of equations 1 and 2, was tested against an "exact" solution generated by a method-of-characteristics solution. The method-of-characteristics solution was previously tested against measured depth

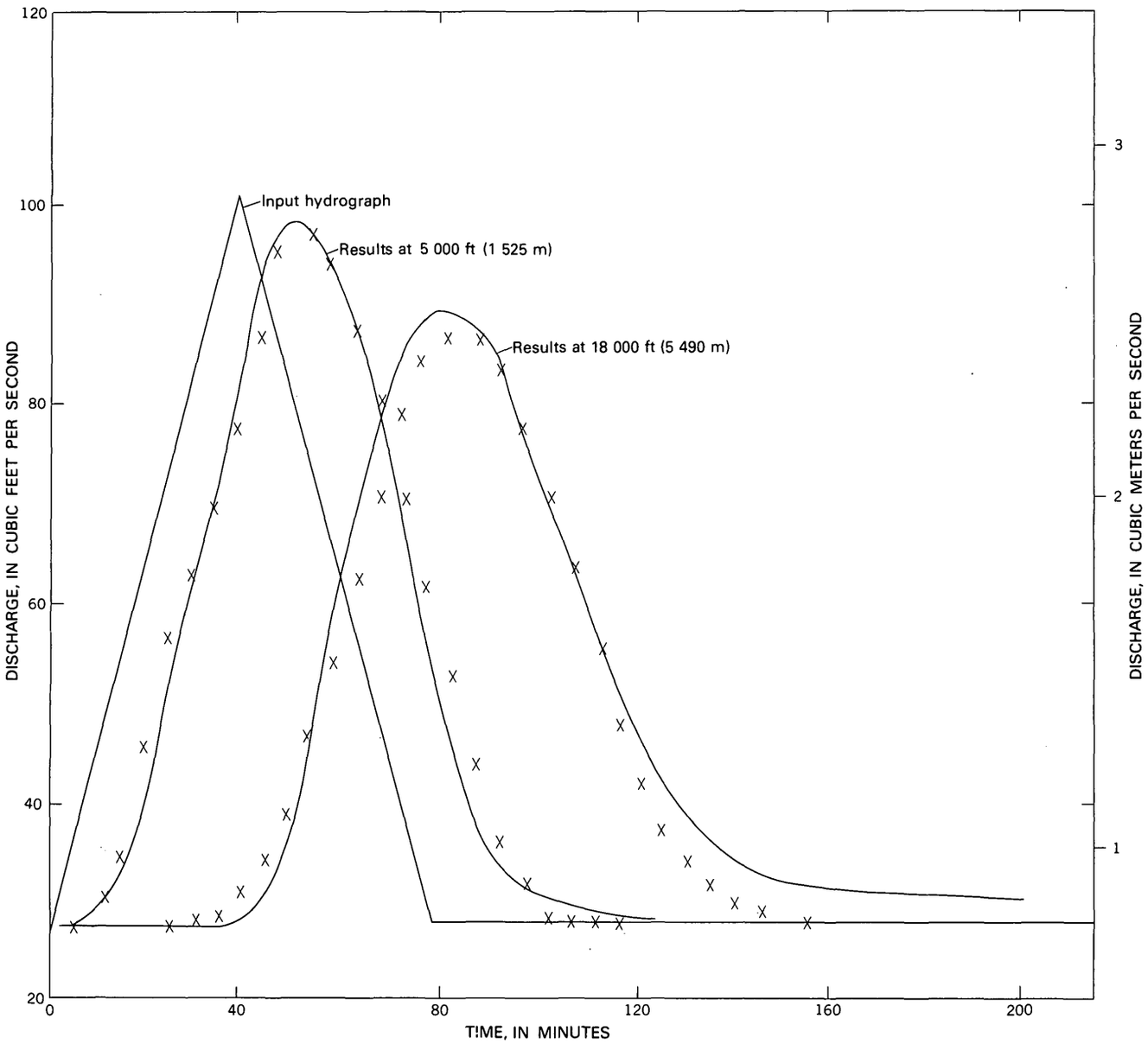

FIGURE 1.—Comparison of Lager, Pyatt, and Shubinski's kinematic-wave model and MLSR (multiple-linearization storm-drain routing) model for a 6-ft(1830-mm)-diameter circular pipe. Slope is 0.001 ft/ft (0.0003 m/m); Manning's n is 0.012. Results shown for 5000-ft (1525-m) and 18 000-ft (5490-m) pipe lengths. Solid curved lines indicate the kinematic-wave model (Lager and others, 1971); X's indicate the MLSR model.

hydrographs (Yevjevich and Barnes, 1970) obtained on a 3-ft(920-mm)-diameter, 822-ft(250-m)-long pipe at Colorado State University. Very good agreement was reported for the test. Probably because the Colorado State University data cannot be considered typical of urban catchment field conditions (most hydrographs lasted about 50 seconds), comparisons with the now-verified method of characteristics solution were made by Lager, Pyatt, and Shubinski (1971) for a hypothetical conduit with characteristics as given in figure 1. Shown in figure 1 is the hypothetical input hydrograph, the kinematic-wave solution of Lager, Pyatt, and Shubinski (1971), and the results of the MLSR model. MLSR results compare well with the Lager results for reach lengths of 5000 ft (1525 m) and 18 000 ft (5490 m). It should be noted that such long routing distances are only occasionally encountered in actual field conditions. Not shown are the data points for the "exact" solution by the method of characteristics which substantially agree with the Lager, Pyatt, and Shubinski (1971) results. Results (not shown) of a storage-routing model (Terstriep and Stall, 1974) for the 18 000-ft (5490-m) reach distance were extremely damped.

Data and results for another comparison of storm-drain routing models for a hypothetical situation are given in Brandstetter (1974) for a 2-ft(610-mm-diameter, 10 000-ft(3050-m)-long pipe and are shown in figure 2. The results of four storm-drain routing models are for the kinematic-wave methods of Lager, Pyatt, and Shubinski (1971) and Brandstetter (1974), the storage-routing model of Lanyon and Jackson (1974), and the MLSR model. According to Brandstetter (1974), the method of Lager, Pyatt, and Shubinski (1971) assumes zero initial flow conditions and displays more numerical dispersion than his result due to a different kinematic-wave solution method. The result based on the method of Lanyon and Jackson (1974) is extremely damped with a later peak. The MLSR results superimposed in figure 2 agree fairly well with the results of Lager, Pyatt, and Shubinski (1971). However, an observed or theoretically "actual" hydrograph is not available.

A final set of results is shown in figure 3 for the Lager, Pyatt, and Shubinski (1971) data situation for a reach distance of 1000 ft (305 m), which is more typical of field situations. Only results for a storage-routing method (Terstriep and Stall, 1974) and the proposed MLSR method are shown. Except for the inability of the storage-routing model to begin from a designated base flow of 28 cubic feet per second (0.79 cubic meters per second), the results are practically identical. One can imagine that, in this case at least, a time-offset method would also produce acceptable re-

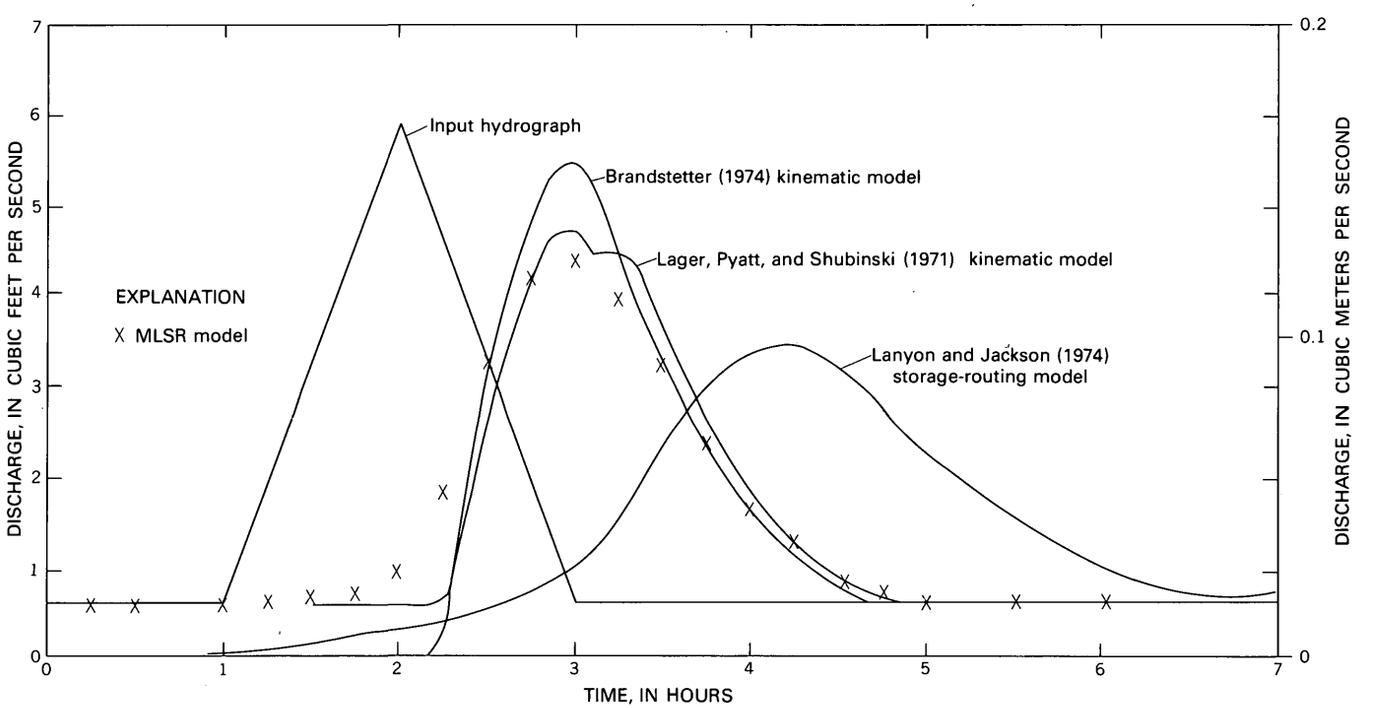

Figure 2.—Comparisons of Lager, Pyatt, and Shubinski (1971) and Brandstetter (1974) kinematic-wave models, Lanyon and Jackson (1974) storage-routing model, and MLSR (multiple-linearization storm-drain routing) model for a 2-ft (610-mm)-diameter circular pipe. Slope is 0.0005 ft/ft (0.000 15 m/m), Manning's *n* is 0.01. Results shown for 10 000-ft (3050-m) pipe length.

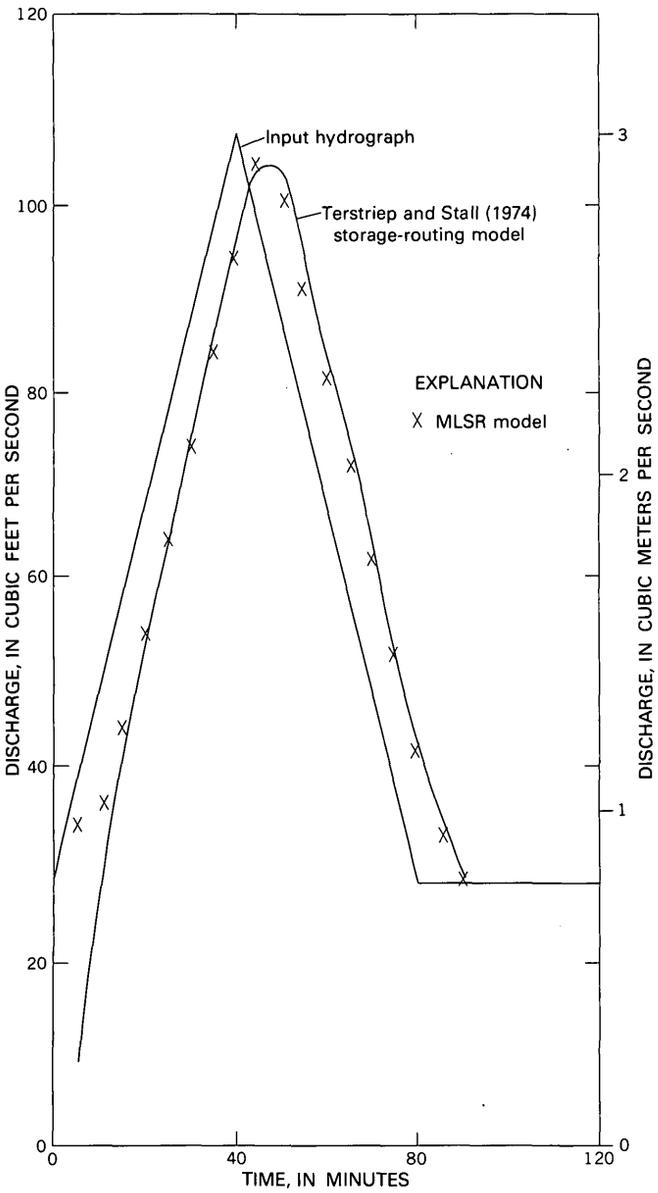

FIGURE 3.—Comparison of Terstriep and Stall (1974) storage routing model and MLSR (multiple-linearization storm-drain routing) model for a 6-ft (1830-mm)-diameter circular pipe. Slope is 0.001 ft/ft (0.0003 m/m). Manning's n is 0.012. Results for 1000-ft (305-m) pipe length.

sults, especially considering the errors generally inherent in estimating inflow hydrographs.

SUMMARY

A method of storm-drain flow routing called the MLSR model has been presented based on a diffusion-wave concept for the equations of open-channel flow (Keefer and McQuivey, 1974). The model performs well when compared with results from more complex models for long, hypothetical reaches. Although the long reaches considered are well beyond expected field conditions, they represent critical situations for testing routing models. The MLSR model has none of the numerical solution problems of more complex methods nor any of the drawbacks of simpler methods. Although only results for circular storm drains have been presented here, the method has been shown by Keefer (1976) to work equally well for rectangular and trapezoidal channels. Special problems such as routing through reaches with undersized storm drains, which causes temporary detention storage, and compatibility for routing of pollutants are easily handled by the MLSR model.

Unfortunately, due to the lack of available data from gaged storm-drain reaches, the comparisons given above are rather weak.

REFERENCES CITED

Brandstetter, Albin, 1974, Comparative analysis of urban stormwater models, *in* Application of stormwater management (short Course, Massachusetts Univ., Aug. 19–23, 1974) : Columbus, Ohio, Battelle Memorial Inst. Rept. BN–SA–320, 88 p.

Harley, B. M., 1967, Linear routing in uniform open channels: Cork, Ireland, Univ. Coll., M., Eng. thesis, 151 p.

Hyami, S., 1951, On the propagation of flood waves: Kyoto, Japan, Kyoto Univ., Disaster Prevention Research Inst. Bull. 1., 16 pp.

Keefer, T. N., 1974, Desktop computer flow routing: Am. Soc. Civil Engineers Proc. Hydraulics Div. Jour., v. 100, no. HY7, p. 1047–1058.

Keefer, T. N., 1976, Comparison of linear systems and finite-difference flow-routing techniques: Am. Geophys. Union, Jour. Water Resources Research (In press.)

Keefer, T. N, and McQuivey, R S, 1974, Multiple linarization flow routing model: Am. Soc. Civil Engineers Proc. Hydraulics Div. Jour., v. 100, no. HY7, p. 1031–1046.

Lager, J. A., Pyatt, E. G., and Shubinski, R. P., 1971, Stormwater management model: Florida Univ. and Water Resources Engineers, Environmental Protection Agency Rept. EPA–11024DOC 07/71, 352 p.

Lanyon, R. F., and Jackson, James, 1974, Flow simulation system: Am. Soc. Civil Engineers Proc., Hydraulics Div. Jour., v. 100, no. HY8, p. 1089–1105.

Leclerc, Guy, and Schaake, J. C., Jr., 1973, Methodology for assessing the potential impact of urban development on urban runoff and the relative efficiency of runoff control alternatives: Cambridge, Mass., Massachusetts Inst. Technology, Dept. Civil Eng., Rept. 167, 257 p.

McQuivey, R. S., and Keefer, T. N., 1974, Simple method for predicting dispersion in streams: Am. Soc. Civil Engineers Proc., Environmental Eng. Div. Jour., v. 100, no. EE4, p. 997–1011.

Preul, H. C., and Papadakis, Constantine, 1970, Urban runoff characteristics: Environmental Protection Agency Rept. EPA–11024 DQU 10/70, 341 p.

Terstriep, M. L., and Stall, J. B., 1974, The Illinois urban drainage area simulation: Illinois State Water Survey, ILLUDAS Bull. 58, 90 p.

Yen, Ben Chie, 1973, Methodologies for flow prediction in urban storm drainage systems: Urbana-Champaign, Illinois Univ., Water Resources Center Rept. 72, 150 p; U.S. Dept. Commerce, Natl. Tech. Inf. Service, PB–225 480/3GI, 163 p.

Jour. Research U.S. Geol. Survey
Vol. 5, No. 3, May–June 1977, p. 307–318

ANALYSIS OF THE RECHARGE POTENTIAL OF STORM-WATER BASINS ON LONG ISLAND, NEW YORK

By DAVID A. ARONSON and ROBERT C. PRILL, Mineola, N.Y.

Abstract.—Many of the more than 2,200 storm-water basins on Long Island, N.Y., are potential sites for infiltration of large volumes of reclaimed water (highly treated domestic and industrial sewage). By use of a finite-difference method of calculation, changes in basin storage during idealized high-intensity storms were determined for the North Massapequa basin, a typical basin on Long Island. Calculations for a 100-year storm, in which a runoff coefficient of 20 percent was used but in which infiltration rate, storm intensity, storm duration, and return period were varied, indicate that this test basin would not overflow even if the infiltration rate declined from its present 1.5 feet per hour (0.46 meter per hour) to about 0.03 ft/h (0.009 m/h). The large reserve capacity of the test basin and similar basins on Long Island demonstrates the feasibility of using storm-water basins for infiltration of a supplemental water supply (supplemental recharge). If reclaimed water were ponded to a depth of 4 ft (1.2 m) in the test basin and if water application were alternated for equal periods between the test basin and a nearby basin with similar characteristics, the volume of infiltration would be slightly more than two million gallons per day (0.09 cubic meters per second) at an infiltration rate of 1.5 ft/h (0.46 m/h). With supplemental recharge, 60 percent of available storage capacity would be used during a 10-yr storm, and 80 percent would be used during a 100-yr storm, using a runoff coefficient of 20 percent.

Infiltration of reclaimed water to ground-water reservoirs is receiving increasing emphasis on Long Island, N.Y. (fig. 1). Recharge of reclaimed water by basins is particularly well suited to Long Island, where more than 2,200 storm-water basins are presently (1976) used for disposal of runoff from urban and suburban areas in Nassau and Suffolk Counties. Because of the generally high permeability of surficial deposits on Long Island, the large majority of the basins dispose of storm runoff efficiently, usually emptying within several hours after rainfall; most basins are empty during most of the year. Therefore, storm-water basins are potential sites for infiltration of large amounts of reclaimed water, provided that the infiltration rate is and will remain sufficiently high and that such recharge will not interfere with the basins' normal function of disposing of storm runoff.

Effects of infiltration rate, storm duration and intensity, and runoff coefficient on the operation of a typical storm-water basin on Long Island are described in this report. Specifically described are (1) a method for determining basin storage during storm runoff, (2) application of the method to show how storm runoff will collect in a basin, and (3) how the basin would respond if a supplemental supply of reclaimed water were added.

DESCRIPTION OF STORM-WATER BASINS ON LONG ISLAND

In general, storm-water basins are open pits of various shapes and sizes excavated in moderately to highly permeable sand and gravel deposits of glacial origin. Most basins are equipped with some type of overflow structure, whereby overflow water is carried by pipes, flumes, or street gutters to another basin or to a nearby stream. Floors of most storm-water basins in Nassau County have two or more levels. The lower level, which serves as a settling pool to collect inflowing sediment and trash, is at the elevation of the invert (bottom) of the inflow pipe. The higher level, commonly about 2 feet (0.6 meter) above the lower, serves as a platform for maintenance work when the lower level is flooded. The higher level also facilitates infiltration of water into the ground because it remains almost free of sediment.

Storm-water basins are primarily used for disposal of storm runoff from highways and residential, industrial, and commercial areas; however, about 30 basins are used for disposal of treated sewage. Area of individual basins ranges from 0.1 to 30 acres (400 to 1.21×10^5 square meters) and averages between 1 and 2 acres (4,000 and 9,000 m^2). Depth of most basins is 10 to 15 ft (3.0–4.6 m) below land surface, but the depth of some is as much as 40 ft (12 m). In 1969, 2,132 basins in Nassau and Suffolk Counties recharged approximately 61 Mgal/d (million gallons per day) or

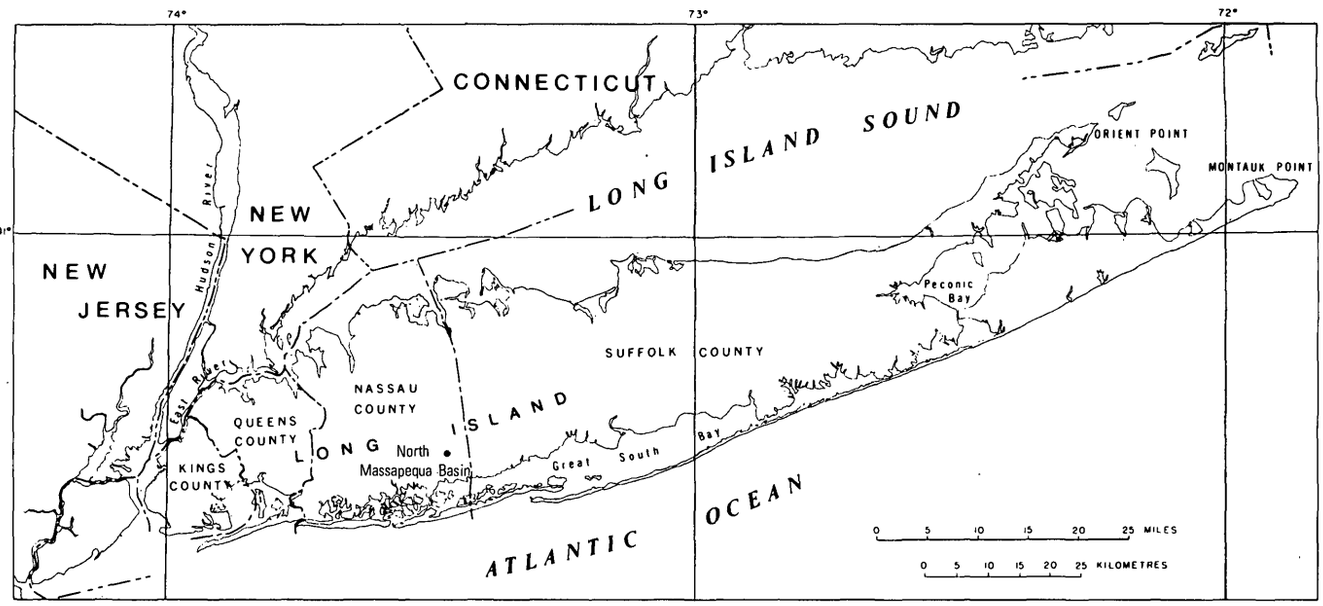

FIGURE 1.—Location and general geographic features of Long Island, N.Y., and position of test basin.

2.67 m^3/s (cubic meters per second) of storm runoff to the ground-water reservoir (Seaburn and Aronson, 1974).

Most design criteria for storm-water basins on Long Island have evolved by trial and error during the past 40 years. In Nassau County, the required size (volume) of the basin below the overflow elevation is estimated by multiplying (1) the volume of water equivalent to 5 in (130 mm) of rainfall on the total drainage area of the basin by (2) a runoff coefficient (ratio of volume of runoff to volume of precipitation) ranging from 30 to 90 percent. A runoff coefficient of 40 percent is used in most residential areas, whereas a coefficient of as much as 90 percent is used in industrial areas, where the ratio of impermeable to permeable surfaces is greater than in residential areas. Infiltration into the floor and the sides of the basin is neglected in the design, which results in an additional factor of safety. Similar design criteria are used by the towns of Suffolk County, although values assigned to the design rainfall and runoff coefficient may differ slightly.

Disposing of storm runoff in Nassau County by storm-water basins was begun in 1935 by the Nassau County Sanitation Commission (Welsch, 1935) as part of a comprehensive drainage plan. Use of storm-water basins not only satisfied the need to conserve storm runoff and to augment the freshwater reservoir serving the residents of Long Island but also eliminated a costly alternative of building long trunk storm sewers to discharge storm runoff into streams and tidewater. The concept also was adopted throughout Suffolk County. Use of basins developed slowly until after World War II, when the postwar building boom was accompanied by a large increase in the number of basins throughout the island. In 1950, there were only 14 basins in Nassau and Suffolk Counties. By 1960 the number had increased to more than 700 and, by 1974, to more than 2,200.

Location of basins used for disposal of storm runoff on Long Island as of 1969 is shown in figure 2. Most basins are in areas where the water table is sufficiently deep to remain below the floor of the basin. Most future basins will be constructed in the suburban and rural areas of eastern Long Island as urban growth advances eastward.

LOCATION AND DESCRIPTION OF TEST BASIN

A basin in operation since 1954 in the village of North Massapequa, southeastern Nassau County (fig. 1), is used to demonstrate the method for assessing basin operation during infiltration of storm runoff and the potential of storm-water basins for supplemental recharge. This basin, hereafter referred to as the North Massapequa basin, is typical of those on Long Island. It is excavated in outwash deposits of glacial origin that consist predominantly of homogeneous gravelly sand but also contain thin, discontinuous stringers and laminations of silt and clay. The soil cover of the drainage area consists mainly of Haven loam, a yellowish-brown to dark-brown loam and silt loam soil (Louns-

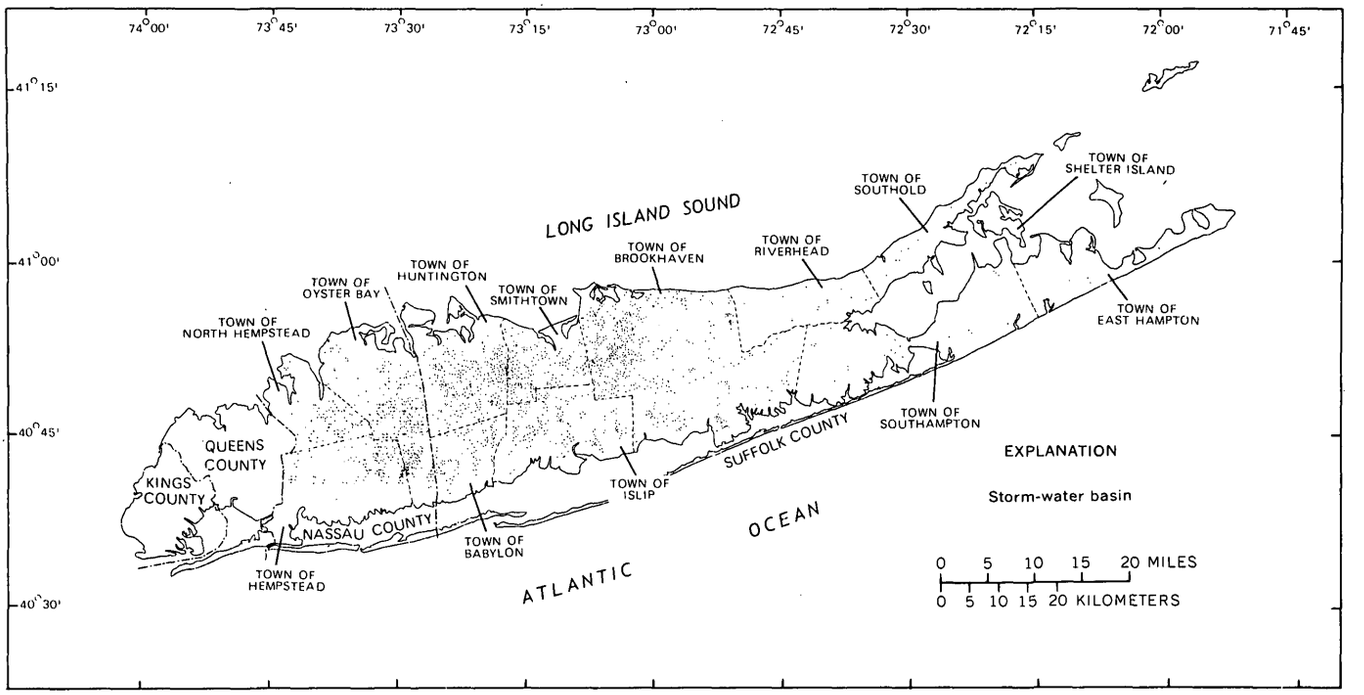

FIGURE 2.—Location of storm-water basins used for disposal of storm runoff on Long Island, N.Y., in 1969 (from Seaburn and Aronson, 1973).

bury and others, 1928; Seaburn and Aronson, 1973). The North Massapequa basin, which receives runoff from a residential drainage area of approximately 31 acres (0.125 square kilometer), is designed to accomodate the volume of runoff from a 5.0-in (130-mm) rainfall over a 24-h period with a runoff coefficient of 40 percent.

The area of the basin floor is approximately 13,000 ft² (1,200 m²). Depth of the floor ranges from 9.5 to 10.5 ft (2.9–3.2 m) below the basin overflow level. Storage capacity is 180,000 ft³ (5,100 m³). The relations of storage volume and infiltration area (projected horizontal plan area) to water stage (elevation of stored water from the lowest point in the basin) are shown in figure 3.

The water table is about 12 ft (3.7 m) below the basin floor. Flow to the water table is vertical, and rate of infiltration of water at the basin floor is about 1.5 ft/h (0.46 m/h) at 15.6°C (60°F) and a water stage of 1.0 ft (0.3 m).

METHOD FOR DETERMINING BASIN STORAGE DURING STORM RUNOFF

Basic Equations

The manner in which water accumulates in a basin during a storm depends on infiltration rate and volume of storm runoff. Accumulation of storm runoff can be determined by the continuity equation

$$S_t = \sum_{i=1}^{n} (V_i - I_i), \tag{1}$$

where i is the interval of time since the start of inflow;

S_t is water in storage at a specified time after start of storm, in cubic feet;

V_i is volume of storm runoff during ith time interval, in cubic feet;

I_i is volume of infiltration during ith time interval, in cubic feet; and

n is the number of time intervals used to determine S_t.

Volume of runoff entering the basin is determined by the equation

$$V_i = D \cdot C \cdot \frac{P_i}{12} \cdot t_i, \tag{2}$$

where D is the contributing drainage area, in square feet;

C is a dimensionless runoff coefficient;

P_i is precipitation intensity during ith time interval, in inches per hour; and

t_i is the length of the ith time interval, in hours.

Volume of infiltration is determined by the equation

$$I_i = A_i \cdot R \cdot t_i, \tag{3}$$

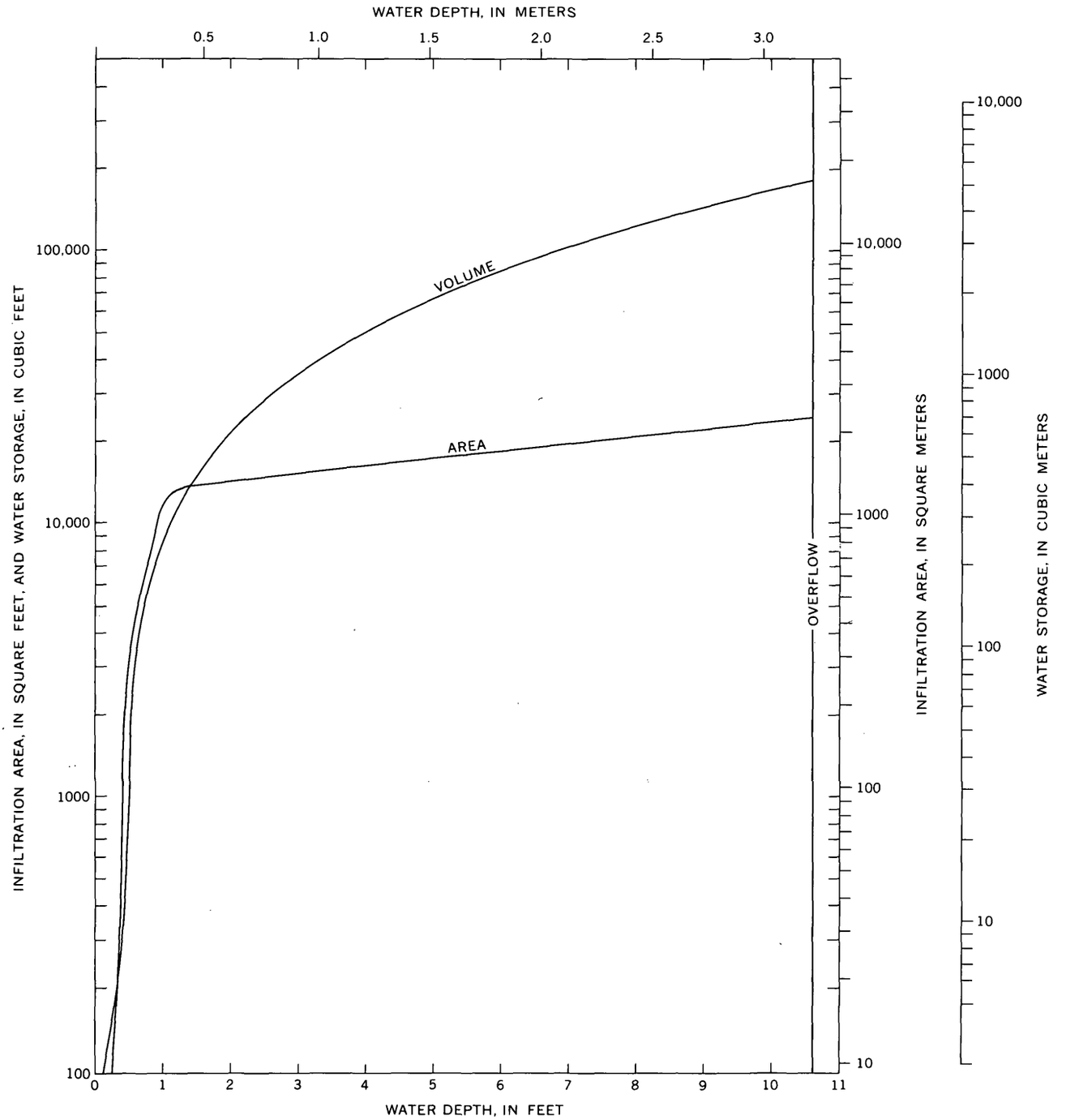

FIGURE 3.—Relations of storage volume and infiltration area to water stage for the North Massapequa basin.

where I_i is the volume of infiltration during the ith interval, in cubic feet;

A_i is the average infiltration area during the ith interval, in square feet;

R is the infiltration rate, in feet per hour.

The computational procedure for solving equation 1 requires that cumulative storage be determined for the start of each time interval. The infiltration area at the start of a time interval can be determined from graphs that relate basin stage to infiltration area and depth of impounded water (fig. 3). If this value is used as the infiltration area during the ith time interval, equation 1 can be expressed as

$$S_x = S_o + V_i - (A_o \cdot R \cdot t_i), \qquad (4)$$

where S_x is the water in storage (S_t) at the end of the ith interval, in cubic feet;

S_o is the water in storage at the beginning of the ith interval, in cubic feet;

A_o is the infiltration area for S_o, in square feet.

S_x is a preliminary estimate of S_t in equation 1. During periods of rising stage, the value S_x is an overestimate of maximum water in storage for a selected time interval because the infiltration area and, correspondingly, the volume of infiltration is constantly increasing. Similarly, during intervals of declining stage, the value S_x is an underestimate of maximum storage because the infiltration area is decreasing. Thus, in order to calculate S_t in equation 1, average infiltration area (A_i) during the time interval must first be determined and can be computed by using the equation

$$A_i = \frac{A_o + A_x}{2}, \qquad (5)$$

where A_x is the infiltration area for the volume of water S_x, in square feet.

Selection of Parameters

Storm

Equations 1 through 5 can be used for determining the rate at which water will accumulate in a basin during any storm. Such an evaluation is best done for storms of large magnitude when the ability of the basin to dispose of runoff is under maximum stress. Idealized high-intensity storms derived from statistical analyses of historical storm data provide the necessary information for selecting storms of large magnitude. In this report, storms having return periods of 10, 25, 50, and 100 yr were used to evaluate basin operation during supplemental recharge. Table 1 summarizes the relation between storm-return period, storm duration, and precipitation intensity in the New York City area as determined by Miller and Frederick (1969).

TABLE 1.—*Average precipitation intensity during storm-return periods of 10, 25, 50, and 100 years in the New York City area*

Storm duration (hours)	Average precipitation intensity, in inches per hour, for indicated storm-return period, in years			
	10	25	50	100
0.083	7.10	7.75	8.61	9.70
.25	4.45	5.20	5.90	6.60
.5	3.10	3.78	4.30	4.80
1	2.05	2.58	2.92	3.30
2	1.35	1.72	1.92	2.12
4	.83	1.03	1.17	1.32
8	.51	.62	.70	.78
12	.38	.45	.51	.57
18	.28	.33	.37	.41
24	.22	.26	.29	.33
36	.17	.19	.21	.24
48	.13	.15	.17	.19
72	.09	.11	.12	.14

NOTE.—Inches per hour (in/h) × 25.40 = millimeters per hour (mm/h).

Time interval

Selection of the length of the time interval (t_i) is a compromise between accuracy and computational cost. As a general rule, the interval should be sufficiently short so that S_x, as computed by equation 4, is not appreciably larger than S_o. The use of a minicomputer made possible the use of short-time intervals for the computations in this report. The time intervals selected range from 5 minutes to 24 h and are listed in table 1.

Runoff coefficient

In much of Nassau and Suffolk Counties, precipitation on impervious areas, such as roofs, driveways, sidewalks, and streets, and, to a considerably lesser extent, on soil surfaces drains into storm sewers that empty into storm-water basins. The ratio of the amount of runoff to the amount of rainfall represents the runoff coefficient (C).

Studies by Seaburn (1970) and Seaburn and Aronson (1974) have shown that the percentage of total inflow resulting from high-intensity storms is closely proportional to the percentage of impervious area in a basin's drainage area. Based on field reconnaissance of paved and other impervious areas, a runoff coefficient of 20 percent was determined for the drainage area of the North Massapequa basin; this value is used in analyses of basin performance discussed in this report.

The runoff coefficient used by basin designers on Long Island is considerably larger than the percentage of impervious area indicates to allow for storms of extraordinary intensity or for storms over frozen ground, during which time the runoff coefficient may increase and infiltration rate of the basin may decrease considerably. However, significant rainfalls over frozen ground are infrequent on Long Island. Inasmuch as the North Massapequa test basin was constructed using a 40-percent runoff coefficient, comparisons are made between basin performance characteristics using runoff coefficients of 20 and 40 percent.

Infiltration rate

The infiltration rate (R) of a basin is the rate of percolation of water out of the basin through the wetted area, measured in feet of water per hour. This parameter is probably the one most subject to variation. The rate depends on several factors, such as water temperature, water stage, antecedent-moisture conditions,

and the length of the flooding period. Despite such variability, the infiltration rate during storm runoff is probably best treated as a constant for any storm. An average rate of 1.5 ft/h (0.46 m/h) obtained at the North Massapequa basin for short-term infiltration tests at low-water stage should provide a good approximation of the rate during inflow of storm runoff.

BASIN PERFORMANCE DURING RECHARGE OF STORM RUNOFF

Suitability of a storm-water basin for supplemental recharge depends on how efficient the basin is in recharging the storm runoff from its watershed. Efficiency can be evaluated if sufficient data for determining the parameters for solving equations 1 through 5 are available. The authors evaluated the efficiency of the North Massapequa basin for recharging runoff from a storm with a 10-yr recurrence interval. The basin has an infiltration rate of 1.5 ft/h (0.46 m/h) and its drainage area has a runoff coefficient of 20 percent. These parameters were used in computing changes in basin storage for a series of six statistical storms having a recurrence interval of 10 yr. Results of these analyses are shown in table 2. The storms have durations of 5, 15, 30, 60, 120, and 240 min and average precipitation intensities of 7.10, 4.45, 3.10, 2.05, 1.35, and 0.83 in/h (180, 113, 79, 52, 34, and 21 mm/h), respectively. Precipitation intensity is assumed to be uniform for each storm, and runoff is also assumed to be uniform. Uniform runoff results in a progressive increase in basin storage until a maximum is reached at the end of the storm. The nature of this increase is illustrated graphically in figure 4, where storage values from table 2 are plotted for the 1-, 2-, and 4-h storms.

If computations such as those in table 2 are continued for other 10-yr storms of longer duration, storage values at the end of each storm can be used to generate a graph that shows maximum basin storage for a wide range of durations. Figure 5 depicts the maximum quantity of water in basin storage for any 10-yr storm with a duration of up to 72 h. The figure shows that the basin would be under greatest stress from storms of short duration and that peak loading is associated with a storm of about 1-h duration. The maximum quantity of water in storage is 28,000 ft^3 (790 m^3), which is only 16 percent of the basin capacity. Only part of the basin floor would be flooded during most storms. The quantity of water must reach

TABLE 2.—*Data tabulation of storage in North Massapequa basin during 10-yr storms of differing duration at an infiltration rate of 1.5 ft/h and a runoff coefficient of 20 percent*

[This table is a copy of computer-generated calculations; significant figures shown exceed precision warranted by input values]

Storm		Time interval t_i		Precipitation intensity, P_i (in/h)	Storm runoff V_i (ft^3)	Infiltration area at start of time interval, A_o (ft^2)	Storage, S_x (ft^3)	Infiltration area, A_x, at S_x (ft^2)	Average infiltration area for time interval, A_i (ft^2)	Volume of infiltration, I_i (ft^3)	Storage at end of time interval, S_t (ft^3)
No.	Duration (hours)	No.	Duration (hours)								
1	0.083	1	0.083	7.10	13,255	0	13,255	13,490	6,745	843	12,412
2	.25	1	.083	4.45	8,308	0	8,308	12,331	6,165	771	7,537
		2	.167	4.45	16,615	9,015	21,899	14,095	11,555	2,889	21,264
3	.5	1	.083	3.10	5,787	0	5,787	7,487	3,744	468	5,319
		2	.167	3.10	11,575	7,013	15,141	13,594	10,303	2,576	14,318
		3	.250	3.10	17,362	13,541	26,603	14,495	14,018	5,257	26,424
4	1	1	.083	2.05	3,827	0	3,827	6,086	3,043	380	3,447
		2	.167	2.05	7,654	5,317	9,772	12,911	9,114	2,278	8,822
		3	.250	2.05	11,481	12,062	15,781	13,636	12,849	4,818	15,486
		4	.500	2.05	22,963	13,617	28,236	14,618	14,117	10,588	27,860
5	2	1	.083	1.35	2,520	0	2,520	4,652	2,326	201	2,230
		2	.167	1.35	5,041	3,884	6,299	7,810	5,847	1,462	5,808
		3	.250	1.35	7,561	7,032	10,732	13,146	10,089	3,784	9,586
		4	.500	1.35	15,122	12,822	15,092	13,601	13,212	9,909	14,799
		5	1.000	1.35	30,244	13,567	24,692	14,346	13,957	20,935	24,108
6	4	1	.083	.83	1,550	0	1,550	2,882	1,441	180	1,370
		2	.167	.83	3,099	2,218	3,914	6,173	4,196	1,049	3,420
		3	.250	.83	4,649	5,313	6,076	7,681	6,497	2,437	5,632
		4	.500	.83	9,297	7,025	9,660	12,866	9,946	7,459	7,470
		5	1.000	.83	18,594	8,988	12,582	13,447	11,218	16,826	9,238
		6	2.000	.83	37,188	12,740	8,206	12,010	12,375	37,134	9,301

NOTE.—Conversion of U.S. customary units to SI (International System of Units) equivalents:

feet per hour (ft/h)	×	0.3048	= meters per hour (m/h)
inches per hour (in/h)	×	25.40	= millimeters per hour (mm/h)
cubic feet (ft^3)	×	0.02832	= cubic meters (m^3)
square feet (ft^2)	×	0.092903	= square meters (m^2)

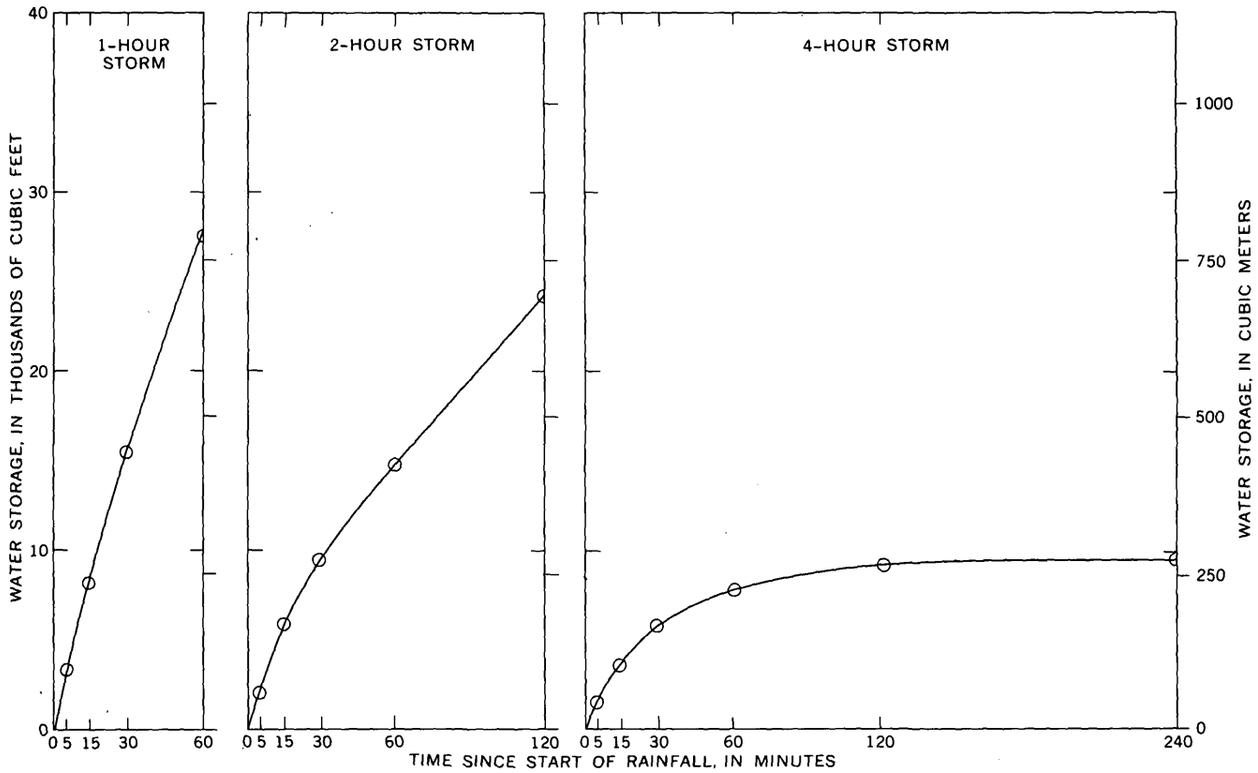

FIGURE 4.—Maximum water storage in the North Massapequa basin for 10-yr storms having durations of 1, 2, and 4 h, an infiltration rate of 1.5 ft/h (0.46 m/h), and a runoff coefficient of 20 percent.

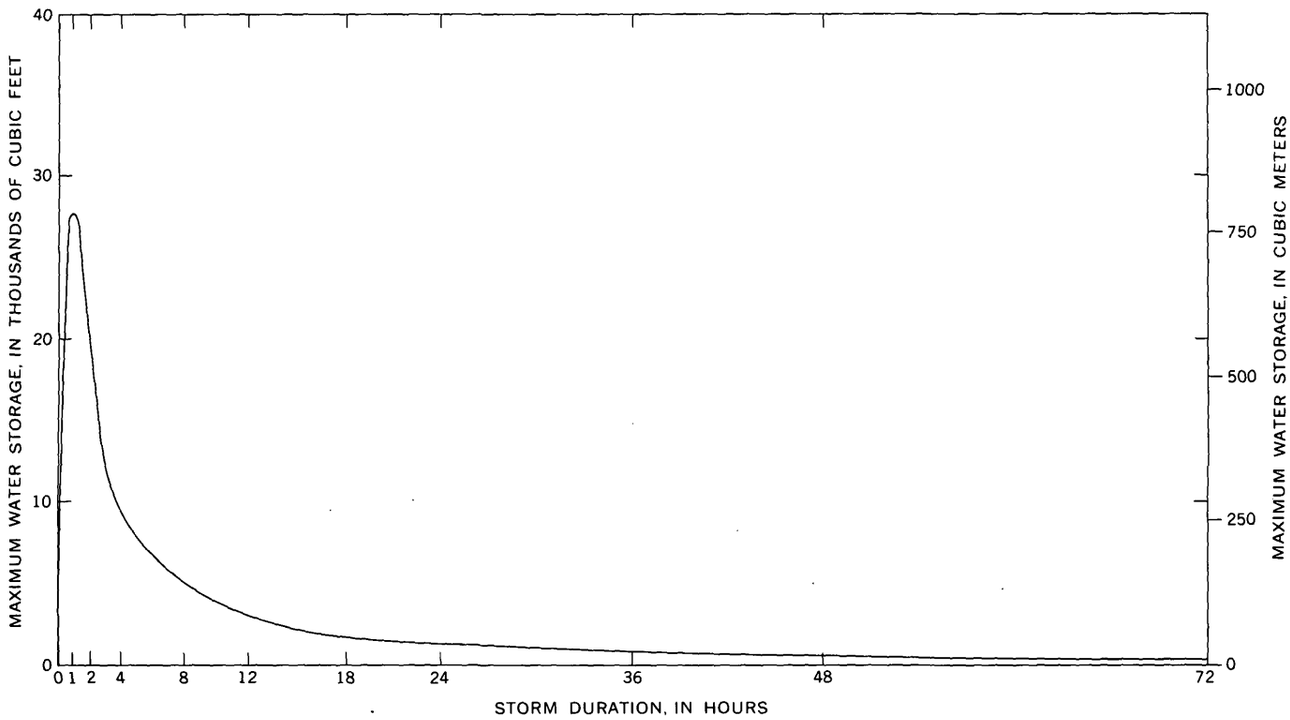

FIGURE 5.—Maximum water storage in the North Massapequa basin for 10-yr storms of differing duration, an infiltration rate of 1.5 ft/h (0.46 m/h), and a runoff coefficient of 20 percent.

12,000 ft³ (340 m³) before the entire basin floor is covered. (See figure 3.) Peak storages for storms of durations of 4 h or more are less than this, which indicates that the entire basin floor would be flooded only infrequently.

At an infiltration rate of 1.5 ft/h (0.46 m/h), the North Massapequa basin has considerable reserve capacity for the recharge of water in addition to storm runoff. A concern would be the effect that a change in infiltration rate would have on the reserve capacity of the basin. This effect can be shown by plotting maximum basin storage as a function of storm duration for a range of infiltration rates. Graphs of maximum basin stage for 10-yr storms of differing duration, at infiltration rates ranging from 0 to 1.5 ft/h (0–0.46 m/h) are shown in figure 6. The runoff coefficient is assumed to be 20 percent. The basin is shown to have sufficient storage capacity to hold all the runoff from 10-yr storms of as much as 72-h duration, regardless of the infiltration rate. Even at the low infiltration rate of 0.05 ft/h (0.015 m/h), only 58 percent of the basin capacity is utilized. At a rate of 0.25 ft/h (0.076 m/h), a value that is one-sixth of the measured rate, 35 percent of the basin capacity is utilized.

The frequency at which the whole basin floor is flooded increases as infiltration rate decreases. At a rate of 1.5 ft/h (0.46 m/h), peak storage is 28,000 ft³ (790 m³), and the entire basin floods during storms of less than 3 h when basin storage is more than 12,000 ft³ (340 m³), as shown in figures 5 and 6. In contrast, at a rate of 0.25 ft/h (0.08 m/h), peak storage is 63,000 ft³ (1,780 m³) and the entire basin floor floods during storms of less than 40 h. At an infiltration rate of 0.25 ft/h (0.08 m/h), peak storage is associated with a

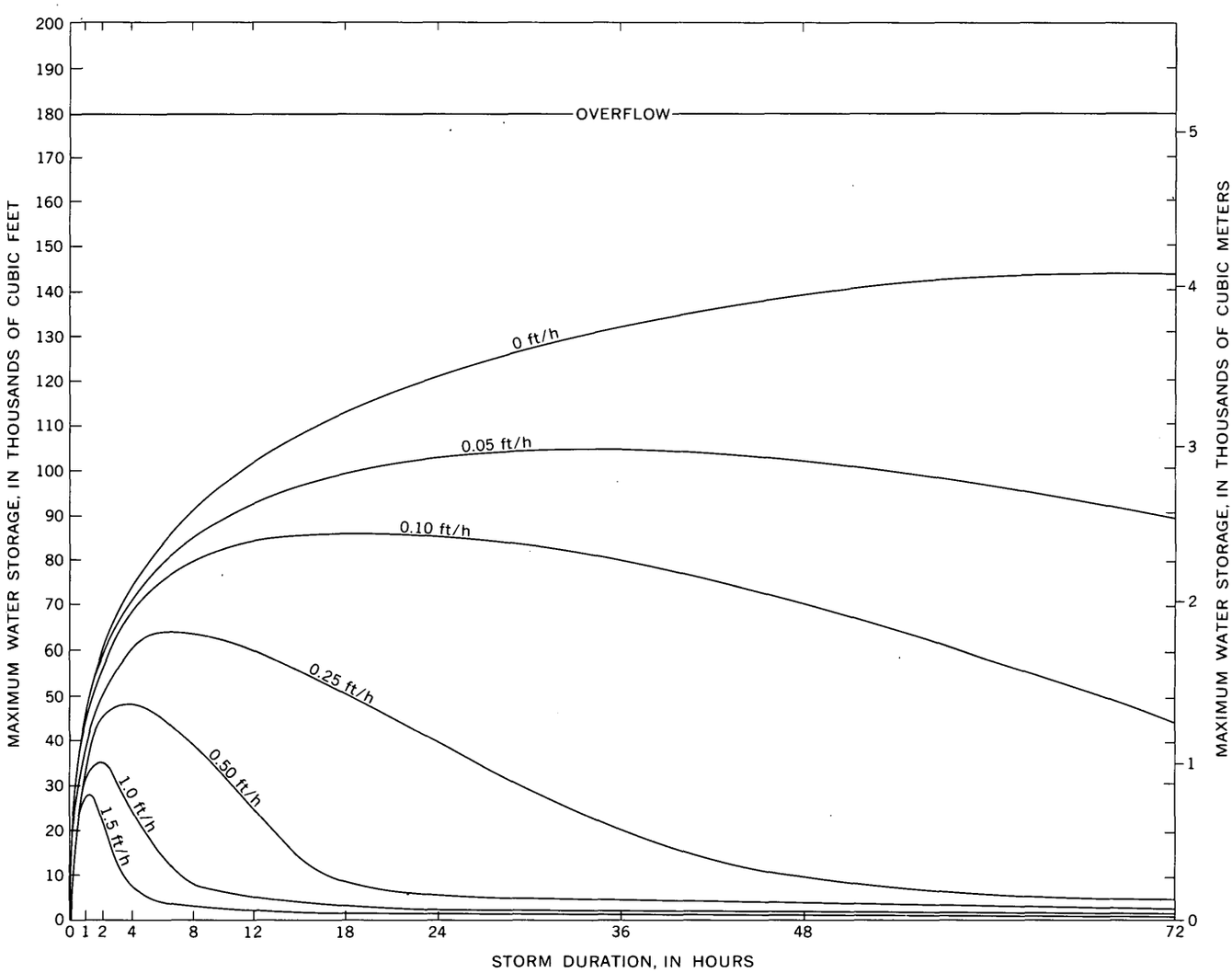

FIGURE 6.—Maximum water storage in the North Massapequa basin for 10-yr storms of differing duration, infiltration rates ranging from 0 to 1.5 ft/h (0–0.46 m/h), and a runoff coefficient of 20 percent.

storm of 6-h duration. In contrast, at an infiltration rate of 1.5 ft/h (0.46 m/h) there is peak storage during a storm of 1 h. Flooding of the basin floor will be much more frequent at the lower rate.

If several graphs of the type in figure 6 are plotted for various combinations of infiltration rates, storm-return periods, and runoff coefficients, the highest values from each of the graphs can be used to develop a single graph that will show maximum storage for almost any combination of parameters. Such a graph for the North Massapequa basin is presented in figure 7. Selected values from this graph are listed in table 3.

As shown in figure 7, the infiltration rate for a runoff coefficient of 20 percent could drop to a rate many times lower than the present rate of 1.5 ft/h (0.46 m/h) without affecting the basin ability to handle storm runoff adequately. Even for a 100-yr storm, the basin would not overflow unless the rate dropped to about 0.03 ft/h (0.009 m/h). The result would be quite different if the runoff coefficient were 40 percent. Then, the risk of overflow that could be tolerated would be critical. For a 10-yr storm and a 40-percent runoff coefficient, the basin would not overflow unless the rate dropped to 0.14 ft/h (0.04 m/h); for a 100-yr storm

TABLE 3.—*Selected values pertaining to the performance characteristics of the North Massapequa basin as obtained from figure 7*

Storm recurrence interval (years)	Runoff coefficient (percent)	Maximum water storage at an infiltration rate of 1.5 ft/h		Infiltration rate at which overflow would occur (ft/h)
		Volume (ft^3)	Percentage of total capacity	
10	20	28,000	16	<0.01
	40	76,000	42	.14
25	20	39,000	22	.01
	40	107,000	59	.28
50	20	47,000	26	.02
	40	122,000	68	.46
100	20	55,000	31	.03
	40	140,000	78	.75

NOTE.—Conversion of U.S. customary units to SI (International System of Units) equivalents:

feet per hour (ft/h) × 0.3048 = meters per hour (m/h)

cubic feet (ft^3) × 0.02832 = cubic meters (m^3)

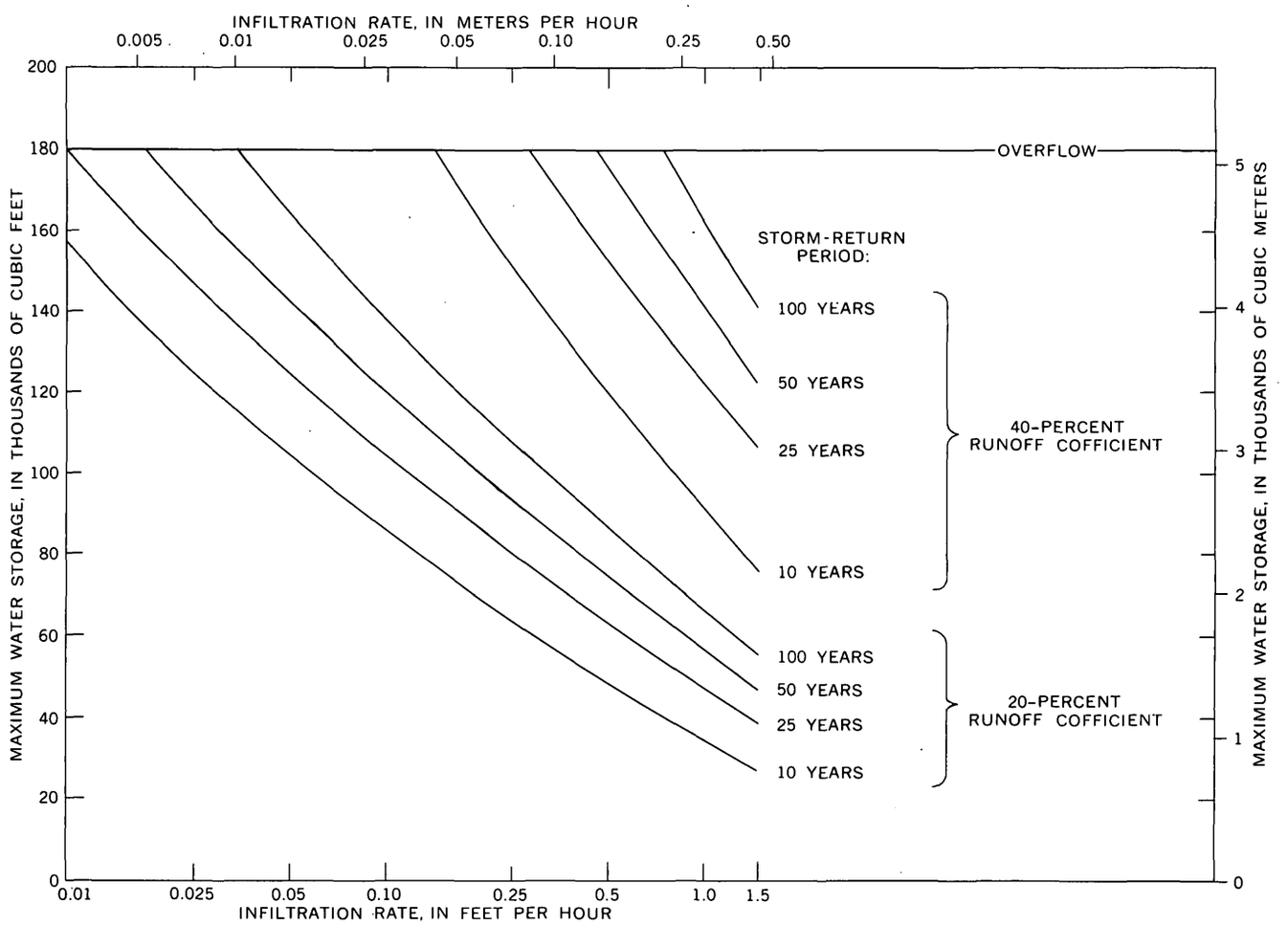

FIGURE 7.—Maximum water storage in the North Massapequa basin associated with various combinations of infiltration rate, storm-return period, and runoff coefficient.

the basin would overflow at an infiltration rate of 0.75 ft/h (0.23 m/h), which is only half of the present rate.

For any increase in the runoff coefficient, the percentage change in the quantity of water added to basin storage will be greater than the percentage change in runoff coefficient because the volume-area relationship is nonlinear. (See figure 3.) For the values in table 3, a doubling of the runoff coefficient from 20 to 40 percent results in an increase in storage values by a factor that ranges from 2.5 to 2.7.

Although the preceding analyses were made for only one basin, the method of performance evaluation can be applied to any basin. The design criteria for most of the more than 2,200 basins on Long Island are similar to those for the North Massapequa basin. Thus, the storage capacity per unit drainage area would also be similar. About 80 percent of the basins are in outwash deposits (Seaburn and Aronson, 1974), where infiltration rates would be expected to be high and runoff coefficients for the drainage areas, low. Basins with infiltration rates and runoff coefficients similar to those for the North Massapequa basin have the potential for supplemental recharge. Even if the basin had an infiltration rate much less than 1.5 ft/h (0.46 m/h) or a runoff coefficient somewhat higher than 20 percent, it still should have some reserve capacity for supplemental recharge. There are probably many basins on Long Island that have potential for the recharge of a supplemental water supply.

BASIN PERFORMANCE DURING SUPPLEMENTAL RECHARGE

The preceding analyses indicate that a sizable part of the storage capacity of the North Massapequa basin could be used for infiltration of reclaimed water without interfering with the normal disposal of storm runoff. The approach to such supplemental recharge would probably be to flood all or a part of the basin floor with reclaimed water. Flooding would not be continuous. With continuous application, the infiltration rate would probably decline with time, regardless of the quality of the effluent (McGauhey and Krone, 1967). However, reductions of infiltration rate would be minimized by use of a suitable application-rest cycle. Certain maintenance of the basin floor during the rest part of the cycle would improve infiltration capacity; for example, periodic tilling or scarification of the basin floor would improve the porosity and hydraulic conductivity of the soil cover.

Flooding the floor of a basin would reduce both storage capacity and infiltration area available for storm runoff. If reclaimed water were ponded to a constant depth, the effective infiltration area available for storm runoff would be the part of the basin walls above the water level of the reclaimed water. Thus, a modification of the procedures described in the section "Method for Determining Basin Storage During Storm Runoff" is required before changes in basin storage during dual recharge can be calculated. Assuming a 4-ft (1.2-m) depth of reclaimed water, initial basin storage would be 52,000 ft^3 (1,470 m^3), as shown in figure 3. By subtracting the infiltration area of reclaimed water (16,100 ft^2 or 1,500 m^2) from the total infiltration area of reclaimed water and storm runoff, the infiltration area of the storm runoff can be calculated (A_o and A_x in eq 4 and 5). Calculations of changes in basin storage during dual recharge can then proceed as in the analysis of basin performance during inflow of storm runoff described earlier.

The way that storm runoff is likely to accumulate in the North Massapequa basin if reclaimed water is ponded to a depth of 4 ft (1.2 m) is shown in figure 8. Graphs are presented for 10-, 25-, 50-, and 100-yr storms of differing durations. The infiltration rate above the 4-ft (1.2-m) level is taken as 1.5 ft/h (0.46 m/h) and the runoff coefficient, as 20 percent. Application of the reclaimed water is assumed to be alternated for equal periods between the North Massapequa basin and another basin having similar characteristics, and storm runoff is assumed to infiltrate the basin walls above the 4-ft (1.2-m) level during periods when the reclaimed water is being applied.

Storage capacity of the basin is sufficient to handle all the storm runoff, regardless of the storm-return period, at an infiltration rate of 1.5 ft/h (0.46 m/h), as shown in figure 8. For a 10-yr storm, about 60 percent of the storage capacity available for storm runoff is utilized; for a 100-yr storm, about 80 percent of the capacity is utilized.

The rate of reclaimed water that can be recharged depends on the infiltration area, application-rest cycle, and infiltration rate of the basin floor. Flooding the basin to a depth of 4 ft (1.2 m) provides an infiltration area of 16,100 ft^2 (1,500 m^2). Because the application-rest cycle consists of equal periods of application and rest, the average quantity recharged by each basin will be equal to half of the product of infiltration area and infiltration rate. Average rates of recharge of reclaimed water ponded to a 4-ft (1.2 m) depth in the North Massapequa basin for infiltration rates that range from 0.1 to 1.5 ft/h (0.03 to 0.46 m/h) are shown in table 4. At the present infiltration rate of 1.5 ft/h (0.46 m/h), the average daily recharge would be slightly more than 2 Mgal/d (0.09 m^3/s). If the rate should

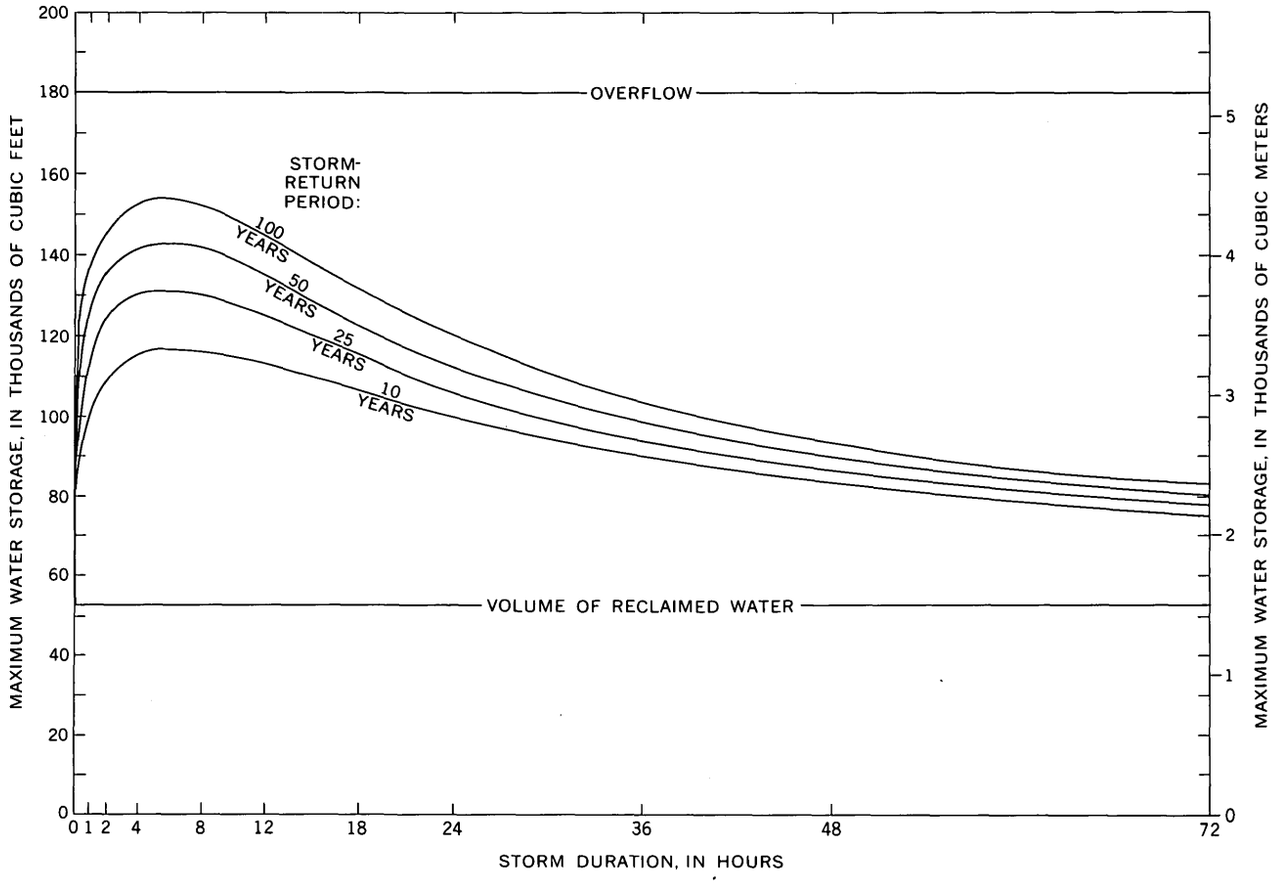

FIGURE 8.—Maximum water storage in the North Massapequa basin for 10-, 25-, 50-, and 100-yr storms, an infiltration rate of 1.5 ft/h (0.46 m/h), and a runoff coefficient of 20 percent when basin is flooded with reclaimed water to a depth of 4 ft (1.2 m).

drop to one-sixth of the present rate, to 0.25 ft/h (0.08 m/h), the quantity of recharge would be about 0.36 Mgal/d (0.016 m^3/s).

SUMMARY

Many of the more than 2,200 storm-water basins on Long Island having runoff and infiltration characteristics similar to those of the North Massapequa basin are potential sites for the infiltration of large volumes of reclaimed water.

Suitability of a basin for supplemental recharge depends on basin performance during inflow of storm runoff. Basin performance is determined from several parameters, including volume and pattern of precipitation and resulting runoff, volume-area relationships of the basin, and rate of infiltration. Precipitation data can be obtained from a real storm or a statistical analysis of historical storm data; runoff coefficient, by the proportion of impervious area in the basin's contributing drainage area; volume-area relationships, by topographic planimetering of the basin floor and walls; and infiltration rate, by ponding tests or other similar test procedures.

TABLE 4.—*Average daily volume of infiltration in North Massapequa basin for assumed 4-ft depth of reclaimed water over an area of 16,100 ft² and equal periods of application and rest*

Infiltration rate of basin floor (ft/h)	Average daily volume of infiltration	
	Cubic feet	Gallons
0.10	19,300	144,600
.25	48,300	361,400
.75	144,900	1,084,100
1.00	193,200	1,445,600
1.25	241,500	1,806,900
1.50	289,800	2,168,300

NOTE.—Conversion of U.S. customary units to SI (International System of Units) equivalents:

feet (ft)	×	0.3048	=	meters (m)
feet per hour (ft/h)	×	0.3048	=	meters per hour (m/h)
cubic feet (ft^3)	×	.02832	=	cubic meters (m^3)
square feet (ft^2)	×	.092903	=	square meters (m^2)
gallons (gal)	×	3.785	=	liters (L)

By use of the preceding parameters, formulas were devised to aid in the calculations of changes in basin storage at various time intervals since the start of storm inflow. Calculations using various infiltration

rates, storm durations, and return periods indicate that the North Massapequa basin would not overflow even if infiltration rate declined to 0.01 ft/h (0.003 m/h) during a theoretical 100-yr storm of constant intensity. Because the infiltration rate of the North Massapequa basin is approximately 1.5 ft/h (0.46 m/h) and significant long-term changes in infiltration rate are not expected, there seems to be a large safety factor inherent in the design of this and similar storm-water basins on Long Island. The main reason for such overdesign is the requirement that basins hold storm runoff without consideration of contemporaneous infiltration.

Procedures for determining changes in basin storage during simultaneous inflow and infiltration outlined in this report can be used to determine the relation between maximum basin stage attained during a storm, infiltration-rate, storm intensity and duration, and length of time required to attain maximum basin stage for any present or planned storm-water basin. Evaluations also can be made of the suitability of using storm-water basins for supplemental recharge of reclaimed water. Analyses of basin performance during inflow of reclaimed water and storm runoff indicate that the North Massapequa basin could infiltrate more than 2 Mgal/d (0.09 m^3/s) of reclaimed water at an infiltration rate of 1.5 ft/h (0.46 m/h) and still retain reserve capacity for disposal of runoff from a 100-yr storm.

REFERENCES CITED

Lounsbury, Clarence, Howe, F. B., Zautner, R. E., Moran, W. J., and Beers, P. D., 1928, Soil survey of Suffolk and Nassau Counties, New York: U.S. Dept. Agriculture, Ser. 1928, no. 28, 46 p.

McGauhey, P. H., and Krone, R. B., 1967, Soil mantle as a wastewater treatment system: Univ. Calif., Berkely, SERL Rept. no. 67–11, 201 p.

Miller, J. F., and Frederick, R. H., 1969, The precipitation regime of Long Island, New York: U.S. Geol. Survey Prof. Paper 627–A, 21 p.

Seaburn, G. E., 1970, Preliminary results of hydrologic studies at two recharge basins on Long Island, New York: U.S. Geol. Survey Prof. Paper 629–C, 17 p.

Seaburn, G. E., and Aronson, D. A., 1973, Catalog of recharge basins on Long Island, N.Y., in 1969: New York State Dept. Environmental Conserv. Bull. 70, 80 p.

———1974, Influence of recharge basins on the hydrology of Nassau and Suffolk Counties, Long Island, N.Y.: U.S. Geol. Survey Water-Supply Paper 2031, 66 p.

Welsch, W. F., 1935, Comprehensive drainage plan for Nassau County, New York—summary report: Nassau County Sanitation Comm., 23 p.

Jour. Research U.S. Geol. Survey
Vol. 5, No. 3, May–June 1977, p. 319–324

A RECONNAISSANCE INVESTIGATION OF A LARGE MEROMICTIC LAKE IN SOUTHEASTERN ALASKA

By GEORGE A. McCOY, Anchorage, Alaska

Abstract.—Redoubt Lake is one of the largest documented meromictic lakes in North America. The chemocline extends in depth from 80 to 100 m (meters) and the steepest gradient is between 98 and 100 m. The monimolimnion is anoxic, contains hydrogen sulfide, and has a salinity about two-thirds that of seawater. Turnover appears to introduce additional sodium chloride from the chemocline to the mixolimnion, but diffusion is probably the dominant mixing mechanism. Vertical profiles show a dichothermic temperature curve. A minimum temperature of 3°C in the chemocline is unexplained, but higher temperatures in the monimolimnion may be a result of solar radiation. At the lower limit of the chemocline there is a sharp decrease in pH, which could be due to bacterial action. Redoubt Lake is probably a relict fiord. The data presented herein support the hypothesis that the lake was gradually isolated from the sea by uplift. While seawater was entering the lake, it probably mixed with the freshwater in the mixolimnion and therefore the monimolimnion is less saline than seawater. Geologic and geophysical evidence support the speculation that significant amounts of saltwater inflow probably ceased about 650–800 years before the present.

Redoubt Lake was one of six lakes sampled in a reconnaissance program in southeastern Alaska in 1974 to assess their primary productivity and sport-fishery potential. The program was carried out in cooperation with the Alaska Department of Fish and Game.

Redoubt Lake lies in a cryptodepression at the head of Redoubt Bay on the west side of Baranof Island, 10.7 km south of Sitka (fig. 1). The lake surface is now 4 m above mean sea level, 1.25 m above mean high tide, and 0.6 m above maximum high tide. The lake has a drainage area of 112.7 km², a volume of 2,311 hm³, and a surface area of 16.6 km². The maximum known depth is 266 m and the average depth is about 139 m (fig. 2). The outlet is located at the end of a shallow bay (depth less than 2 m) that is approximately 0.3 km long. The outlet stream enters the ocean via Redoubt Bay about 40 m from the lake.

The geology of Baranof Island has been mapped by Loney, Pomeroy, Brew, and Muffler (1964) and Loney, Brew, Muffler, and Pomeroy (1975). Redoubt Lake is bordered on the south by intrusive igneous rocks of Tertiary age; these rocks are primarily hornblende-

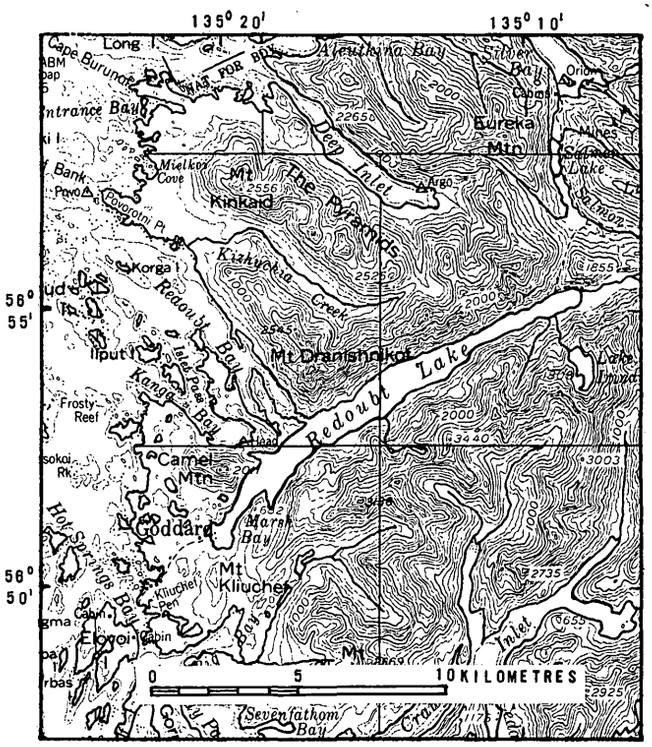

FIGURE 1.—Location of Redoubt Lake study area. Base from U.S. Geological Survey, Port Alexander, Alaska, 1951, scale 1:250,000. Contour interval, 200 feet or 61 meters.

biotite tonalite, and they grade into subordinate biotite tonalite and hornblende granodiorite. The north side of the lake is underlain by Sitka Graywacke of Late Jurassic and Early Cretaceous age which consists of hornfels, commonly with relict clastic and cataclastic textures.

During the course of this study it was discovered that Redoubt Lake is meromictic. The data presented in this paper are of a reconnaissance nature, and more work is needed to adequately define and describe this unusual system. The data collected thus far indicate that Redoubt Lake is anomalous, not only in terms of other described lakes in southeastern Alaska but also in this hemisphere. It is possible that other large

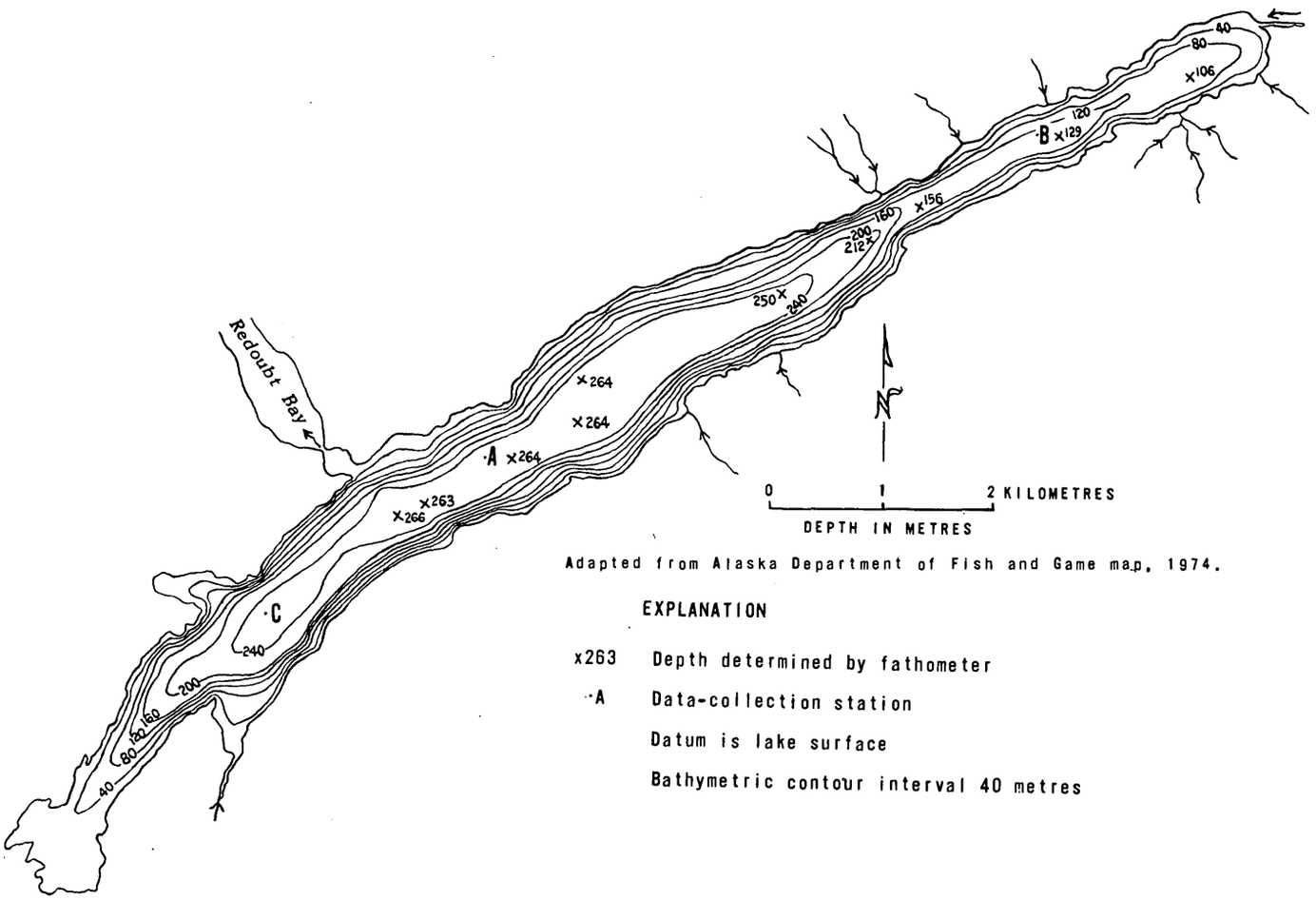

FIGURE 2.—Redoubt Lake with location of sampling stations.

meromictic lakes exist in southeastern Alaska, but none have been documented. A search of the literature does not reveal information on meromictic lakes that approach Redoubt in size or in the extreme depth of the chemocline and monimolimnion (Walker, 1974; Takahashi and others, 1968; Edmondson and Anderson, 1965; Brunskill and Ludlam, 1969; Weimer and Lee, 1973). Northcote and Johnson (1964) described meromictic Sakinaw Lake in British Columbia. Sakinaw Lake is morphologically similar to Redoubt Lake, but is smaller in area and has a maximum depth of only 140 m and a chemocline from 30 to 60 m.

SAMPLING METHODS

Water samples were collected from several depths in the lake and from the outlet. Analyses were made for major inorganic constituents and selected trace metals. Additional data from Redoubt Lake are presented in the U.S. Geological Survey's "Water Resources Data for Alaska, 1974." All chemical samples were collected and analyzed in accordance with standard methods of the U.S. Geological Survey (Brown and others, 1970). Information permitting the drawing of vertical profiles for specific conductance, temperature, dissolved oxygen, and pH was gathered by means of a Martek Mark II water-quality monitoring system (fig. 3). Profiles are drawn only to 100 m which was the maximum cable length available for the instrument. Samples from depths greater than 100 m were collected with a van Doren bottle.

ANALYTICAL RESULTS

The vertical profiles in figure 3 indicate that Redoubt Lake is meromictic and has a mixolimnion extending to approximately 80 m, a chemocline from 80 to 100 m, and a monimolimnion that most likely extends from 100 m to the bottom.

Chemical data were collected to a depth of 125 m,

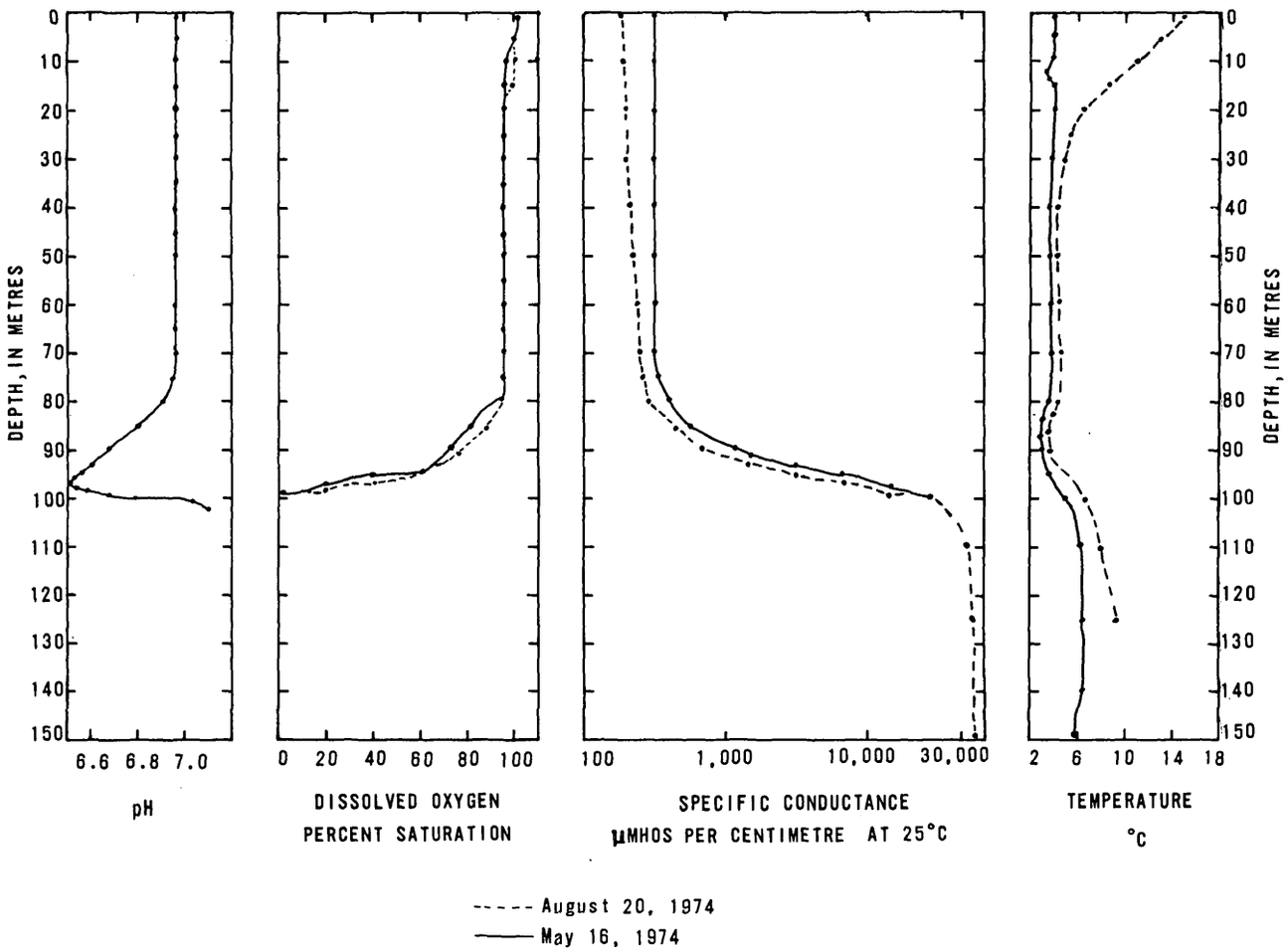

FIGURE 3.—Vertical profiles of pH, dissolved oxygen, specific conductance, and temperature in Redoubt Lake, at Station A. pH profiles are identical and show as one line.

but specific conductance and temperature were measured at 150 m. The concentration of all but one major inorganic constituent increased with depth. Manganese was the exception, reaching a maximum concentration in the chemocline and decreasing in the monimolimnion. Of the minor elements for which analyses were performed, only boron showed an appreciable change, having higher concentrations in the monimolimnion than in the mixolimnion (table 1). In samples retrieved from the monimolimnion a strong odor of hydrogen sulfide and frothing were observed. The absence of dissolved oxygen and the presence of hydrogen sulfide indicate that the monimolimnion is isolated and probably permanently anoxic.

Samples which permitted the construction of vertical profiles were collected on two occasions: May 16, 1974, when the mixolimnion was homothermous (one profile) and on August 20 when temperature stratification was well developed (three profiles). There were no significant differences in profiles drawn from data collected at the three stations in the lake on August 20, so it was concluded that stratification is horizontally uniform in the lake. Dissolved-oxygen concentration and pH were similar in May and August. Figure 3 presents a comparison of May and August profiles at one site.

In the mixolimnion, pH was uniform; it decreased in the upper part of the chemocline, then increased rapidly near the top of the monimolimnion. Dissolved oxygen was near saturation in the mixolimnion and decreased rapidly in the chemocline, reaching a concentration of 0 mg/L at 100 m. Specific conductance increased gradually with depth in the mixolimnion, then rapidly in the chemocline, and was constant from 110 to 150 m. The specific conductance in the mixolimnion was higher in May than in August.

Temperature stratification in the mixolimnion occurred to a depth of 40 m in August. In both May and

TABLE 1.—*Concentrations of selected chemical constituents in Redoubt Lake*

Date	Depth (m)	Dissolved: Manganese (Mn)	Silica (SiO_2)	Calcium (Ca)	Magnesium (Mg)	Sodium (Na)	Potassium (K)	Sulfate (SO_4)	Chloride (Cl)	Bicarbonate (HCO_3)	Dissolved solids, calculated	Hardness (Ca,Mg): Noncarbonate	Total	Color (platinum-cobalt units)	Boron total (B)
		(µg/L)	Milligrams per litre												(µg/L)
5-16-74	0.3*	0	2.1	3.3	4.4	35	1.7	9.0	65	7.0	126	18	26	5	120
	16	0	2.2	3.2	4.5	36	1.8	11.0	63	----	127	18	27	7	220
	100	490	3.0	11	29	530	9.4	82	690	37	1,380	110	150	8	410
8-19-74	.3*	0	1.7	2.7	2.6	22	1.3	6.3	42	7.4	84	9	17	2	30
8-20-74	6	0	1.7	3.0	2.9	20	1.2	6.1	38	13	79	9	19	3	230
	30	0	2.1	3.3	4.3	33	1.8	8.4	63	10	121	18	26	6	50
	100	730	16	240	720	6,000	200	1,000	11,000	635	19,500	3,000	3,600	50	550
	110	300	19	280	840	6,900	240	1,200	13,000	734	22,800	3,600	4,200	90	3,400
	125	90	20	270	820	7,000	250	1,100	13,000	764	22,800	3,400	4,100	200	3,600

* Collected at the outlet; all other samples were collected at station A (fig. 2).

August there is a decrease in temperature to below 4°C in the chemocline and an increase in the monimolimnion.

DISCUSSION

The proximity of Redoubt Lake to the sea, the dilute nature of surface water in this area, and the similarity of the ratio of the inorganic ions in the monimolimnion to that of seawater suggest ectogenic meromixis (Hutchinson, 1957, p. 481). Sodium and chloride are transported upward from the monimolimnion through the chemocline by one or a combination of two mechanisms. Diffusion probably accounts for a significant amount of sodium chloride in the mixolimnion. The data collected suggest that virtually all the concentration change takes place in less than 2 m. The mass m of sodium chloride which diffuses through the cross section A in time t is

$$m = \frac{\Delta A (d_2 - d_1) t}{h}$$

where Δ is the diffusivity, d_2 and d_1 are the concentration of sodium chloride in the two layers, and h is the height of the chemocline. If this chemocline is spread over 2 m, then the rate of diffusion from the monimolimnion to the mixolimnion is 4.4×10^{12} mg/yr of sodium chloride (J. T. Turk, written commun., 1975). This is about 11 percent of the rate at which sodium is lost through the outlet of (3.92×10^{13} mg/yr). If most of the concentration changes takes place in a meter or less (instead of 2 m), then diffusion is probably the dominant mechanism. However, a more precise profile of the chemocline would be necessary to accurately determine the rate of diffusion through the chemocline.

Spring and fall turnover may account for a minor part of the transport of sodium chloride into the mixolimnion. The observed concentrations of these ions were higher during spring turnover than during summer stratification. However, it is unlikely that mixing during turnover occurs far enough into the chemocline to affect the steepest part of the chemical gradient; consequently, this is probably not a significant mechanism.

The temperature profiles in figure 3 show that the coldest water is in the chemocline and that temperature increases in the monimolimnion. Hutchinson (1957) terms this type of curve dichothermic. The warmer temperatures in the monimolimnion of a meromictic lake may be a result of heat input from one or a combination of three sources: solar radiation, bacterial activity (exothermic anerobic reactions), or, considering the depth of Redoubt, heat of geothermal origin.

Hoare (1968) attributes warming of monimolimnetic waters at 49–63 m in an Antarctic lake to solar radiation. The maximum temperature Hoare observed was 25°C. At 100 m only 3 percent of the incident surface radiation is still available under ideal conditions, and it is questionable that the summer radiation

flux is high enough to account for the heat needed to warm the monimolimnion to the extent measured in Redoubt, However, the maximum temperature recorded in the monimolimnion of Redoubt Lake (8.5°C) is consistent with Hoare's observations, considering the reduced penetration of solar radiation to the deeper monimolimnion of Redoubt Lake.

The increase in temperature in the monimolimnion between May and August is significant. It suggests that heat energy from the monimolimnion is dissipated during turnover and that temperature increase during the summer months could be a result of bacterial action or solar radiation. This seasonal change is difficult to explain in terms of geothermal heat input, even though Goddard Hot Springs near the southwest end of the lake are geothermal. There are no data to support or discount this type of heat flow into Redoubt Lake.

J. T. Turk (written commun., 1976) suggests that the minimum temperature in the chemocline may be a result of mixing saltwater and freshwater. If seawater is diluted, the temperature of the resulting solution is lowered by the mixing process. This could account for a drop of 0.3°C, which, considering the inherent errors in the measurement of temperature, is a possible explanation of the observed temperature decrease.

The pH profiles for May and August are nearly identical (fig. 2). There was a decline in pH in the chemocline to a minimum at 98 m, then an increase in the monimolimnion. A similar minimum in the pH curve was noted by Takashashi and Ichimura (1968) in Japanese lakes. They attributed this minimum to "plates" of photosynthetic bacteria at the interface of the mixoliminion and the monimolimnion. The production of carbon dioxide by bacteria would cause a lowering of the pH.

The specific conductance of the water in the monimolimnion is approximately two-thirds that of seawater. Carter (1965) reported similar chemical conditions in the monimolimnion of Tessiarsuk, a meromictic landlocked fiord in northern Labrador. Tessiarsuk is below mean high tide, and saltwater enters the basin at high tide on 2 days out of 3. Carter attributed the lower salinity in the mixomlimnion to the mixing of saltwater with freshwater as the denser water flowed downward through the mixolimnion. It is likely that there was similar mixing in Redoubt Lake before it was elevated above mean high tide level. Considering this mixing mechanism, it is possible that layers of still more saline water may be present deeper in the monimolimnion, though no evidence of these layers is seen in the data.

Three possible mechanisms for the introduction of saltwater into this basin are considered. They include catastrophic events such as a tsunami or extreme high tide(s), intrusion of saltwater as ground water, and gradual uplift closing off a fiord.

Because of the location and configuration of Redoubt Bay (fig. 1) and the lack of historic evidence for tsunamis in this area, the probability of a large tsunami entering Redoubt Lake is considered remote. Extreme high tides could have introduced saltwater into Redoubt Lake, but no evidence of such extreme high tides was found. Since there are no data to document an event which could have brought 1,000 hm^3 of saltwater into this basin, addition of this saltwater by a catastrophic event or extreme high tides has been set aside but not ruled out.

Similarly, the intrusion of saltwater as ground water through an aquifer does not appear to be very likely. The closest body of saltwater is Redoubt Bay, which is separated from the lake by metamorphic and igneous rocks which have low primary permeability. Joints and contacts, which may have moderate secondary permeability, are parallel to the long axis of the lake (northeast–southwest), hence saltwater would have to move perpendicular to the direction of secondary permeability (G. S. Anderson and W. W. Barnwell, oral commun., 1975; Loney and others, 1964, 1975). However, the well-developed foliation in the metamorphic rocks trends about northwest–southeast indicating moderate to low secondary permeability (Brew and others, 1963).

Uplift or land emergence seems to be the most likely mechanism to explain the presence of saltwater in Redoubt Lake. If it is assumed on the basis of topography that Redoubt Lake was a fiord, then restricted mixing of seawater and freshwater occurred until the time the lake level was elevated above mean high tide. There would have been a gradual reduction in the amount of seawater introduced as the area was elevated. Southeastern Alaska is a geologically active area where land emergence has been thoroughly documented (Pierce, 1960; Hicks and Shofnos, 1965; Goldthwait, 1963). The rate of uplift, however, has not been precisely determined. Hicks and Shofnos (1965) estimated the rate at Sitka to be between 0.2 and 0.25 cm/yr. This assumes 0.1–cm/yr uplift rate due to glacial-eustatic rise and an additional 0.1 to 0.15 cm/yr during the last 275 years of Glacier Bay rebound. Assuming that the 0.1–cm/yr uplift can be applied back through the most recent glacial advance (approximately 500 to 2,700 years before the present (Goldthwait, 1963, p. 44)), then Redoubt Lake would have been at mean sea level about 3,700 years B.P., and at mean high tide level at least 830 years B.P.

If these assumptions are valid, then the length of time that Redoubt Lake has been isolated from the ocean can be estimated if one further assumes a constant rate of loss of sodium chloride through flushing by runoff since isolation. The length of time it would take for the chemocline to fall to its present level would be a function of the rate of loss of sodium chloride and the total amount of sodium chloride lost.

Where the rate of outflow (R) is 4.91×10^{11} L/yr, the change in concentration of sodium plus chloride in the mixolimnion (C_m) is 19,900 mg/L (table 1), the volume of the mixolimnion (V_m) is 1.31×10^{12} L, and the concentration of sodium chloride in the outlet water (C_o) is 80 mg/L, then:

$$\text{Time}=\frac{\text{Total amount lost}}{\text{Loss per year}}=\frac{C_m\ V_m}{C_o\ R}$$

$$=\frac{(19{,}900\ \text{mg/L})\ (1.31\times10^{12}\ \text{L})}{(80\ \text{mg/L})\ (4.91\times10^{11}\ \text{L/yr})}=665\ \text{yr.}$$

This is less than the length of time that Redoubt Lake has been above mean high tide as calculated by the rate of uplift. However, since the rates are of the same order of magnitude, the theories that meromixis in Redoubt Lake is ectogenic in origin and that Redoubt Lake is a relict fiord gradually isolated from the ocean by land emergence appear to be the most plausible explanation for the present chemical conditions. The difference between the times of isolation could easily be a result of inaccuracy in the measurement of the rate of uplift or underestimation of the rate of sodium chloride loss. Other contributing mechanisms, such as a disturbance of the chemocline or a greater rate of sodium chloride loss at an earlier time, are further possible explanations for this time difference.

FURTHER STUDY

This reconnaissance study suggests several possibilities for further investigation. Accurate profiles of the chemocline would allow a more precise determination of the diffusion flux. Monthly measurements of temperature stratification and specific conductance would give an indication of the role of turnover in the mixing process and in the thermal regime of the lake. Profiles to the bottom of the lake are essential to define the temperature regime and determine the chemical homogeneity or heterogeneity of the monimolimnion. Confirmation of the presence and identification of the bacteria in "plates" at the interface of the mixolimnion and monimolimnion and their role in the chemical and physical processes are desirable. Sediment cores would provide additional information on the past history of the lake. Finally, assuming that Redoubt Lake is not currently receiving saltwater, this system would be ideal for the study of freshening in an open meromictic basin.

REFERENCES CITED

Brew, D. A., Loney, R. A., Pomeroy, J. S., and Muffler, L. J. P., 1963, Structural influence on development of linear topographic features, southern Baranof Island, southeastern Alaska: U.S. Geol. Survey Prof. Paper 475–B, p. B110–B113.

Brown, Eugene, Skougstad, M. W., and Fishman, M. S., 1970, Methods for collection and analysis of water samples for dissolved minerals and gases: U.S. Geol. Survey Techniques Water-Resources Inv., book 5, chap. A1, 160 p.

Brunskill, G. J., and Ludlam, S. D., 1969, Fayetteville Green Lake, New York—Pt. I. Physical and chemical limnology: Limnology and Oceanography, v. 14, no. 6, p. 817–829.

Carter, J. C. H., 1965, The ecology of the calanoid copepod *Pseudocalanus minutus* Kroyer in Tessiarsuk, a coastal meromictic lake of northern Labrador: Limnology and Oceanography, v. 10, p. 345–353.

Edmondson, W. T., and Anderson, G. C., 1965, Some features of saline lakes in central Washington: Limnology and Oceanography, v. 10 (Supplement-Redfield anniversary volume), p. R87–R96.

Goldthwait, R. P., 1963, Dating the Little Ice Age in Glacier Bay, Alaska: Internat. Geol. Cong., 21st, Copenhagen 1960, Rept., pt. 27, p. 37–46.

Hicks, S. D., and Shofnos, William, 1965, The determination of land emergence from sea level observations in southeast Alaska: Jour. Geophys. Research, v. 70, no. 14, p. 3315–3320.

Hoare, R. A., 1968, Thermohaline convection in Lake Vanada, Anarctica: Jour. Geophys. Research, v. 73, no. 2, p. 607–612.

Hutchinson, G. E., 1957, A treatise on limnology: New York, John Wiley and Sons, Inc., v. 1, 1015 p.

Loney, R. A., Brew, D. A. Muffler, L. J. P, and Pomeroy, J S., 1975, Reconnaissance geology of Chichagof, Baranof, and Kruzof Islands, southeastern Alaska: U.S. Geol. Survey Prof. Paper 792, 105 p.

Loney, R. A., Pomeroy, J. S., Brew, D. A., and Muffler, L. J. P., 1964, Reconnaissance map of Baranof and Kruzof Islands, Alaska: US. Geol. Survey Misc. Geol. Inv. Map I–411.

Northcote, T. G., and Johnson, W. E, 1964, Occurrence and distribution of sea water in Sakinaw Lake, British Columbia: Fisheries Research Board Canada Jour., v. 21, p. 1321–1324.

Pierce, Charles, 1960, Is sea level falling or the land rising in southeast Alaska?: Am. Cong. on Surveying and Mapping, 20th Ann. Mtg., Washington, D.C., 1960, 11 p.

Takahashi, Masayuki, and Ichimura, Shun-ei, 1968, Vertical distribution and organic matter production of photosynthetic sulfur bacteria in Japanese lakes: Limnology and Oceanography, v. 13, p. 644–655.

Takahashi, Taro, Broecker, Wallace, Yuan, H. L., and Thurber, David, 1968, Chemical and isotopic balances for a meromictic lake: Limnology and Oceanography, v. 13, p. 272–292.

U.S. Geological Survey, 1974, Water resources data for Alaska, 1973—Pt. 1, Surface water records; Pt. 2, Water quality records: U.S. Geol. Survey annual State data-compilation report, 323 p.

Walker, K. F., 1974, The stability of meromictic lakes in central Washington: Limnology and Oceanography, v. 19, p. 209–222.

Weimer, W. C., and Lee, G. F., 1973, Some considerations of the chemical limnology of meromictic Lake Mary: Limnology and Oceanography, v. 18, p. 414–425.

Jour. Research U.S. Geol. Survey
Vol. 5, No. 3, May–June 1977, p. 325–329

CAULDRON SUBSIDENCE NEAR MOUNT LEWIS, NEVADA–A MISCONCEPTION

By JAMES GILLULY, Denver, Colo.

Abstract.—The map and interpretation of the geology of the Mount Lewis quadrangle, northern Shoshone Range, Nev., contained in U.S. Geological Survey Professional Paper 465 (1965) have recently been criticized and reinterpreted by C. T. Wrucke and M. L. Silberman in Professional Paper 876 (1975). I contend, however, that the reinterpretation ignores much cogent evidence and is quite inconsistent with the geometric disposition of the rocks. No justification exists for postulating a caldera.

The faults considered by Wrucke and Silberman to constitute the bounding faults of a caldera—hence normal faults downthrown toward the "caldera"—are in part nonexistent, in part a strike-slip fault formed concurrently with the Roberts thrust fault in Devonian and Mississippian time, and in part a listric thrust branching into the hanging wall of the main thrust. In short, the two real faults of Wrucke and Silberman's postulated caldera ring are about 200 million years older than the Oligocene volcanic rocks dated by Wrucke and Silberman. The paucity of dikes associated with the faults is thus readily understood, whereas it would be highly anomalous were the faults defining a caldera. The evidence for our thrust-fault interpretation was presented in the text, map, and sections of Professional Paper 465; further detail is included here. The evidence is clear and unequivocal: no caldera is here present.

During seven field seasons, 1950–1956, my colleague, Olcott Gates, and I, with the assistance at various times of 10 other geologists, mapped the Mount Lewis and Crescent Valley quadrangles, which cover much of the northern Shoshone Range, Nev. Altogether, the work occupied 58 man-months. Nearly 40 percent of the area of the two quadrangles is masked by alluvium, to which we gave only cursory attention; we averaged about 10 km^2 of bedrock coverage per man-month.

The mapping was done by plane table and open-sight alidade on an excellent topographic base at a scale of 1:15,840, a rather detailed scale, but one that was needed to unravel the highly complex geology. All the contacts mapped were walked out and cross-tied by transverse traverses. Mapping stations were at intervals nowhere exceeding 200 m and commonly much less. I consider the map, which was reduced for publication to half the field scale, as an unusually detailed representation of the rock distribution. Although I do not claim that it is free from error, it is definitely not a "sketch map," but a carefully controlled engineering product.

The dominant geologic feature of these and many other quadrangles in the region is the Roberts thrust fault, of Late Devonian to Early Mississippian age, whose westernmost exposure in this latitude is in the Mount Lewis quadrangle. This great fault, which has a demonstrable displacement of more than 100 km, separates two dramatically contrasting facies of Devonian and older rocks—an eastern parautochthonous miogeosynclinal facies (largely carbonate rocks) and a western allochthonous eugeosynclinal facies (largely quartzite, chert, and greenstone). Although small exposures of the allochthonous formations might be confused with each other, the major facies differ so strikingly that they can hardly be confused.

I cannot accept the structural interpretations made by Wrucke and Silberman (1975). Not only is their postulated caldera non-existent, but none of the faults they consider to bound it are normal. One segment of their postulated caldera boundary—that which they drew from the pluton on Goat Peak to the range front—simply cannot exist, for several reasons.

First, a fault on this course passes between klippen of upper-plate rocks, but the Roberts thrust bottoming the klippen projects across the postulated fault without offset. Second, several flat-lying sheets of Roberts Mountains Limestone of the window pass directly across the trace of the postulated fault without offset. Third, the klippen that rest on the western mountain slope show that the Roberts thrust cannot have lain more than a few feet above the present slope anywhere near this course; therefore, normal displacement of any consequence at all would have to drop the upper plate so that it would cover the lower slope of the south wall of Trout Creek canyon. Instead, the rocks of the window cover the whole south wall and extend well up the north wall.

Thus, it is geometrically impossible to have a significant normal fault where the sketch map of Wrucke and Silberman (1975, fig. 4B) shows one on the northwestern slope of Goat Peak. Their postulated fault would extend the Trout Creek fault on the same trend that it has east of the pluton of Goat Peak; this, however, is geometrically impossible.

The Trout Creek fault (fig. 1), which Wrucke and Silberman consider part of their ring fault, lacks any evidence of normal movement down on the north, as it should have. It is clearly a strike-slip fault with about 3 km of left-lateral displacement, caused by the inversion of the Roberts thrust, as detailed later. I refer the reader to plate 1 of Gilluly and Gates (1965) and to Gilluly (1960). I turn now to a detailed discussion of the postulated ring fault, following it counterclockwise from the range-front fault on the southwest.

THE POSTULATED RING FAULT

Although Wrucke and Silberman's sketch map (1975, fig. 4B) shows a normal fault downthrown to the north and extending in a gentle arc from the small pluton on the crest of Goat Peak (C, fig. 1, this paper) northwest to the mountain front south of Trout Creek, I have cited above the conclusive evidence that no significant fault can there exist. As will later appear, even if the fault did exist, it would not validate the caldera hypothesis. An understanding of the geologic relations in this complex area requires description of the faults bounding the Goat Peak window in the Roberts thrust.

The window exposes eastern-facies rocks from the mountain front between Trout Creek and Hancock Creek east-southeast for about 6 km, though its exposures are interrupted at many places by residual klippen of western-facies rocks. The north side of the window exposes mostly Cambrian rocks (Shwin Formation), except for some flat-lying sheets of Roberts Mountains Limestone (Silurian and Devonian) low on the western slope. Farther south, other Cambrian, Ordovician, and Silurian rocks appear in much-faulted array. These rocks are distinguished separately on plate 1 of Gilluly and Gates, (1965) but not on figure 1 of this paper.

Near Hancock Canyon, the Roberts thrust virtually coincides in attitude and location with the west-facing Basin and Range frontal fault. About a half a kilometer south of Trout Creek, the thrust leaves the frontal fault, with a strike east of north and a northwest dip of about 20°. Near the mouth of Trout Creek, the thrust turns abruptly east in a curve convex to the north. It cannot, therefore, be a normal fault of a caldera rim, nor can it be an alternative to the proposed fault shown farther south on the map of Wrucke and Silberman (1975, fig. 4B) and suggested as part of a caldera rim.

From point A, near the mouth of Trout Creek canyon, the thrust bears almost due east, and its trace rises diagonally up the north wall of the canyon to an altitude almost 200 m above the valley floor. In this stretch, the thrust steepens from a northwest dip of about 30° to a north dip of 70°. The fault here separates Slaven Chert (Devonian) of the western facies from Shwin Formation (Cambrian) of the window.

From the high point on its trace eastward, the thrust bends slightly southward and downhill on a course south of east, leaving an eastward-thickening wedge of western facies Valmy Formation of Ordovician age to intervene below the Slaven fault block. This is the beginning of the overturn of the Roberts thrust described in detail in Gilluly (1960). This split off the Roberts thrust is the youngest of several more and more deformed branches that break off from the main thrust just to the east, described in detail in Gilluly (1960). The other branches are omitted from figure 1, but their evidence, corroborative of the overturn of the thrust, has been fully described in the cited paper.

The main thrust continues to steepen eastward on a more southeasterly course, almost to the canyon floor near B in figure 1. Between A and B, the thrust is cut at high angles by two siliceous dikes of the Oligocene volcanic rocks.

From the low point near B, the trace of the fault again rises eastward up the north wall of the canyon for about 100 m. It then curves south in a sharp hairpin curve. The fault is clearly overturned so that the Cambrian carbonate rocks of the window come to overlie the Valmy Formation of the upper plate. This overturned antiform in the thrust is clearly exposed and can be readily identified, not merely on the outcrop but from a kilometer away.

The overturned limb of the antiform dips westward at about 50°, and its trace extends nearly due south up the canyon wall.

The northward plunge of the fold in the thrust roughly parallels the slope of the hillside, about 40°, for all the way from valley floor to ridge crest (near C in fig. 1) the rocks of the window overlie those of the frame at about the same angle. This is the place referred to by Wrucke and Silberman where limestone overlies the western facies rocks, for it is indeed the only place in the western part of the quadrangle where this relation prevails.

The overturned antiform in the Roberts thrust thus agrees with abundant regional evidence in showing that motion on the thrust was nearly due east. Deep mullions on the overturned limb plunge nearly due

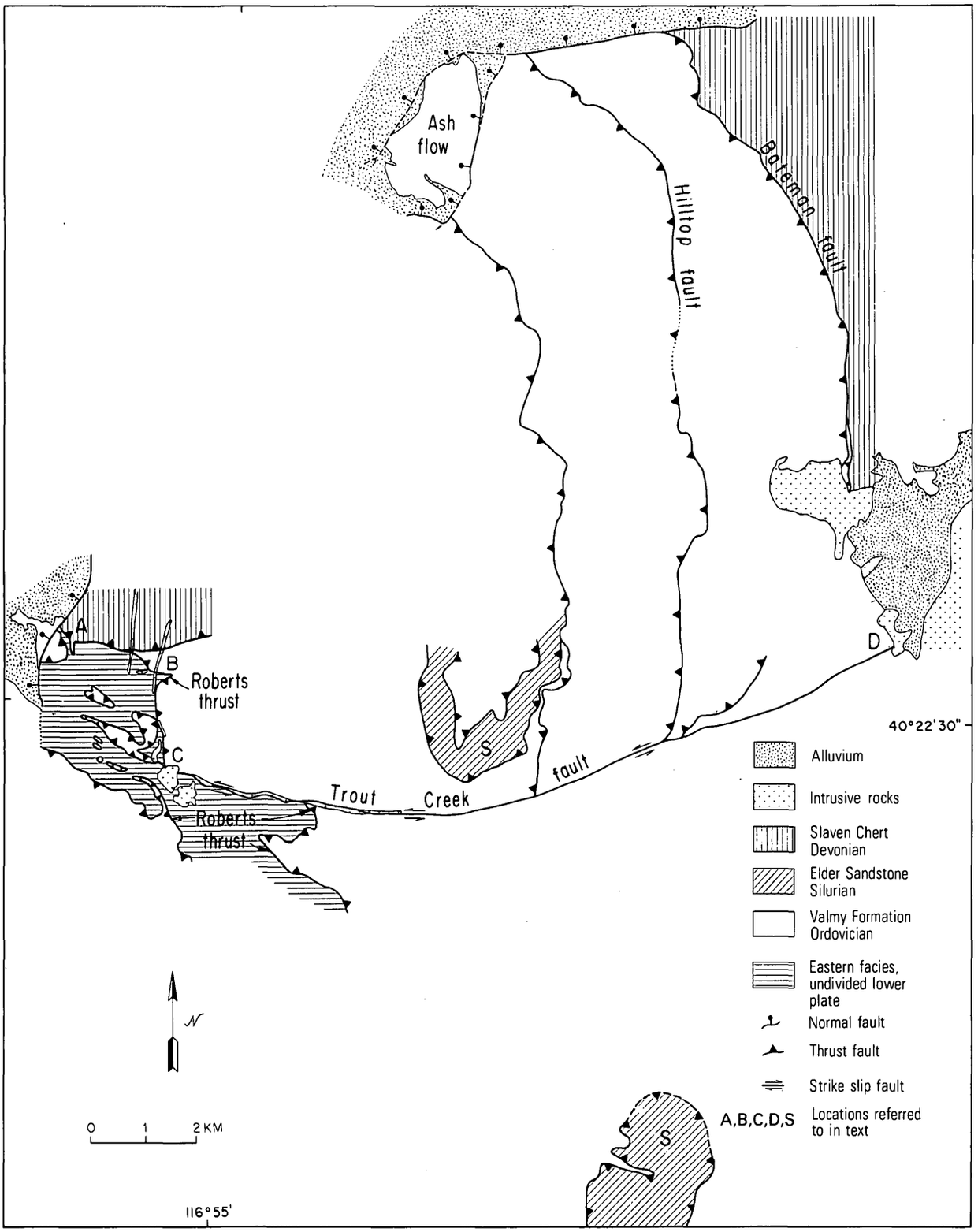

FIGURE 1.—Simplified geology of the area of the supposed caldera of Wrucke and Silberman (1975). Only the geology pertinent to the caldera problem is retained in full from plate 1 of Gilluly and Gates (1965). Most faults within the upper plate of the Roberts thrust are omitted, except those pertinent to the caldera question.

west, and the axis of the fold trends nearly due north in response to east-west compression.

At the crest of the ridge (C in fig. 1), the overturned antiform in the Roberts thrust terminates against a small pluton of granodiorite about 500 m in diameter. The pluton is not faulted, nor is the overturned thrust found anywhere to the south. It ends at the boundary of the pluton. Clearly the Roberts thrust is offset from a point within the pluton to a point about 3 km to the east, where it reappears upright and gently sloping to the east. At this point, the thrust terminates northward against a nearly vertical fault—the Trout Creek fault of figure 1.

The Trout Creek fault extends eastward in a gentle arc for about 13 km. Its eastern terminus is against a small outlier of the Granite Mountain pluton near D in figure 1. No extension can be found east of Granite Mountain. To the west, it ends at the east side of the pluton that ends the overturned Roberts thrust. It fails to cut this pluton, nor can it extend west of it, though such an extension appears on Wrucke and Silberman's map (fig. 1975, 4B). I have already pointed out that no significant normal fault can be found on this trend west of the pluton without dropping the upper plate of the Roberts thrust into the lower slopes of Trout Creek canyon, which exposes only rocks of the lower plate.

The Trout Creek fault is obviously a major fault, as it bounds the Goat Peak window for about 3 km over considerable relief. The overturned thrust stops at the same small pluton at which the Trout Creek fault also terminates. It is thus clear that the Trout Creek fault proxies for the thrust and is a strike-slip fault along which the thrust has been offset for 3 km. There is no evidence of vertical movement, for no marker horizon can be identified on both sides, but the strike-slip displacement is obvious.

The strike-slip displacement on the Trout Creek fault is recorded not merely in the displacement of the Roberts thrust but by a roughly equivalent displacement of shallow synforms of Silurian sandstone (Elder Sandstone). One remnant of the synform underlies Mount Lewis, where its axis strikes almost due north. South of the Trout Creek fault, a similar synform of Elder Sandstone is near Utah Mine Camp. Each segment of the synform is marked with an S on figure 1. This offset was called to my attention by E-an Zen in 1955 (oral commun.).

The synform is offset slightly more than the thrust, as exposed. This is readily explained by the half dozen eastward-thickening thrust slices that spring into the hanging wall of the main thrust at the site of its overturn. Clearly, the thickness of the thrust packet of the upper plate east of the overturn is as much as 3 km greater than that west of the antiform. One result of this thickening is that the Silurian plate in the synform north of the tear fault is more than 300 m higher than that south of it. This contrast, although opposite to that expected were the Trout Creek fault a caldera ring fault, is not conclusive, because of the possibility of postthrust deformation. Nevertheless, the evidence is conclusive that the Trout Creek fault and the Roberts thrust were formed simultaneously, 200 million years before the volcanism.

Wrucke and Silberman have extended a fault branching off the Trout Creek fault about 3 km west of D on figure 1 on a north-northeast course to connect with the Bateman fault. I was unable to trace this fault for more than about 1.5 km from the Trout Creek fault, but they may very well be right. If so, it has no bearing on the caldera question.

West of the Bateman fault, the upper plate of the Roberts thrust is a series of randomly intercalated thrust sheets in which mostly various parts of the Valmy Formation are shuffled together with lesser amounts of Silurian sandstone and Devonian chert. To the east is a large block of much less sheared and contorted Devonian chert. The Bateman fault is the third and easternmost of three generally similar arcuate thrusts north of the Trout Creek fault. Despite the randomly intercalated minor thrust sheets in the upper plate of the Roberts thrust, it so happens that each of the three most conspicuous thrusts happens to have older rocks over younger.

The three thrusts all dip rather steeply, at angles of 35° to 45°, and all curve slightly as they approach the Trout Creek fault, against which they end, with no recognizable extensions beyond it to the south. Accordingly, we consider them contemporaneous and cogenetic with the Trout Creek fault, and hence with the Roberts thrust. They are thus of Devonian and Mississippian age, far older than any of the volcanic rocks. No volcanic rocks are associated with any of them.

SUMMARY

Of the approximately 26 km of supposed ring faults postulated by Wrucke and Silberman, only about 6 km are followed by dikes—a striking paucity for a caldera. These dikes follow a fault of incontestable left-lateral strike-slip displacement with no evidence whatever for normal movement. Furthermore, the relation of this, the Trout Creek fault, with the offset of the Roberts thrust—a tear fault relation—demonstrates that they were formed concurrently, as were the listric thrusts to the north.

Thus, even if the fault postulated by Wrucke and Silberman west of the pluton on Goat Peak exists, as

I contend it does not, the picture would not be changed. The Trout Creek and Bateman faults are genetically part of the Roberts thrust system and formed 200 million years before the volcanic episode and certainly are not parts of a ring-fault system. Our failure to recognize a caldera was not due, as our critics suggested, to our unfamiliarity with calderas but to the absence of a caldera—none exists here.

Acknowledgments.—I am very grateful to Paul Sims, Fred Cater, and E-an Zen for critically reading the typescript. Their help has much improved the clarity of the paper.

REFERENCES CITED

Gilluly, James, 1960, A folded thrust in Nevada—Inferences as to time relations between folding and faulting: Am. Jour. Sci., v. 258–A (Bradley Volume), p. 68–79.

Gilluly, James, and Gates, Olcott, 1965, Tectonic and igneous geology of the northern Shoshone Range, Nevada: U.S. Geol. Survey Prof. Paper 465, 153 p.

Wrucke, C. T., and Silberman, M. L., 1975, Cauldron subsidence of Oligocene age at Mount Lewis, northern Shoshone Range, Nevada: U.S. Geol. Survey Prof. Paper 876, 20 p.

Jour. Research U.S. Geol. Survey
Vol. 5, No. 3, May–June 1977, p. 331–335

CAULDRON SUBSIDENCE OF OLIGOCENE AGE AT MOUNT LEWIS, SHOSHONE RANGE, NEVADA—A REASONABLE INTERPRETATION

By CHESTER T. WRUCKE and MILES L. SILBERMAN,
Reston, Va., Menlo Park, Calif.

Abstract.—James Gilluly has rejected the interpretation of Wrucke and Silberman (U.S. Geol. Survey Prof. Paper 876, 1975) that a thrust fault and tear fault mapped by Gilluly and Gates (U.S. Geol. Survey Prof. Paper 465, 1965) as structures bounding the upper plate of the Roberts Mountains thrust at Mount Lewis are parts of a ring fracture around an area that underwent volcanic collapse. In his discussion (this volume) of our paper, Gilluly fails to consider important questions that we presented in support of the subsidence hypothesis. Instead of answering these critical questions, Gilluly merely recapitulates the interpretations that he and Gates gave in Professional Paper 465. We presented new information, including a map of one critical area along the cauldron boundary where, among other significant differences in geologic interpretation, we found the ring fault where previously no steep fault was shown. Gilluly believes that the paucity of dikes along the ring fracture at Mount Lewis is highly anomalous for cauldrons. However, the amount of dike rock is comparable to that in known cauldrons (some cauldrons have none) and is what might be expected at high levels in subsidence structures that have undergone relatively little resurgent igneous activity after collapse. Gilluly concludes that in formulating our interpretation of volcanic collapse, we have ignored much evidence that he and Gates have presented on thrust faulting in the Shoshone Range. On the contrary, we have considered their ideas and have reinterpreted them using new evidence that strongly supports the concept of cauldron subsidence at Mount Lewis.

The possibility of cauldron collapse as proposed by Wrucke and Silberman (1975) for a conspicuous circular structure at Mount Lewis (fig. 1) has been emphatically rejected by Gilluly (this volume). Indeed, he states that some structural features identified by us are "in part nonexistent," are "geometrically impossible," or "have no bearing on the caldera[1] question," and he concludes that "no caldera is here present." These strong statements imply that our observations and interpretations are completely without merit and scientific basis. We believe, however, that our structural interpretations on the geology of Mount Lewis are in accord with the currently available data.

We began our study at Mount Lewis in an attempt to learn how the Tertiary igneous rocks there fit within the framework of Cenozoic volcanic history in central

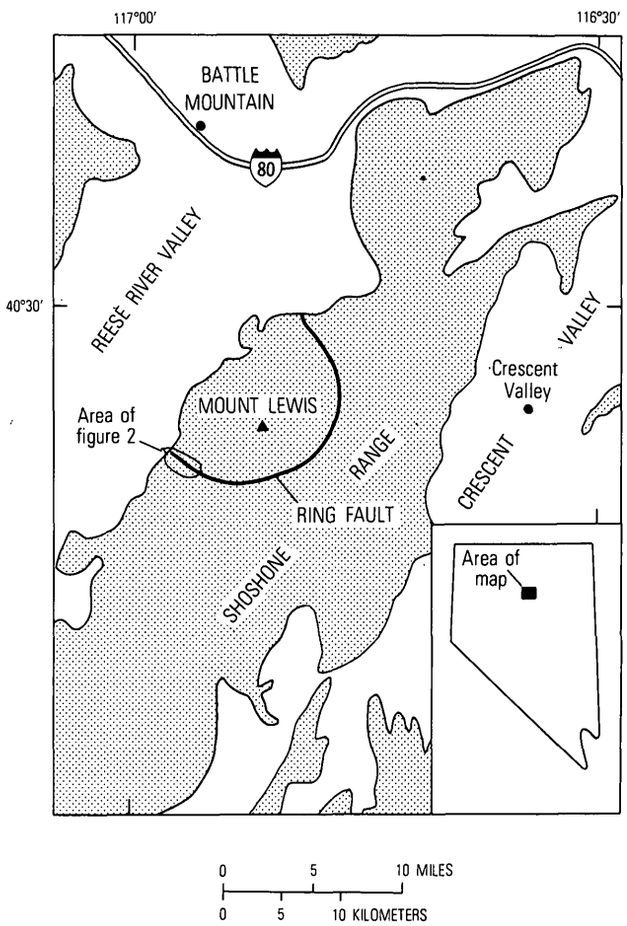

FIGURE 1.—Map of part of north-central Nevada showing location of ring fault at Mount Lewis.

[1] We use "cauldron" rather than "caldera," as no topographic expression remains of the original collapse depression.

Nevada as described by McKee and Silberman (1970), McKee, Silberman, Marvin, and Obradovich (1971), and Silberman and McKee (1974). Our conclusions were discussed in the last three sections of U.S. Geological Survey Professional Paper 876 (Wrucke and Silberman, 1975, p. 16–19), in which we defined a new cauldron-subsidence structure.

Our work in the Mount Lewis area was preceded by geologic studies in the Shoshone Range and by extensive research on volcanism in Nevada. Wrucke spent 7 years in geologic and geochemical studies of rocks in the upper and lower plates of the Roberts Mountains thrust in the Gold Acres and Tenabo mining areas on the east side of the Shoshone Range. This work consisted of regional mapping (Wrucke, 1974) and of detailed studies at the Gold Acres open-pit mine (Wrucke and Armbrustmacher, 1975; Wrucke and others, 1968) and resulted in new interpretations of Shoshone Range geology. Silberman had a background of 7 years research on igneous geology in Nevada and elsewhere, particularly in K-Ar dating of igneous rocks in many parts of the State, and, in collaboration with E. H. McKee of the U.S. Geological Survey, studies of the timing and nature of igneous activity and its relation to tectonic control (McKee and Silberman, 1970; McKee and others, 1971; Silberman and McKee, 1972, 1974; Silberman and others, 1976).

Acknowledgments.—We appreciate the helpful suggestions made by R. A. Bailey, D. C. Noble, and G. W. Walker, who reviewed the manuscript, and the advice on stratigraphy offered by R. K. Hose.

ANALYSIS OF FORMER WORK

Before examining Gilluly's criticisms of our work and presenting the considerable basis for our own interpretations, we will summarize the contributions Gilluly and Gates have made to the understanding of Shoshone Range geology and place their work in historical perspective.

The report on the tectonic and igneous geology of the northern Shoshone Range by Gilluly and Gates (1965) is a significant contribution to the knowledge of Nevada geology. Included are a detailed geologic map showing complex thrust faults in two 15-minute quadrangles, important contributions to stratigraphy, a detailed analysis of the tectonic history resulting from two exceedingly complicated episodes of thrusting, and considerable information on igneous rocks.

When Gilluly and Gates began field studies there in 1950, the only geologic maps then available (Emmons, 1910; Lee and others, 1915) presented no structural detail, and they either incorrectly gave the age of the lower or middle Paleozoic rocks as Carboniferous, on the basis of the work of Hague (1877a, b), or they identified them simply as Paleozoic. No hint of the geology as it now is known is evident in these early reports and maps, which are of use only as historic records.

As a result of the Gilluly and Gates study, we know the following: Most of the exposed rocks are in the upper plate of the Roberts Mountains thrust (formerly the Roberts thrust) of Early Mississippian age. During the orogeny that culminated in this episode of thrust faulting, chert, argillite, greenstone, quartzite, and other dominantly siliceous rocks of eugeosynclinal origin were transported eastward over limestone, dolomite, and quartzite of a dominantly carbonate sequence. The allochthonous mass, now thought to have moved at least 145 km (Stewart and Poole, 1974), actually is a stack of innumerable thrust plates that commonly juxtapose originally diverse parts of the eugeosynclinal stratigraphic sequence. This shuffling took place as plates overrode other plates, causing deformation and further imbrication in underlying, previously displaced rock masses.

Gilluly and Gates made sense out of the confusing mass of thrust slices. To do this, they had to understand stratigraphic units that nowhere are undeformed; in fact, all type sections of upper-plate rocks have fault contacts against other formations and are themselves broken by thrusts. Lower-plate rocks also contain thrust faults and are, therefore, only parautochthonous. Orogenic movements in early Mesozoic time climaxed in additional thrust faulting, although only relatively small areas of the Shoshone Range expose rocks involved in this event. Laudable as these contributions are, reexamination of field data and reinterpretation of observations are still possible. Our alternative interpretation for the geology at Mount Lewis is intended as a contribution that builds on the work of Gilluly and Gates. We see no reason to believe that the conclusions reached by them are irrefutable and not open to reinterpretation.

THE CASE FOR CAULDRON SUBSIDENCE

Important questions can be asked about the geology of the Mount Lewis area as Gilluly and Gates (1965, pl. 1) have depicted it. Is it merely fortuitous that the combination of faults shown as partly encompassing a volcanic center resembles a ring fault? Why do thrust sheets within the ring structure, as illustrated in our paper (Wrucke and Silberman, 1975, fig. 5), dip systematically inward toward breccia pipes in the central part of the Mount Lewis area? What caused the structural grain shown in Wrucke and Silberman (1975, fig. 5) to be so different within and without the ring

structure? Why are Mesozoic rocks present only within the ring structure? Gilluly and Gates apparently did not consider the cauldron hypothesis as one possible explanation for these relationships.

During our study we were aware of all the structural interpretations that Gilluly (this volume) points out in support of his work in the Shoshone Range, as they are recapitulations of parts of the paper by Gilluly and Gates (1965). In our search for materials suitable for K-Ar dating at Mount Lewis, we found that the geology differs in some important aspects from that shown by Gilluly and Gates. In one area critical to the concept of cauldron subsidence, we mapped the geology on aerial photos at a scale of 1:15,840 and presented the results as a sketch map (Wrucke and Silberman, 1975, fig. 4B). This area is critical because it contains a steeply dipping fault where Gilluly and Gates showed no steep faults. We labeled the map as a sketch map because we had not devoted the time required to work out all details. The map, however, is sufficiently detailed to show the considerable divergence of our observations from those of Gilluly and Gates. We questioned not only the location and extent of faults and contacts, but on the basis of our knowledge of formations on the east side of the range and of observations of colleagues who had extensive experience in the stratigraphy of miogeosynclinal rocks throughout northern Nevada, we also questioned the identification of stratigraphic units. We are convinced that future workers will have the same difficulty that we had in understanding Gilluly's and Gates' map of this part of the Mount Lewis area.

After publication of Professional Paper 876, we returned to this critical area and refined our map, presented here as figure 2. Some of the map units that we had originally designated by lithology alone (Wrucke and Silberman, 1975, fig. 4B) are identified now by formation names, and the stratigraphic unit that we showed as shale, quartzite, and limestone (sql) of Cambrian(?) and Ordovician(?) age now is designated as Ordovician(?). Microfossils were not found in two limestone samples from this unit. The Ordovician(?) age is our best interpretation of the age on the basis of the structural and assumed stratigraphic position of the unit between known Ordovician and Silurian formations. The sql unit does not resemble any formation in the lower plate of the Roberts Mountains thrust in Nevada, according to R. K. Hose (oral commun., 1976), and it clearly is not part of the Roberts Mountains Formation or the Hanson Creek Formation as mapped by Gilluly and Gates (1965).

The differences between our revised map (fig. 2) and the map of the same area by Gilluly and Gates (1965, pl. 1) are considerable. Important differences, in addition to those already discussed, include our interpretations that a slice of the Roberts Mountains Formation north of the ring fault at the east edge of the mapped area is within the upper plate of the Roberts Mountains thrust, that the Shwin Formation in the north part of the area also is part of the upper plate and overlies rather than underlies a thrust slice of Valmy Formation, and that the ring fault extends across the mapped area to the mountain front. These interpretations are important in showing that revisions to the map of Gilluly and Gates are possible and that upper-plate rocks are in contact with lower-plate rocks along a steep fault that we interpret as part of the ring fracture.

Gilluly (this volume) points out the paucity of dikes along the ring fault and suggests that this is highly anomalous for calderas. Dikes are abundant within the cauldron, but they are present along only 5.6 km of the 29-km exposure of the boundary fault. There is no reason, however, why igneous rock had to invade much of the ring fault. Dikes are present along a relatively small part of the ring fracture that bounds the cauldron at Alnsjø, Norway, as illustrated by Smith and Bailey (1968), and none are shown by McKee (1974) for the Northumberland caldera, Nevada, or by Ashley (1974) along the inferred trace of the ring fracture at Goldfield, Nev. The small amount of dike rock in the ring fault at Mount Lewis is explained easily if, as Smith and Bailey (1968, p. 654) proposed, most igneous rock in ring structures is of postcollapse origin. Available evidence suggests that relatively little resurgent igneous activity took place at the present level of exposure (Wrucke and Silberman, 1975, p. 11) after cauldron collapse at Mount Lewis, and the same appears to be true for collapse structures at Northumberland and Goldfield. The cauldron at Alnsjø has more dike rock than the Nevada examples discussed here and also more evidence of resurgent magmatic intrusion.

The Mount Lewis cauldron is one of 32 calderas and cauldrons identified in Nevada, as summarized by Stewart and Carlson (1976). These authors also noted four volcano-tectonic depressions and five volcanic centers in the State, and recently Ekren and Byers (1976) described an additional vent. Most of these structural features were identified after Gilluly and Gates completed work at Mount Lewis. In fact, the first discussion of the widespread distribution of ash-flow tuffs in Nevada was by Cook in 1965. Many workers have attempted before and after 1965 to locate the source areas from which the widespread ash-flow tuffs

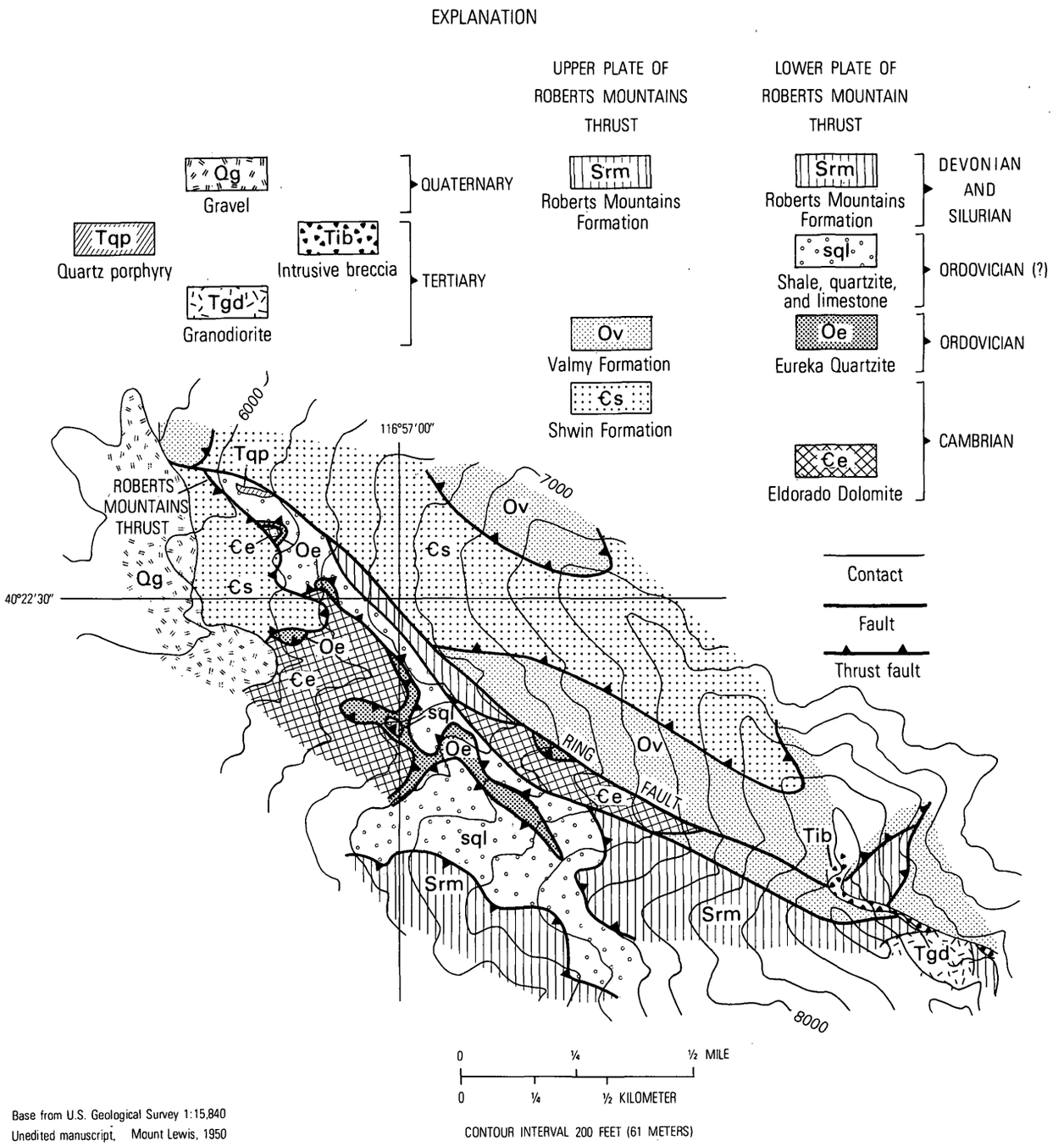

FIGURE 2.—Geologic map of the southwestern margin of the Mount Lewis area.

in Nevada were erupted. The Mount Lewis cauldron so far is the oldest of these source areas.

Our conclusions in Professional Paper 876 were offered not in criticism, as Gilluly (this volume) states, but as interpretations that amplify and extend the usefulness of Gilluly's and Gates' work. However, Gilluly's preemptory dismissal of an alternative interpretation is philosophically and scientifically unacceptable to us. Gilluly is emphatic in believing that a cauldron does not exist. We think that our evidence is reasonable, well founded, and strongly indicative of cauldron subsidence at Mount Lewis.

REFERENCES CITED

Ashley, R. P., 1974, Goldfield mining district, *in* Guidebook to the geology of four Tertiary volcanic centers in central Nevada: Nevada Bur. Mines and Geology Rept. 19, p. 49–66.

Cook, E. F., 1965, Stratigraphy of Tertiary volcanic rocks in eastern Nevada: Nevada Bur. Mines Rept. 11, 61 p.

Ekren, E. B., and Byers, F. M., Jr., 1976, Ash-flow fissure vent in west-central Nevada: Geology, v. 4, no. 4, p. 247–251.

Emmons, W. H., 1910, A reconnaissance of some mining camps in Elko, Lander, and Eureka Counties, Nevada: U.S. Geol. Survey Bull. 408, 130 p.

Gilluly, James, and Gates, Olcott, 1965, Tectonic and igneous geology of the northern Shoshone Range, Nevada: U.S. Geol. Survey Prof. Paper 465, 153 p.

Hague, Arnold, 1877a, Shoshone Range and Carico Peak, *in* Hague, Arnold, and Emmons, S. F., Descriptive geology: U.S. Geol. Explor. 40th Parallel (King), v. 2, p. 618–625.

——— 1877b, Region east of Reese River, *in* Hague, Arnold, and Emmons, S. F., Descriptive geology: U.S. Geol. Explor. 40th Parallel (King), v. 2, p. 627–635.

Lee, W. T., Stone, R. W., Gale, H. S., and others, 1915, Guidebook of the Western United States, Pt. B, The Overland Route * * *: U.S. Geol. Survey Bull. 612, 244 p.

McKee, E. H., 1974, Northumberland Caldera and Northumberland Tuff, *in* Guidebook to the geology of Four Tertiary volcanic centers in central Nevada: Nevada Bur. Mines and Geology Rept. 19, p. 35–41.

McKee, E. H., and Silberman, M. L., 1970, Geochronology of Tertiary igneous rocks in central Nevada: Geol. Soc. America Bull., v. 81, no. 8, p. 2317–2328.

McKee, E. H., Silberman, M. L., Marvin, R. E., and Obradovich, J. D., 1971, A summary of radiometric ages of Tertiary volcanic rocks in Nevada and eastern California; Pt. I, Central Nevada: Isochron/West, no. 2, p. 21–42.

Silberman, M. L., and McKee, E. H., 1972, A summary of radiometric age determinations on Tertiary volcanic rocks from Nevada and eastern California; Pt. II, Western Nevada: Isochron/West, no. 4, p. 7–28.

——— 1974, Areas of Tertiary volcanic rocks and hydrothermal precious-metal deposits in central and western Nevada, *in* Guidebook to the geology of four tertiary volcanic centers in Central Nevada: Nevada Bur. Mines and Geology Rept. 19, p. 67–72.

Silberman, M. L., Stewart, J. H., and McKee, E. H., 1976, Igneous activity, tectonics, and hydrothermal precious-metal mineralization in the Great Basin during Cenozoic time: Am. Inst. Mining, Metall., Petroleum Engineers, Soc. Mining Engineers Trans., v. 260, p. 253–263.

Smith, R. L., and Bailey, R. A., 1968, Resurgent cauldrons, *in* Coats, R. R., Hay, R. L., and Anderson, C. A., eds., Studies in volcanology—A memoir in honor of Howel Williams: Geol. Soc. America Mem. 116, p. 613–662.

Stewart, J. H., and Carlson, J. E., 1976, Cenozoic rocks of Nevada—Four maps and brief description of distribution, lithology, age, and centers of volcanism: Nevada Bur. Mines and Geology Rept. (in press).

Stewart, J. H., and Poole, F. G., 1974, Lower Paleozoic and uppermost Precambrian Cordilleran miogeocline, Great Basin, Western United States, *in* Dickinson, W. R., ed., Tectonics and sedimentation: Soc. Econ. Paleontologists and Mineralogists Spec. Pub. 22, p. 28–57.

Wrucke, C. T., 1974, Geologic map of the Gold Acres-Tenabo area, Shoshone Range, Lander County, Nevada: U.S. Geol. Survey Misc. Field Studies Map MF–647, 2 sheets.

Wrucke, C. T., and Armbrustmacher, T. J., 1975, Geochemical and geologic relations of gold and other elements at the Gold Acres open-pit mine, Lander County, Nevada: U.S. Geol. Survey Prof. Paper 860, 27 p.

Wrucke, C. T., Armbrustmacher, T. J., and Hessin, T. D., 1968, Distribution of gold, silver, and other metals near Gold Acres and Tenabo, Lander County, Nevada: U.S. Geol. Survey Circ. 589, 19 p.

Wrucke, C. T., and Silberman, M. L., 1975, Cauldron subsidence of Oligocene age at Mount Lewis, northern Shoshone Range, Nevada: U.S. Geol. Survey Prof. Paper 876, 20 p.

Jour. Research U.S. Geol. Survey
Vol. 5, No. 3, May–June 1977, p. 337–342

HYDRATION DATING OF VOLCANISM AT NEWBERRY CRATER, OREGON

By IRVING FRIEDMAN, Denver, Colo.

Abstract.—Obsidian hydration dating of pumice and obsidian from Newberry Crater, Oreg., shows that the postcaldera activity began about 6700 yr ago and that the latest major eruptive event occurred about 1400 yr B.P. Two of the hydration dates correlate with ^{14}C-dated pumice eruptions.

Dating of rhyolitic volcanism by measuring the hydration rind on obsidian was first attempted by Friedman (1968). Shortly after publication of that paper, N. V. Peterson, E. A. Groh, and R. E. Corcoran suggested that Newberry Crater would be an excellent area in which to apply the hydration-dating technique. Not only were there multiple events whose relative ages were known, but a rate of hydration that might be applicable to the site had been published by Johnson (1969).

This is not the report of an exhaustive and definitive study of the many eruptive events at Newberry Crater. Rather it is a reconnaissance in the application of a new tool to an interesting and complex area.

Newberry Crater, a caldera at the summit of Newberry volcano, was described first by Russell (1905) and more recently by Williams (1935) and Higgins and Waters (1967). The caldera is situated about 30 km (kilometers) south of Bend, Oreg. Figure 1 is an aerial photograph of the area showing some of the volcanic features. Peterson and Groh (1969) have described Holocene eruptive events on the flanks of Newberry volcano and have shown that much of the activity took place from about 6400 yr B.P. (years before present) to about 1200 yr B.P. (radiocarbon years). Mount Mazama ash (6600 yrs B.P.) is found within the caldera, but it does not mantle many flows that erupted after the caldera collapse. Therefore, much of the volcanic activity that occurred after caldera collapse appears to be younger than 6600 yr B.P. M. W. Higgins (written commun., 1975) concludes that some of the postcollapse features are covered with Mazama ash and that the collapse may predate 6600 years.

N. V. Peterson, E. A. Groh, and R. E. Corcoran accompanied the author on several collecting trips; during these trips attempts were made to collect obsidian samples that contained at least one surface judged to have been formed during the emplacement of the flow or dome. Some of the criteria that were used are as follows:

1. Tension cracks, similar to those shown by Friedman (1968). Unfortunately, this type of crack is rare in the flows sampled.
2. Surfaces showing a white deposit of silica that appears to have been deposited by steam that was probably emitted during cooling of the flow. Whereas this criterion is valid, a silica deposit makes measurement of the underlying hydration difficult.
3. Samples that contained vesicles produced by released gas during flowage. Many of these vesicles were pulled out into elongate, sheetlike cavities. Fracture of the obsidian, while flowing or during cooling, allowed the atmosphere to penetrate into these large, cracklike vesicles.

Five to ten hand specimens were collected from different areas of each feature. Usually two or more thin sections were cut from each specimen.

Over 200 thin sections were examined. Although precise measurements were made on only about 85 of the best sections, preliminary measurements on the discarded sections were in general agreement with the results reported here. All measurements were made using a Vickers image-splitting eyepiece, and the results are precise to ± 0.1 μm (micrometers).

In order to convert hydration thickness into an age, the rate of hydration must be known. Johnson (1969) measured a number of obsidian artifacts from archeological horizons that he had dated by ^{14}C. These archeological sites were all in the Klamath Basin, about 200 km south of Newberry Crater and 1000 m (meters) lower in elevation. The rate that he calculated was 3.5 $\mu m^2/1000$ ^{14}C years. If we convert ^{14}C years to calendar years, using published conversions (Olsson, 1970, p. 3), the corrected rate is 3.1 $\mu m^2/1000$ yr. Because the hydration rate is temperature dependent, we would expect the hydration to proceed somewhat more slowly in Newberry Crater than in the Klamath Basin. The hydration rate is dependent on the chemical composi-

FIGURE 1.—Aerial photograph of Newberry Crater area, central Oregon.

tion of the volcanic glass; the chemical composition of the obsidian used by Johnson is not reported, and the hydration rate that he derived may not apply to the obsidian from Newberry.

Johnson's rate, however, was measured on archeological material that was buried and that did not experience the wide and frequent temperature fluctuations of obsidian exposed at the Earth's surface. A higher rate of hydration can be expected for obsidian at or near the surface. Not only does such material experience the normal air-temperature fluctuation, but solar heating can cause temperatures of obsidian to exceed 50°C during a bright, sunny day.

From September 1971 through September 1972, temperatures were recorded at Pine Mountain Observatory, 20 km east-northeast of East Lake, Newberry Crater. The data for Pine Mountain are given in table 1. In calculating the hydration rate, the equation relating hydration rate to temperature, derived experimentally (Friedman and Long, 1976) on obsidian from the east lobe of the East Lake flow, Newberry (rate in $\mu m^2/10^3$ years$=1.429\times10^{15}e^{-9668.8(1/T)}$, where T is temperature in kelvins), was solved for the temperatures measured hourly at Pine Mountain Observatory. These hourly determined rates of hydration were then averaged for one calendar year. This average rate was then substituted in the above equation to calculate the effective hydration temperature. This temperature, if maintained continuously, will cause the obsidian sample to hydrate at the calculated rate.

TABLE 1.—*Rates of hydration and effective temperature of hydration, Pine Mountain Observatory, Deschutes County, Oreg.*

[Mean annual air temperature, 1931-60 = 4.67°C]

	Rate of hydration ($\mu m^2/10^3$ yr)	Effective temperature (°C)
Surface of obsidian exposed to Sun	7.2	20.4
Probe in soil, 30 cm depth	2.3	10.6
Probe in soil, 60 cm depth	2.1	9.8
Probe in air	2.8	12.2

The elevation at the observatory is 1902 m as compared with 1930 m at East Lake. Both sites have very similar climates, except that the snow cover at Newberry is more extensive and persists for a longer time than at the observatory. The effective temperature of hydration at Newberry is probably about 2°C higher than at Pine Mountain Observatory.

Because most of the samples were collected 30–60 cm (centimeters) below the surface, the effective hydration temperature as measured at Pine Mountain at the 30-cm depth was increased by 2.0°C to compensate for the increased snow cover at Newberry as compared with Pine Mountain. This correction results in a rate of hydration of 2.9 $\mu m^2/10^3$ yr. The hydration rate is also dependent on the chemical composition and, particularly, the SiO_2 content of the glass. With the exception of Big Obsidian flow, all the glasses collected at Newberry have a SiO_2 content of 73.2–74.2 percent. Big Obsidian flow has a silica content of 72.2–72.9 percent and hydrates at a much lower rate than the other Newberry glasses. The hydration rate used for Big Obsidian flow, based on the previously quoted published hydration experiments at elevated temperatures and water pressures, is 0.7 $\mu m^2/10^3$ yr.

The hydration rate that was used in calculating the ages of the Interlake and Game Hut flows cannot be significantly less than 2.9 $\mu m^2/10^3$ yr, inasmuch as a lower rate would yield an age greater than the Mount Mazama eruption, an event that preceded these events. The rate that applies to Interlake and Game Hut flows cannot be very different from that used for the Pumice Cone and East Lake flows because the groupings of hydration thickness between the four sets of flows indicate a common rate of hydration.

The results of the measurements are plotted in figure 2. On many specimens more than one thickness of hydration were found, and in several, hydration layers of different thicknesses could be found on the same thin section. In some sections, vesicles were found that had been ruptured upon emplacement. In all instances, these vesicles showed the maximum thickness of hydration found on any specimens from the unit sampled.

In any unit showing multiple hydration thicknesses, the measurements always occurred in definite groupings rather than in a continuous distribution of thicknesses. For example, samples from Game Hut flows show hydrations of 4.4, 4.1, 3.6, 3.2, and 2.9 μm, whereas samples from Pumice Cone flows have thicknesses of 3.6, 2.9, and 2.2 μm. The conclusion is drawn that the Game Hut eruption occurred 6700 yr ago (4.4–μm hydration thickness) and that the eruption of Pumice Cone flow at 4500 yr B.P. (3.6 μm) caused cracking of the obsidian in Game Hut flows about 1 km away. An event that could have caused additional cracking at about 1700 yr B.P. (2.2 μm) was the pumice eruption that was radiocarbon-dated by Higgins and Waters (1970) at about 1700 yr B.P.

Interlake flow, which also erupted 6700 yr ago (4.4 μm), similarly records cracks at 4500 yr B.P. (3.6 μm) (eruption of Pumice Cone central flow); 3500 yr B.P. (3.2 μm) (eruption of East Lake west and east flows); and 1400 yr B.P. (1.9 μm) (pumice eruption ^{14}C dated[1] and eruption of Big Obsidian flow).

[1] C-657, 2054±230 yr B.P. (Libby, 1952); TX-245, 1270±60 yr B. P. (Pierson and others, 1966); W-2777, 1390±200 yr B.P. (Meyer Rubin, written commun., 1974).

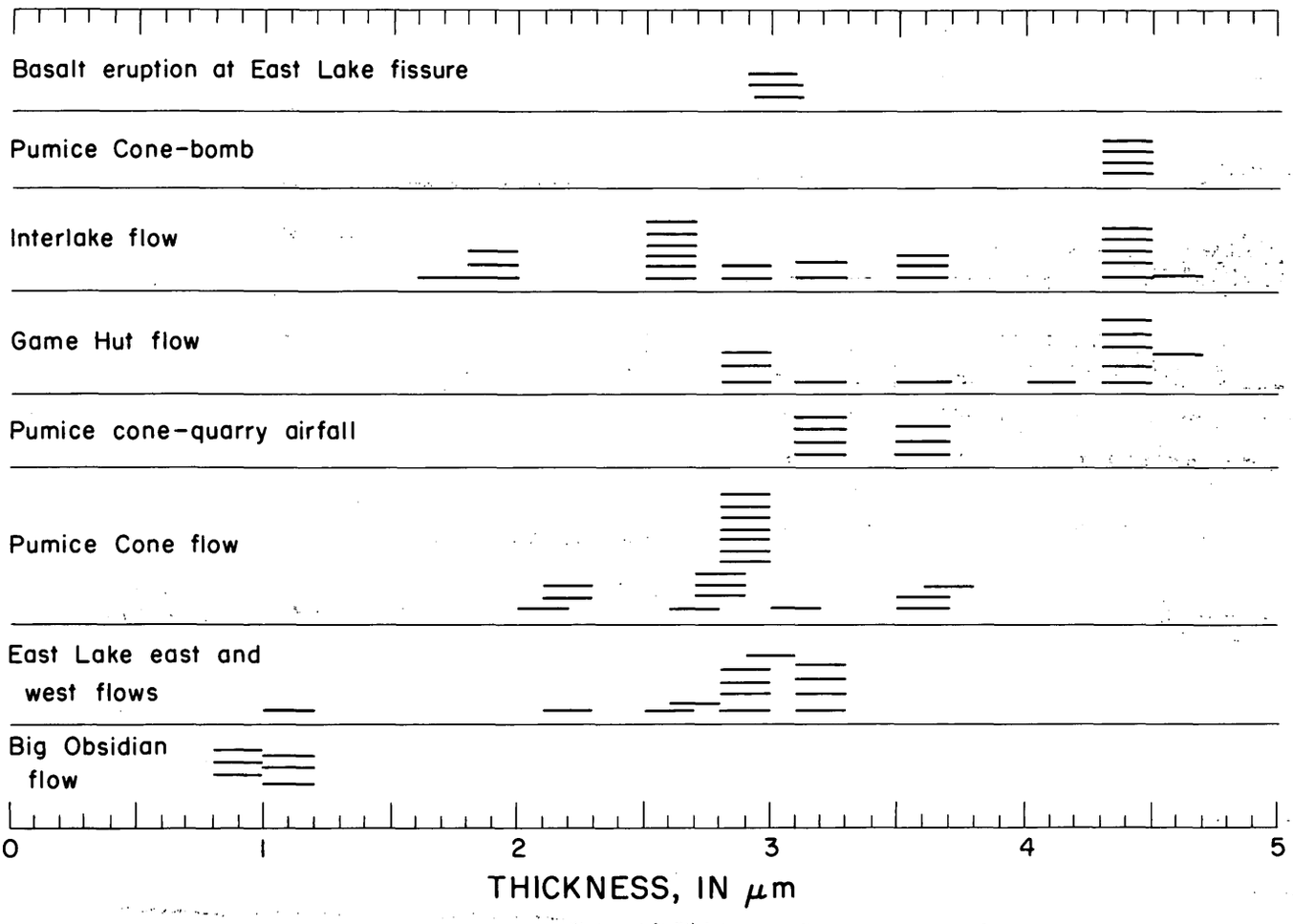

FIGURE 2.—Plot of measured hydration thickness of samples from Newberry Crater. Position of each horizontal line represents thickness of hydration along crack or edge. Length of line represents estimated measuring error.

In all samples, the thickest hydration is believed to represent the surface created during the eruptive event that originally emplaced the material. Subsequent cracking is assumed to have been due to either earthquakes or renewed movement of the flow or dome caused by nearby eruptions. It should be noted that all the eruptive events were very close geographically—all occurred within a square of about 5 by 5 km.

Pumice Cone flows (4500 yr B.P.), a series of flows that occupies the crater of Central Pumice cone, seemingly give an anomalous age. From the field relations, it is clear that Interlake flow (dated at 6700 yr B.P.) forked when it reached Central Pumice cone and that Central Pumice cone must therefore be older than Interlake flow. Dating of some of the coarser pumice bombs from Central Pumice cone gave a date of 6700 yr (4.4 μm, fig. 3), indicating that Central Pumice cone was formed by a pumice eruption just prior to the eruption of Interlake flow. Subsequent eruptions, probably from the same vent area, resulted in the emplacement of the Pumice Cone obsidian flows.

Game Hut flows erupted from a vent near the base of Central Pumice cone also at 6700 yr B.P. (4.4 μm); and, from the relationship to Central Pumice cone, they must have erupted after the pumice eruption that created the cone. The flows that now occupy the crater-like depression in the top of Central Pumice cone must have been erupted about 2200 yr after the formation of Central Pumice cone. These flows were preceded by a pumice eruption; large blocks of pumice and fragments of obsidian having a hydration thickness of 3.6 μm are found in the upper part of Central Pumice cone, just below the breached crater.

Higgins (1969) has studied the distribution of a 1,700-year-old ash and pumice layer present in most of the Newberry Crater area. From isopach maps, he has concluded that the ash originated from Central Pumice cone. Since the vent in Central Pumice cone was

plugged about 4500 yr ago by Pumice Cone flow, the ash layer must have been derived from another vent in the vicinity. It is possible that Big Obsidian flow (1400 yr B.P.) has covered the source of the ash layer studied by Higgins.

Higgins and Waters (1970) reevaluated the mixed basalt-rhyolite material found in the East Lake fissure and showed that the obsidian at this locality was formed by remelting of older rhyolite by the basalt flow. They dated the event as less than 1,970 years old, because the fissure is not covered by ash from Central Pumice cone, dated previously by Higgins as 1720±250 yr B.P. Friedman and Peterson (1971) measured the hydration thickness of the obsidian and found a thickness of 3.0±0.2 μm. They reported an age of 2900±400 yr B.P. for this event, using a hydration rate of 3.1 μm^2/1000 yr. As discussed previously, this event would have occurred 2600 to 3400 yr ago. The obsidianlike material from this locality is reported by Higgins and Waters (1970) as having a silica content of 71.8 percent. Analysis of the samples used by Friedman, Peterson, and Groh (1972) shows a silica variation from 69 to 72 percent. Glasses of these compositions may hydrate at a different, probably slower, rate than the other obsidians found at Newberry. Therefore the date given for this event may be too low, in which case the discrepancy between the results reported by Higgins and Waters and the results reported in this paper increase. The possibility of hydrothermal activity affecting the hydration rate of the "fissure" was suggested by Higgins and Waters (1972) and rejected by Friedman, Peterson, and Groh (1972).

The absence of pumice cover on the fissure must be used with caution as an age indicator. The 1720-yr-B.P. pumice studied by Higgins probably did not originate from Central Pumice cone. If it erupted from a vent southwest of Central Pumice cone, Central Pumice cone may have acted as a deflector and shielded the fissure, which is located about 1 km northeast of the flanks of Central Pumice cone (fig. 1).

This shielding by Central Pumice cone may account for the fact that the 1400-yr-old pumice, which is found near the southwest base of Central Pumice cone and which probably originated from a vent under Big Obsidian flow, is also not found on the fissure. According to both Higgins and Waters (1970) and Friedman and Peterson (1971), this fissure must be older than the ^{14}C-dated pumice fall.

The sequence of events that occurred during the past 6700 yr, as deduced by hydration and ^{14}C dating, is summarized in figure 3.

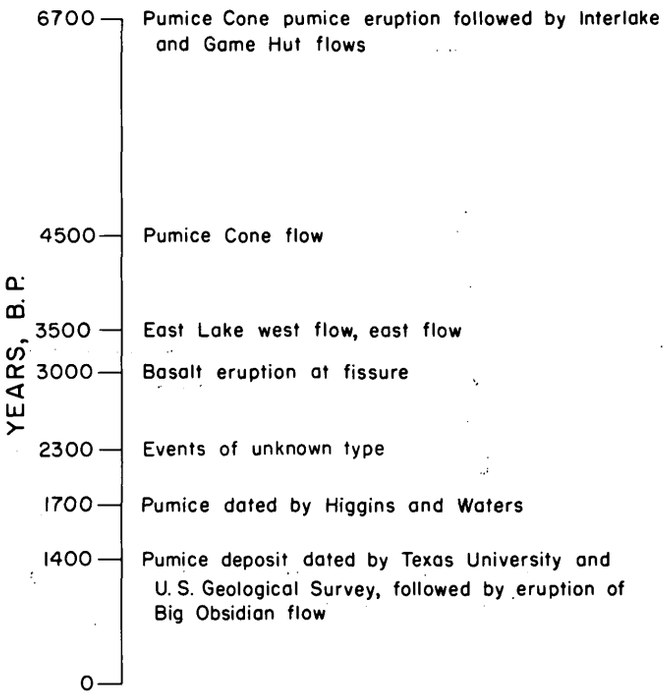

FIGURE 3.—Sequence of major eruptive events during the past 6700 yr at Newberry Crater.

ACKNOWLEDGMENTS

This report was reviewed by N. V. Peterson and M. W. Higgins. The latter reviewer does not agree with all of the conclusions reached by the author. The author acknowledges the help of Mel Johnson and especially of William Long, both of the U.S. Geological Survey, for their help in making the thin sections. The aid of Norman Peterson and Edward Groh both in suggesting the problem and helping with the interpretation of the data is also gratefully acknowledged.

REFERENCES CITED

Friedman, Irving, 1968, Hydration rind dates rhyolite flows: Science, v. 159, p. 878–879.

Friedman, Irving, and Long, W. D., 1976, Hydration rate of obsidian: Science, v. 191, p. 347–352.

Friedman, Irving, and Peterson, N. V., 1971, Obsidian hydration dating applied to dating of basaltic volcanic activity: Science, v. 172, p. 1028.

Friedman, Irving, Peterson, N. V., and Groh, E. H., 1972, Obsidian hydration dating applied to basaltic activity—A reply: Science, v. 176, p. 1259–1260.

Higgins, M. W., 1969, Airfall ash and pumice lapilli deposits from Central Pumice Cone, Newberry Caldera, Oregon, *in* Geological Survey research 1969: U.S. Geol. Survey Prof. Paper 650–D, p. D26–D32.

Higgins, M. W., and Waters, A. C., 1967, Newberry Caldera, Oregon—A preliminary report: The Ore Bin, v. 29, p. 37–60.

——— 1970, A re-evaluation of basalt-obsidian relations at East Lake fissure, Newberry Caldera, Oregon: Geol. Soc. America Bull., v. 81, p. 2835–2842.

——— 1972, Obsidian hydration dating applied to dating of basaltic volcanic activity: Science 176, p. 1259.

Johnson, L., Jr., 1969, Obsidian hydration rate for the Klamath Basin of California and Oregon: Science, v. 165, p. 1354–1356.

Libby, W. F., 1952, Chicago radiocarbon dates III: Science, v. 161, p. 673–681.

Olsson, I. U., ed., 1970, Radiocarbon variations and absolute chronology—Nobel Symposium, 12th, Upsala, 1969 Proc.: New York, John Wiley and Sons, 652 p.

Peterson, N. V., and Groh, E. A., 1969, The ages of some Holocene volcanic eruptions in the Newberry volcano area, Oregon: The Ore Bin, v. 31, p. 73–87.

Pierson, F. J., Jr., Davis, E. M., and Tamers, M. A, 1966, University of Texas radiocarbon dates IV: Radiocarbon, v 8, p. 453–466.

Russell, I. C., 1905, Preliminary report on the geology and water resources of central Oregon: U.S. Geol. Survey Bull. 252, 138 p.

Williams, H., 1935, Newberry volcano of central Oregon: Geol. Soc. America Bull., v. 46, p. 253–304.

Jour. Research U.S. Geol. Survey
Vol. 5, No. 3, May–June 1977, p. 343–357

BOREHOLE GEOPHYSICAL INVESTIGATIONS IN THE SOUTH TEXAS URANIUM DISTRICT

By JEFFREY J. DANIELS, JAMES H. SCOTT, PAUL D. BLACKMON, and HARRY S. STARKEY, Denver, Colo.

Abstract.—Contrasts of electrical properties between uranium deposits and their host rocks in South Texas are subtle. In places where deposits are small or deep, conventional geophysical well-logging techniques and hole-to-hole measurements may be the only practical method to detect changes in rock properties associated with the occurrence of uranium ore deposits. Two separate ore-producing areas in South Texas were chosen for studying borehole geophysical techniques applied to uranium-exploration problems. Extensive measurements of physical properties were made on cores and taken from holes where electrical-resistivity, induced-polarization and gamam-ray logs were run. These analyses show that: (1) induced-polarization anomalies are caused by a change in pyrite content and clay-sized material content and (2) resistivity anomalies are associated with a change in clay-sized material content and cementation. In addition to conventional borehole techniques, hole-to-hole induced-polarization and resistivity tests were made in South Texas. These measurements were made by placing a current source down one hole and a receiver cable down an adjacent hole whose separation ranged from 30 to 300 m and hole depths varied from 80 to 270 m. These tests show that hole-to-hole measurements can be used to detect changes in physical properties, associated with uranium ore, that occur between boreholes. Hole-to-hole measurements provide a link between surface measurements and well logs and can minimize the amount of drilling needed to locate an ore deposit. Accordingly, borehole geophysics will become an increasingly important evaluation tool as mineral exploration goes deeper.

Uranium was first discovered in western Karnes County in the Coastal Plains of southeast Texas in 1954. Since then, extensive exploration has uncovered most of the shallow, high-grade (more than 0.20-percent U_3O_8) uranium ore in this district. Further exploration efforts will be concentrated on shallow, low-grade deposits (less than 0.02-percent U_3O_8) and on higher grade, deeper deposits.

Economical exploration for these low-grade deposits will require the development of new techniques that will minimize the amount of exploration drilling. Successful exploitation of the deposits, by efficient mining operations, will require economic techniques to establish the physical and chemical properties of the host rocks. Here, borehole geophysical techniques will be useful in delimiting ore and in providing an inexpensive means of determining physical and chemical rock properties.

Uranium minerals in South Texas have been found in bentonitic clay, silt, or tuffaceous sand in various stratigraphic positions ranging in age from Eocene to Pliocene (Eargle and Weeks, 1968). The uranium minerals occur in four different geologic units: the Goliad Sand of Pliocene age, the Oakville Sandstone of Miocene age, the Catahoula Tuff of Miocene age, and the Jackson Group of Eocene age (Eargle, and others, 1971). At the present time, most of the exploration activity is concentrated in the Oakville, Catahoula, and Jackson.

This study is primarily concerned with property 1 in the Oakville and property 2 in the Catahoula. (Exact locations of properties 1 and 2 are proprietary information.) A line of holes was drilled on property 1 in order to gather borehole geophysical data and cores from which data on mineralogic and physical rock properties were obtained. The borehole geophysical information at property 1 included induced-polarization, gamma-ray, and resistivity well logs. Hole-to-hole resistivity and IP (induced-polarization) measurements were also made in a line of drill holes on property 1. Borehole geophysical measurements on property 2, where the drill holes penetrate the Catahoula Tuff, include gamma-ray and neutron well logs and hole-to-hole resistivity and IP measurements.

GEOLOGY

A geologic cross section for a line across property 1 is shown in figure 1. The sand-clay beds dip to the east. The sands are unconsolidated and contain fine- to medium-sized grains. The lower sand contains the highest gamma-ray count and is the "ore sand" in this area. A sand is assumed to be an "ore sand" if its gamma-ray count is at least five times higher than the background gamma-ray count.

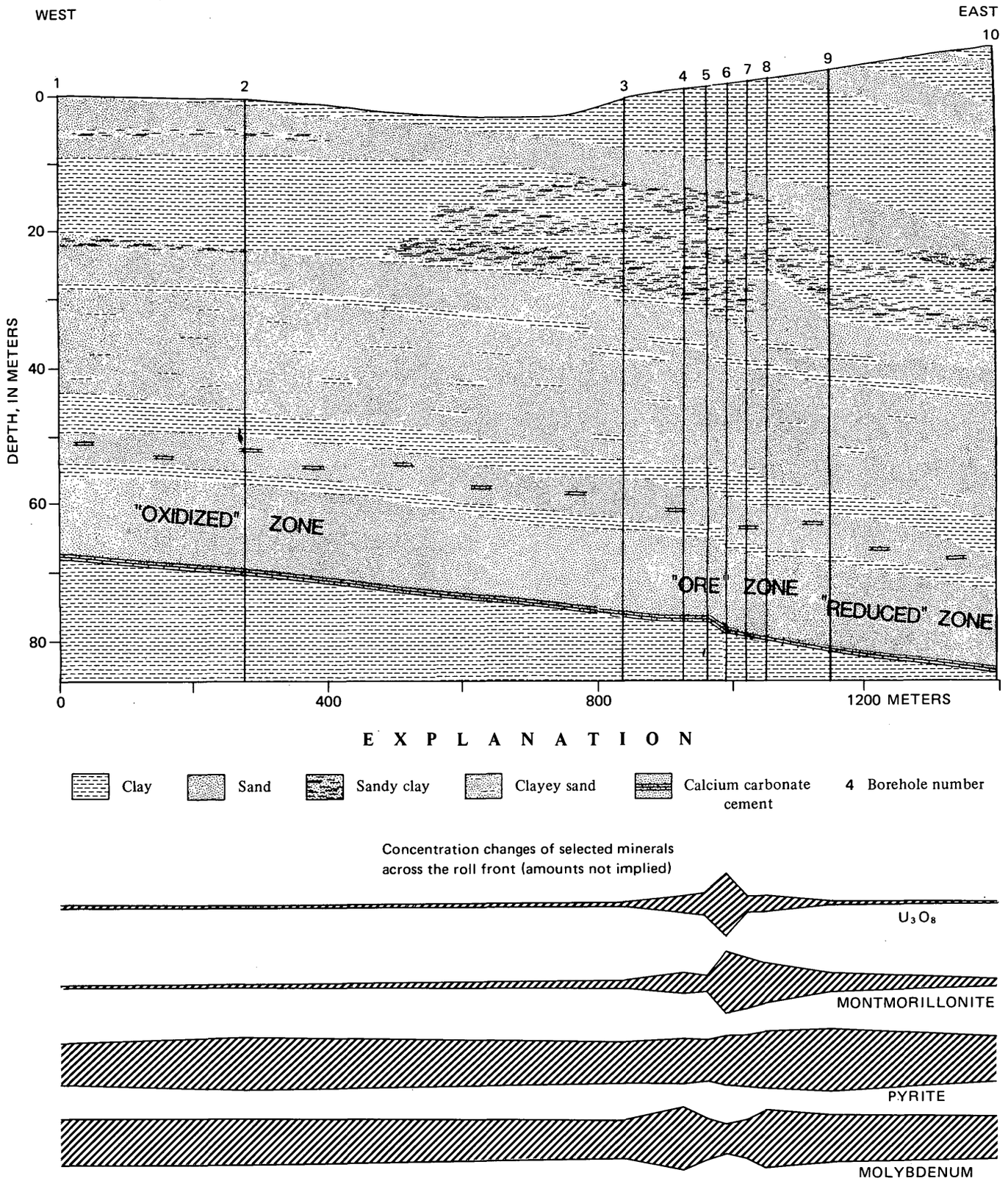

FIGURE 1.—Geologic cross section on property 1 through holes drilled in the Oakville Sandstone.

Petrographic analysis of cores from the "ore sand" indicates that the dominant minerals are quartz, montmorillonite, and illite while the minor constituents are calcite, pyrite, and jordisite. Marcasite, clinoptilolite, and anatase are found only in trace amounts. A summary of the analysis of the sand-clay, pyrite, molybdenum, and uranium oxide (U_3O_8) for the ore sand in boreholes 3 through 8 is given in table 1. References to clay content in this paper refer to clay-sized particles (<2 micrometers) rather than clay mineral content. In general, there is an increase in pyrite content across the ore zone, while the total clay content remains relatively unchanged across the ore zone. Molybdenum content and the montmorillonite clay fraction increase with an increase in U_3O_8.

TABLE 1.—*Sand, total clay, montmorillonite, pyrite,* U_3O_8, *and molybdenum content for samples in boreholes 3–8, property 1*

[ppm, parts per million; ?, questionable; <, less than; and ---, no data]

Sample No.	Depth, in meters	Sand	Total clay	Montmorillonite	Pyrite	U_3O_8	Mo (ppm)
		Percent					
3-29	75	9.2	63.2	25.0	1.65	0.037	46
19	69	83.4	5.3	3.7	.5	.0014	4
15	66	69.5	10.1	6.1	1.05	.0024	16
5	49	44.5	34.6	6.9	?	.0003	<2
24	72	86.9	3.38	2.3	.3	.002	2
28	75	85.0	6.3	3.8	.6	.0017	12
4-12	70	69.3	13.6	6.8	1.8	.0075	18
6	66	19.3	55.0	17.0	1.35	<.0002	2
26	77	4.4	62.4	12.5	.2	.13	36
2	64	78.9	8.4	4.2	.5	<.0002	2
27	78	8.1	62.7	31.4	.1	.007	100
25	77	72.5	8.0	4.0	.65	.002	44
17	73	85.4	3.9	1.4	1.15	.0011	2
22	75	77.0	11.8	8.3	.40	.002	23
5-13	72	81.0	5.3	3.2	2.0	.003	4
10	70	79.0	6.2	3.1	.75	.046	36
5	67	65.0	12.0	6.0	1.7	.0007	12
22	76	85.0	4.6	2.8	1.5	.14	200
8	69	79.0	7.7	4.6	1.4	.017	60
15	73	84.0	5.6	2.8	1.0	.003	4
2	65	28.0	50.0	15.0	2.0	<.0002	2
6-19	79	83.5	4.3	1.7	1.0	.0070	100
15	76	82.8	5.2	2.1	.25	.091	100
10	73	84.3	5.4	2.2	1.7	.0065	120
7	71	70.0	8.3	1.7	.3	.005	65
4	69	20.0	8.3	4.2	.3	.0002	8
18	78	80.6	6.8	3.4	---	.014	50
7- 5	69	42.7	20.2	8.1	1.45	.0003	10
19	79	85.7	3.9	2.0	.40	.0075	46
21	80	78.2	6.0	2.4	.40	.0032	42
8	71	69.6	14.5	7.3	.65	.0065	26
11	74	78.2	5.9	3.5	.85	.0065	80
15	76	76.8	7.1	2.8	1.05	.046	240
22	80	72.4	14.0	8.4	1.3	.0095	65
8- 6	70	38.5	24.4	14.6	1.2	.0003	4
11	74	83.3	5.9	3.5	1.8	.0095	100
9	72	80.0	9.1	6.3	2.15	.0034	18
13	75	82.8	4.4	2.6	1.0	.029	70
15	77	86.0	3.2	1.9	1.1	.021	50
19	79	85.5	2.9	1.1	1.2	.0055	100
22	80	83.9	3.6	2.2	.50	.0045	44
24	81	79.3	4.2	2.1	1.4	.0038	36

A "roll-front" uranium deposit has been defined by Rubin (1970) as: ". . . a C-shaped interface between the altered and unaltered portions of a sandstone along which uranium has been deposited. The interface probably is caused by oxidizing agents moving down dip through a carbonaceous and pyritic water saturated sandstone (reducing environment)."

The general geologic characteristics of the roll front on property 1 are shown in figure 1. On the basis of the gamma-ray logs, the front can be divided into three geochemical zones: an "oxidized" zone, an "ore" zone, and a "reduced" zone. However, the mineral content and color of the lower sand indicates a reducing environment for the cross section. Fresh sand samples indicate the presence of H_2S gas. It is possible that an oxidized-reduced front existed at an earlier time, but the "oxidized" zone has been reduced by the introduction of H_2S gas.

A lithologic cross section for property 2 (fig. 2) shows a sand-shale sequence similar to that for property 1. There is no comprehensive mineral analysis available for property 2. However, gamma-ray and lithologic logs indicate the presence of a roll front as indicated in figure 2.

RESISTIVITY AND INDUCED-POLARIZATION CORE-SAMPLE MEASUREMENTS

Resistivity and IP measurements were made on core samples taken from various depths in the "ore sand" on property 1. The unconsolidated core samples were packed into a soft plastic tube for making the IP and resistivity measurements. Figure 3 shows the sample measuring system that was used. The input signal was generated from a constant-current source and the signal was received by a recorder-integrator.

The input signal was a square wave with an off-time of the same duration as the positive and negative on-time (±5 mA). An analog integrator was used to provide a continuous record of the transient response of the sample. The integrator was started at time t_d and recorded a continuous record of the integrated transient signal as is shown in figure 3. The curves represent the transient signal, the integrated positive transient signal, and the integrated negative transient signal.

Table 2 shows the results of these measurements. The resistivity was calculated using the following equation:

$$\rho = K(V_p/I)$$

where ρ is the resistivity of the sample,
K is the geometric factor,
V_p is the primary voltage, and
I is the current put into the sample.

Induced polarization, IP, was calculated by dividing area A by area B shown in figure 3, where each is measured over an equal time interval.

Comparison of table 2 with table 1 shows that the relationship between electrical properties and mineral-

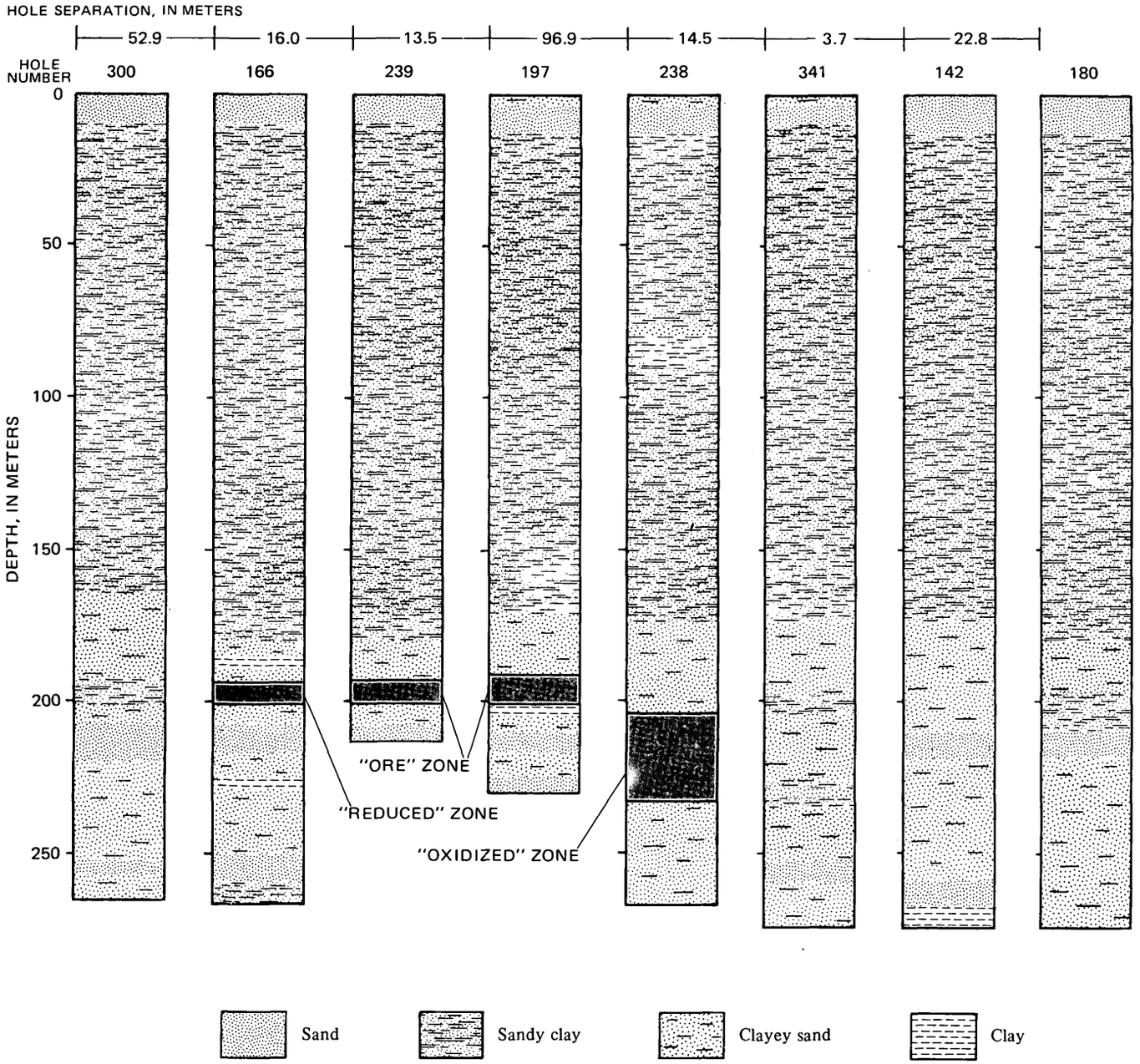

FIGURE 2.—Lithologic cross section for property 2. Holes drilled in the Catahoula Tuff.

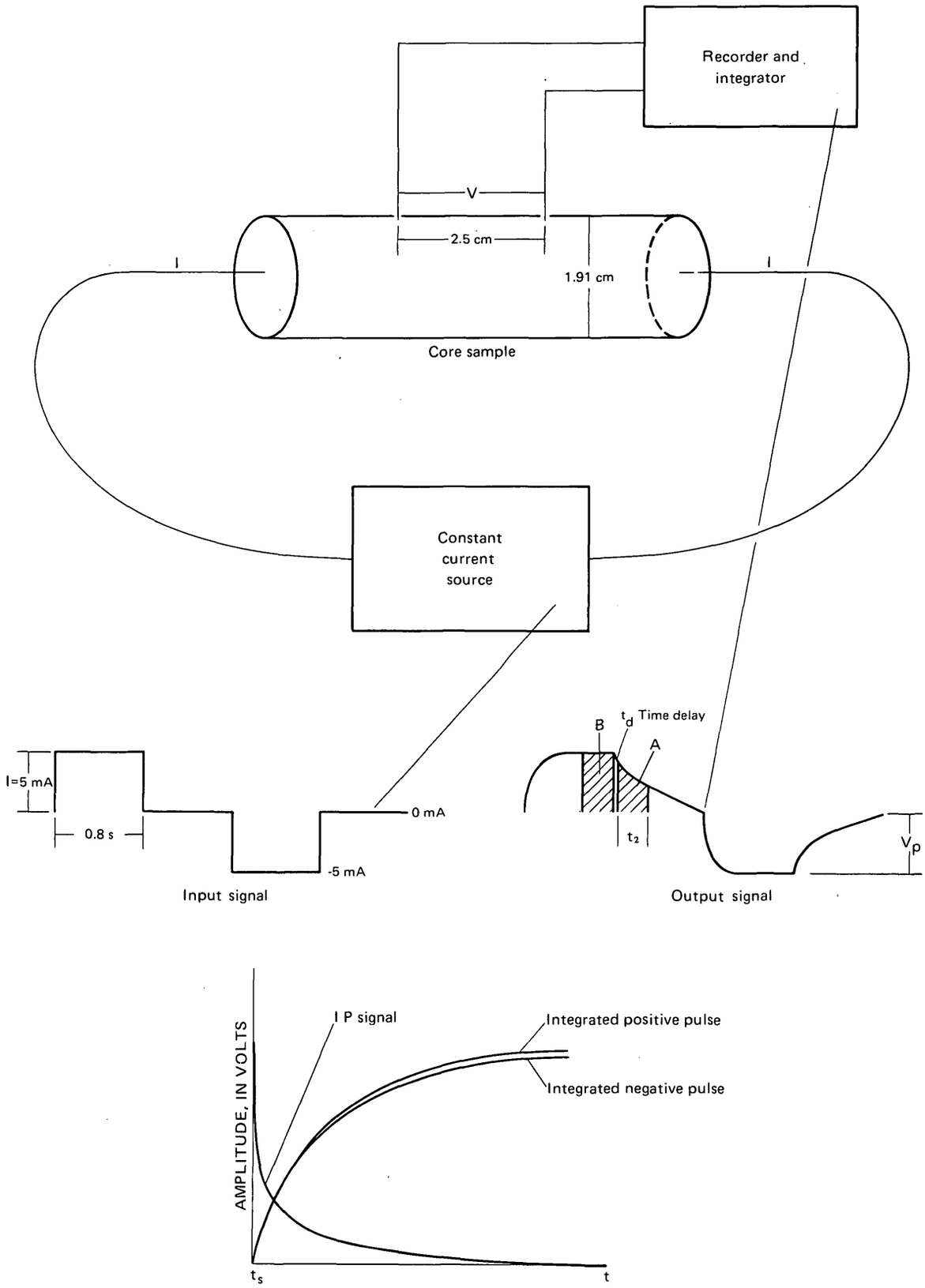

FIGURE 3.—IP (induced polarization) and resistivity laboratory measuring system. *A* and *B* are areas of equal time intervals (t_2) and (t_s–t) is the time interval over which the area was measured. Sample used here is 5–13.

TABLE 2.—*IP and resistivity laboratory measurements on core samples taken from the South Texas uranium district boreholes 3–8, property 1*

[ρ, resistivity; Ω·m, ohm meters; IP, induced polarization; mv/V, millivolts per volt]

Sample No.	Depth, in meters	ρ (Ω·m)	IP $\frac{mV}{V}$	Sample No.	Depth, in meters	ρ (Ω·m)	IP $\frac{mV}{V}$
3-29	75	3.17	2.4	6-19	79	13.4	1.8
19	69	11.69	3.4	15	76	10.8	1.6
15	66	11.0	3.0	10	73	11.5	4.4
24	72	12.9	5.4	4	69	6.21	1.5
5	49	7.06	1.4	7	71	11.7	1.0
9	63	3.44	1.8	18	78	11.7	0.79
28	75	13.06	2.3	7- 4	69	5.63	1.1
4-12	70	6.82	2.9	5	69	9.2	2.0
6	66	4.05	0.1	19	79	14.5	3.1
26	77	2.16	1.3	21	80	12.7	1.9
2	64	10.31	1.2	8	71	10.2	1.9
27	78	3.14	0.0	11	74	13.8	2.5
25	77	15.4	2.6	15	76	11.2	2.8
17	73	12.61	2.1	22	80	8.3	1.4
22	75	8.47	1.9	8- 6	70	5.4	0.9
5-13	72	11.28	5.0	11	74	11.9	2.9
5	67	8.66	2.5	9	72	13.5	2.4
10	70	11.2	3.0	13	75	13.3	2.0
22	76	10.1	4.4	15	77	13.5	1.7
8	69	11.0	2.9	19	79	13.1	2.2
15	73	12.1	2.9	22	80	13.4	1.1
23	77	3.36	0.09	24	81	13.1	1.5
2	65	4.8	0.2				

ogy is not simple. Resistivity is approximately inversely proportional to the clay content. In general, samples whose resistivity is less than 5 Ω·m (ohm meters) contain more than 50 percent clay, while samples with resistivities greater than 5 Ω·m contain less than 50 percent clay. Figure 4 is a plot of resistivity versus clay content and clearly shows the high correlation between them. From this relationship, a prediction formula for clay content can be derived from resistivity logs for property 1.

The relationship between IP effect and mineral content is more complicated than that between resistivity and mineral content. Clay and pyrite are the two constituents which have the largest effect on the IP. In general, samples containing a high pyrite content have a high IP response. However, this relationship is affected by the clay content. Sample 5–2 in tables 1 and 2 has a relatively high pyrite content, but its high clay content offsets the IP effect of the pyrite causing the total IP of the sample to be low. When the sand and clay content is constant, such as in samples 6–10 and 6–15, the IP effect is increased by an increase in the pyrite content. Figure 5 demonstrates the relationship between pyrite content and IP effect. The two points above the envelope drawn around the high concentration of points contain an abnormally high percentage of montmorillonite while the two points below the line contain a high percentage of kaolinite.

The relationship between clay content and IP effect

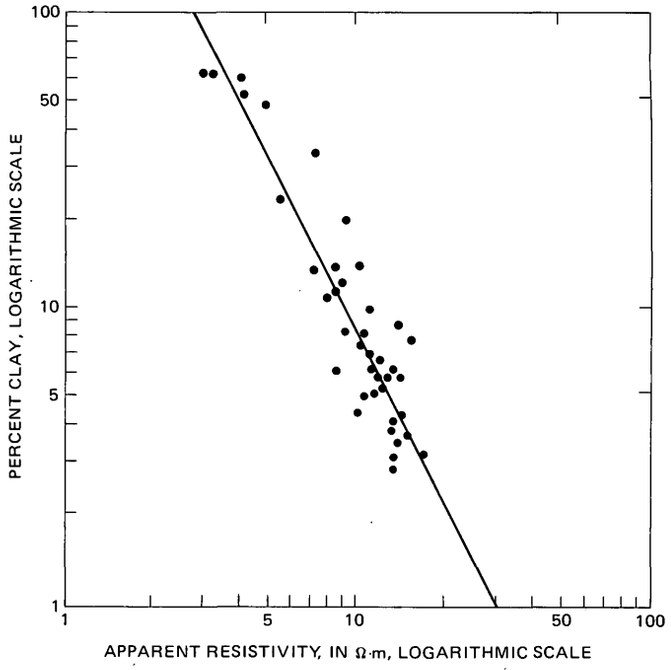

FIGURE 4.—The effect of clay-sized (<2 micrometers) particle content on resistivity for the sample values shown in tables 1 and 2.

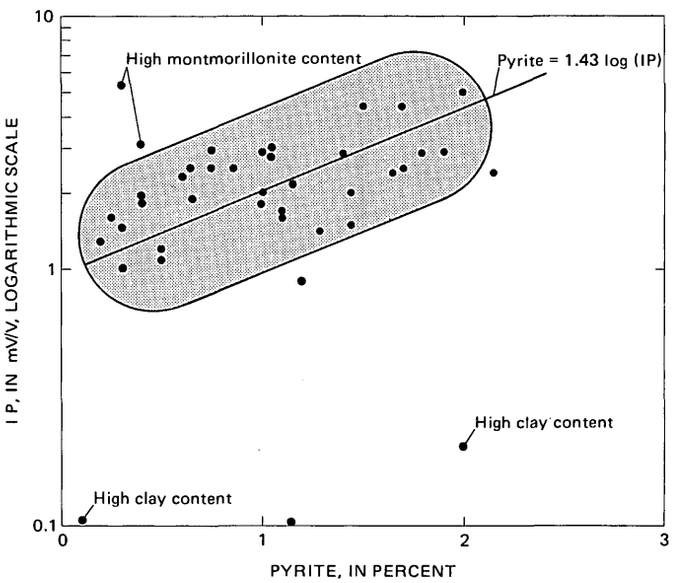

FIGURE 5.—Relationship between pyrite and IP (induced polarization) effect for the sample values (dots) shown in tables 1 and 2. Envelope represents area of low clay content.

is not as clear as the relationship between pyrite and IP effect. Figure 6 shows the effect of clay on IP. There is a general decrease in IP effect as the clay content is increased for clay percentages greater than 10 percent. If the total clay content is less than 10 percent, clay does not appear to have a significant effect on IP. When total clay content is high (>50 percent, in this case), the IP effect is low, except where the montmorillonite content is high.

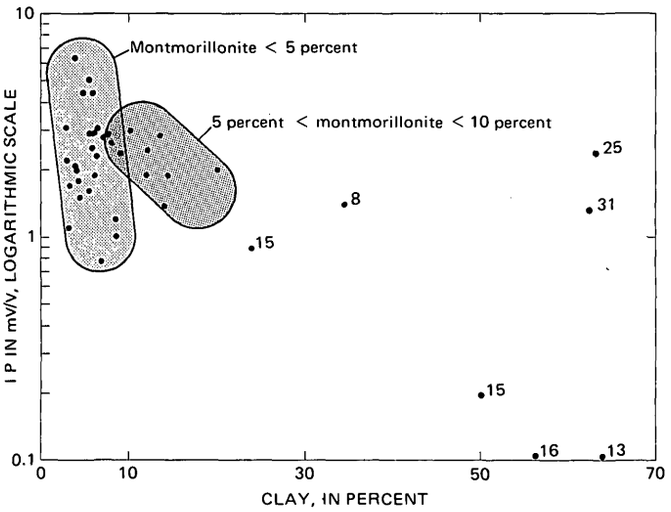

FIGURE 6.—Effect of clay-sized material on IP (induced polarization) response. The numbers on the scattered points give the percentage of montmorillonite in the clay.

GEOPHYSICAL WELL LOG RESULTS

Geophysical well-log information for property 1 and log data close to property 2 are shown in figures 7 and 8, respectively. The log suite for property 1 includes lithology, gamma-ray, resistivity, and induced-polarization logs, while for property 2, the suite consists of lithology, neutron, and gamma-ray logs.

The largest gamma-ray anomaly on property 1 occurs in the lower sand shown in figure 1. The anomaly increases from left to right as the "ore" content increases, and this is characteristic of a roll-front deposit. A low count is shown except for a single spike on the logs from drill holes 1 and 2, which are at a distance from the "ore" in the "oxidized" zone. As the "ore" zone is approached, from the "oxidized" side, the anomaly is first represented by two thin high-count zones at drill holes 3, 4, and 5, which broaden to form a single maximum over the "ore"-zone drill holes 6 and 7). The anomaly then decreases away from the "ore" on the "reduced" side of the roll-front drill holes (9 and 10). This anomaly pattern is similar to that shown by Rubin (1970) for Wyoming-type uranium roll-front deposits. This pattern, along with the geologic information (table 1) supports the idea that the "ore" may have been originally deposited at a typical oxidized-reduced interface which was later reduced.

The resistivity and induced-polarization logs provide important rock-characteristic information about property 1. It has been shown in figure 4 that there is a correlation between the clay content and the resistivity response. This information shows that the clay content is approximately constant across the "ore" zone. The high resistivity anomaly just above the "ore" sand is caused by a calcite-cemented sand layer. The resistivity of the "ore" sand is not anomalous when compared with either the horizontal or vertical position of the "ore". However, an induced-polarization high-amplitude anomaly does occur in the "ore" sand. This anomaly corresponds to the high pyrite and montmorillonite content shown in figure 1.

Figure 8 shows the lithologic, gamma-ray, and neutron logs for property 2. The high gamma-ray count occurs in the lower clayey sand section. Individual roll fronts are difficult to distinguish, however, a deposit of the roll-front type is indicated in the gamma-ray logs with a peak between drill holes 239 and 197. The "oxidized" side of the roll front occurs at drill hole 238. The neutron logs register higher values in the less clayey zones. The high gamma-ray zones in drill holes 239 and 197 correspond to "low" shaly (or clayey) zones as indicated by the neutron logs.

The nature of the neutron logs makes it difficult to predict the actual amount of clay contained in these zones. The logs and information taken from property 1 indicate that a resistivity log would be useful in quantitatively establishing the amount of clay contained in the "ore" sand. The amount of clay could be a factor in determining whether or not a low-grade deposit, such as the deposit in figure 9, is economic as an in-situ solution-mining deposit. The suite of logs shown in figure 8 also fails to give any indication of the amount of calcite cementation in the sands or the pyrite-montmorillonite content as is shown by figure 7 in the resistivity and induced-polarization logs.

Figure 9 shows the ore-zone section of the logs for boreholes 6 through 8 on property 1. The pyrite and clay content is shown for the depths corresponding to the log depths. The correlation that was shown in figure 5 for pyrite and laboratory IP can also be seen for the pyrite content and IP logs shown in figure 9. The samples contain a high clay content in places where the high pyrite values do not correspond to high IP values. A point-for-point correlation cannot be expected since the pyrite sample covers approximately 3 cm^2 (square centimeters) of the borehole surface and does not penetrate outside the borehole,

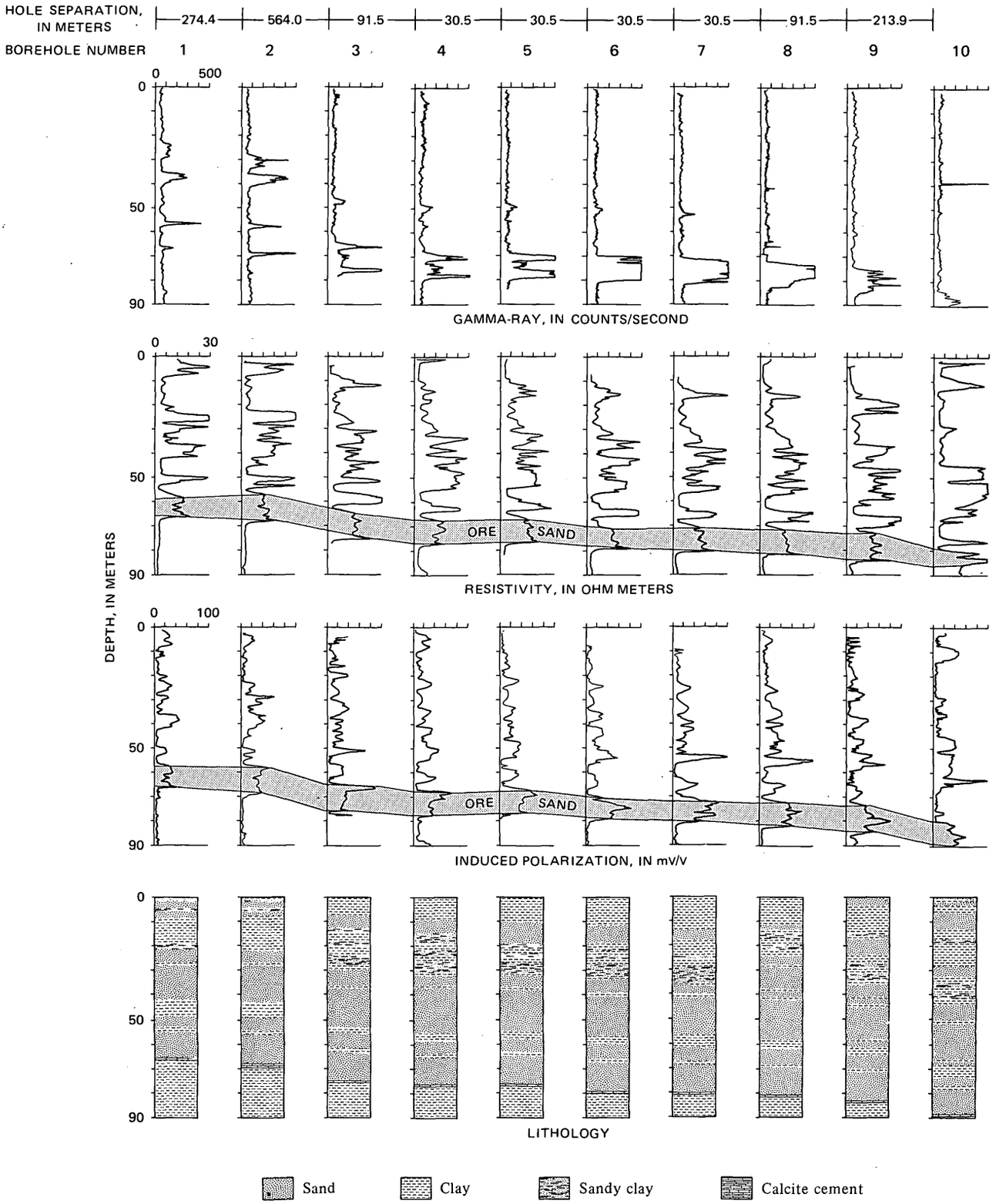

FIGURE 7.—Borehole data across a south Texas uranium roll-front deposit (property 1).

while the IP logging tool has an effective length of about 1 meter (m) and is affected by the borehole wall.

Laboratory resistivity and IP values given in table 2 are shown as dots on the resistivity and IP logs in figure 9. Laboratory resistivity values correspond closely to log values in spite of the difference in sampling between the two techniques. However, laboratory and log IP values correlate only in a very gross sense owing to the different charging and recording times for the two measurements. The IP logging tool, which operates at 10 Hz (hertz), records the ratio of a point voltage measured at 5-ms (milliseconds) delay on the transient decay to the primary voltage V_p, while the laboratory measurements, made at approximately 0.3 Hz, are integrated over a time interval on the decay curve. Anderson and Keller (1964) have also noted the lack of correspondence between laboratory and field induced-polarization measurements.

HOLE-TO-HOLE ELECTRICAL MEASUREMENTS

Hole-to-hole measurements are made by placing a current source down a borehole and a voltage measuring device down an adjacent borehole. By using this setup it is possible to eliminate much of the near-surface geologic noise inherent in conventional surface electrical measurements and to detect the small contrasts in electrical properties associated with roll-front uranium deposits.

Hole-to-hole resistivity and induced-polarization measurements were made on property 1 and property 2 using the measurement system shown in figure 10. The source transmitter was an induced-polarization transmitter that is capable of transmitting 20 amperes at 400 volts. The source electrode pair used for the examples in this paper was the surface-to-downhole electrode pair. The receiver was a time-domain IP receiver using signal sampling similar to that shown in figure 3.

Figure 11 shows hole-to-hole IP and resistivity measurements made on property 1. These measurements show an increase in the induced polarization across the roll-front ore zone (source at hole 3 and receiver at hole 8) in contrast to induced-polarization measurements off the roll front (source at hole 1 or hole 9 and receiver at hole 2 or hole 10, respectively). This increase corresponds to the increase shown in the well logs in figure 7.

The resistivity values can be explained by reference to the well logs in figure 7. A resistivity high occurs just above the "ore" sand in the calcite-cemented sand. The calcite-cemented sand is almost completely replaced by clay in drill hole 1. The presence of the calcite-cemented sand causes the resistivity high in the hole-to-hole measurements between holes 3 and 8 and holes 9 and 10 and the resistivity low in the measurements between holes 1 and 2. Recent experience indicates that a higher density of measurement points would probably help to clarify these relationships.

Figure 12 shows hole-to-hole induced-polarization and resistivity measurements made in "reduced" ground on property 2. The gamma-ray logs show a very small anomaly in drill hole 2 at a depth of about 150 m. The neutron log shows that this is a clayey sand. The hole-to-hole resistivity measurements between drill holes 1 and 2 show a resistivity high in the vicinity of the sand located at a depth of about 120 m in drill hole 2. In general, the resistivity hole-to-hole measurements show high values in the sands and low values in the clays.

The induced-polarization hole-to-hole measurements in figure 11 also show high values in the sands. However, the induced-polarization measurements in the lower sand are less erratic than the resistivity measurements and show essentially the same profile for each set of hole-to-hole measurements.

Figure 13 shows gamma-ray logs, neutron logs, and hole-to-hole measurements across an oxidized-reduced front on property 2. The gamma-ray logs have higher values than in figure 12, but they are not high enough to consider this a good ore deposit. The neutron logs do not exhibit much variation from the upper shale section to the lower sand section.

The hole-to-hole resistivity survey exhibits a resistivity low in the lower sand. This low is negative and is probably due to the effect of the geometry rather than a true resistivity low. The induced polarization shows a high value in the lower sand. The presence of an induced-polarization high across an oxidized-reduced roll front is similar to the correspondence of high induced-polarization values and the occurrence of the oxidized-reduced interface seen on property 1.

CONCLUSIONS

Studies of physical properties on property 1 indicate that:

1. There is a high degree of correlation between clay content and resistivity.
2. There is good correlation between pyrite content and induced-polarization response.
3. There is an inverse correlation between induced-polarization response and [total] clay content.

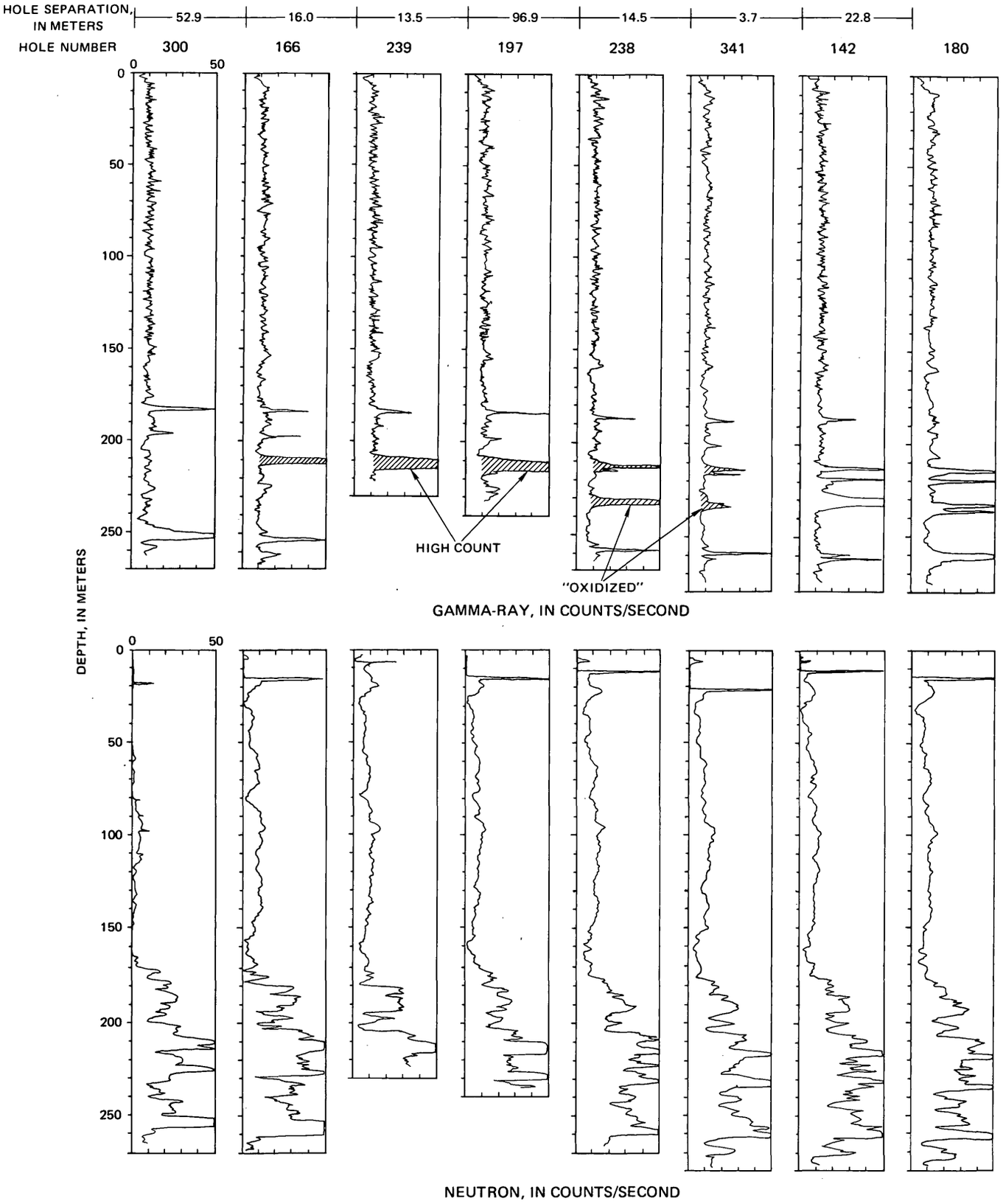

FIGURE 8.—Well log information for property 2.

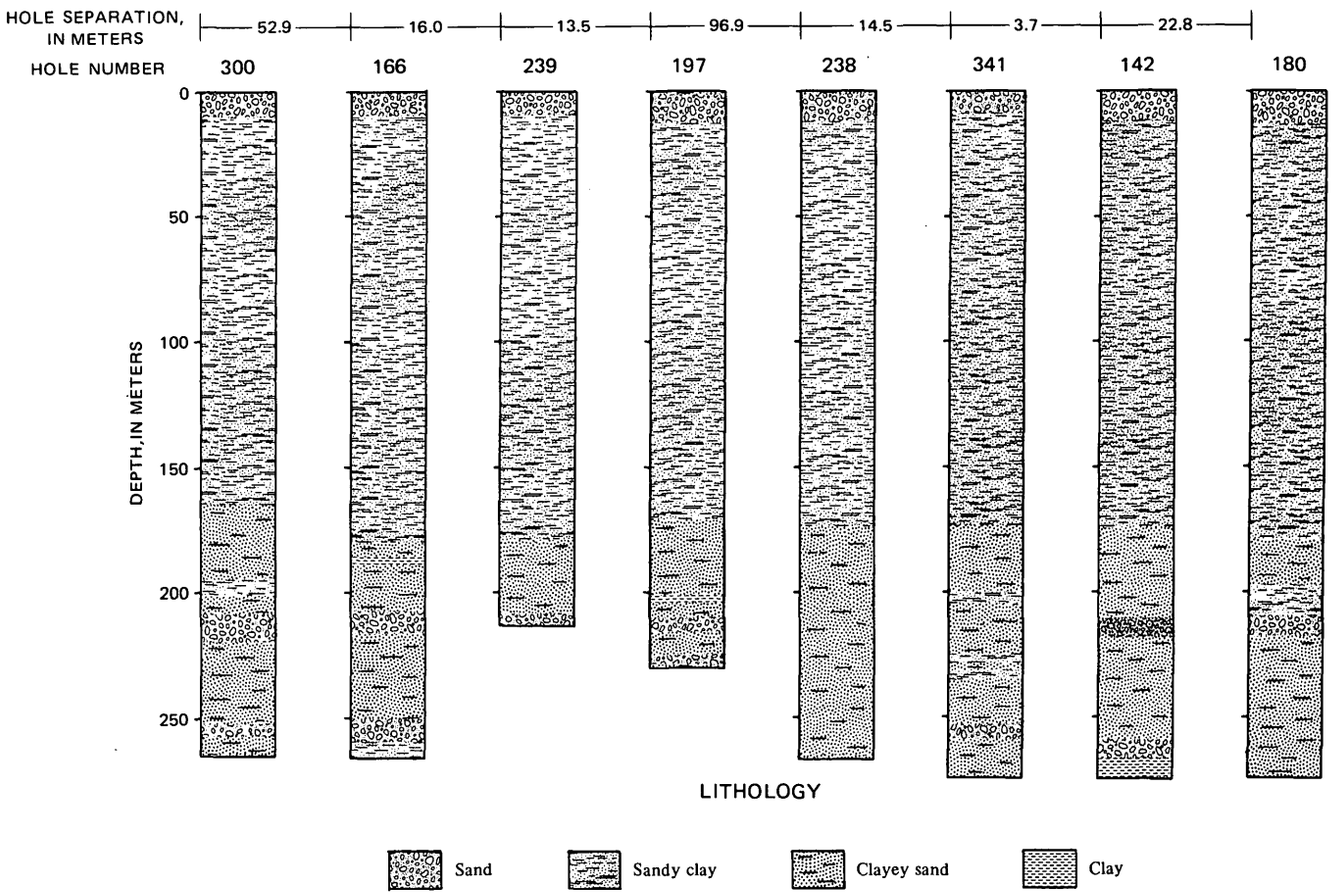

FIGURE 8.—Continued.

These relationships imply that it may be possible to use resistivity logs to predict clay content and to use this clay-content information to correct the induced-polarization logs so that they can be used to predict pyrite content. The estimation of pyrite could be important in establishing the historical movement of the roll front. The estimation of clay and pyrite content will be important guides in determining geological engineering parameters necessary for solution mining.

Hole-to-hole induced-polarization and resistivity measurements exhibit anomalies similar to the conventional induced-polarization and resistivity well logs. Hole-to-hole induced-polarization measurements can detect the anomaly associated with roll-front deposits at a considerable savings in drilling time and cost.

It must be cautioned that the conclusions drawn in this paper are derived from work on only two deposits in South Texas. More data is needed to confirm these results. In particular, the correlation between pyrite and induced-polarization response may be reflecting more general characteristics of the roll-front environment than just the pyrite content. These results do show that borehole measurements contain quantitative information which can aid the explorationist in evaluating the economics of marginal-grade uranium deposits.

Figures 9—13 follow "References Cited."

REFERENCES CITED

Anderson, L. A., and Keller, G. V., 1964, A study in induced polarization: Geophysics, v. 29, no. 5, p. 848–864.

Eargle, D. H., Hinds, G. W., and Weeks, A. M. D., 1971, Uranium geology and mines, South Texas: Texas Univ., Bur. Econ. Geol., Guidebook no. 12, 59 p.

Eargle, D. H., and Weeks, A. M. D., 1968, Factors in the formation of uranium deposits, Coastal Plain of Texas: South Tex. Geol. Soc. Bull., v. 9, no. 3, 12 p.

Rubin, Bruce, 1970, Uranium roll front zonation in the southern Powder River basin, Wyoming: Wyo. Geol. Assoc. Earth Science Bull., v. 3, no. 4, p. 5–12.

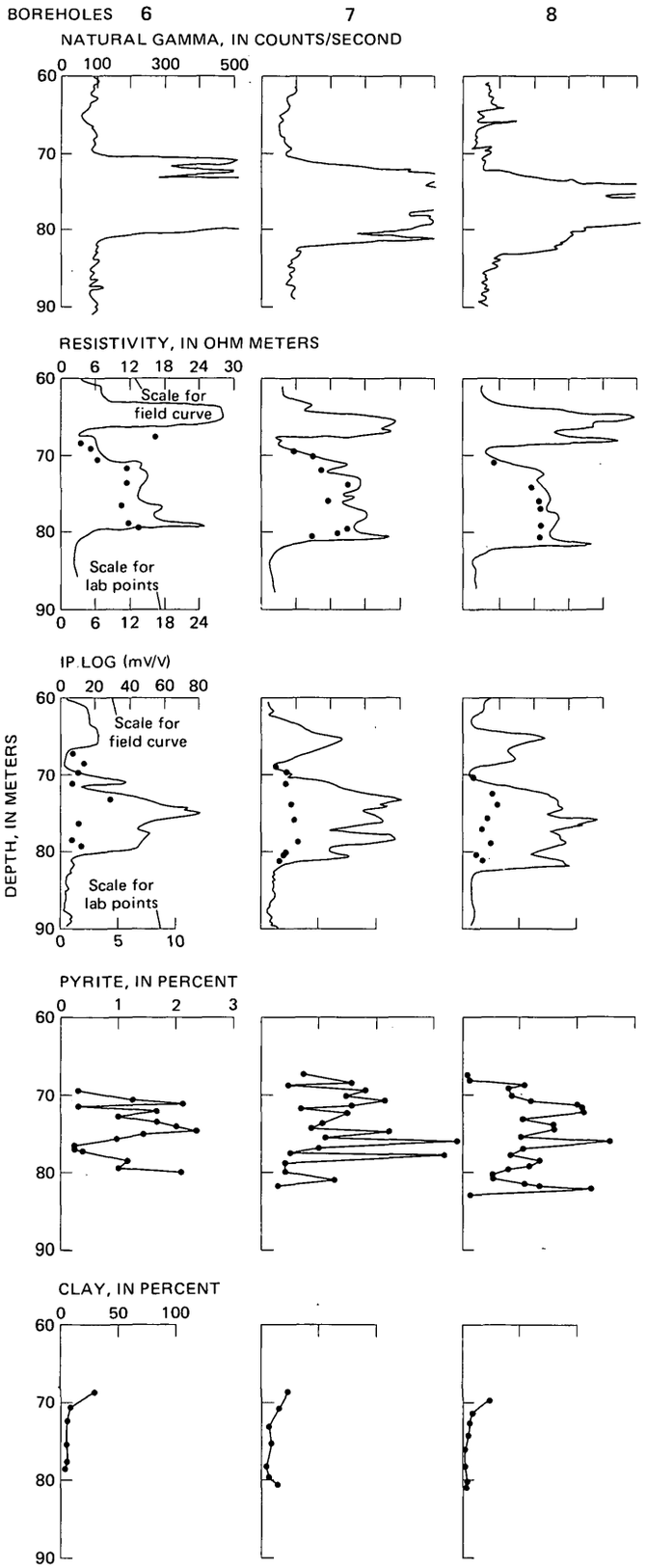

FIGURE 9.—Analysis of natural gamma count, resistivity, IP, and pyrite and clay content in the "ore" zone, for boreholes 6 through 8 on property 1.

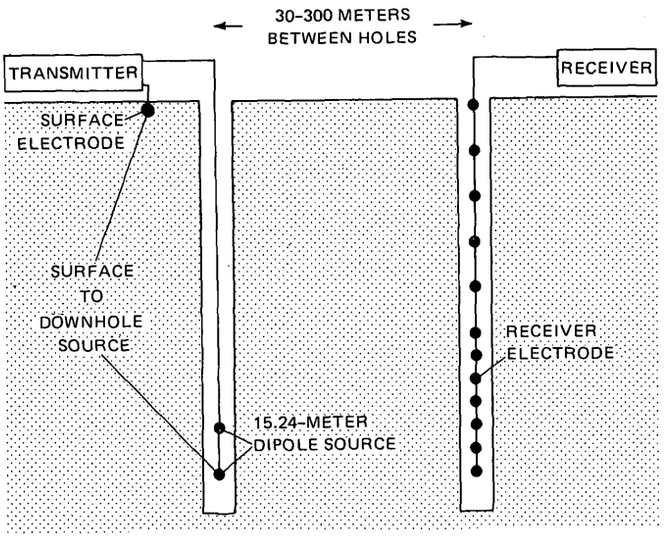

FIGURE 10.—Source-receiver electrode configuration for hole-to-hole measurements.

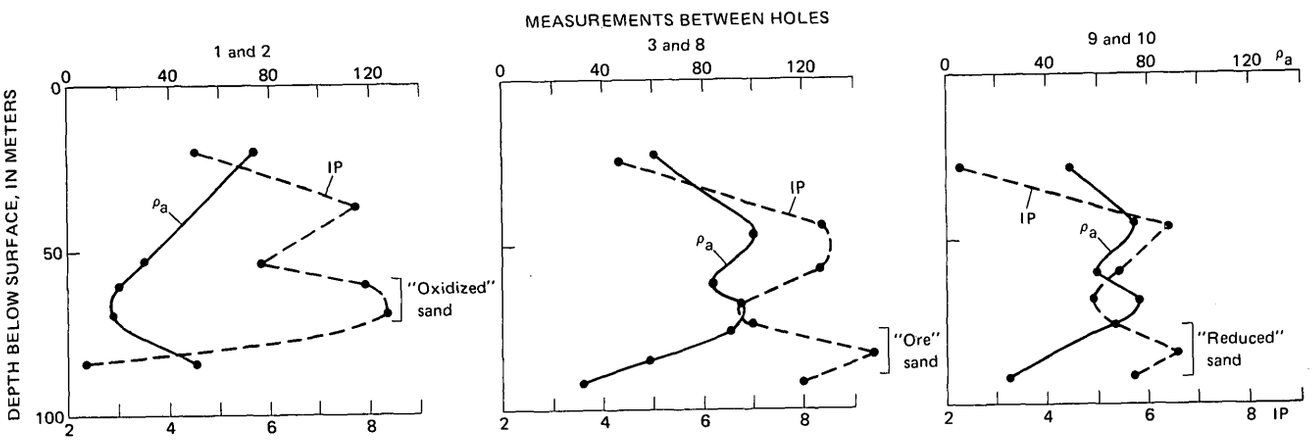

FIGURE 11.—Hole-to-hole resistivity (ρ_a), in ohm meters, and induced polarization (IP) measurements, in millivolts per volt, on property 1. Source current, 10 amperes; receiver dipole length, 15.24 meters. There is a source electrode at the surface and one at a depth of 46 meters.

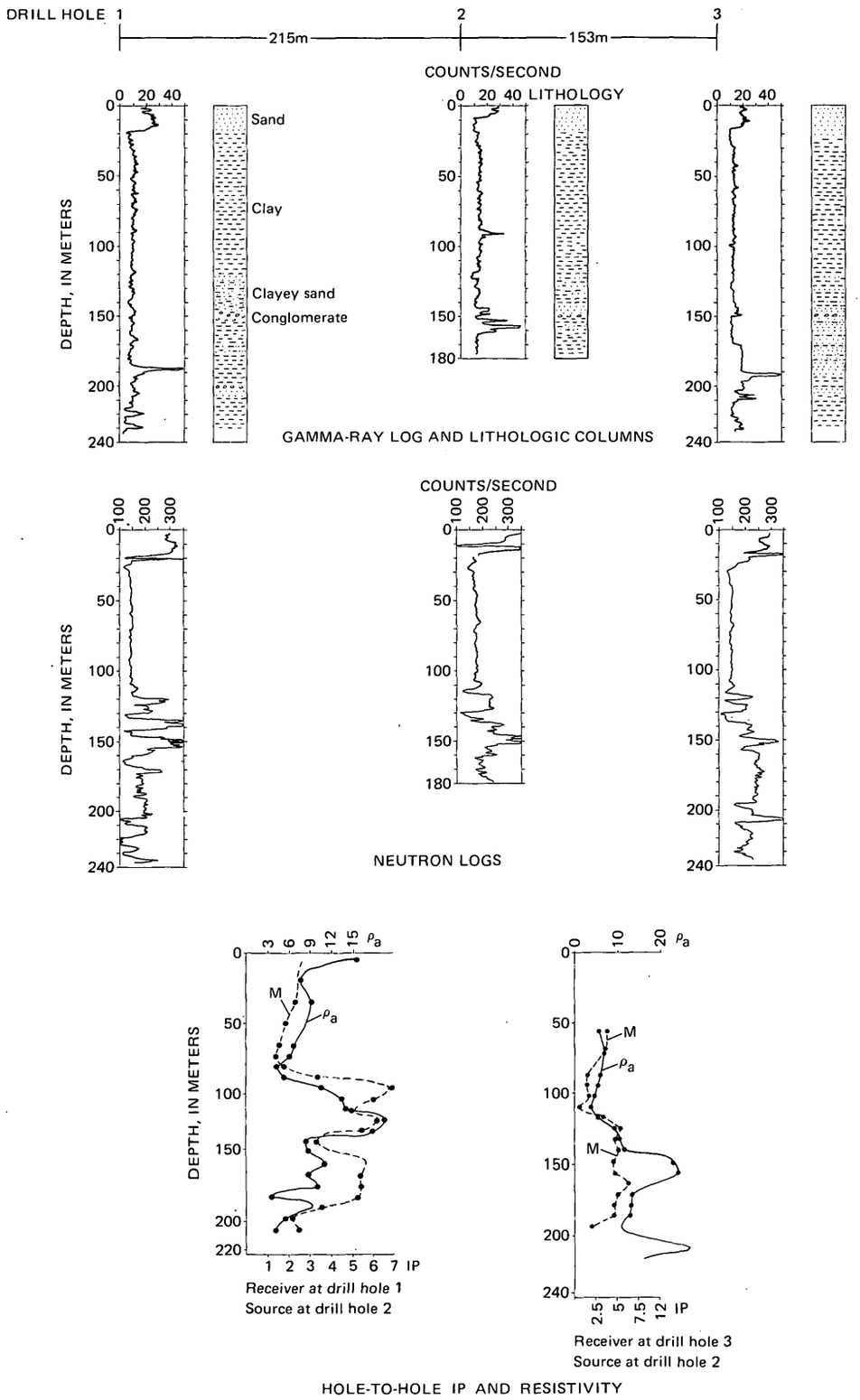

FIGURE 12.—Well logs and hole-to-hole measurements in a non-"ore" zone on property 2. Surface electrode to downhole electrode is 154.2 meters and current is 5 amperes on hole-to-hole IP (induced potential) and ρ_a (resistivity) logs. Apparent resistivity is measured in ohm meters, and IP is measured in millivolts per volt.

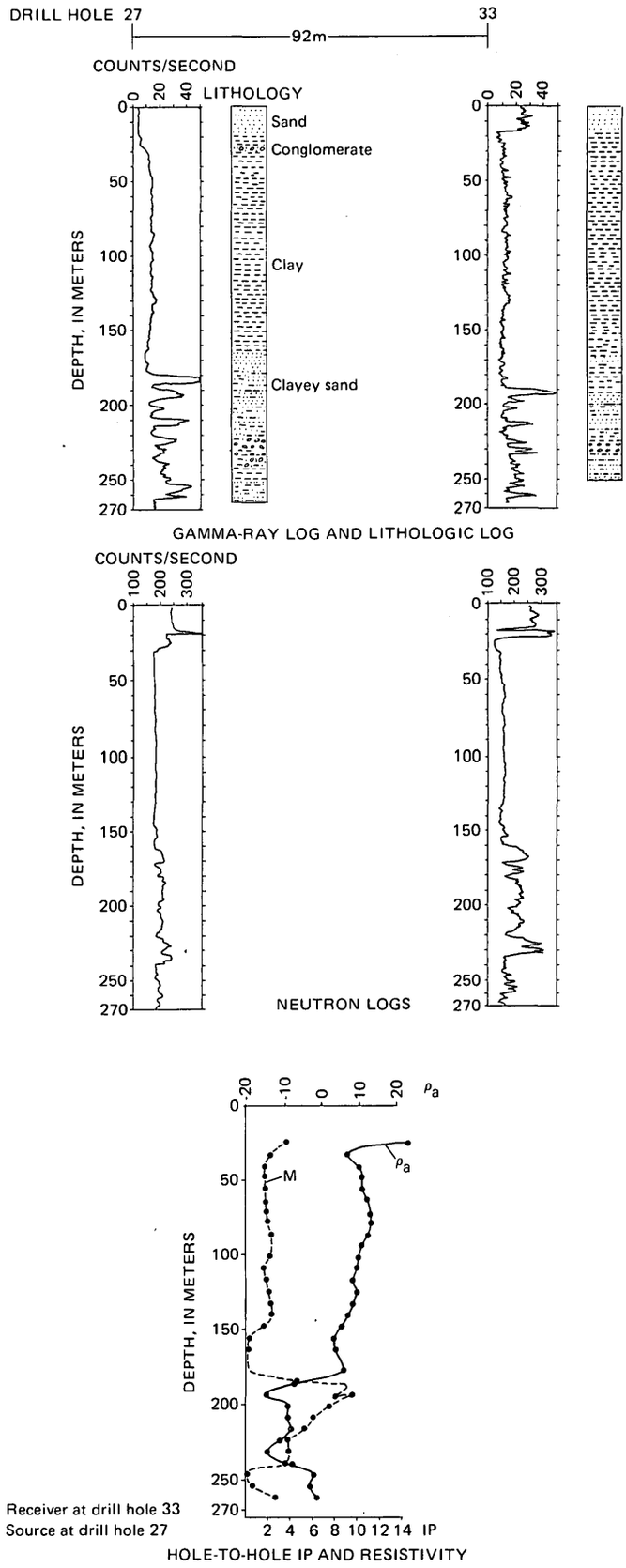

FIGURE 13.—Well logs and hole-to-hole measurements across a roll-front deposit on property 2. Surface electrode to downhole electrode is 152.4 meters, and current is 5 amperes on hole-to-hole IP (induced polarization) and ρ_a (resistivity) log. Apparent resistivity is measured in ohm meters, and IP is measured in millivolts per volt. Receiver dipole separation is 15.24 meters.

Jour. Research U.S. Geol. Survey
Vol. 5, No. 3, May–June 1977, p. 359–363

GRAVITATIONAL SPREADING OF STEEP-SIDED RIDGES ("SACKUNG") IN COLORADO

By DOROTHY H. RADBRUCH-HALL; DAVID J. VARNES, and
ROGER B. COLTON; Menlo Park, Calif.; Denver, Colo.

Abstract.—Large-scale gravitational spreading and fracturing of steep-sided ridges in the mountainous area of Colorado are characterized by horizontal linear fissures, trenches, and uphill-facing scarps on tops and sides of ridges. A pronounced north-trending cleft and several minor scarps have split a ridge extending northward from Dolores Peak in the San Miguel Mountains of southwestern Colorado. This ridge is capped by granogabbro of a Tertiary laccolith that intruded the Cretaceous Mancos Shale. Numerous active landslides in shale mantle the once glaciated lower slopes. Trenches in the granogabbro probably originated after glacial ice melted, leaving steep sides of the ridge unsupported. The soft Mancos shale moved outward toward the direction of least stress, placing the overlying granogabbro under tension. A ridge that extends southwest from Bald Eagle Mountain, north of Mount Massive in central Colorado, is marked by a graben on the top and several trenches on the northwest side, parallel to the long axis of the ridge. Rock exposed in graben and trenches is the Precambrian St. Kevin Granite, which includes some schist and migmatite. Gravitational movement probably took place after steepening of the valley sides by glacial erosion and melting of the glaciers. Movement followed preexisting discontinuities in the rock. A survey course approximately 2.4 km (1.5 mi) long has been placed across the fractured ridge. It will be monitored periodically to determine whether movement is continuing, and if so, at what rate.

Large-scale gravitational spreading and displacement along fractures of steep-sided ridges are common in various parts of the Rocky Mountains of Colorado. Such features have been observed in the past by Ogden Tweto and other geologists, and many new ones were noted by R. B. Colton during mapping of landslide deposits of Colorado (Colton and others, 1976). The usual topographic expression of this type of gravitational movement consists of horizontal linear fissures, trenches, and uphill-facing (antislope) scarps on steep slopes and ridge crests. These gravitational features have long been recognized in other parts of the world (Kobayshi, 1956; Nemčok, 1972; Zischinsky, 1966), but they have been little studied in the United States. The process is herein referred to as "Sackung" (literally "sagging") from the term suggested by Zischinsky (1966, 1969) for large-scale gravitational movement that takes place by slow movement along a series of disconnected planes or by slow plastic deformation of a rock mass without formation of a through-going sliding surface. It may pass into or be combined with movement along a slide surface, but Zischinsky suggested that the term be applied to movement in which the amount of closely distributed deformation across a zone of movement is large in relation to displacement along a discrete basal surface of sliding.

Few implications regarding mechanics are suggested in the usage in this report, as the mechanics of the movement are still incompletely understood. Earthquake shaking, tectonic uplift, rapid stream erosion, steeping of valley sides by glaciation, and removal of lateral support as glaciers melted all could have acted, separately or in combination, to cause this type of movement. In some places, the movement is probably caused by valleyward squeezing out of weak, ductile rocks overlain by or interbedded with more rigid rocks, resulting in tensional fracturing and outward movement of the more rigid layers. In other places, gravity acting on more homogeneous steep-sided ridges probably caused tensional spreading of the ridge, which then fractured along approximately vertical planes parallel to the long axis of the ridge. Movement along these fractures or along preexisting discontinuities formed trenches and uphill-facing scarps as the sides of the ridge bulged outward and the top subsided. A survey net has been established across one fractured ridge to determine whether it is still moving and, if so, at what rate. Other nets will be established and monitored in additional localities.

Recognition and understanding of sackung features and the mechanism (or mechanisms) that causes them are pertinent to the site selection and design of major engineering structures in high mountains. Bulges on valley walls caused by gravitational sagging of the ridges give rise to numerous rockfalls and landslides

from the valley sides. In places where valley sides are moving or bulging outward, engineering structures along valley sides or in the valley bottom may be subjected to high lateral pressure. If the fractures extend to considerable depth, and if movement is still occurring along them, tunnels through the ridges could be damaged.

DESCRIPTION OF LOCALITIES

Some of the numerous sackung features that have been recognized in Colorado have been noted only on aerial photographs, others have been seen and photographed from the air but not on the ground, and a few have been examined on the ground. Two representative localities in two different geologic settings are described below.

Dolores Peak

A longitudinally fractured ridge extends northward from the main body of Dolores Peak and Middle Peak in the Wilson Mountains Primtive Area of the San Miguel Mountains in southwestern Colorado. A pronounced north-trending cleft down the long axis of the ridge has split it in two (fig. 1); on the east side of the ridge subsidiary parallel fractures are marked by trenches bounded on the downhill side by uphill-facing scarps (fig. 2). Maximum height from the base of the principal cleft to the top of the walls is about 60 meters (200 feet); the west half of the ridge is slightly higher than the east half. Width of the trough is 60 m (200 ft) or more across the top. The walls of subsidary trenches on the eastern slope are a maximum of 10 m (35 ft) in height.

Local relief is about 915 m (3000 ft); the uppermost 300 m (1000 ft) of the ridge is above treeline. Rock is well exposed in both walls of the main trench and in the walls of the subsidiary trenches, and talus covers the floors and extends part of the way up the sides. The floor of the main trench is irregular. It slopes gently upward toward the south, but the slope is not uniform; in places it is interrupted by closed depressions that contain snow most of the year.

The area has been geologically mapped by Bush and Bromfield (1966), who interpreted the core of Dolores Peak and Middle Peak as a stock of Tertiary age that intruded the Cretaceous Mancos Shale. The north-trending split ridge is considered by them to be a laccolith extending northward and outward from the stock. The maximum thickness of the laccolith was estimated at about 550 m (1800 ft), and about 425 m (1400 ft) where the trenches formed. The laccolith is underlain by Mancos Shale, but most of the shale has

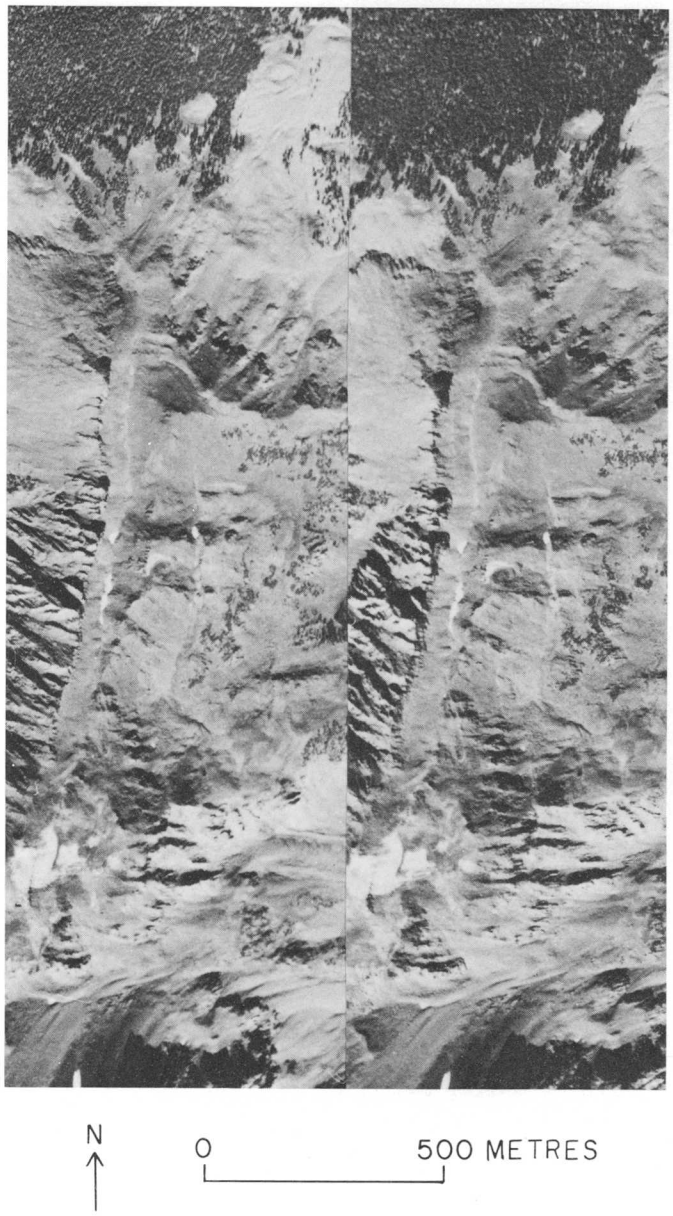

FIGURE 1.—Stereopair of aerial photographs showing gravitational trenches on ridge north of Dolores Peak, Colo.

been eroded from the top of the intrusive body. Bush and Bromfield describe the rock of the laccolith, which forms the walls of the trenches, as predominantly granogabbro. It is very closely fractured. A pronounced joint set trends northward approximately parrallel to the walls of the main trench and may have controlled its location and direction; another set trends approximately at right angles. The main set parallel to the walls is vertical at the west wall but dips about 75° westward (into the trench) on the east wall. It is not known whether the movement that caused the trenches to form is still continuing, but it may be; the

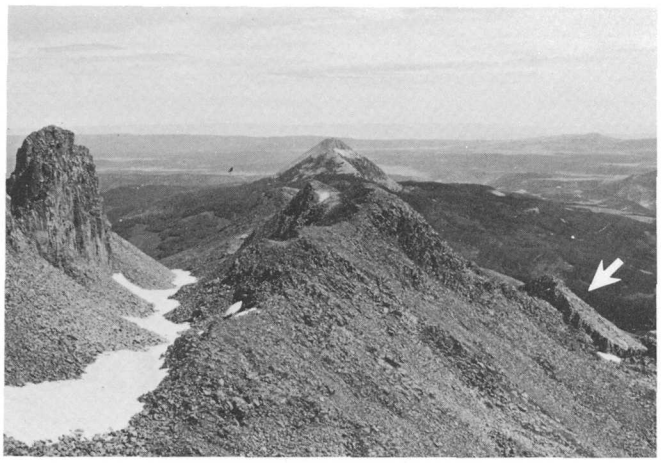

FIGURE 2.—Northward view of trenches on ridge north of Dolores Peak. Arrow indicates general location of subsidiary trenches on east side of ridge. Top of pinnacle at left is about 60 m (200 ft) above bottom of the large trench.

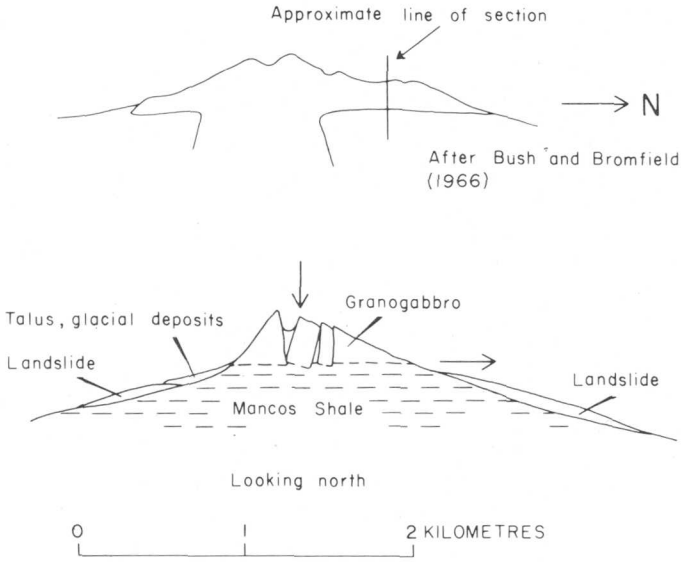

FIGURE 3.—Diagrammatic cross sections across Dolores Peak–Middle Peak area showing probable structure and direction of movement (large arrows).

walls of the trench are fresh, and talus still falls from them. The trace of one trench appears to extend across fresh talus. The outer slopes of the ridge, which are very steep, appear to be the walls of cirques. Mancos shale is exposed on some slopes below the granogabbro. Numerous landslides in Mancos shale on the lower slopes appear still to be active.

We believe that the trench originated after preglacial and glacial erosion created steep slopes and removal of the ice left the sides of the ridge unsupported. The soft Mancos shale under the laccolith moved outward toward the direction of least stress, placing the overlying granogabbro under tension. As movement continued, the more rigid granogabbro cracked parallel to the long axis of the ridge (at right angles to the direction of greatest stress relief) and also began to move; the east half of the split ridge also tilted slightly outward. As the ridge continued to spread, additional cracks formed on the east side of the ridge, and the rock on the outer, downhill side of each crack moved up relative to the uphill side owing perhaps in part to a sagging of the downslope part of the granogabbro and in part to the tilting and sinking down of the central eastern part of the ridge (fig. 3).

This site is typical of others with a similar geologic setting, where rigid rocks overlie softer, plastic material. The type of movement is somewhat analogous to that described by and measured by Yeend (1969, 1973) at the edge of Grand Mesa in Colorado, and by Matula and Nemčok (1968) in the volcanic rock overlying siltstone at Handlovà in Czechoslovakia. Movement at the edge of Grand Mesa was determined by Yeend (1973) to average 1.1 centimeters (0.43 inch) per year. Similar conditions appear to exist at Crested Butte in Colorado, where extensive construction of various kinds is now being planned.

Bald Eagle Mountain

A small graben lies along the top of a ridge extending southwest from Bald Eagle Mountain, north of Mount Massive, about 13 km (8 mi) west of Leadville, Colo., in the Sawatch Range. The northwest side of the ridge is marked by several trenches with antislope scarps on their northwest sides. Both graben and trenches trend about 50° northeast, roughly parallel to the long axis of the ridge. The graben is about 455 m (1500 ft) long and 60–90 m (200–300 ft) wide; the walls range in height from a few centimeters (inches) to about 6 m (20 ft). The trenches are a similar length, with a maximum depth of about 10 m (35 ft) and a width of 30 m (100 ft). They are easily visible on aerial photographs (fig. 4), particularly because of the absence of trees in the trenches. Rock exposed in places in the walls of the graben and trenches is largely frost-rived rubble. Most trench walls are covered with rubble, dwarf alpine trees, or tundra (fig. 5). The steep-sided glacial valley of Busk Creek bounds the ridge on the northwest side; the southeast side is a steep-walled cirque. The distance across the ridge top, from the valley edge on the northwest to the top of the cirque on the southeast is about 820 m (2700 ft, about half a mile). The trenches are slightly arcuate, convex downhill.

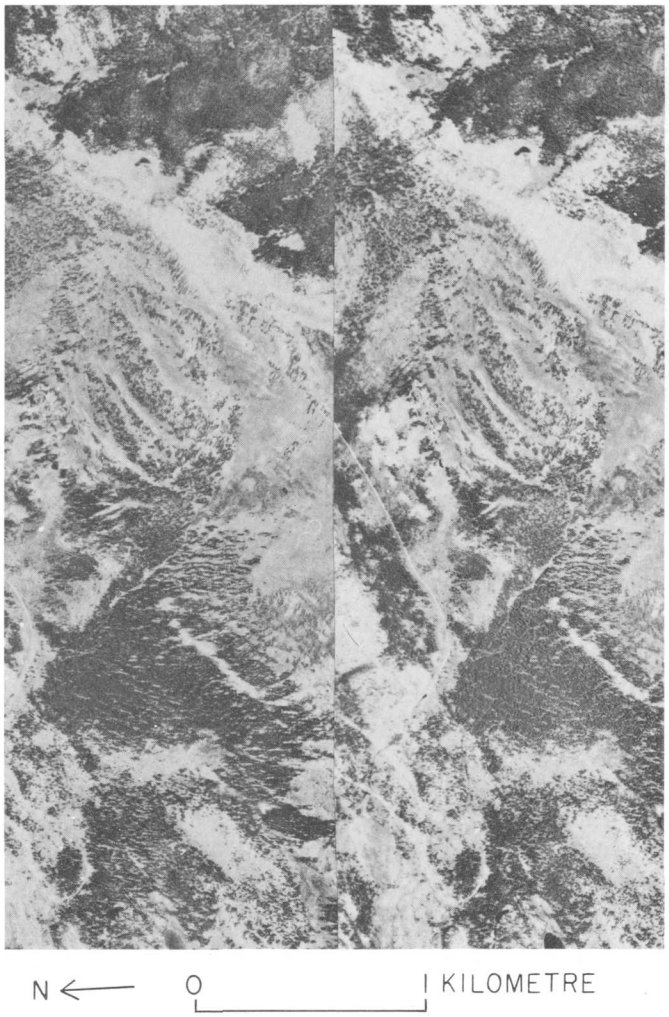

FIGURE 4.—Stereopair of aerial photographs showing graben and trenches on ridge southwest of Bald Eagle Mountain, Colo.

FIGURE 5.—Northeastward view of hillside trench on northwest side of ridge southwest of Bald Eagle Mountain.

Rock exposed in the graben and trenches is migmatite, consisting of schist cut by stringers and masses of granite and pegmatitic rocks. It has been assigned by Tweto (1974) to the St. Kevin Granite, undivided, which includes some schist and migmatite. The rocks are intensely jointed with one prominent, nearly vertical joint set trending roughly northeast and another approximately at right angles to it; a third set is subhorizontal. Attitude of the prominent, nearly vertical set, where measured in the cirque walls and in a quarry in the valley northwest of the ridge, ranged from N. 87° E. to N. 20° E. The slightly arcuate trenches may follow two joint sets or may follow fractures that are slightly inclined into the hill.

Below the trenches, on the northwest side of the ridge, a pronounced bulge has formed in the valley wall. Abundant rock debris has fallen into the valley from the oversteepened face of the bulge (fig. 4). This type of graben and trench development in granitic rock, commonly with a similar bulge, has been observed in other places, for example Chabenec in Slovakia (Nemčok, 1972).

In each of these places, gravitational movement of the ridges probably took place after steepening of the valley sides by glacial erosion and melting of the glaciers, which left the oversteepened sides of the ridges unsupported. Movement followed preexisting discontinuities in the granitic rock. It is not known whether movement is still continuing.

A survey course, approximately 2.4 km (1.5 mi) long, has been placed southeastward across the fractured ridge southwest of Bald Eagle Mountain. The range in elevation along the line is about 328 m (1075 ft). The course was established using a Wild T–2 theodolite and a small laser AGA Model 76 Geodimeter.

The initial observations have been reduced, by a U.S. Geological Survey triangulation-trilateration computer program, to the geoid at a common elevation of the lowest point. This point, which is at the northwest end of the line across the valley of Busk Creek from Bald Eagle Mountain, is assumed to be stable. The computations indicate that the maximum probable error in length of lines between points is of the order of 1.5 cm (0.05 ft) and the average probable error of angular observations of azimuth is 1.72 seconds. The survey course will be monitored periodically to determine whether movements are still continuing and, if so, at what rate. From the initial observations, it may be possible to detect movements of the order of a few centimeters unless the survey points are disturbed by frost heave or other near-sur-

face movements. Future refinement of observing methods may make possible the isolation of surface disturbances and the detection of smaller mass movements.

REFERENCES CITED

Bush, A. L., and Bromfield, C. S., 1966, Geologic map of the Dolores Peak quadrangle, Dolores and San Miguel Counties, Colorado: U.S. Geol. Survey Geol. Quad. Map GQ–536, scale, 1:24,000.

Colton, R. B., Holligan, J. A., Anderson, L. W., and Patterson, P. E., 1976, Preliminary map of landslide deposits in Colorado: U.S. Geol. Survey Misc. Geol. Inv. Map I–964, scale 1:500,000.

Kobayshi, Kunio, 1956, Periglacial morphology in Japan: Builetyn Perglacjalny, no. 4, p. 15–36 (Lodzkie towarzystwo naukowe societas scientarium lodziensis, Wydzial III, sectio III).

Matula, Milan and Nemčok, Arnold, 1968, Engineering geology of Slovak Carpathians: Internat. Geol. Cong., 23rd, Czechoslovakia, Guide to Excursion 28 AC, 39 p.

Nemčok, Arnold, 1972, Gravitational slope deformation in high mountains: Internat. Geol. Cong., 24th Montreal, Canada, sec. 13, Proc., p. 132–141.

Tweto, Ogden, 1974, Geologic map and sections of the Holy Cross quadrangle, Eagle, Lake, Pitkin, and Summit Counties, Colorado: U.S. Geol. Survey Misc. Geol. Inv. Map I–830, scale 1:24,000.

Yeend, W. E., 1969, Quaternary geology of the Grand and Battlement Mesas area, Colorado: U.S. Geol. Survey Prof. Paper 617, 50 p.

——— 1973, Slow-sliding slumps, Grand Mesa, Colorado: Mtn. Geologist, v. 10, no. 1, p. 25–28.

Zischinsky, Ülf, 1966, On the deformation of high slopes: Internat. Soc. Rock Mechanics Cong., 1st, Lisbon, Proc., v. 2, p. 179–185.

——— 1969, Über Sackungen: Rock Mechanics, v. 1, p. 30–52.

Jour. Research U.S. Geol. Survey
Vol. 5, No. 3, May–June 1977, p. 365–372

DEPOSITIONAL ENVIRONMENTS AS A GUIDE TO URANIUM MINERALIZATION IN THE CHINLE FORMATION, SAN RAFAEL SWELL, UTAH

By ROBERT LUPE, Denver, Colo.

Abstract.—Uranium deposits in the San Rafael Swell are related to sedimentary depositional environments in the Upper Triassic Chinle Formation. The sedimentary textures resulting from depositional processes operating in low-energy environments appear to have influenced uranium mineralization. The Chinle consists of three fining-upward, fluvial-lacustrine sequences. Uranium minerals are concentrated in the lower part of the lowest sequence in areas where sediments of low-energy environments are complexly interbedded with sediments of other environments. Areas favorable for uranium exploration exist in the subsurface to the north, west, and south of the Chinle outcrop in the Swell. This determination is based on the spatial distribution of depositional environments and the pattern of Chinle deposition through time.

Uranium deposits in the San Rafael Swell, Utah, are spatially related to rocks representing certain depositional environments in the Triassic Chinle Formation. This relationship can serve as an important guide in selecting areas favorable for uranium exploration.

Many researchers in the Colorado Plateau during the uranium "boom" of the fifties concluded that the texture and composition of the host rock helped control uranium mineralization (Finch, 1959, p. 144; Fischer, 1974). The rock compositions and textures resulted from sedimentary processes unique to each depositional environment; hence, the distribution of the rocks of certain depositional environments may be similar to the distribution of uranium host rocks. The distribution of uranium deposits is also similar to the distribution of both collapse features and potential source rocks. These factors will be discussed briefly.

This report is the first part of a study of the sedimentary geology of uranium-bearing Triassic rocks of the Colorado Plateau.

GEOLOGIC SETTING

The San Rafael Swell is a doubly plunging, asymmetric anticline formed in early Tertiary time (Gilluly, 1929, p. 126); the Chinle Formation is exposed around its flanks (fig. 1). The Swell lies south of the Uinta Basin, and, except for a few outcrops north of the Uinta Basin, the outcrops in the Swell are the northernmost exposures of the Chinle on the Colorado Plateau.

OBJECTIVE

The objective of this study was to determine the areal and stratigraphic distribution of depositional environments in the Chinle Formation and their relation to uranium host rocks. Depositional environments were interpreted, and rock textures and compositions were noted at each station shown in figure 1. Transport directions were also determined and were used to project outcrop observations into areas where the Chinle was not exposed.

RESULTS

The stratigraphic distribution of rocks of various depositional environments is shown in cross sections *A–A′* and *B–B′* (fig. 2). The Chinle Formation consists of three fining-upward sequences, numbered in ascending stratigraphic order, 1 through 3, with each sequence generally finer grained than its predecessor. The sedimentary rocks also grade laterally from a main area of deposition into finer grained rocks.

Each sequence generally grades upward and laterally from proximal braided-stream sandstones and conglomerates, through distal braided-stream sandstones, to flood-plain or overbank fine-grained sandstones, siltstones, and mudstones, and, finally, to lacustrine siltstones and mudstones. The sequences are commonly capped by paleosols. This sequence of depositional environments reflects a gradual change to environments of lower energy as deposition continued. The sequences also indicate either an increase in distance from the source area or a decrease in relief during later stages of deposition.

The lateral and vertical distributions of depositional environments are similar. The lateral decrease in grain size indicates a trend toward lower energy depositional

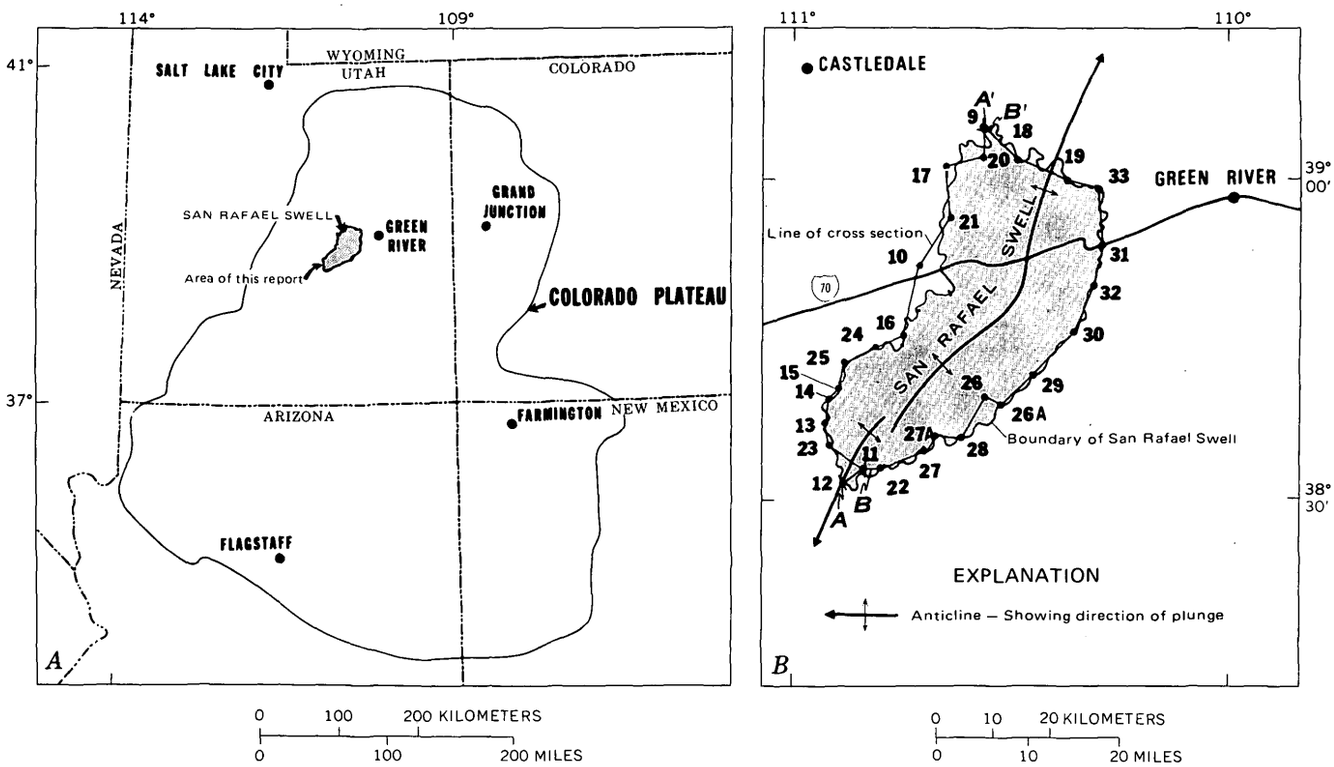

FIGURE 1.—Locations of the San Rafael Swell, cross sections *A–A'* and *B–B'*, and sample stations.

environments away from the main locus of deposition in the middle part of the Swell (fig. 2).

The diagnostic criteria used to distinguish various depositional environments are as follows:

1. Proximal braided-stream deposits (fig. 3*A*) are conglomeratic sandstone containing ripped-up intraclasts near their strongly erosional bases. They reflect the highest transport energies during Chinle deposition. Their sedimentary structures are relatively simple, consisting mainly of unstructured and flat beds. There is little vertical change in grain size. Proximal braided-stream rock bodies are lenticular in cross section, and foreset bedding and channel axes indicate unidirectional transportation.
2. The distal braided-stream deposits, which usually overlie and laterally abut the proximal braided-stream deposits (fig. 2), contain sand-sized sediment that is finer grained than the proximal deposits and that is commonly typified by foreset bedding of transverse bar origin (fig. 3*B*) (Smith, 1970, p. 3000; Asquith and Cramer, 1975, p. 660). Sediment transport in these deposits was also unidirectional.
3. Flood-plain or overbank deposits can be confused with lacustrine sediments where outcrops are poor. Flood-plain sediments show abundant subaerial features such as mudcracks, tracks, and sediment tubes disgorged by feeding animals. They are often rhythmically bedded, show unidirectional flow features, and are coarser grained and less burrowed than lacustrine beds (fig. 3*C*).
4. On the other hand, lacustrine sediments lack bedding because of heavy burrowing, show little evidence of subaerial exposure, and are generally finer grained than flood-plain deposits (fig. 3*D*).
5. Paleosols (fig. 3*E*), common at the top of these fining-upward sequences, are both calcareous and siliceous. They formed in a semiarid climate (Cooke and Warren, 1973, p. 114).

One feature deserving special attention is the complex interbedding of rocks deposited in various environments near the north and south ends of the Swell (fig. 2). In these areas, the sediment bodies are also generally smaller. This complex interbedding may have played an important part in control of uranium mineralization.

In reconstructing the areal distribution of depositional environments, it is helpful to examine transport directions for specific horizons in the Chinle. Transport directions for the lower part of sequence 1 are shown in figure 4. The rose diagram defines a strong

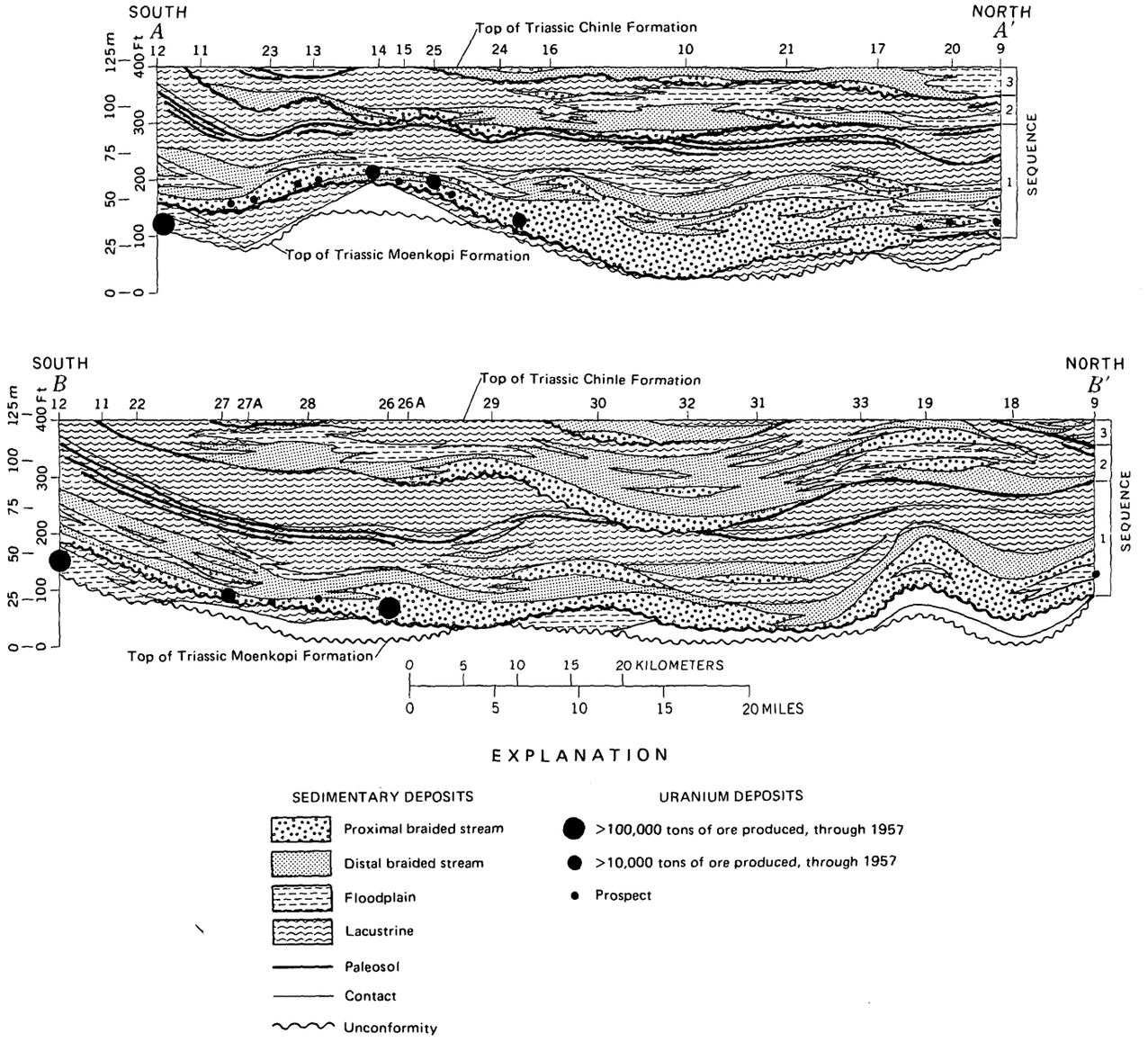

FIGURE 2.—Cross sections (*A–A'* and *B–B'*) showing sedimentary depositional environments and the stratigraphic distribution of uranium deposits in the Triassic Chinle Formation, San Rafael Swell, Utah. Numbers indicate sample stations shown in figure 1. The lower part of sequence 1 is roughly equivalent to the Moss Back Member of Stewart, Poole, and Wilson (1972, p. 31). Uranium data are from Hawley, Robeck, and Dyer (1968).

northwesterly transport trend with minor divergence. Geographically, that trend is represented by a corridor of deposition across the central part of the Swell (fig. 4). The divergences from the trend in this interval of the Chinle are in the north and south ends of the Swell where streams trended slightly away from the axis of the corridor. The pattern suggests that currents were weaker in the north and south. This inference is supported by the greater abundance of low-energy environments in these areas (fig. 2).

A paleogeographic reconstruction of the lower part of sequence 1 is shown in figure 5. These environments, generalized from figure 2, were tied together schematically by using transport trends.

These studies indicate that a system of braided-stream sediments trended toward the northwest across the central part of the Swell during early Chinle time. At the northwest end and off the flanks of the corridor, currents waned and lower energy environments prevailed. Furthermore, these flanking distal areas were more complexly interbedded.

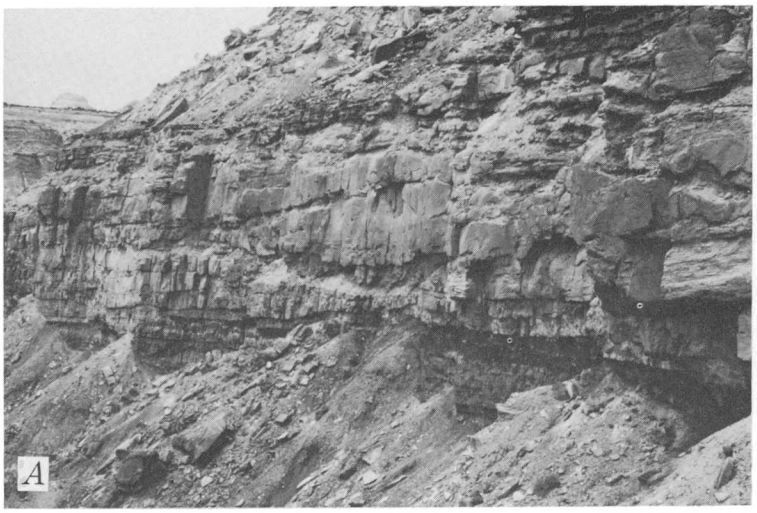
A

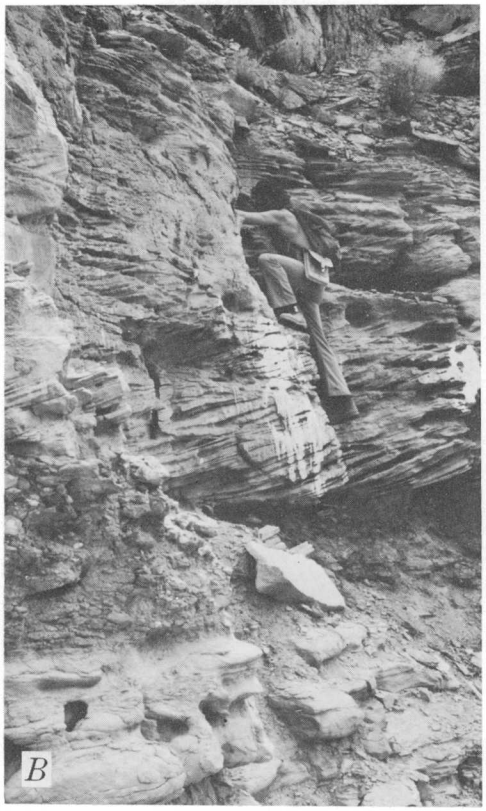
B

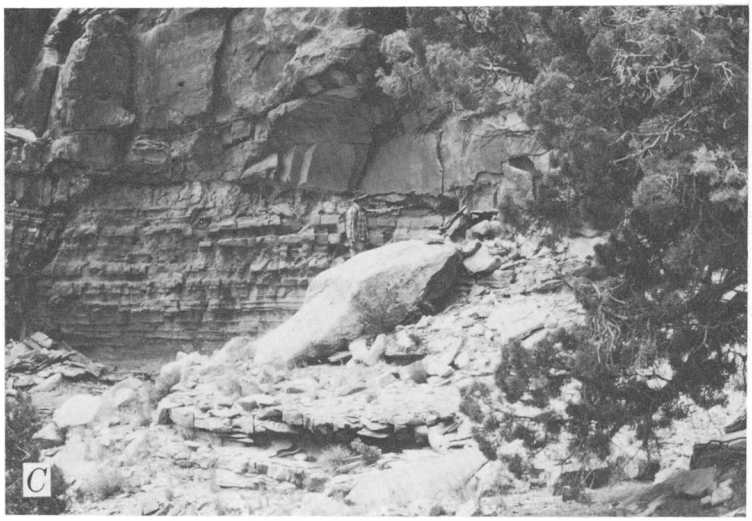
C

E

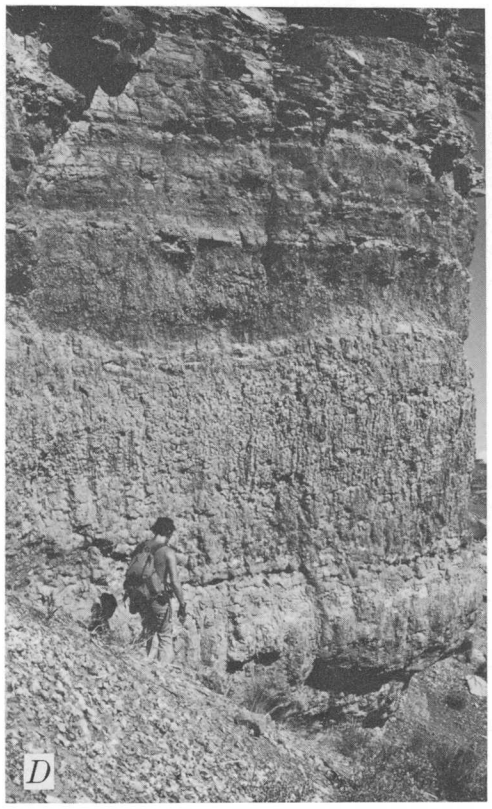
D

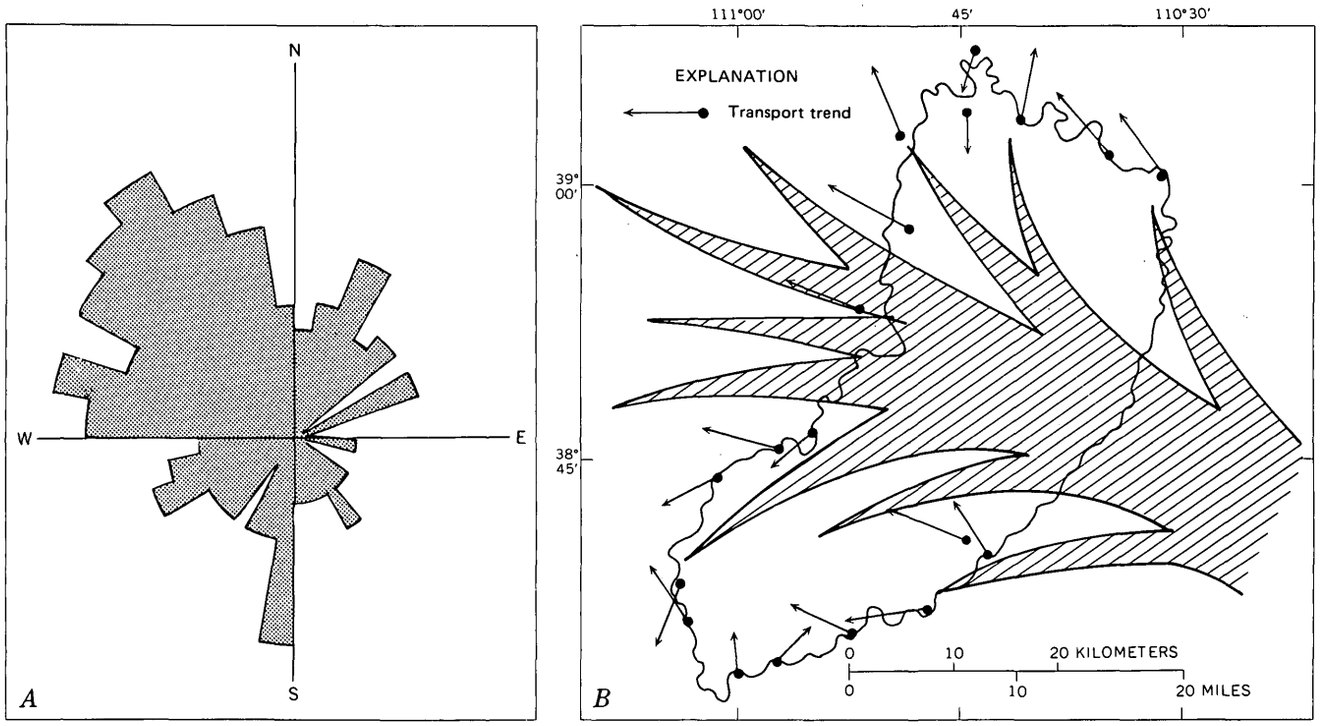

FIGURE 4.—Transport directions of the lower part of sequence 1 of the Chinle Formation, San Rafael Swell, Utah. *A*, Equal-area rose diagram of the total of 130 measurements. *B*, Geographic distribution of transport trends. The patterned area suggests the stream dispersal pattern during deposition of the lower part of sequence 1.

URANIUM

The distribution of uranium deposits in the San Rafael Swell is shown in figures 2 and 5. There is a close relationship between uranium deposits and the complexly interbedded, low-energy sediments; rocks in areas of uranium mineralization consist of sediment bodies of greatly contrasting textures that are interbedded on a relatively small scale. Apparently, interbedding of rocks of diverse textures influenced uranium mineralization—an inference supported by Fischer (1974), who felt that interbedded sandstones and mudstones were favorable host rocks. It is not known exactly what rock properties—hydrological, geochemical, or mineralogical—influenced uranium mineralization.

AREAS FAVORABLE FOR URANIUM EXPLORATION

Favorable host rocks apparently exist in the subsurface off the north, west, and south margins of the Swell (fig. 6). This conclusion is based on the relationship between depositional environments and uranium. The areas to the north and the south are extensions of the deposits and environments shown in figure 5. The area to the west was also apparently an area of low-energy environments, which is inferred from the distribution of environments and the change in transport trends during later Chinle time. During that time, the distribution of environments contracted around an area in the east-central part of the Swell (fig. 7), so that low-energy sediments were deposited on the high-energy sediments of the lower part of sequence 1. This contraction was caused by a decrease in the energy level of the system (compare figs. 5, 7) and accompanied a rotation of transport trends to the east (fig. 7). By reversing this pattern of contraction back to the time of the lower part of sequence 1, a distribution of environments is inferred that predicts an area of low-energy sediments in the subsurface to the west.

OTHER FACTORS

The distribution of collapse features and the location of possible source rock may also have affected the localization of uranium in the Chinle in the San Rafael Swell. However, neither factor produces an entirely satisfactory relationship. The distribution of collapse features (fig. 8) does not explain the many

FIGURE 3.—Sediments of various Chinle depositional environments. *A*, Proximal braided-stream deposits exposed in cliff. *B*, Distal braided-stream deposits showing typical foreset bedding. *C*, Rhythmically bedded overbank deposits. *D*, Heavily burrowed lacustrine beds. *E*, A typical rubbly weathering paleosol.

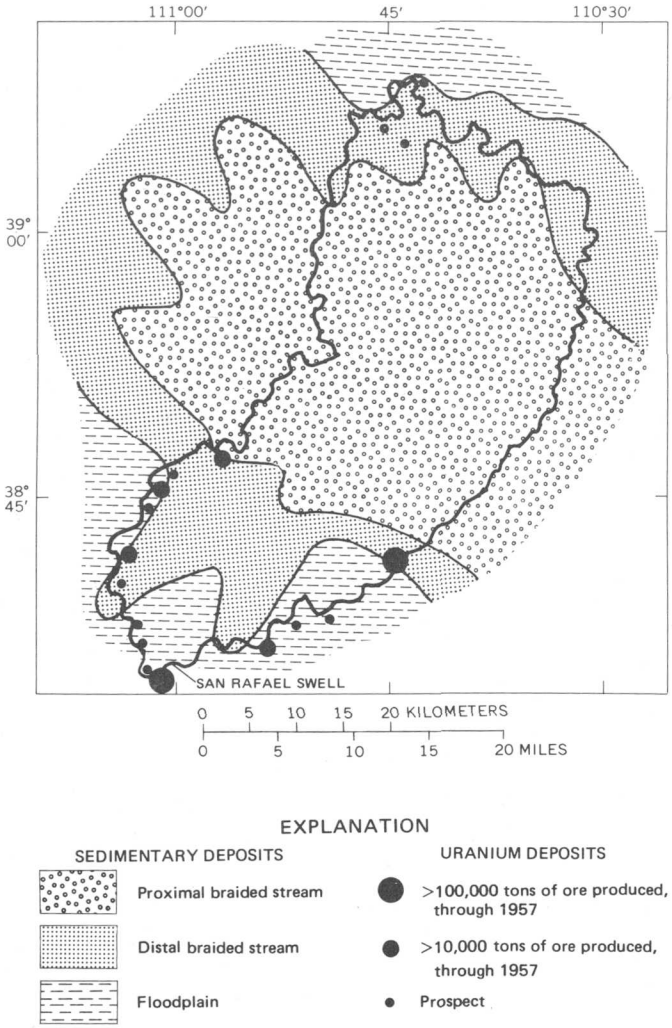

FIGURE 5.—Distribution of depositional environments and uranium deposits, lower part of sequence 1, Chinle Formation, San Rafael Swell, Utah. Uranium data are from Hawley, Robeck, and Dyer (1968).

uranium deposits which are located in the south end of the Swell. (Hawley, Robeck, and Dyer, 1968, p. 31, discuss this relationship more thoroughly.) And if candidates for source rock are limited to volcaniclastic material within the Chinle, then the only source rock in the Swell would be at the south end (fig. 8). Most uranium deposits have been found in the south, but there are also deposits at the north end, where there is apparently no Chinle source material.

SUMMARY

A number of factors probably combined to influence uranium mineralization of Chinle rocks in the San Rafael Swell. One of these, the texture of the host rocks, resulted from processes operating in certain

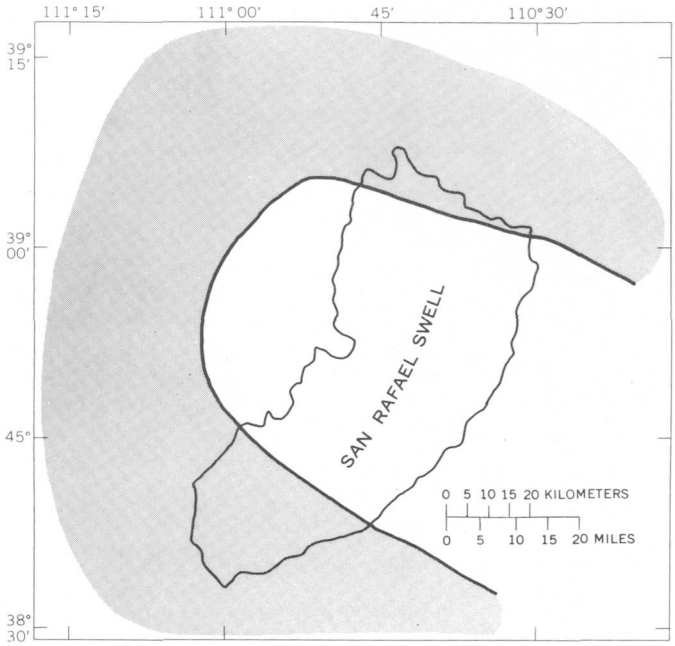

FIGURE 6.—Areas favorable for uranium exploration (patterned), San Rafael Swell, Utah.

depositional environments. Therefore, by using depositional environments as a guide, areas favorable for uranium exploration may be selected.

Figures 7 and 8 follow "References Cited."

REFERENCES CITED

Asquith, G. B., and Cramer, S. L., 1975, Transverse braid bars in the upper Triassic Trujillo Sandstone of the Texas Panhandle: Jour. Geology, v. 83, p. 657–661.

Cooke, R. U., and Warren, Andrew, 1973, Geomorphology in deserts: Berkeley, California Univ. Press, 374 p.

Finch, W. I., 1959, Geology of uranium deposits in Triassic rocks of the Colorado Plateau region: U.S. Geol. Survey Bull. 1074–D, p. 125–164.

Fischer, R. P., 1974, Exploration guides to new uranium districts and belts: Econ. Geology, v. 69, p. 362–376.

Gilluly, James, 1929, Geology and oil and gas prospects of part of the San Rafael Swell, Utah: U.S. Geol. Survey Bull. 806–C, p. 69–130.

Hawley, C. C., Robeck, R. C., and Dyer, H. B., 1968, Geology, altered rocks, and ore deposits of the San Rafael Swell, Emery County, Utah: U.S. Geol. Survey Bull. 1239, 115 p.

Smith, N. D., 1970, The braided stream depositional environment: comparison of the Platte River with some Silurian clastic rocks, north central Appalachians: Geol. Soc. America Bull., v. 81, p. 2993–3014.

Stewart, J. H., Poole, F. G., and Wilson, R. F., 1972, Stratigraphy and origin of the Chinle Formation and related upper Triassic strata in the Colorado Plateau region: U.S. Geol. Survey Prof. Paper 690, 336 p.

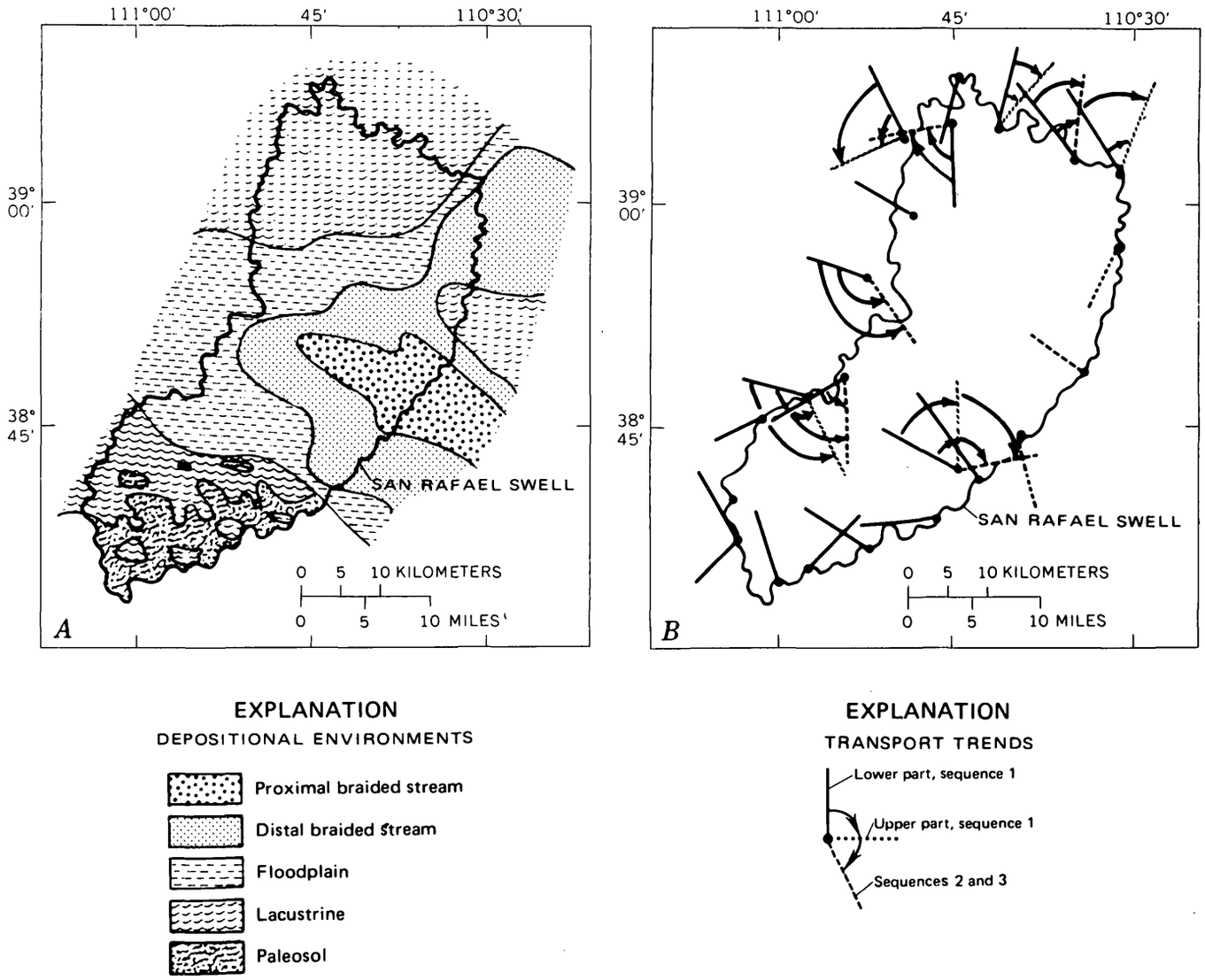

FIGURE 7.—San Rafael Swell, Utah. *A*, Distribution of depositional environments, upper part of sequence 1, Chinle Formation. *B*, Rotation of transport trends with time for the entire Chinle Formation.

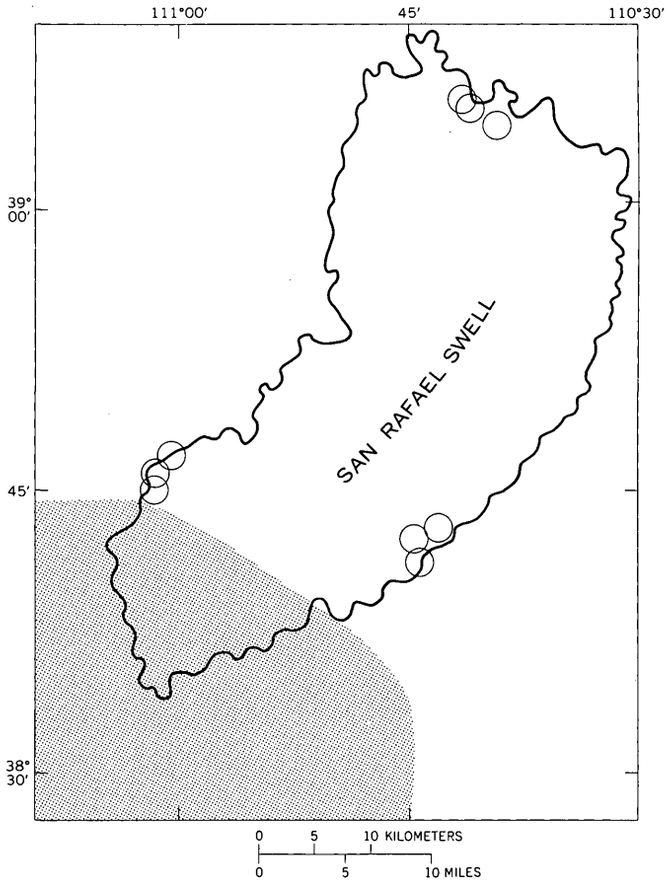

FIGURE 8.—Distribution of collapse features (circles) and of possible uranium source rocks (shaded area) in the Chinle Formation, San Rafael Swell, Utah. Data on collapse features from Hawley, Robeck, and Dyer (1968).

Jour. Research U.S. Geol. Survey
Vol. 5, No. 3, May–June 1977, p. 373–388

DISTRIBUTION OF SOME BIOSTRATIGRAPHICALLY DIAGNOSTIC OSTRACODES IN THE PLIOCENE AND LOWER PLEISTOCENE OF VIRGINIA AND NORTHERN NORTH CAROLINA

By JOSEPH E. HAZEL, Washington, D.C.

Abstract.—Ostracodes are abundant and diverse in Pliocene and lower Pleistocene deposits of Virginia and North Carolina. Many readily identified species are short ranging or have well-defined beginning and (or) end points to their stratigraphic range. These microscopic crustaceans, therefore, are very useful in zonation and correlation in the region. In this paper, 54 particularly useful species are illustrated, and their ranges are indicated graphically. The range zones, concurrent range zones, and local range zones of these forms allow the recognition of the chronozones of previously proposed ostracode assemblage zones in Virginia and North Carolina as well as in other regions.

In Cretaceous and Cenozoic deposits of the Atlantic and Gulf Coastal Plain, ostracodes are one of the most diverse and abundant invertebrate groups in the size range of about 300 to 1,500 micrometers. More than 200 species of these small crustaceans have been found in Pliocene and lower Pleistocene rocks of the middle Atlantic Coastal Plain as a result of investigations by the U.S. Geological Survey (Hazel, 1971a,b; in press; unpub. data, 1976). Many of these species occur commonly, have well-defined and relatively short stratigraphic ranges, at least locally, or have well-defined range end points, and are distributed widely. These are characteristics of useful biostratigraphic indicators. The purpose of this paper is to illustrate and indicate the stratigraphic distribution of 54 species (table 1) whose range zones and concurrent range zones have proved useful in correlating Pliocene and lower Pleistocene rocks in the Atlantic Coastal Plain, particularly in the Virginia and North Carolina region. This work, and that at Lee Creek mine, North Carolina (Hazel, in press), supplement the assemblage-zone analysis of Hazel (1971a), and provide further documentation of biostratigraphically useful taxa.

Figure 1 indicates the area in southeastern Virginia and northern North Carolina in which rocks of Pliocene and early Pleistocene âge crop out in natural exposures or open pit mines or occur in the shallow subsurface within easy reach of the power auger (shallower than about 100 ft, or 30 m). Ostracodes have been listed or described from exposures or from the subsurface of this area by Ulrich and Bassler (1904), Swain (1951, 1974), Malkin (1953), McLean (1957, 1966), Brown (1958), and Brown, Miller, and Swain (1972). In addition, Edwards (1944), Puri (1953), Pooser (1965), Swain (1968), and Puri and Vanstrum (1971) have provided valuable occurrence data from this area or from areas to the south. All these data have been used where possible in interpreting the distribution of the taxa used in this work, but the principal references are the materials used in Hazel (1971a) and subsequent U.S. Geological Survey collections. The resulting faunal slides are housed in the collections of the U.S. Geological Survey at the National Museum of Natural History, Washington, D.C.

In general, most of the outcrops in Virginia and North Carolina on which this study is based have been placed in the Yorktown Formation, which traditionally has been considered to be of late Miocene age (see discussion in Hazel, 1971a). However, Hazel (1971a) delineated three ostracode assemblage zones in what was then considered to be the Yorktown and placed the upper of these in the Pliocene, suggesting that more of the traditional Atlantic Coast upper Miocene would turn out to be of Pliocene age. Akers (1972, 1973) identified Pliocene planktic foraminifers and calcareous nannofossils from localities of the Yorktown Formation in Virginia and North Carolina. Subsequently, Hazel (in press), using various lines of planktic and radiometric evidence, has endeavored to show that the rocks previously assigned to the Yorktown Formation include deposits of both Pliocene and early Pleistocene age, and has presented a correlation chart for Atlantic Coastal Plain Pliocene and Pleistocene formations. This chart (reproduced here as fig. 2) was constructed

TABLE 1.—*Alphabetical listing of the 54 species used in this study*

[The number assignment of the species on the range chart (fig. 3) is indicated as is the figure illustrating the species]

Species	Species No. (in fig. 3)	Illustration (fig. No.)
Actinocythereis captionis Hazel	26	8*c*
dawsoni (Brady)	12	8*g*
mungorffi (Swain)	18	8*h*
Aurila sp. B	15	6*b*
Bensonocythere bradyi Hazel	30	9*g*
calverti (Ulrich and Bassler)	1	4*d*
gouldensis Hazel	21	4*a*
ricespitensis Hazel	34	4*c*
rugosa Hazel	29	4*b*
trapezoidalis (Swain)	13	10*f*
whitei (Swain)	46	4*e*
sp. M	52	4*f*
Campylocythere laeva Edwards	38	9*f*
Caudites asymmetricus Hazel	54	7*f*
Cytheridea campwallacensis Hazel	14	5*f*
carolinensis Hazel	40	5*e*
virginiensis (Malkin)	22	5*g*
aff. *C. virginiensis* (Malkin)	3	5*h*
Cytheromorpha incisa Hazel	9	9*a*
macroincisa Hazel	51	9*c*
suffolkensis Hazel	39	9*d*
Cytheropteron? *yorktownensis* (Malkin)	19	6*g*
Echinocythereis leecreekensis Hazel	53	10*h*
planibasalis (Ulrich and Bassler)	11	10*g*
Hermanites ascitus Hazel	6	6*h*
Loxoconcha edentonensis (Swain)	49	9*f*
sp. A	5	9*h*
sp. U	16	9*e*
Malzella conradi (Howe and McGuirt) (angulate form)	17	6*c*
evexa Hazel	20	6*d*
Microcytherura choctawhatcheensis (Puri)	27	5*d*
expanda Hazel	50	5*c*
minuta Hazel	31	5*b*
similis (Malkin)	41	5*a*
Muellerina bassiounii Hazel	44	10*d*
blowi Hazel	32	10*c*
canadensis petersburgensis Hazel	7	10*b*
wardi Hazel	24	10*a*
Murrayina barclayi McLean	4	8*d*
Neocaudites triplistriatus (Edwards)	37	7*d*
Orionina vaughani (Ulrich and Bassler)	28	8*a*
Palaciosa minuta (Edwards)	43	7*c*
Paracytheridea edwardsi Hazel	36	7*a*
mucra Edwards	33	7*b*
rugosa Edwards	47	7*e*
Peratocytheridea sandbergi Hazel	23	7*h*
"*Pontocythere*" sp. I	2	10*e*
Pterygocythereis inexpectata (Blake)	10	7*g*
Puriana carolinensis Hazel	25	8*b*
convoluta Teeter	42	8*f*
mesacostalis (Edwards)	45	8*d*
Radimella confragosa (Edwards)	35	6*a*
Thaerocythere carolinensis Hazel	48	6*f*
schmidtae (Malkin)	8	6*e*

by using, primarily, He/U and K/Ar dates and planktic foraminifer data to correlate with radiometric and planktic time scales; ostracode data were used to make regional correlations.

Hazel (in press and herein) refers the beds of *Puriana mesacostalis* assemblage zone age in Virginia and the Chowan River area of North Carolina, for want of better terminology, to the "Yorktown." The beds above the Yorktown at the Lee Creek mine near Aurora, N.C., are placed in the Croatan Formation

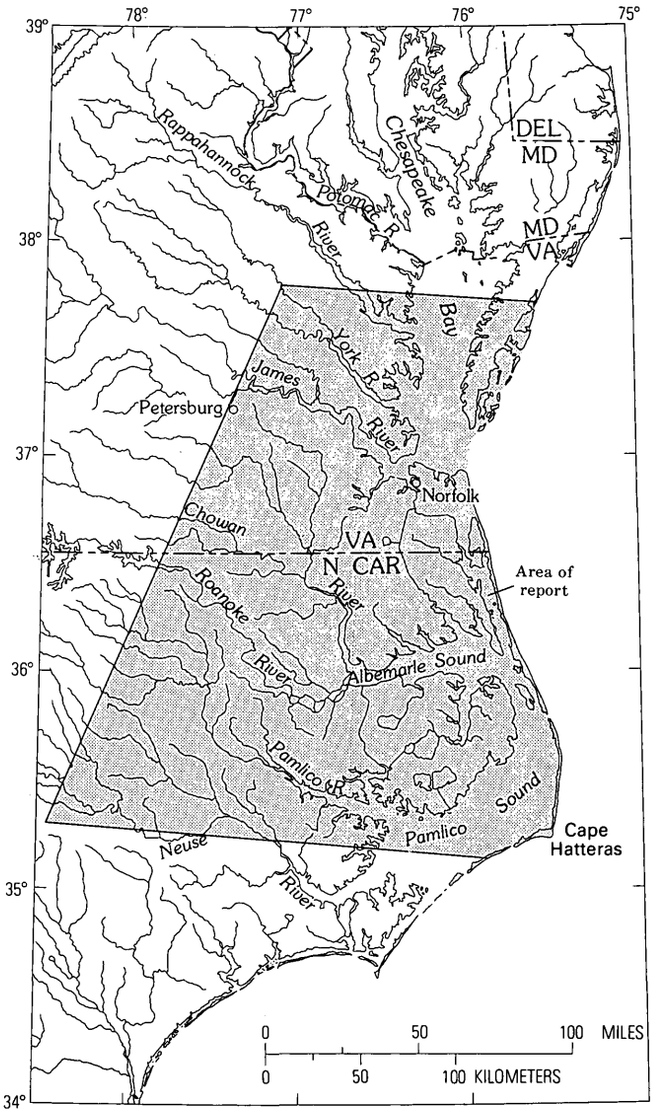

FIGURE 1.—Map showing the general area in Virginia and northern North Carolina where marine deposits of Pliocene to early Pleistocene age crop out in natural exposures or open pit mines or occur in the subsurface at depths (about 100 ft, or 30 m, and less) easily reached by use of a power auger.

(also see DuBar and others, 1974b, who reached the same conclusion but used the junior team "James City Formation"). The *Puriana mesacostalis* assemblage zone in the Chowan River area and in southeastern Virginia may also be referable to the Croatan, but this remains to be demonstrated.

BIOSTRATIGRAPHY

Perhaps when the ostracode assemblages of the Duplin, Bear Bluff, and Waccamaw Formations are more fully known, the ostracode assemblage zones of Hazel

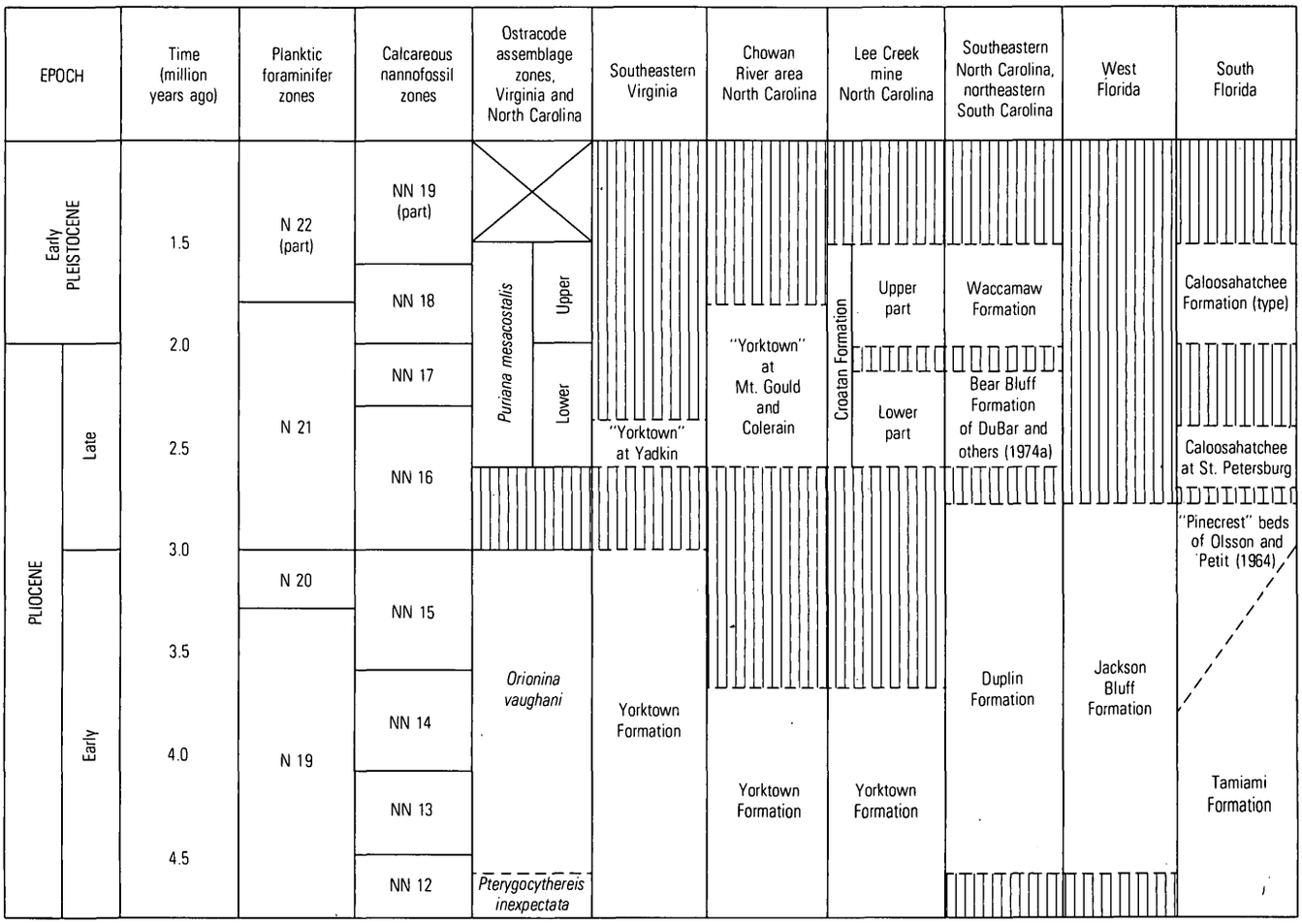

FIGURE 2.—Correlation chart for Pliocene and lower Pleistocene formations of the middle and southern Atlantic Coastal Plain and Florida. Time scale and planktic foraminifer and nannofossil zones are mainly from Berggren and Van Couvering (1974). Correlation with the time scale is based on scattered radiometric dates (see Hazel, in press) and planktic foraminifers. The planktic organism zones are shown mainly for comparative purposes. With some exceptions, age-diagnostic planktic organisms do not occur at most localities of the formational units shown in the figure. Ostracode assemblage zones are from Hazel (1971a) and are applicable in Virginia and northern North Carolina. Figure taken from Hazel (in press).

(1971a) may be traceable at least in part into southern North Carolina and South Carolina. However, results to date suggest that the *Pterygocythereis inexpectata*, *Orionina vaughani*, and *Puriana mesacostalis* assemblage zones are applicable with confidence only in Virginia and North Carolina as far south as the Pamlico River or, perhaps, the Neuse River. Although the assemblages in the two biogeographic regions are distinct, many species occur in both, and correlation between the regions is best effected by use of the range zones and concurrent range zones of these species.

Figure 3 shows the stratigraphic ranges of 54 species judged to be particularly useful in biostratigraphy in the Middle Atlantic Coastal Plain. Diagrams such as figure 3 must be used with care because considerable circular logic is involved in their construction. Outcrops containing fossils are correlated by these fossils as well as by physical criteria to form a composite section for areas, and then the same fossils are plotted against the composite to indicate their ranges. Therefore, the ranges must reflect the composite stratigraphy, and this accounts for the apparent coincidences in range end-points of many species (see discussion in Hazel, 1970, 1971a). Nevertheless, as long as the method of construction is understood, such range charts can be informative graphic devices. (See Hazel, 1971a, fig. 4, for an example of much of the data used in figure 3 presented in a different format.)

The ranges in figure 3 are based on collections from the southeastern Virginia and northeastern North Carolina region and other areas and from many published and unpublished sources. Other species show

potential for biostratigraphic utility, but further study is needed to refine their taxonomy or distribution. The ranges of the species utilized in figure 3 and discussed below should provide the interested worker with the basic data for ostracode range zones and concurrent range zone biostratigraphy in the Pliocene and lower Pleistocene of at least the middle part of the Atlantic Coastal Plain. The species are illustrated in figures 4–10 (also see Hazel, in press).

Taxon range zones

The rocks in the Atlantic Coastal Plain and Florida that can be referred to the *Pterygocythereis inexpectata*, *Orionina vaughani*, and *Puriana mesacostalis* ostracode assemblage zones, or demonstrated to be time equivalents of them, can be thought of as a chronostratigraphic unit of nearly stage magnitude, if, that is, stages by definition are to be chronostratigraphic rather than biostratigraphic units. This interval of approximately 3.5 m.y. is coincident with the range zones of *Cytheropteron? yorktownensis*, *Malzella evexa*, *Bensonocythere gouldensis*, *Cytheridea virginiensis*, *Actinocythereis mundorffi*, *Muellerina wardi*, and *Puriana carolinensis*. Therefore, the composite chronozone of the three assemblage zones can be recognized by the presence of these species.

The range zones of *Loxoconcha* sp. U and *Aurila* sp. B seem to indicate a Yorktown age for the deposits in which they occur. The former species occurs only in the subsurface of the Eastern Shore of Virginia, however, and *Aurila* sp. B is relatively rare.

The presence of the angulate form of *Malzella conradi* indicates rocks of Pliocene age (chronozone encompassing the *Pterygocythereis inexpectata* to lower *Puriana mesacostalis* assemblage zones). The less angulate form (anterodorsal angle more obtuse and set farther to the posterior), however, occurs in the upper Miocene Red Bay Formation of Puri and Vernon (1964) in Florida as well as in Pliocene deposits. The subspecies *Muellerina canadensis petersburgensis* may also indicate the same interval as the angulate form of *Malzella conradi*.

The chronozone encompassing the *Orionina vaughani* and *Puriana mesacostalis* assemblage zones can be recognized by the range zones of *Bensonocythere rugosa*, *B. bradyi*, *B. ricespittensis*, *Microcytherura minuta*, *Muellerina blowi*, *Paracytheridea mucra*, *Radimella confragosa*, *Paracytheridea edwardsi*, *Cytheromorpha suffolkensis*, *Cytheridea carolinensis*, and *Microcytherura similis*. However, *Bensonocythere rugosa* does not occur in deposits of the upper part of the *Puriana mesacostalis* assemblage zone or its equivalents, and *Cytheridea carolinensis* and *Microcytherura similis* seem not to occur in the lower part of the *Orionina vaughani* assemblage zone and equivalents. In Virginia and northern North Carolina, the thermo-

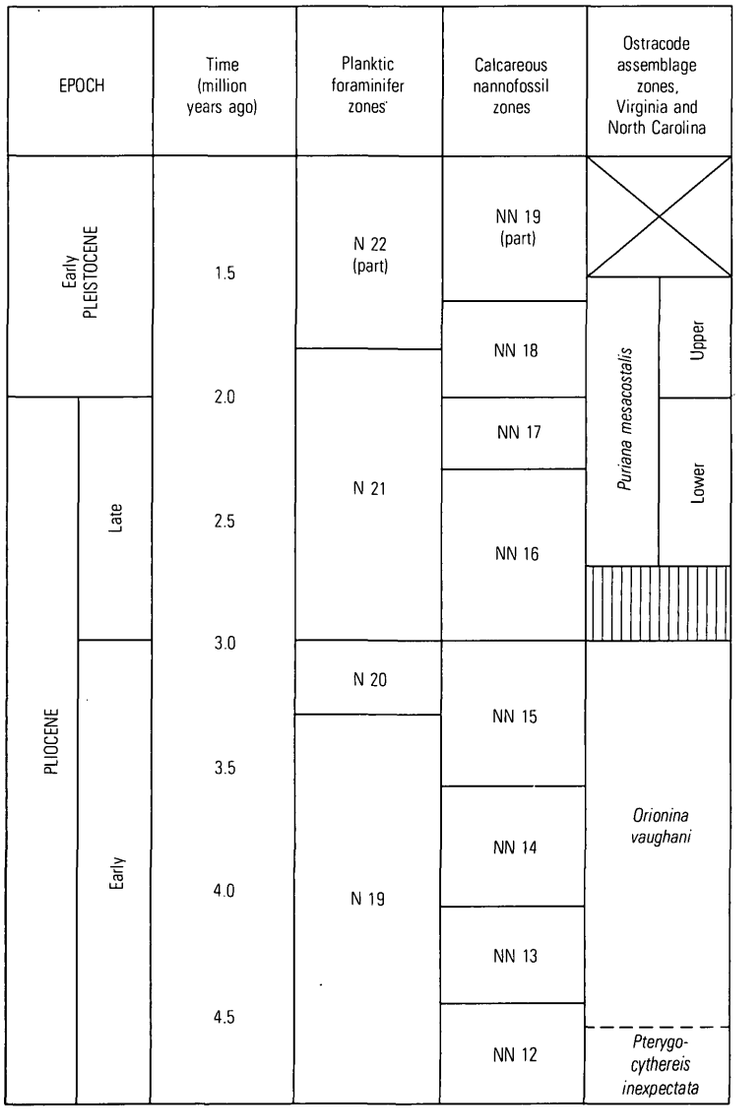

FIGURE 3.—Range chart for 54 species whose range zones and chronozones of the ostracode assemblage zones shown. The ranges their local ranges in the Virginia and northern North Carolina resent the best estimate of their stratigraphic distribution in the listed alphabetically in table 1; the figure number and number

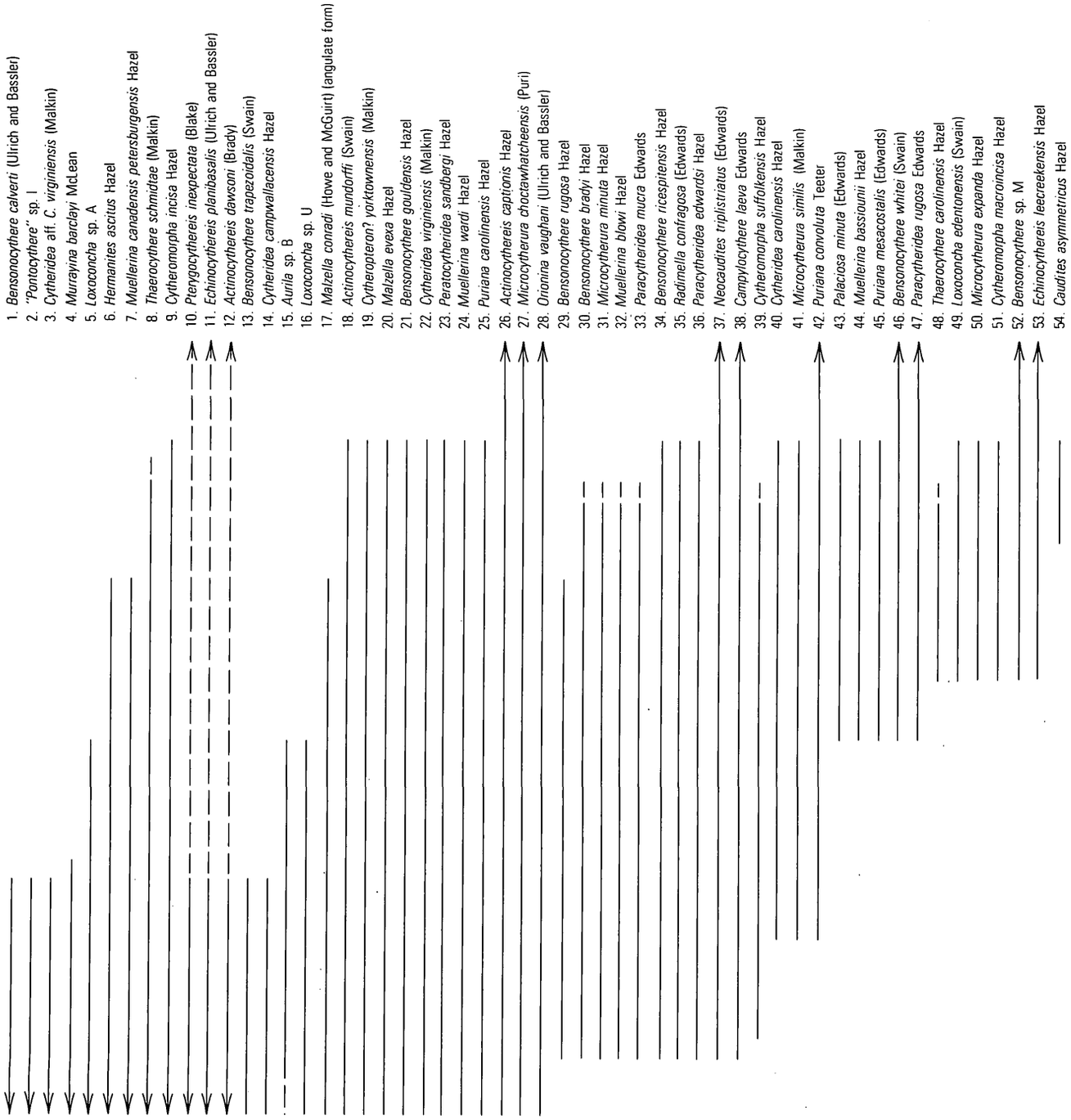

concurrent range zones have proved to be useful in correlating the formations shown in figure 2 and in recognizing the indicated by solid lines for *Pterygocythereis inexpectata, Echinocythereis planibasalis,* and *Actinocythereis dawsoni* are area; these fossils are known to occur elsewhere in older deposits and younger deposits. Ranges for all other species rep- Atlantic Coastal Plain and Florida on the basis of data from all sources. The species are illustrated in figures 4–10 and given the species in figure 3 are indicated after the name in table 1.

philic species *Radimella confragosa* occurs only in the *Puriana mesacostalis* assemblage zone, but it occurs in the chronozone of the *Orionina vaughani* assemblage zone farther south in the Coastal Plain.

The range zones of *Loxoconcha edentonensis*, *Thaerocythere carolinensis*, *Cytheromorpha macroincisa*, and *Microcytherura expanda* appear to be coincident, or approximately so, with the *Puriana mesacostalis*

assemblage zone. In the Virginia and northern North Carolina region, *Palaciosa minuta*, *Muellerina bassiounii*, and *Puriana mesacostalis* also indicate the chronozone of the *Puriana mesacostalis* assemblage zone. However, in southern North Carolina, these forms first appear in the uppermost part of the Duplin Formation, which is either correlative with the upper part of the *Orionina vaughani* assemblage zone or, as suggested in figure 3, with the unconformity between that zone and the *Puriana mesacostalis* assemblage zone. As far as is known, the species *Caudites asymmetricus* indicates the chronozone of the upper part of the *Puriana mesacostalis* assemblage zone from North Carolina to southern Florida.

Local range zones

Several species have a stratigraphic distribution in the Coastal Plain as a whole that is greater than that in the study area. For example, in the Virginia and northern North Carolina region, *Pterygocythereis inexpectata*, *Actinocythereis dawsoni*, and *Echinocythereis planibasalis* are found only in the lower part of the Yorktown and subjacent deposits. Their presence indicates an early *Orionina vaughani* assemblage zone or older age. The probably mild-temperate marine climate of *Pterygocythereis inexpectata* assemblage-zone time apparently changed by *Orionina vaughani* assemblage-zone time to a warm-temperate climate in which bottom temperatures apparently exceeded 20°C (Hazel, 1971b). The three species mentioned above live today on the Atlantic Continental Shelf and slope poleward or seaward of the 20°C bottom isotherm for the warmest month.

Concurrent range zones

Figure 3 shows that the overlap in range of many species provides several useful biostratigraphic tools, too many to discuss individually. The chronozone of the *Pterygocythereis inexpectata* assemblage zone cannot be recognized at present by concurrent range zones. The chronozone of the lower part of the *Orionina vaughani* assemblage zone can be recognized, at least in the Virginia and northern North Carolina region, by concurrent range zones. These zones are formed by the overlap in the local range of the long-ranging cryophilic species *Pterygocythereis americana*, *Actinocythereis* dawsoni, and *Echinocythereis planibasalis* and of the seemingly short-ranging species *Cytheridea campwallacensis* and "*Pontocythere*" sp. I with several species that first appear at about the boundary of the *Pterygocythereis inexpectata* and *Orionina vaughani* assemblage zones.

One of the more useful multitaxon concurrent range zones is delineated by the overlap of *Malzella conradi* and *Bensonocythere rugosa* with such species as *Thaerocythere carolinensis*, *Cytheromorpha macroincisa*, *Microcytherura expanda*, and *Echinocythereis leecreekensis*. This zone delineates a biostratigraphic interval that includes the lower part of the Croatan Formation and the lower part of the so-called "Yorktown" Formation in the Chowan River area in North Carolina and the Bear Bluff Formation as used by DuBar and others (1974a) in southern North Carolina and South Carolina.

COMPARISONS WITH OTHER OSTRACODE ZONATIONS

Malkin (1953) proposed two faunizones (assemblage zones) for what she termed the Yorktownian substage. These were termed the *Hemicythere conradi* and *Hemicythere schmidtae* zones. Teilzones (local range zones) that Malkin considered to be important were also listed. Subsequent collecting and taxonomic work has refined the concept of most of the species whose teilzones were listed, so that these biostratigraphic units are now impossible to use as Malkin intended. The deposits of Malkin's *Hemicythere schmidtae* faunizone are approximately equivalent to the *Pterygocythereis inexpectata* and lower part of the *Orionina vaughani* assemblage zones of Hazel (1971a). Her *Hemicythere conradi* faunizone is part of the *Orionina vaughani* assemblage zone of Hazel.

F. M. Swain (in Brown and others, 1972, p. 53) proposed one assemblage zone, the *Aurila conradi-Thaerocythere schmidtae* assemblage zone for the upper Miocene and "lower part of the post-Miocene" rocks of the middle Atlantic Coastal Plain (now known to be of Pliocene to early Pleistocene age). This unit correlates with the three assemblage zones of Hazel (1971a). Swain divided his assemblage zone into the *Thaerocythere schmidtae* and *Radimella confragosa* subzones, which are said to be partial equivalents, the *T. schmidtae* subzone being somewhat older. The chronozones of the *R. confragosa* and *T. schmidtae* range zones are broadly overlapping (fig. 3), but in northern North Carolina the two taxa are found together only in the *Puriana mesacostalis* assemblage zone (Hazel, 1971a; in press).

In table 2 in Brown and others (1972, p. 34), two species, *Aurila conradi* (Howe and McGuirt) and *Trachyleberis exanthemata* (Ulrich and Bassler), are listed as indicating their "Late Miocene unit" in the Virginia and North Carolina region. The occurrences in the wells used by Brown and others (1972) are indi-

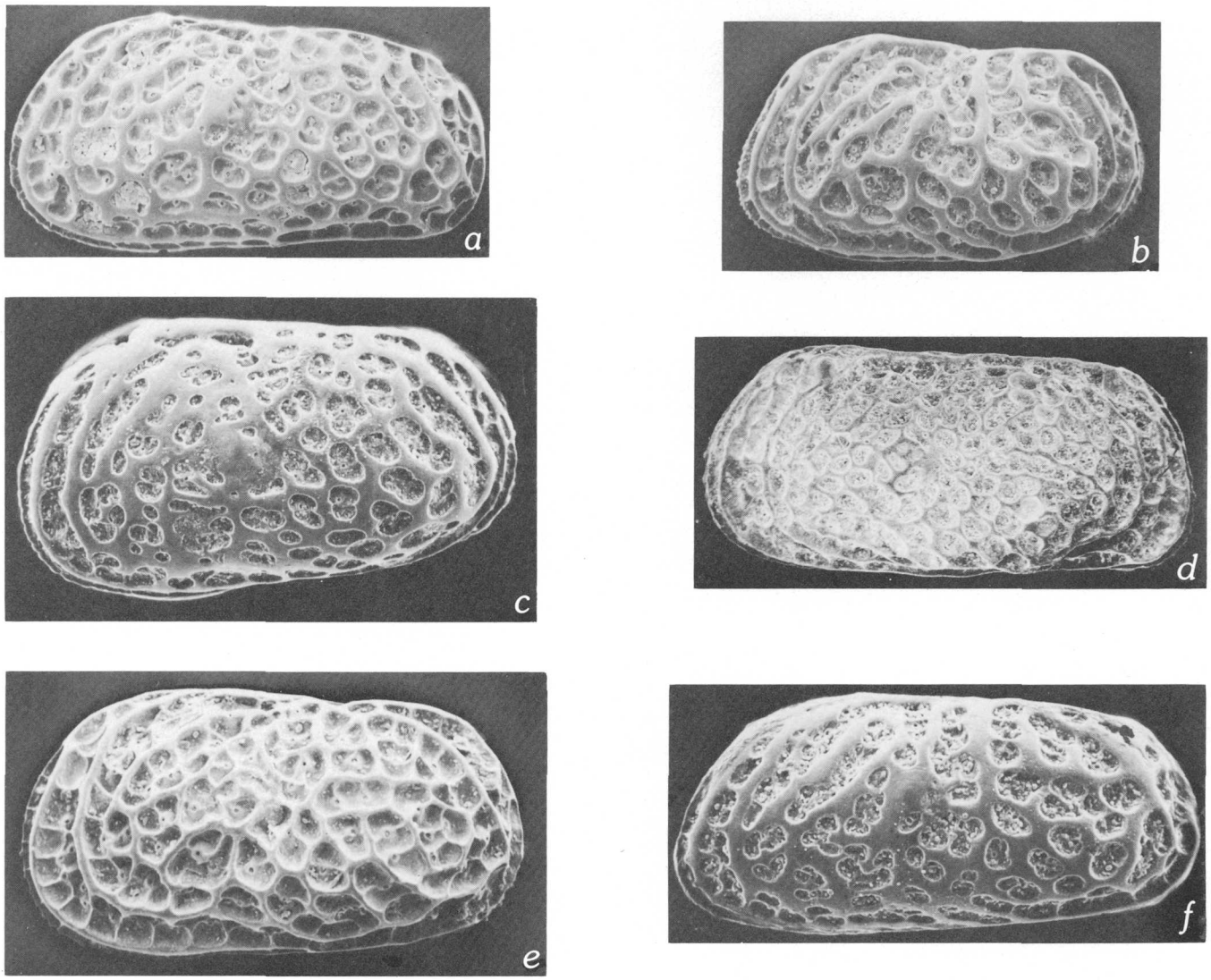

FIGURE 4.—*Bensonocythere.*

a. Bensonocythere gouldensis Hazel, male right valve, "Yorktown" Formation near Mt. Gould, N.C., sample 16 of Hazel (1971a), USGS 24894, × 93, USNM 167380. *b. Bensonocythere rugosa* Hazel, female left valve, Yorktown Formation, Petersburg, Va., sample 29 of Hazel (1971a), USGS 24909, × 88, USNM 167382. *c. Bensonocythere ricespitensis* Hazel, female left valve, Yorktown Formation, Hampton City, Va., sample 36 of Hazel (1971a), USGS 24907, × 103, USNM 167394. *d. Bensonocythere calverti* (Ulrich and Bassler, 1904), male left valve, Yorktown Formation near Palmyra, N.C., sample 11 of Hazel (1971a), USGS 24889, × 70, USNM 167387. *e. Bensonocythere whitei* (Swain, 1951), female left valve, Yorktown Formation, Edenton Naval Air Base, N.C., 55 ft depth in a well (see Swain, 1951), × 112, USNM 560640. *f. Bensonocythere* sp. M, male left valve, "Yorktown" Formation near Yadkin, Va., sample 31 of Hazel (1971a), USGS 24905, × 128, USNM 172495.

cated on their cross sections. On the basis of the illustrations in Swain (1968, 1974), Swain's concept of *Aurila conradi* includes both *Malzella conradi* and *M. evexa*, thus indicating in the Virginia and North Carolina region a Pliocene to early Pleistocene age (fig. 3). *Trachyleberis exanthemata* (Ulrich and Bassler) is the type species of the genus *Actinocythereis* Puri, 1953, and is restricted to rocks of lower and middle Miocene age. On the basis of identification by Swain (1968; 1974), the specimens usually identified as *Trachyleberis exanthemata* in Brown and others (1972) represent the species *Actinocythereis captionis* Hazel, which has a Pliocene to Holocene range (fig. 3). Therefore the "Late Miocene unit," if determined by the presence of

Malzella conradi of Swain (1968, 1974) and *Actinocythereis exanthemata* of Swain (1968, 1974), could be early Pliocene to possibly early Pleistocene age.

Swain (1974) studied ostracodes from the Yorktown Formation from various localities in Virginia and North Carolina and again discussed his *Aurila conradi-Thaerocythere schmidtae* assemblage. He considered the Yorktown Formation to be of late Miocene age; however, it should be pointed out that most of his samples were from his "lower Yorktown," and some of these are actually from the underlying St. Marys Formation (as that term has been used in Virginia) of late Miocene age. Specifically, samples from Swain's "lower Yorktown" localities 5, 6, 7, 9, 10, and 11 may be partly or entirely from the St. Marys Formation.

Swain (1974) also assigned the beds at Colerain Landing and near Mt. Gould Landing on the Chowan River to the Pliocene(?). Hazel (1971a) assigned these same beds to the Pliocene and placed them in the *Puriana mesacostalis* assemblage zone (now considered to be of late Pliocene and early Pleistocene age; see fig. 2).

CONCLUSIONS

The ostracode stratigraphic distributional data presented above permit the following conclusions:

1. Several ostracode species (see fig. 3) are characteristic of and restricted to Pliocene to lower Pleistocene deposits of the Atlantic Coastal Plain and Florida and allow easy recognition of this interval in the Virginia and northern North Carolina region.
2. The chronozone of the *Puriana mesacostalis* assemblage zone of Hazel (1971a) can be recognized both by range zones and concurrent range zones. The chronozone of the lower part (upper Pliocene) of this assemblage zone can be recognized by concurrent range zones. The chronozone of the upper part (lower Pleistocene) of the *Puriana mesacostalis* assemblage zone cannot at present be recognized by concurrent range zones, but the range zone of *Caudites asymmetricus* seems diagnostic.
3. The chronozone of the *Orionina vaughani* assemblage zone can be easily recognized by concurrent range zones based on the ranges of many species.
4. The overlap of several species in the lower part of the *Orionina vaughani* assemblage zone or correlative rocks suggest that this interval is recognizable by several different concurrent range zones.
5. At present, the *Pterygocythereis inexpectata* assemblage zone can only be recognized by its characteristic assemblage (Hazel, 1971a).

Figures 5—10 follow "References Cited."

REFERENCES CITED

Akers, W. H., 1972, Planktonic Foraminifera and biostratigraphy of some Neogene formations, northern Florida and Atlantic Coastal Plain: Tulane Studies Geology and Paleontology, v. 9, no. 1–4, 139 p.

——— 1973, Age of some Neogene formations, Atlantic Coastal Plains, United States and Mexico, *in* Smith, L. A., and Hardenbol, Jan, eds., Symposium on calcareous nannofossils, Proceedings: Houston, Tex., Soc. Econ. Paleontologists and Mineralogists, Gulf Coast Sec., p. 80–84.

Berggren, W. A., and Van Couvering, J. A., 1974, The late Neogene: Biostratigraphy, geochronology, and paleoclimatology of the last 15 million years in marine and continental sequences: Paleogeography, Paleoclimatology, and Paleoecology, v. 16, no. 1/2, p. 1–216.

Brown, P. M., 1958, Well logs from the Coastal Plain of North Carolina: North Carolina Div. Mineral Resources Bull. 72, 68 p.

Brown, P. M., Miller, J. A., and Swain, F. M., 1972, Structural and stratigraphic framework, and spatial distribution of permeability of the Atlantic Coastal Plain, North Carolina to New York: U.S. Geol. Survey Prof. Paper 796, 79 p.

DuBar, J. R., Johnson H. S., Jr., Thom, Bruce, and Hatchell, W. O., 1974a, Neogene stratigraphy and morphology, south flank of the Cape Fear arch, North and South Carolina, *in* Oaks, R. Q., Jr., and DuBar, J. R., eds., Post-Miocene stratigraphy, central and southern Atlantic Coastal Plain: Logan, Utah, Utah State Univ. Press, p. 139–173.

DuBar, J. R., Solliday, J. R., and Howard, J. F., 1974b, Stratigraphy and morphology of Neogene deposits, Neuse River estuary, North Carolina, *in* Oaks, R. Q., Jr., and DuBar, J. R., eds., Post-Miocene stratigraphy, central and southern Atlantic Coastal Plain: Logan, Utah, Utah State Univ. Press, p. 102–122.

Edwards, R. A., 1944, Ostracoda from the Duplin Marl (upper Miocene) of North Carolina: Jour. Paleontology, v. 18, no. 6, p. 505–528.

Hazel, J. E., 1970, Binary coefficients and clustering in biostratigraphy: Geol. Soc. America Bull., v. 81, no. 11, p. 3237–3252.

——— 1971a, Ostracode biostratigraphy of the Yorktown Formation (upper Miocene and lower Pliocene) of Virginia and North Carolina: U.S. Geol. Survey Prof. Paper 704, 13 p.

——— 1971b, Paleoclimatology of the Yorktown Formation (upper Miocene and lower Pliocene) of Virgina and North Carolina, *in* Oertli, H. J., ed., Colloque sur la paleoecologie des ostracodes, Pau, July 20–27, 1970: Centre Recherches Pau-SNPA, Bull., v. 5 (Supp.), p. 361–375.

——— in press, Age and correlation of the Yorktown (Pliocene) and Croatan (Pliocene and Pleistocene) Formations at the Lee Creek, North Carolina, open pit mine: Smithsonian Contr. Paleobiology.

Malkin, D. S., 1953, Biostratigraphic study of Miocene Ostracoda of New Jersey, Maryland, and Virginia: Jour. Paleontology, v. 27 no. 6, p. 761–799.

McLean, J. D., Jr., 1957, The Ostracoda of the Yorktown Formation in the York-James Peninsula of Virginia: Bulls. Am. Paleontology, v. 38, no. 167, p. 57–103.

——— 1966, Miocene and Pleistocene Foraminifera and Ostracoda of southeastern Virginia—Pt. 1, Text; Pt. 2, Taxonomy and fossil plates: Virginia Div. Mineral Resources Rept. Inv. 9, Pt. 1, 79 p.; Pt. 2, 123 p.

Olsson, A. A., and Petit, R. E., 1964, Some Neogene Mollusca from Florida and the Carolinas: Bulls. Am. Paleontology, v. 47, no. 217, p. 509–574.

Plusquellec, P. L., and Sandberg, P. A., 1969, Some genera of the ostracode subfamily Campylocytherinae: Micropaleontology, v. 15, no. 4, p. 427–480.

Pooser, W. K., 1965, Biostratigraphy of Cenozoic Ostracoda from South Carolina: Kansas Univ. Paleont. Contr. [38], Arthropoda 8, 80 p.

Puri, H. S., 1953, Contributions to the study of the Miocene of the Florida panhandle; Part 3, Ostracoda: Florida Geol. Survey Bull. 36, p. 217–345 [1954].

Puri, H. S., and Vanstrum, V. V., 1971, Stratigraphy and paleoecology of the late Cenozoic sediments of south Florida, *in* Oertli, H. J., ed., Colloque sur la paleoecologie des ostracodes, Pau, July 20–27, 1970: Centre Recherches Pau-SNPA, Bull., v. 5 (Supp.), p. 433–448.

Puri, H. S., and Vernon, R. O., 1964, Summary of the geology of Florida and a guidebook to the classic exposures: Florida Geol. Survey Spec. Pub. 5, 312 p.

Swain, F. M., 1951, Ostracoda from wells in North Carolina; Pt. 1, Cenozoic Ostracoda: U.S. Geol. Survey Paper 234–A, 58 p.

——— 1968, Ostracoda from the upper Tertiary Waccamaw Formation of North Carolina and South Carolina: U.S. Geol. Survey Prof. Paper 573–D, 37 p.

——— 1974, Some upper Miocene and Pliocene(?) Ostracoda of Atlantic Coastal region for use in hydrogeologic studies: U.S. Geol. Survey Prof. Paper 821, 50 p.

Ulrich, E. O., and Bassler, R. S., 1904, Systematic paleontology, Miocene Arthropoda: Maryland Geol. Survey, Miocene [volume], p. 98–130.

Figures 5 and 6 are on pages 382 and 383.

FIGURE 5.—*Microcytherura* and *Cytheridea*.

a. Microcytherura similis (Malkin, 1953), male left valve, Yorktown Formation, Nansemond County, Va., sample 32 of Hazel (1971a), USGS 24622, × 129, USNM 191483. *b. Microcytherura minuta* Hazel, female left valve, Yorktown Formation, Williamsburg, Va., sample 45 of Hazel (1971a), × 152, USNM 172750. *c. Microcytherura expanda* Hazel, female? left valve, "Yorktown" Formation, near Mt. Gould, N.C., sample 20 of Hazel (1971a). USGS 24897, × 119, USNM 191482. *d. Microcytherura choctawhatcheensis* (Puri, 1954), male left valve, Waccamaw Formation, pit near Old Dock, N.C., USGS 25445, × 132, USNM 191498. *e. Cytheridea carolinensis* Hazel, female left valve, Croatan Formation, sample 15 of Hazel (in press), USGS 25378, × 108, USNM 191357. *f. Cytheridea campwallacensis* Hazel, female right valve, Yorktown Formation, sample Va. -7 of Malkin (1953; pl. 7, fig. 29), James City County, Va., × 84, USNM 191506. *g. Cytheridea virginiensis* (Malkin, 1953), female left valve, Yorktown Formation, Greenville County, Va., USGS 24830, sample 27 of Hazel (1971a), × 94, USNM 172579. *h. Cytheridea* aff. *C. virginiensis* (Malkin, 1953) female left valve, Yorktown Formation, Beaufort County, N.C., sample 5 of Hazel (1971a), USGS 24883, × 82, USNM 172518.

FIGURE 6.—*Radimella, Aurila, Malzella, Thaerocythere, Cytheropteron*?, and *Hermanites*

a. Radimella confragosa (Edwards, 1944), female carapace, Croatan Formation, Beaufort County, N.C., sample 8 of Hazel (1971a), USGS 24886, × 113, USNM 172675. *b.* Aurila sp. B, male left valve, Yorktown Formation, Petersburg, Va., sample 38 of Hazel (1971a), USGS 24909, × 132, USNM 167405. *c. Malzella conradi* (Howe and McGuirt, 1935), female left valve, angulate form, Yorktown Formation at Williamsburg, Va., sample 44 of Hazel (1971a), USGS 24820, × 103, USNM 167407. *d. Malzella evexa* Hazel, female left valve, "Yorktown" Formation near Mt. Gould Landing, N.C., sample 20 of Hazel (1971a), USGS 24897, × 97, USNM 172653. *e. Thaerocythere schmidtae* (Malkin, 1953), male left valve, Yorktown Formation at Colerain Landing, N.C., sample 14 of Hazel (1971a), USGS 24891, × 110 USNM 172657. *f. Thaerocythere carolinensis* Hazel, male left valve, "Yorktown" Formation near Mt. Gould Landing, N.C., sample 16 of Hazel (1971a), USGS 24893, × 110, USNM 172658. *g. Cytheropteron? yorktownensis* (Malkin, 1953), female left valve. Yorktown Formation at Suffolk, Va., sample of Hazel (1971a), USGS 24814, × 185, USNM 190980. *h. Hermanites ascitus* Hazel, female left value, Duplin Formation, left bank of Lumber River near Lumberton, N.C., USGS 25751, × 125, USNM 172745.

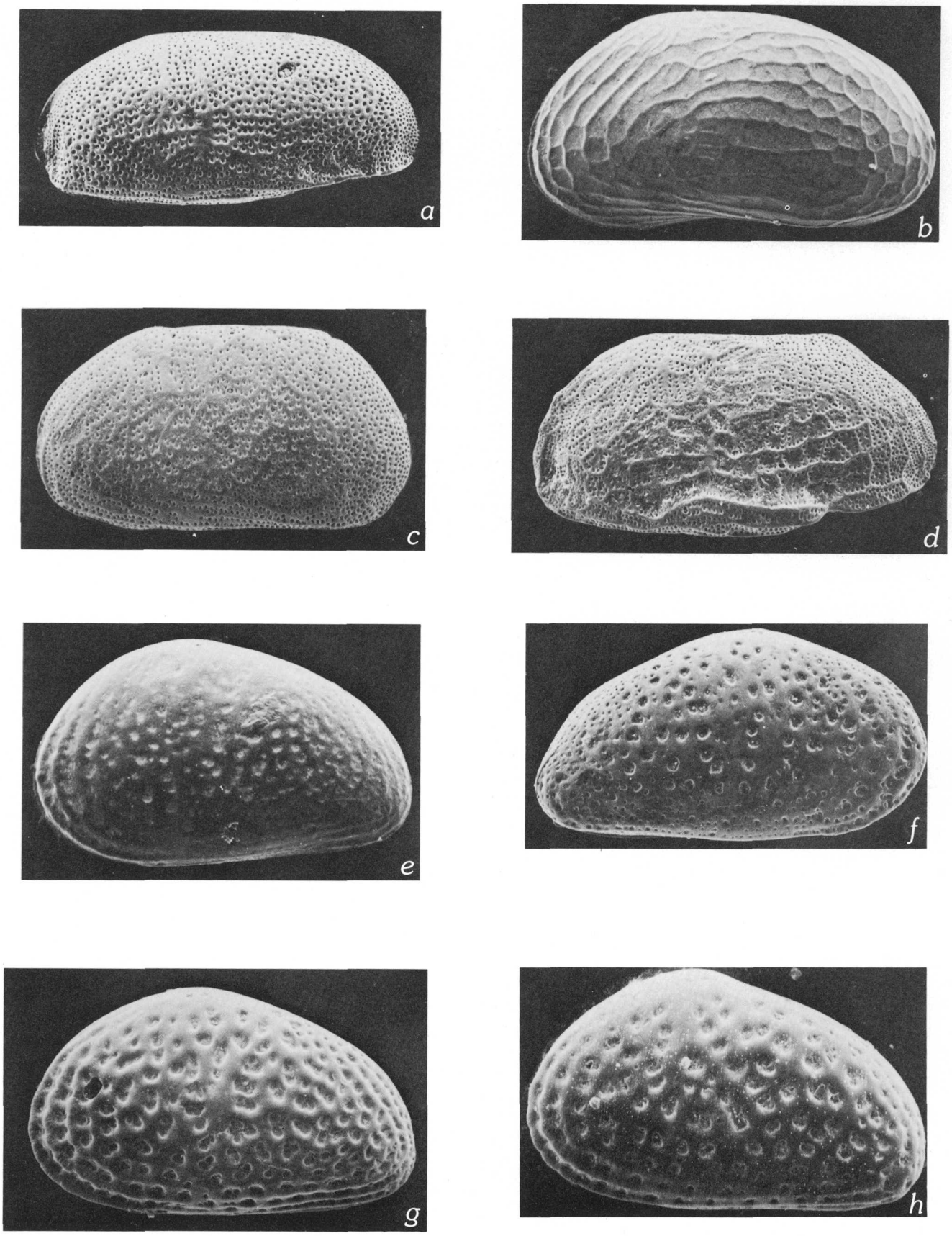

FIGURE 5

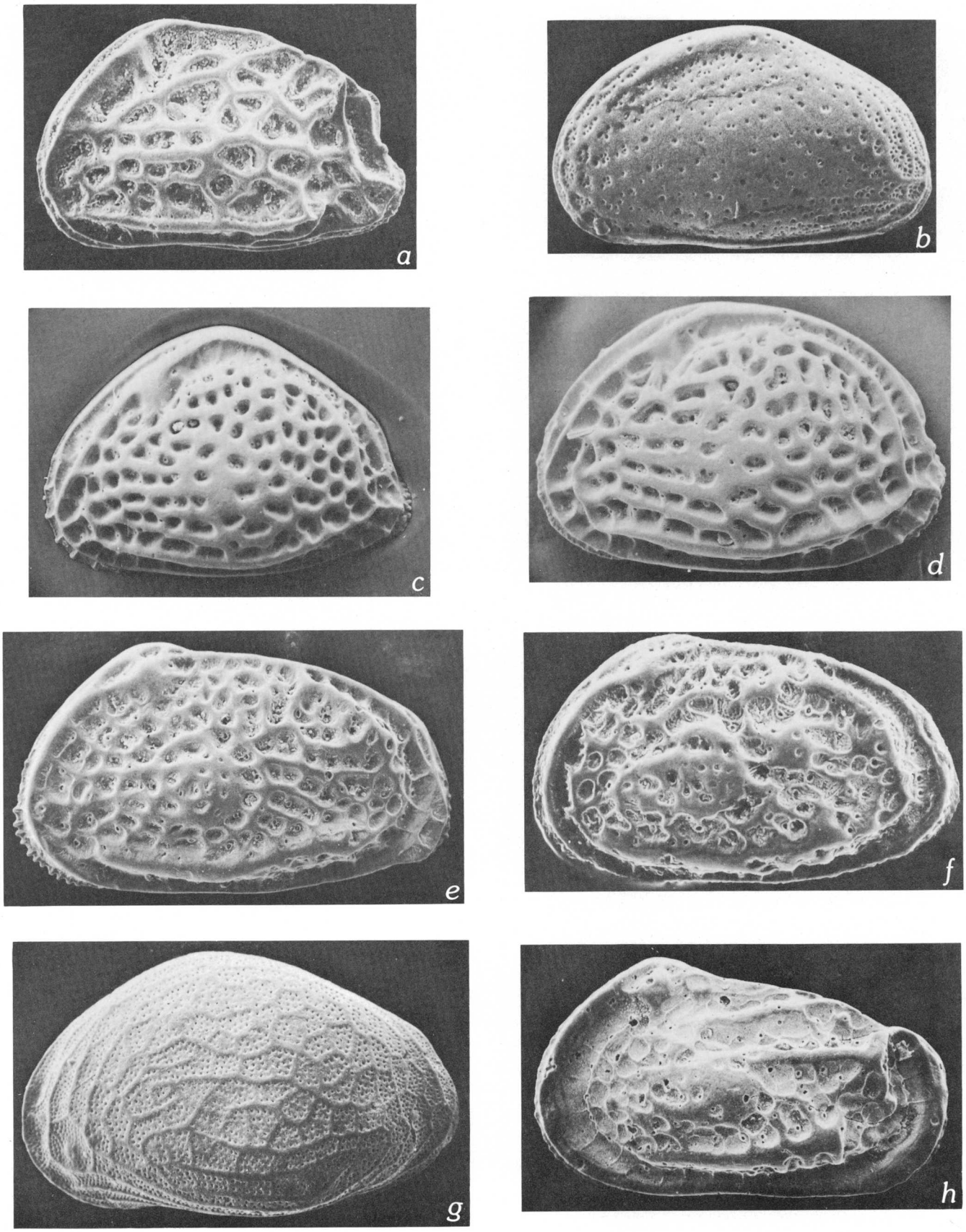

FIGURE 6

Figures 7–10 are on pages 385–388.

FIGURE 7.—*Paracytheridea, Palaciosa, Neocaudites, Caudites, Pterygocythereis,* and *Peratocytheridea.*

a. Paracytheridea edwardsi Hazel, female left valve, type locality of the Duplin Formation (loc. 1 of Edwards, 1944), near Magnolia, N.C., USGS 23639, × 118, USNM 172759. *b. Paracytheridea mucra* Edwards, 1944, female left valve, Yorktown Formation, Suffolk, Va., sample 29 of Hazel (1971a), USGS 24814, × 107, USNM 172758. *c. Palaciosa minuta* (Edwards, 1944), male left valve, Croatan Formation, right bank of Neuse River near James City, N.C., USGS 25444, × 120, USNM 167401. *d. Neocaudites triplistriatus* (Edwards, 1944), female carapace, from type locality of Duplin Formation near Magnolia, N.C., locality 1 of Edwards (1944), USGS 23639, × 143, USNM 172753. *e. Paracytheridea rugosa* Edwards, 1944, female left valve, "Yorktown" Formation, near Mt. Gould, N.C., sample 20 of Hazel (1971a), USGS 24897, × 117, USNM 191497. *f. Caudites asymmetricus* Hazel, female carapace, Croatan Formation, sample 15 of Hazel (in press), USGS 25378, × 117, USNM 172756. *g. Pterygocythereis inexpectata* (Blake, 1929), female left valve, Yorktown Formation, Beaufort County, N.C., sample 5 of Hazel (1971a), USGS 24883, × 69, USNM 172748. *h. Peratocytheridea sandbergi* Hazel, female left valve, Yorktown Formation, sample 3 of Hazel (1971a), USGS 24881, × 91, USNM 172663.

FIGURE 8.—*Orionina, Puriana, Actinocythereis,* and *Murrayina.*

a. Orionina vaughani (Ulrich and Bassler, 1904), male left valve, Yorktown Formation at Williamsburg, Va., sample 43 of Hazel (1971a), USGS 24821, × 82, USNM 172477. *b. Puriana carolinensis* Hazel, female right valve, "Yorktown" Formation, near Mt. Gould, N.C., sample 20 of Hazel (1971a), USGS 24897, × 112, USNM 172649. *c. Actinocythereis captionis* Hazel, male left valve, "Yorktown" Formation, near Mt. Gould Landing, N.C., sample 19 of Hazel (1971a), USGS 24896, ×96, USNM 191593. *d. Puriana mesacostalis* (Edwards, 1944), female left valve, "Yorktown" Formation, near Mt. Gould, N.C., sample 20 of Hazel (1971a), USGS 24897, × 115, USNM 172668. *e. Murrayina barclayi* McLean, 1957, female left valve, Yorktown Formation at Petersburg, Va., sample 38 of Hazel (1971a), USGS 240908, × 90, USNM 172755. *f. Puriana convoluta* Teeter, 1975, male left valve. Waccamaw Formation, Old Dock, N.C. USGS 25445, × 134, USNM 191479. *g. Actinocythereis dawsoni* (Brady, 1870), female left value, Yorktown Formation, James City County, Va., sample 42 of Hazel (1971a), USGS 24912, × 90, USNM 190458. *h. Actinocythereis mundorffi* (Swain, 1951), female left valve, Yorktown Formation, James City County, Va., sample 42 of Hazel (1971a), USGS 24912, × 88, USNM 190457.

FIGURE 9.—*Cytheromorpha, Campylocythere, Loxoconcha,* and *Bensonocythere.*

a. Cytheromorpha incisa Hazel, female left valve, "Yorktown" Formation near Mt. Gould Landing, N.C., sample 18 of Hazel (1971a), USGS 24895, × 143, USNM 172560. *b. Campylocythere laeva* Edwards, 1944 female left valve, Waccamaw Formation, Neills Eddy Landing on the Cape Fear River, N.C., locality 41 of Plusquellec and Sandberg (1969), × 79, USNM 651159. *c. Cytheromorpha macroincisa* Hazel, female left valve, "Yorktown" Formation, near Mt. Gould Landing, N.C., sample 18 of Hazel (1971a), USGS 24895, × 122, USNM 172562. *d. Cytheromorpha suffolkensis* Hazel, female left valve, Yorktown Formation, Suffolk, Va., sample 29 of Hazel (1971a), USGS 24814, × 149, USNM 172551. *e. Loxoconcha* sp. U, female left valve, Yorktown Formation, Assateague Island Accomack County, Va., 80 feet below sea level in power auger hole one-half mile southwest of the bridge over Sheepshead Creek, USGS 25455, × 150, USNM 190966. *f. Loxoconcha edentonensis* (Swain, 1951), female left valve, "Yorktown" Formation, near Mt. Gould Landing, N.C., sample 19 of Hazel (1971a), USGS 24896, × 126, USNM 172603. *g. Bensonocythere bradyi* Hazel, male right valve, "Yorktown" Formation, near Mt. Gould Landing, N.C., sample 16 of Hazel (1971a), USGS 24894, × 95, USNM 167380. *h. Loxoconcha* sp. A, female left valve, Yorktown Formation, Nansemond County, Va., sample 32 of Hazel (1971a), USGS 24622, × 163, USNM 172601.

FIGURE 10.—*Muellerina, "Pontocythere," Bensonocythere,* and *Echinocythereis*

a. Muellerina wardi Hazel, female left valve, "Yorktown" Formation near Mt. Gould Landing, N.C., sample 20 of Hazel (1971a), USGS 24897, × 102, USNM 1674089. *b. Muellerina canadensis petersburgensis* Hazel, female left valve, Yorktown Formation at Petersburg, Va., sample 38 of Hazel (1971a), × 108, USNM 167408. *c. Muellerina blowi* Hazel, female left valve, Yorktown Formation, at Suffolk, Va., sample 29 of Hazel (1971a), USGS 24814, × 102, USNM 167411. *d. Muellerina bassiounii* Hazel, female left valve, Croatan Formation at its type locality near James City, N.C., × 108, USNM 167410. *e. "Pontocythere"* sp. I, male left valve, Yorktown Formation, Halifax, N.C., sample 24 of Hazel (1971a), USGS 24901, × 87, USNM 172524. *f. Bensocythere trapezoidalis* (Swain, 1974), male left valve, Yorktown Formation, near Palmyra, N.C., sample 11 of Hazel (1971a), USGS 24889, × 118, USNM 167395. *g. Echinocythereis planibasalis* (Ulrich and Bassler, 1904), male left valve, Yorktown Formation near Jamestown, Va., sample 41 of Hazel (1971a), USGS 24717, × 73, USNM 172754. *h. Echinocythereis leecreekensis* Hazel, female left valve, Croatan Formation, Beaufort County, N.C., sample 10 of Hazel (in press), USGS 25359, × 73, USNM 191510.

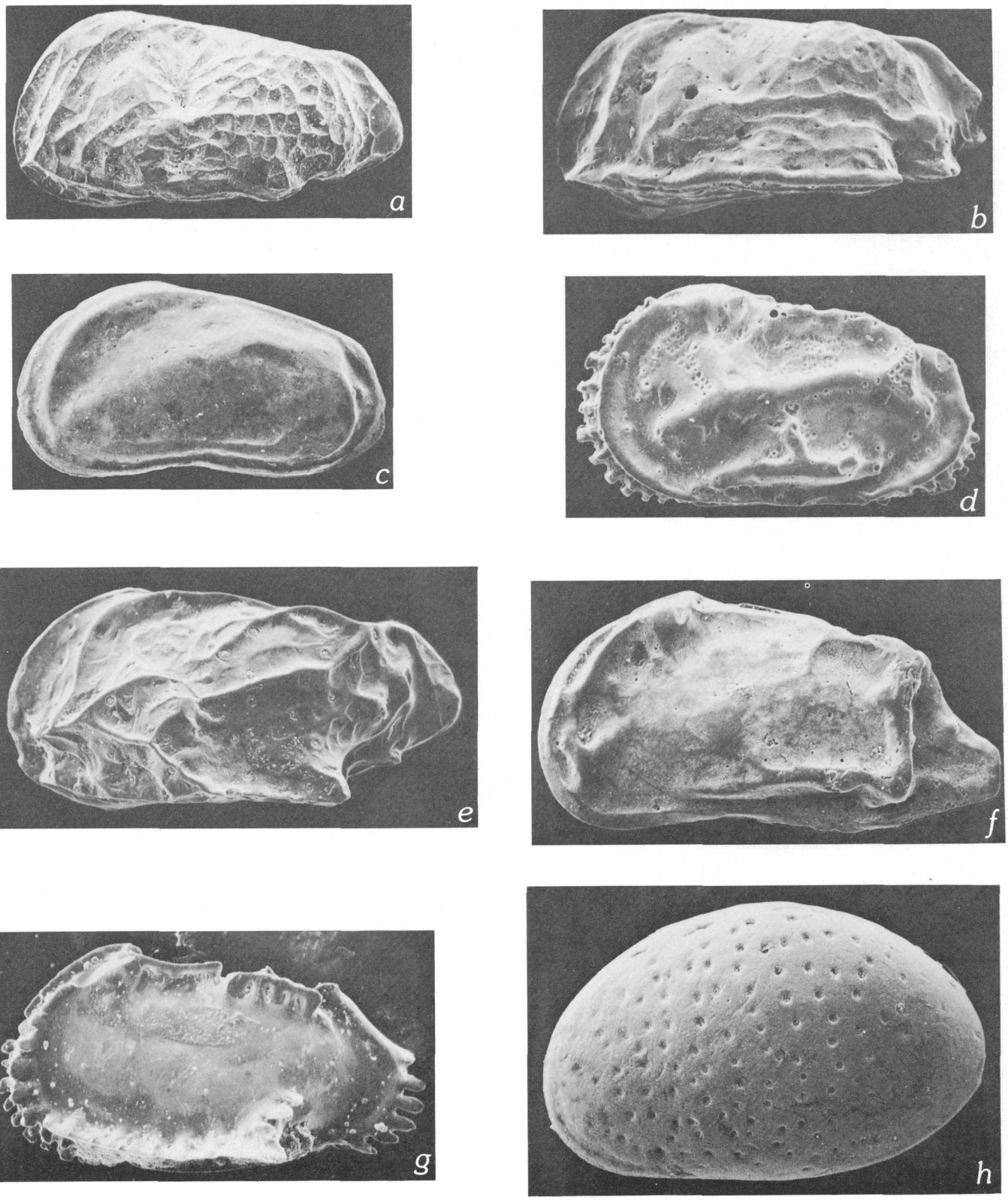

FIGURE 7

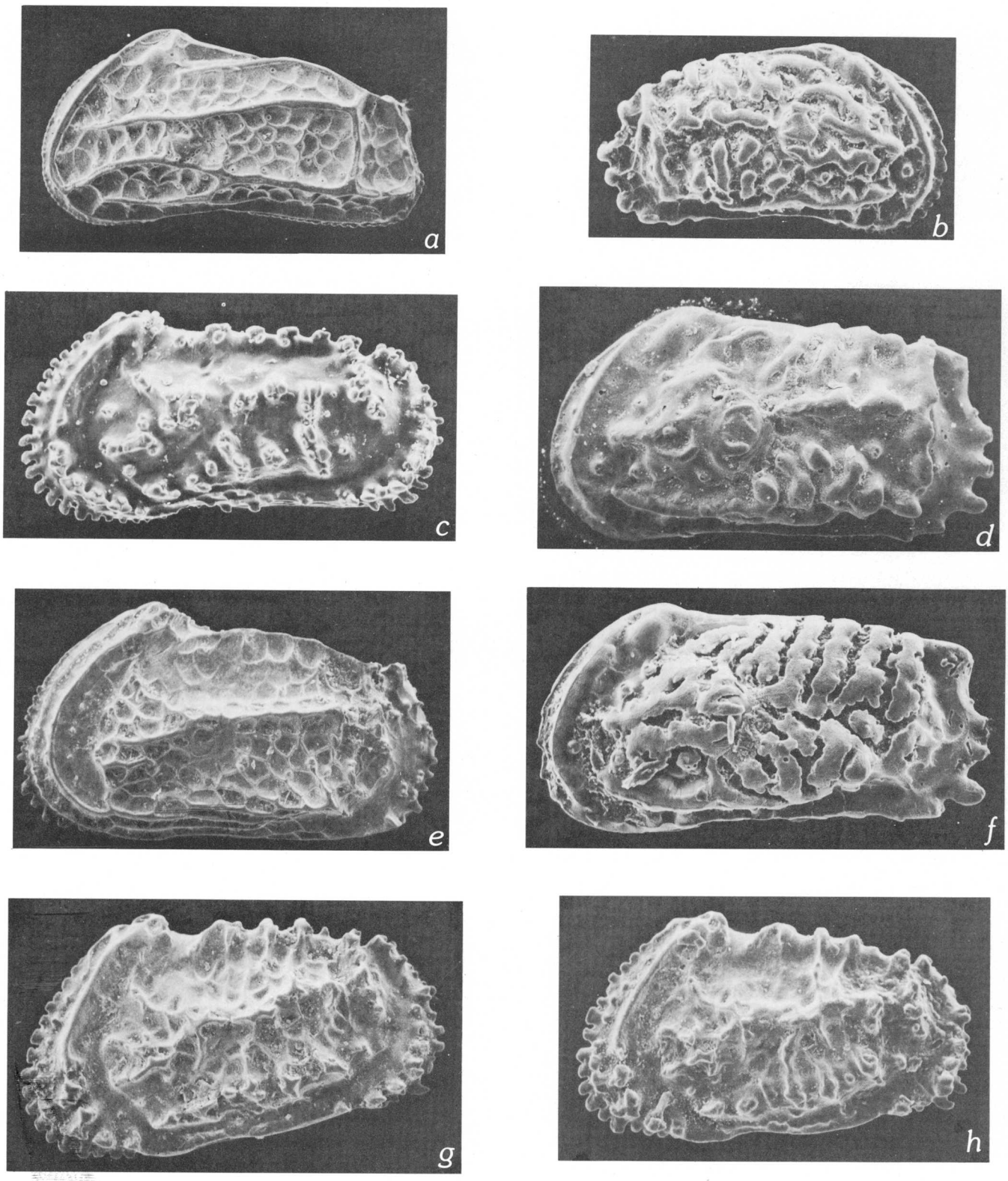

FIGURE 8

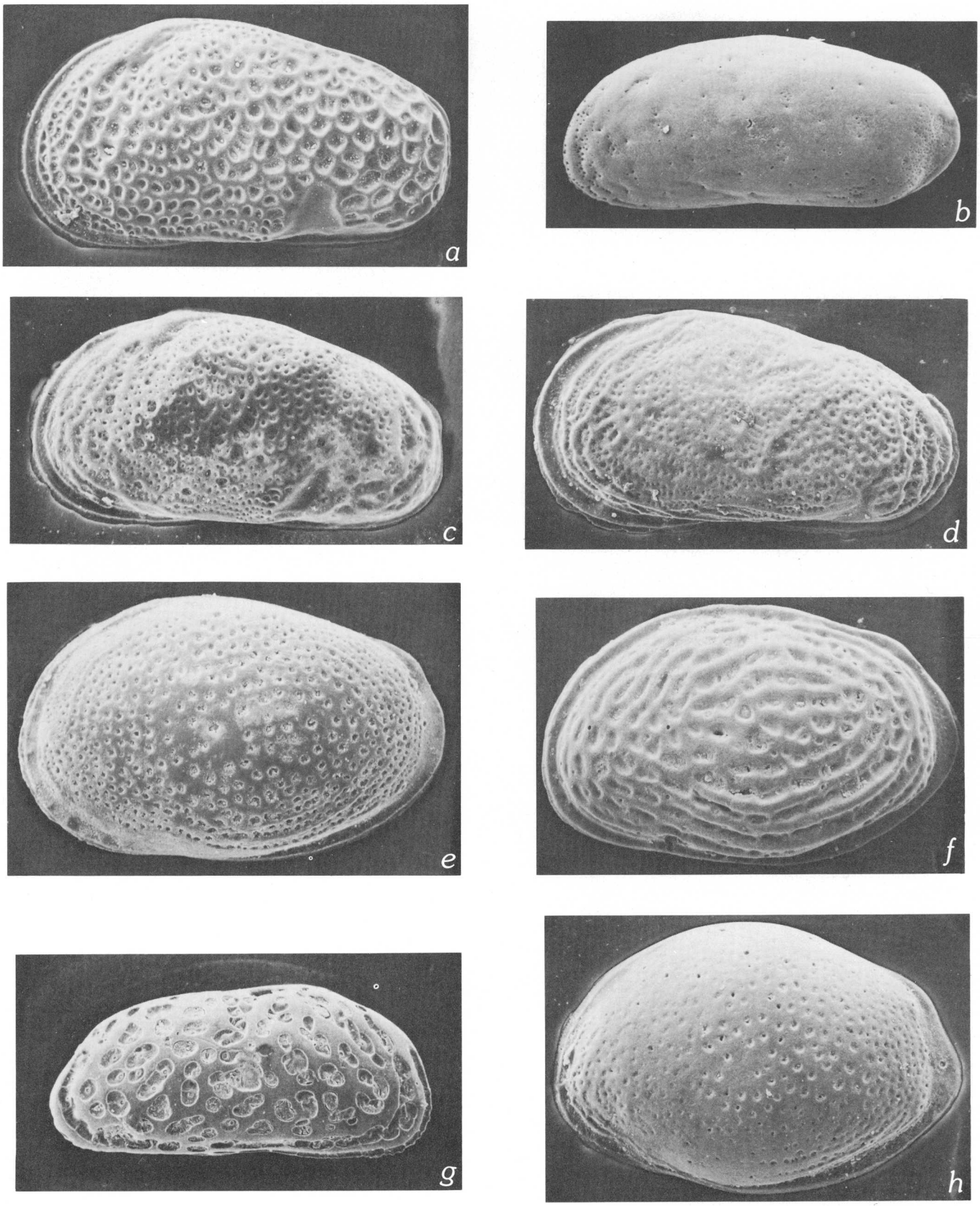

FIGURE 9

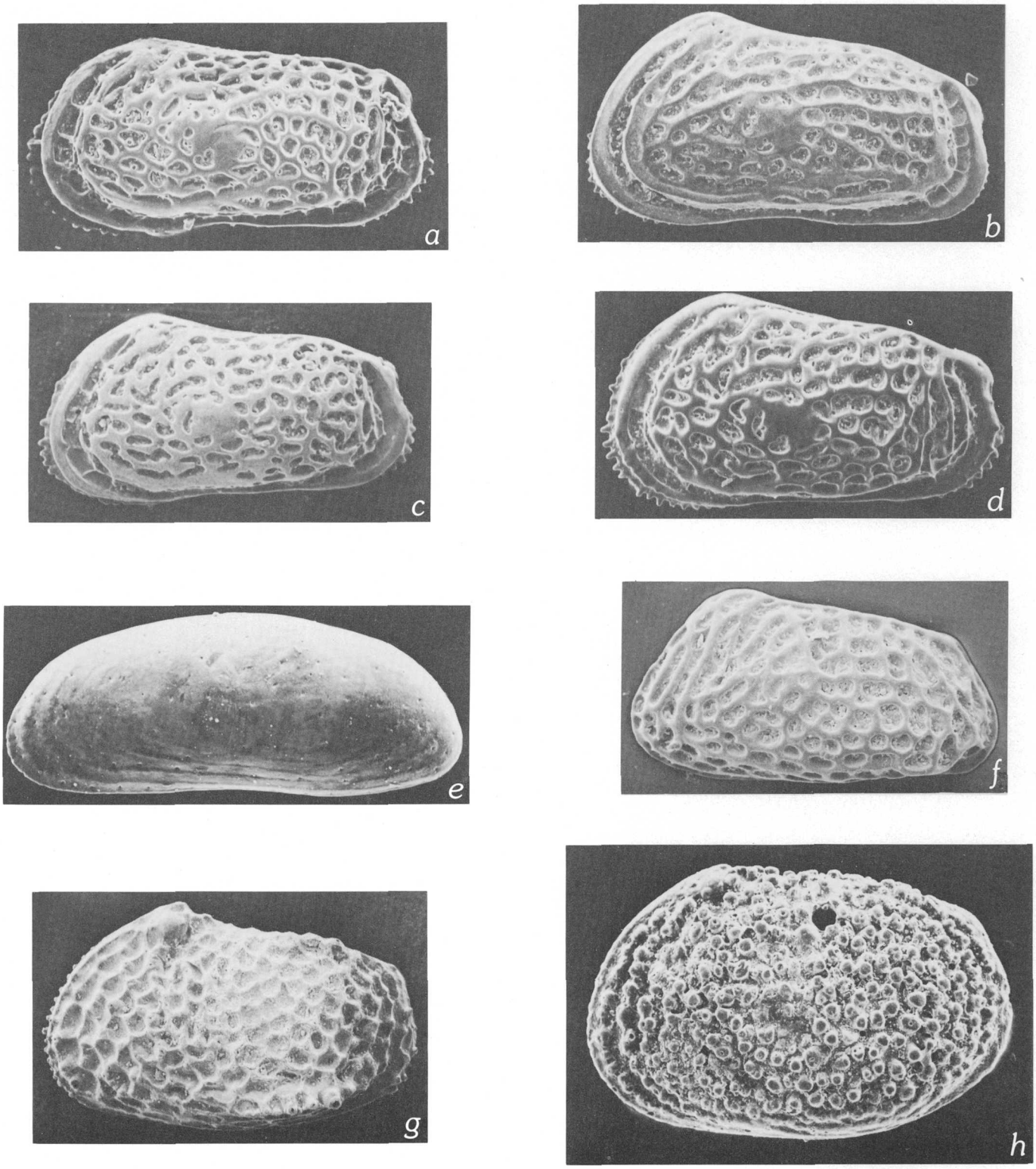

FIGURE 10

Jour. Research U.S. Geol. Survey
Vol. 5, No. 3, May–June 1977, p. 389–395

A NEW METHOD FOR DETERMINING THE SOLUBILITY OF SALTS IN AQUEOUS SOLUTIONS AT ELEVATED TEMPERATURES

By Robert W. Potter II, R. Scott Babcock,[1] and David L. Brown,
Menlo Park, Calif., Bellingham, Wash., Menlo Park, Calif.

Abstract.—A new method for measuring the solubility of simple salts in water at elevated temperatures involves heating assemblages of salt crystals plus solution vapor at a constant rate in a platinum-lined bomb. The dissolution of the last salt crystal is evidenced by a distinct discontinuity in the pressure-temperature curve. Studies of the solubilities of NaCl and of KCl in water yielded equations expressing the solubility as functions of temperature, t in °C, at the vapor pressure of the solutions as follows:

$$\text{weight percent NaCl} = 26.218 + 0.0072\,t + 0.000106\,t^2 \pm 0.05 \text{ weight percent NaCl}$$

$$\text{weight percent KCl} = 27.839 + 0.0794\,t + 0.000027\,t^2 \pm 0.10 \text{ weight percent KCl}$$

The NaCl and KCl data were measured over the temperature range 148° to 425°C and 148° to 371°C, respectively. However, the equation for NaCl appears to be valid over the range 0° to 800°C, and the KCl equation appears valid over the range 100° to 450°C.

Sodium chloride and potassium chloride are the dominant dissolved salts in many natural hydrothermal systems. Experimental studies of the solubilities of these salts in water, as functions of temperature, are fundamental to understanding the complex chemical and physical relationships involved in the formation of ore deposits and water-rock reactions in general at high temperature. Such solubility data are also useful for understanding the formation of the first fluid phase in a vapor-dominated geothermal system and aid in the interpretation of fluid inclusion data.

The available solubility data have been summarized by Stephen and Stephen (1963) and Linke (1965), who also presented an evaluated compilation of graphically smoothed solubilities. These smothed data generally do not exceed temperatures of 450°C, although solubilities of salts in aqueous solutions have been determined at temperatures as high as 650°C (Keevil, 1942). Also, these solubility data generally have a scatter of ±0.1 weight percent salt below 100°C and ±0.3 weight percent salt above 100°C. Ideally, for computer modeling of the complex chemistry of hydrothermal and geothermal systems, the solubility measurements should have a precision of at least ±0.01 to ±0.1 weight percent salt. Therefore, a new experimental method was sought that could provide solubility data with the required precision. This paper describes the method that was adopted.

SUMMARY OF PREVIOUS METHODS

There are three major categories of experimental techniques for determining the solubility of a salt in an aqueous solution as a function of temperature: quench methods, visual methods, and the so-called indirect methods. Quench methods involve separating a representative sample of the saturated solution from the salt crystals at temperature, quickly cooling the separated solution to room temperature, and finally analyzing its salt content. Studies employing the visual method involve viewing a mixture of solution plus salt crystals plus vapor of known bulk composition as temperature is increased slowly until the last salt crystal dissolves. Solubility is determined with the indirect methods by utilizing changes in the intensive properties of a system of salt crystals plus saturated solution plus vapor of known bulk composition to detect the dissolution of the last salt crystal.

The best example of an investigation of the solubility of salts in water employing the quench method is the classic study of the Earl of Berkley (1904) on the solubility of 19 different salts from 0°C up to their respective boiling points. The paper very adequately summarizes all of the difficulties that arise with the quench method as well as some aspects of other methods: density stratification, super saturation, analytical problems, precipitation on quench, and the criteria for establishing equilibrium. Although the technique employed by the Earl of Berkley (1904) was

[1] Department of Geology, Western Washington State College, Bellingham, Wash.

fairly precise, it is limited to temperatures below 250°C even after it is improved with modern technology. In order to obtain solubility data at higher temperatures, much more elaborate methods are required.

The most reliable quenching method developed to date for higher temperatures is the bomb-in-bomb method of Schroeder and others (1935). An empty bomb is sealed in a bomb filled with salt crystals plus solution in such a way that the inner bomb can be opened and closed. The whole assembly is heated in an air bath while being rotated around an axis parallel to the short dimension of the bomb. After the solution and salt have equilibrated, the rotation is stopped with the bomb in a vertical position and the salt is allowed to settle to the bottom of the bomb. The inner bomb is then opened, filled with solution, sealed, and then rapidly quenched. Unfortunately, a series of flexible gaskets is required in the valve system of the inner bomb, and hence the attainable upper temperature limit was 300° to 350°C. Through the use of more modern gasket materials this range could at best be extended to about 400°C.

Benrath and others (1937) have measured the solubility of 32 salts in water at temperatures above 100°C by the visual method. The major limiting factors are: visibility during heating, density stratification, and the effect of devitrification on the ultimate strength of the glass. Solubility data were obtained at temperatures as high as 455°C using heavy-walled silica tubes. Generally, the precision obtained with the method was best at temperatures below 200°C.

The geologic community has been using the data of Keevil (1942) for the solubility of NaCl in water at elevated temperatures. These data were obtained using one of the indirect methods. The method consisted of measuring pressure as a function of the volume of a known bulk composition at constant temperature. The dissolution of the last salt crystal was detected from discontinuities in the pressure-volume curves. The accuracy of the temperature of dissolution was dependent on how closely spaced the isotherms were for the pressure-volume measurement. Solubility data were obtained from 180° to 650°C along with vapor-pressure data.

Other than the tightness of the brackets (which are not given in Keevil, 1942), the major drawback of the method is that the salt crystals plus solution plus vapor were always in equilibrium with mercury at elevated temperatures. Mercury was the medium employed to change the volume of the experimental system. The effect of mercury on the experiment, except for a vapor-pressure correction, was not evaluated.

Another indirect method used for solubility measurements is to measure vapor pressure of the solution as a function of the composition at constant temperature. The composition at which the pressure-composition curve becomes constant is taken as the solubility of the salt at the temperature of the measurement. The limiting factor with respect to the accuracy of the solubility is how closely spaced are the compositions used in the pressure measurements. This method was employed by Liu and Lindsay (1971) to measure the solubility of NaCl in water up to 300°C.

EXPERIMENTAL METHOD

As an assemblage of salt solution plus vapor plus crystals is heated, the pressure is confined to the equilibrium pressure-temperature curve for the assemblage. At the temperature at which the last salt crystal dissolves, the pressure is then confined to the equilibrium pressure-temperature curve defined by the assemblage solution plus vapor. Thus, a discontinuity in the pressure-temperature curve for the system should occur when the last salt crystal dissolves and hence allows the temperature of dissolution to be determined. This phenomenon provides the theoretical basis for the measurement of the solubility of salts in aqueous solutions at elevated temperatures described in this paper.

The experimental configuration used to obtain the pressure-temperature curves is illustrated in figure 1. The apparatus consisted of: a 316-stainless steel bomb with a platinum liner, platinum resistance thermometers, a time-proportioning controller with a variable rate setting, a single-wound electrical-resistance furnace, and a Heise gage that could measure a maximum gage pressure equivalent to about 34 500 kilopascals (5000 psig) and could be read to a precision of about ±10 kPa (±1 psig). The temperature was read using an instrument that digitized the output of the platinum resistance thermometer. The thermometer and measuring circuit were calibrated against standards traceable to the National Bureau of Standards, and temperature could be measured with an accuracy of ±0.1°C.

The following procedure was used to load the bomb for a run: a weighed quantity, ±0.001 g, of salt was placed in the bomb; a weighed amount, ±0.01 g, of distilled water was added; the bomb was immediately sealed, connected to the pressure gage, and placed in the furnace as shown in figure 1. By our following this procedure, the bulk composition in the bomb was known to ±0.02 weight percent salt.

In order to reduce the loss of water to the vapor phase, the bomb (35 cm^3 internal capacity) was loaded such that at the temperature of the run it was about 90 percent full. This was accomplished by using ex-

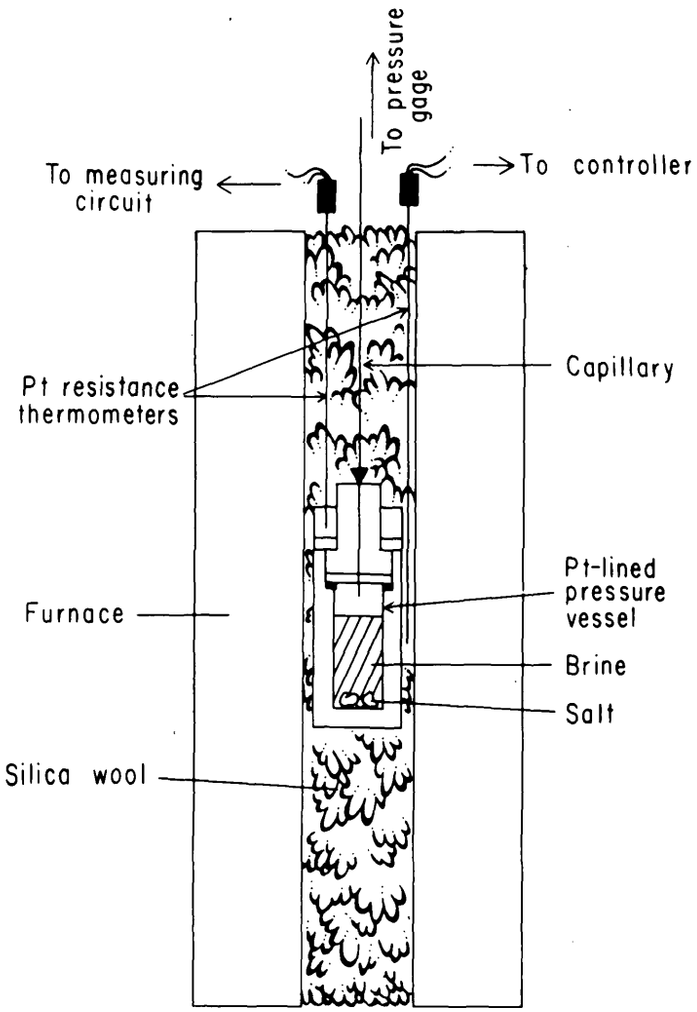

FIGURE 1.—The experimental configuration of the apparatus used to measure the pressure-temperature curves.

trapolations of data on the density of vapor-saturated aqueous salt solutions (Potter and Brown, 1975, 1976). To minimize the loss of water further and to protect the Heise gage, the capillary line ($\cong$0.2 cm^3 internal capacity) leaving the furnace was filled with water. The loaded bomb was heated to a temperature several degrees below that at which the last of the salt crystals was expected to dissolve. Temperature was then held constant for an hour or more to allow equilibration of the water-salt system, and then heating was resumed at a slow constant rate. The temperature and pressure were read simultaneously, approximately every 5 minutes, and plotted on graph paper. When a discontinuity was detected, the heating was continued until the temperature had increased another 10°C at which time the run was terminated. The pressure-temperature data before the break were fit by least-squares regression analysis to an equation, as were the pressure-temperature data after the break. The two equations were solved for their intersection to give the temperature at which the break in slope occurred, that is, the temperature at which the last salt crystal dissolved. Computer fitting was found to be more accurate and reproducible than determining the intersection graphically. The intersections could be determined with a relative uncertainty of ±0.5°C from a computer fit. Figure 2 illustrates some typical pressure-temperature curves with breaks observed in this investigation.

Because of the kinetics of the dissolution of the salt crystals, it is possible that break points could be erroneously determined, particularly if the heating rate significantly exceeded the dissolution rate. In order to evaluate this effect, a series of nine runs with a bulk composition of 29.62±0.02 weight percent NaCl were conducted at various heating rates in three different experimental apparatuses. The results are illustrated in figure 3. There are no significant temperature differences due to heating rates between 0.17°C/min and 0.44°C/min. However, at higher heating rates the ob-

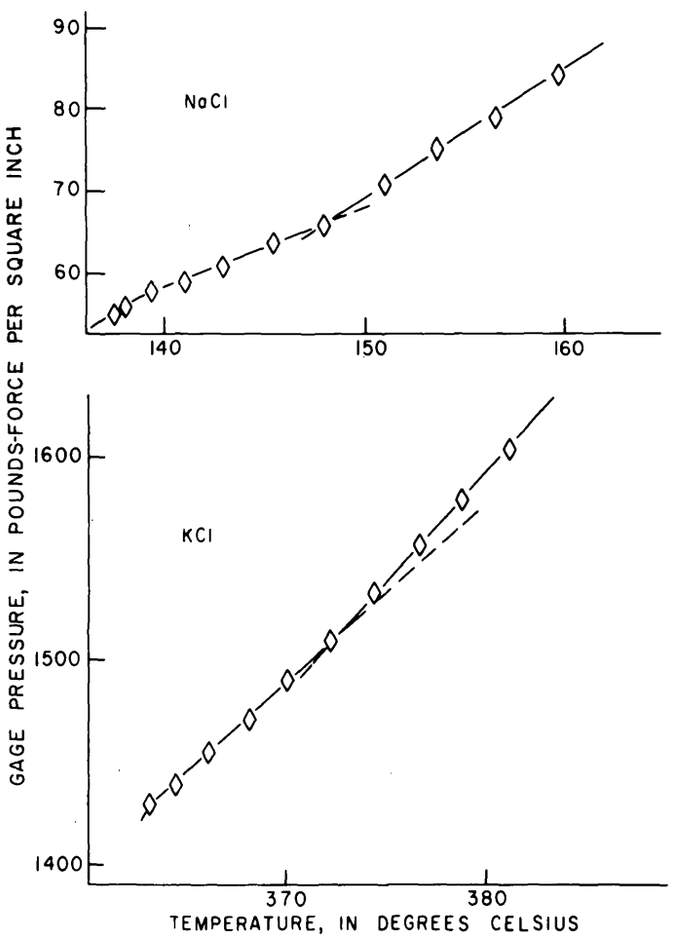

FIGURE 2.—Pressure-temperature curves typical of those found in this investigation (1 lbf/in^2=6.895 kPa).

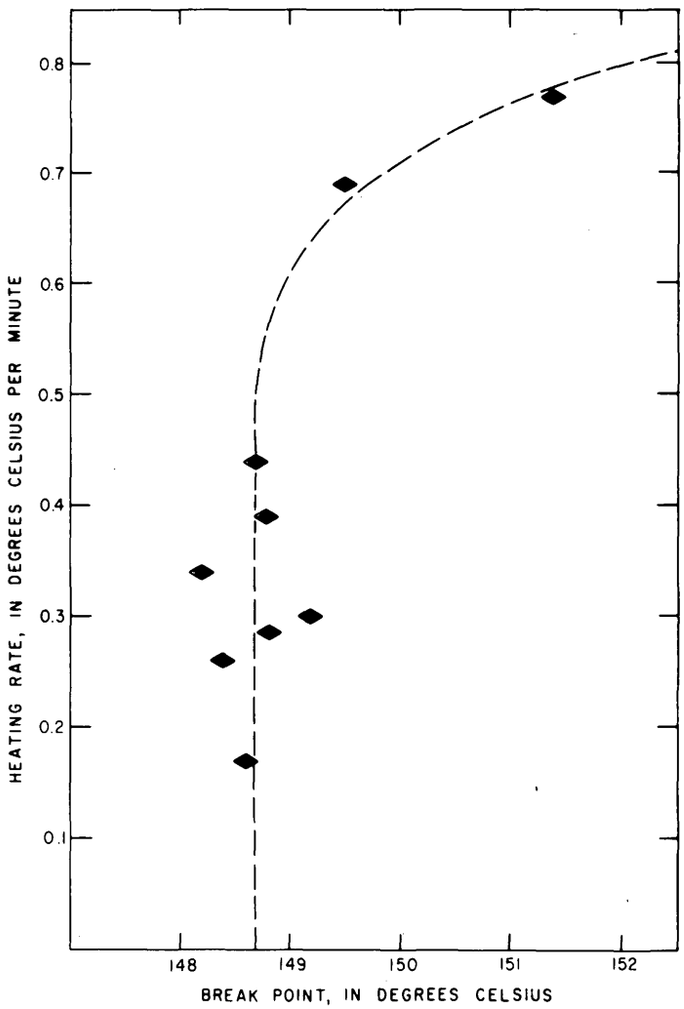

FIGURE 3.—A plot of heating rate versus break point for nine runs with a bulk composition of 29.62±0.02 weight percent NaCl.

served break point generally overshoots the true break point. Therefore, heating rates were kept in the range of 0.2°C/min to 0.4°C/min. On the basis of runs with a heating rate in this range (fig. 3 and table 1), the estimated uncertainty in the determination of the break point is ±0.7°C.

SOLUBILITY OF NaCl IN WATER

Table 1 summarizes the solubility data obtained for NaCl using the new method. The data were fit to an equation (table 1) by least-squares regression analysis. The uncertainty of the equation was taken as two mean standard deviations, that is, ±0.05 weight percent NaCl. The equation has been plotted in figure 4 along with data obtained by other methods. The data obtained by the new method (table 2) are in substantial agreement with the data obtained by other methods.

TABLE 1.—*Experimentally measured solubilities of* NaCl *and* KCl *in water*

[Data were fit to equations of the form: weight percent salt in solution $=a_0+a_1t+a_2t^2$. Values for NaCl were $a_0=26.218$, $a_1=0.0072$, $a_2=0.000106$, and $2\bar{\mu}_s=\pm0.05$. Values for KCl were $a_0=27.839$, $a_1=0.0794$, $a_2=0.000027$, and $2\bar{\mu}_s=\pm0.10$]

Weight percent NaCl	t°C	Weight percent KCl	t°C
29.62	148.7	40.24	148.6
29.62	148.6	40.77	153.4
29.62	148.2	41.43	162.8
29.62	149.0	42.49	173.1
29.62	148.4	44.02	192.3
29.62	148.8	46.00	213.5
29.62	149.2	50.00	256.1
30.08	161.0	52.00	278.0
30.61	172.4	50.98	371.0
32.05	202.3		
32.66	214.5		
36.01	272.9		
40.07	329.4		
48.42	424.8		

The internal consistency of the previous studies was evaluated by fitting their measured solubilities to a second-order equation by least-squares regression analysis. The internal consistency was taken to be two mean standard deviations from the fitted equation. Except for the studies of Schroeder and others (1935) and Keevil (1942), which have internal consistencies of ±0.06 weight percent and ±1.28 weight percent, respectively, the internal consistency of the previous studies was nearly equal to the mean deviation from the equation in table 1.

Although the data that we obtained in this study are limited to the temperature range of 148° to 425°C, the equation for the solubility of NaCl in water (table 1) can probably be used over a wider temperature range. The excellent agreement between this equation and the experimental studies of the Earl of Berkley (1904) and Liu and Lindsay (1971) strongly suggests the validity of the equation down to 0°C. The agreement with data at temperatures greater than 425°C is poorer; however, the internal consistency of the higher temperature data of Keevil (1942) is ±1.28 weight percent, and thus the equation would be at least per-

TABLE 2.—*Comparison of experimental studies and the equation derived for the solubility of* NaCl *in water from the experimental data obtained in this study*

	t range (°C)	$\bar{\mu}_s$ (wt percent)
Earl of Berkley (1904)	0.35 - 107	±0.08
Schroeder and others (1935)	150.00 - 350	±0.03
Benrath and others (1937)	285.00 - 455	±0.42
Keevil (1942)	183.00 - 646	±0.67
Liu and Lindsay (1972)	75.00 - 300	±0.11
This study	148.00 - 425	[1]±0.05

[1] $2\bar{\mu}_s$.

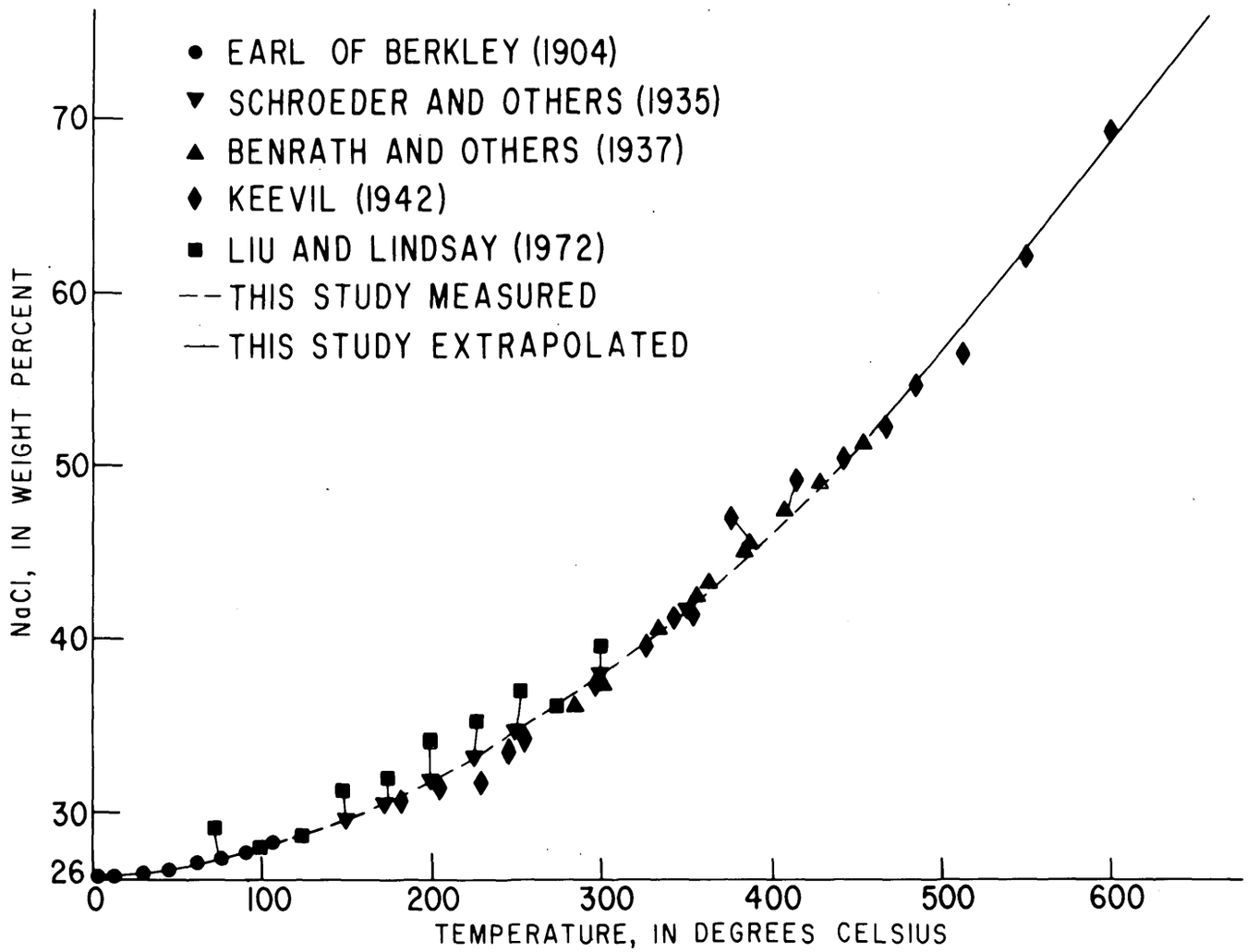

FIGURE 4.—Solubilities of NaCl in water.

missible considering the available data. It has been stated by many workers, for example, Benrath and others (1937) and Keevil (1942), that in simple salt-water systems there is complete miscibility between the molten salt and the aqueous solution, and hence the solubility equals 100 weight percent at the melting point. The melting point of NaCl is 800.7° ± 0.3°C (Robie and Waldbaum, 1968), and the melting point predicted by the equation in table 1 is 801° ± 0.3°C. On the basis of the substantial agreement of the melting point and the excellent agreement with low-temperature experimental data, it is suggested that the equation in table 1 adequately describes the solubility of NaCl in water from 0° to 800°C.

SOLUBILITY OF KCl IN WATER

The experimental solubilities of KCl in water are summarized in table 1. The solubility data were fit to a second-order equation by least-squares regression analysis (table 1). The uncertainty of the equation, ±0.1 weight percent, was defined as two mean standard deviations. In figure 5, the equation has been plotted along with the available experimental data. The mean standard deviation of the solubilities determined by previous investigators from the equation is summarized in table 3. The solubility data determined with the new method in this study are compatible with the solubilities determined by other methods. The internal consistency of the previous studies was evaluated as for NaCl and was found to be within ±25 percent of the value for the deviation from the equation in table 1 (table 3).

Solubility data for KCl were obtained for the temperature range 148° to 371°C. The equation (table 1) that describes these data can be extrapolated down to 100°C, but at lower temperatures it deviates mark-

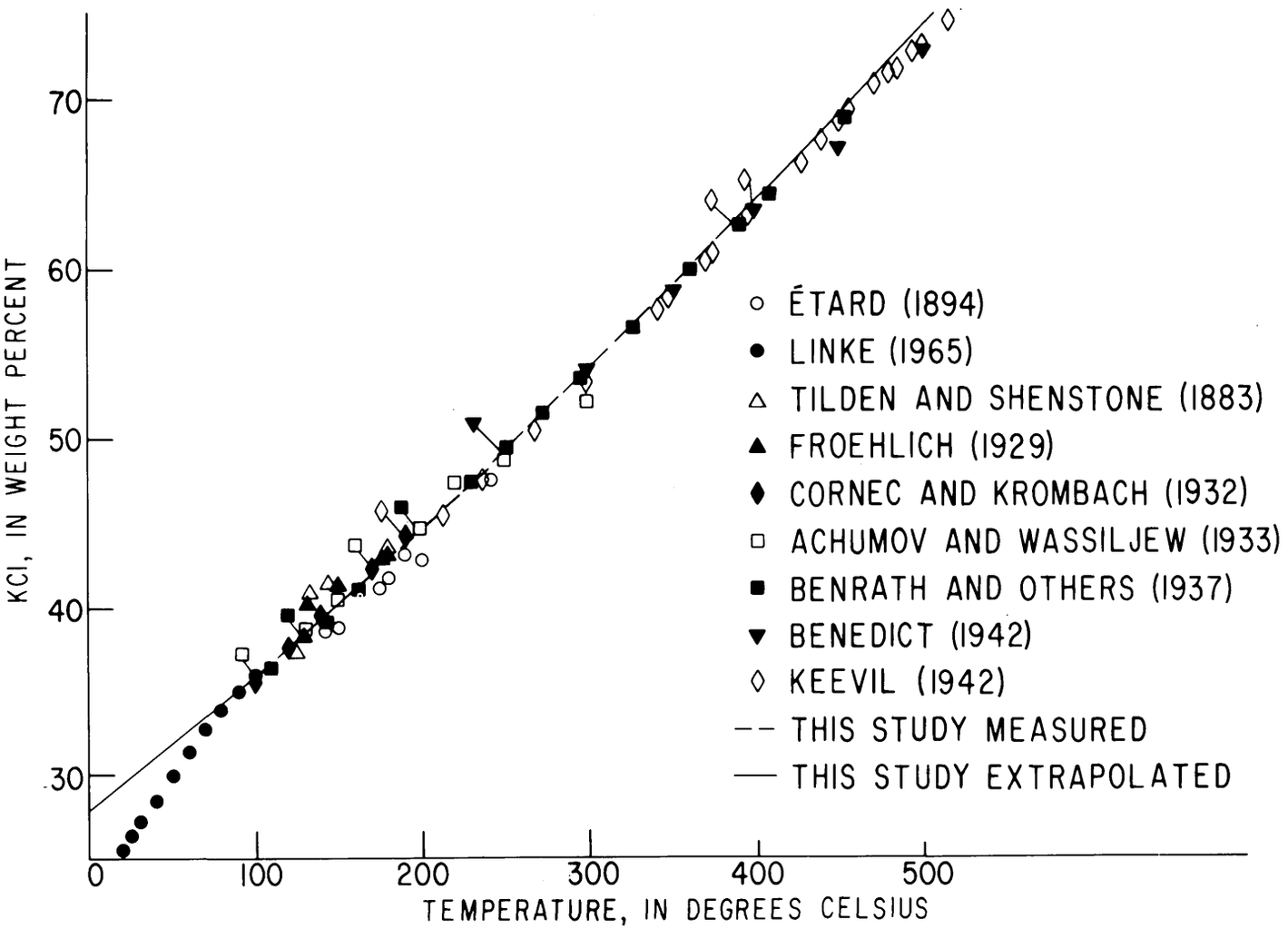

FIGURE 5.—Solubilities of KCl in water.

TABLE 3.—*Comparison of experimental studies and the equation derived for the solubility of* KCl *in water from the experimental data obtained in this study*

	t range (°C)	$\bar{\mu}_s$ (wt percent)
Tilden and Shenstone (1883)	125 - 180	1.1
Etard (1894)	142 - 242	1.3
Froelich (1929)	130 - 180	0.8
Cornec and Krombach (1932)	100 - 189.6	0.25
Achumov and Wassiljew (1933)	100 - 300	0.27
Benrath and others (1937)	110 - 454	0.20
Benedict (1942)	250 - 400	0.23
Keevil (1942)	190 - 645	[1]0.52
This study	148 - 371	[2]0.10

[1] Based on data up to 450°C.
[2] $2\bar{\mu}_s$.

edly from the experimentally observed solubilities summarized by Linke (1965) (fig. 5). The equation agrees well with the experimental data of Benrath and others (1937) and Benedict (1942) up to 450°C. Keevil's (1942) solubilities show a slight flattening of the solubility curve at higher temperatures. Hence, there is an increased discrepancy between the measured values and those calculated by the equation in table 1. This flattening of the solubility curve appears to be real, as the equation (table 1) does not accurately predict the melting point of KCl—it is too low. On the basis of the existing data, the equation for the solubility of KCl in water is considered reliable from 100° to 450°C.

CONCLUSIONS

The method described in this paper for measuring the solubilities of salts in aqueous solutions at elevated temperatures is a reliable method. The pilot studies of the solubilities of NaCl and KCl in water indicate that more precise solubilities can be obtained this way than with the previously used experimental techniques. The method is relatively fast, and only inert platinum is in contact with the solution. The method has been

shown to be useable from 148° to 425°C and can probably be readily used from 130° to 600°C. Care must be taken to establish the optimum heating rate for each type of salt, but there appear to be no other significant drawbacks to the method.

REFERENCES CITED

Achumov, E. I., and Wassiljew, B. B., 1933, [The technological calculations for the equilibrium of the chlorides of potassium, sodium, and magnesium in water at high temperatures]: Jour. Chem. Industry, v. 8, p. 19–23 (in Russian).

Benedict, M., 1942, Properties of saturated aqueous solutions of potassium chloride at temperatures above 250°C: Jour. Geology, v. 47, p. 252–276.

Benrath, A., Gjedebo, F., Schiffers, B., and Wunderlich, H., 1937. Über die löslichkeit von salzen und salzgemischen in wasser bei temperaturan oberhalb von 100°: Zeitschr. Anorg. u. Allg. Chemie, v. 231, p. 285–297.

Cornec, E. ,and Krombach, H., 1932, Équilibres entre le chlorure de potassium, le chlorure de sodium et l'eau depuis −23° jusqu'à +190°: Annales Chim., v. 18, p. 5–23.

Earl of Berkley, 1904, On some physical constants of saturated solutions: Royal Soc. London Philos. Trans., Ser. A, v. 203, p. 189–215.

Étard, 1894, Annales Chim., v. 2, p. 503–574.

Froehlich, W., 1929, Mitteilungan der kali-forschungsanstalt, v. 68, p. 51–68.

Keevil, N. B., 1942, Vapor pressures of aqueous solutions at high temperatures: Am. Chem. Soc. Jour., v. 64, p. 841–850.

Linke, W. F., 1965, Solubilities of inorganic and metal organic compounds [4th ed.]: New York, Am. Chem. Soc., 1914 p.

Liu, C., and Lindsay, W. T., Jr., 1972, Thermodynamic properties of aqueous solutions at high temperatures: Office of Saline Water, Research and Devel. Prog. Rept. 722, 124 p.

Potter, R. W., II, and Brown, D. L., 1975, The volumetric properties of aqueous sodium chloride solutions from 0° to 500°C at pressures up to 2000 bars based on a regression of the available literature data: U.S. Geol. Survey Open-File Rept. 75–636, 31 p.

——— 1976, The volumetric properties of vapor saturated aqueous potassium chloride solutions from 0° to 400° based on a regression of the available literature data: U.S. Geol. Survey Open-File Rept. 76–243, 6 p.

Robie, R. A., and Waldbaum, D. R., 1968, Thermodynamic properties of minerals and related substances at 298.15°K (25°C) and 1 atmosphere (1.013 bars) pressure and at higher temperatures: U.S. Geol. Survey Bull. 1259, 256 p.

Schroeder, W. C., Gabriel, A., and Patridge, E. P., 1935, Solubility equilibria of sodium sulfate at temperatures of 150 to 350°. I, Effect of sodium hydroxide and sodium chloride: Am. Chem. Soc. Jour., v. 57, p. 1539–1546.

Stephen, H., and Stephen, T., 1963, Solubilities of inorganic and organic compounds, *in* Binary systems, vol. I: New York, Macmillan Co., 1933 p.

Tilden, W. T., and Shenstone, W. T., 1883 Solubilities of inorganic salts: Royal Soc. [London] Proc., v. 35, p. 345–346.

Jour. Research U.S. Geol. Survey
Vol. 5, No. 3, May–June 1977, p. 397–402

DETERMINATION OF 22 MINOR AND TRACE ELEMENTS IN 8 NEW USGS STANDARD ROCKS BY INSTRUMENTAL ACTIVATION ANALYSIS WITH EPITHERMAL NEUTRONS

By J. J. ROWE AND EILIV STEINNES,[1] Reston, Va.

Abstract.—Epithermal neutron-activation analyses results of the 8 new USGS standard rocks are compared with results by spectrographic, X-ray fluorimetric, atomic absorption, radiochemical neutron-activation, instrumental neutron-activation (thermal neutrons), isotope-dilution mass spectrometric, spectrofluorimetric, radioisotopic dilution and delayed-neutron techniques for 22 elements. Results indicate the technique to be useful and dependable especially for Ni, Se, Rb, Sr, Mo, Ba, Tm, Ta, Th and U.

A study of the precision and accuracy of results obtained by instrumental epithermal neutron-activation analysis (ENAA) was made to evaluate the utility and feasibility of this technique. Analyses of the eight new U.S. Geological Survey standard rocks by ENAA are compared with those obtained by various accepted methods. Some of the techniques used for comparison are instrumental thermal neutron-activation analysis (INAA), using Ge(Li) detectors, and spectrographic, atomic absorption, X-ray fluorescence, and spectrophotometric methods.

The eight new standard rocks recently issued by the U.S. Geological Survey are nepheline syenite (STM–1), rhyolite obsidian (RGM–1), quartz latite (QLO–1), mica schist (SDC–1), Hawaiian basalt (BHVO–1), Cody shale (SCo–1), Green River shale (SGR–1), and marine sediment (MAG–1). A description of the new standards and presentation of many major-, minor-, and trace-element data for each sample are given in Flanagan (1976).

Neutron-activation analysis has played a significant role in the last two decades in providing information on recommended values for many minor and trace elements in geologic and other reference materials. After the introduction of Ge(Li) detectors for gamma-ray spectrometry, the purely instrumental activation analysis became a useful tool for multielement analysis. Several elements present in trace concentrations in silicate rocks can be determined by this technique. (See, for example, Gordon and others, 1968.)

If the samples are irradiated with epithermal neutrons, using a cadmium cover to shield against the thermal neutrons in the reactor, additional elements may be determined, and conditions are improved for some others (Steinnes, 1971). ENAA was previously applied to the determination of 12 minor and trace elements in some of the earlier USGS standard rocks (Brunfelt and Steinnes, 1969). We undertook a similar study on the eight new standard rocks, taking advantage of recent improvements in detection and computation techniques. The results of this study are reported here and discussed in relation to other data on the same rocks. The experimental details will be published elsewhere (P. A. Baedecker and others, unpub. data, 1976).

In our opinion the data so far presented on the eight new standards indicate that the among-bottle variation for most minor and trace elements is no greater than the analytical errors of most methods used in this concentration region. The present study was therefore based on duplicate analyses using 100-milligram portions from the same bottle.

Acknowledgment.—This work was carried out at the time when one of the authors (Steinnes) held a Senior Scientist Fellowship granted by the Royal Norwegian Council for Science and Technology.

RESULTS AND DISCUSSION

The data in table 1, based on measurements carried out within 2 weeks after the end of the irradiation, compares the results for the determination of 22 elements in the 8 rocks by ENAA with the literature data for each of the elements reported. The radionuclide photon energies and type of detector used for each element are also shown in the table. Results for each duplicate are given in parentheses to indicate the

[1] On leave from the Institutt for Atomenergi, Kjeller, Norway.

TABLE 1.—*Comparison of data from the present work with data found in the literature*

[N, no peak detected by computer program. All data given in parts per million. Results for each duplicate are given in parentheses after ENAA data]

C: Coaxial Ge(Li) detector.
ENAA: Instrumental activation analysis with epithermal neutrons.
OS–SQ: Optical spectroscopy–semiquantitative.
INAA: Instrumental activation analysis with thermal neutrons.
XRF: X-ray fluorescence spectrometry.
OS: Optical spectroscopy–quantitative.
AA: Atomic absorption spectrometry.
LEPD: Low-energy planar detector.
SpFl: Spectrofluorimetry.
RID: Radiosotope dilution.
IDMS: Isotope-dilution mass spectrometry.
SSMS: Spark source mass spectrometry.
RCNA: Radiochemical neutron-activation analysis.
DNAA: Delayed neutron-activation analysis.
Flour: Fluorimetry.

Sample	STM–1	RGM–1	QLO–1	MAG–1	SDC–1	BHVO–1	SCo–1	SGR–1
Sc (^{46}Sc; 889.3 keV; C)								
ENAA (this work)	0.68 (0.68, N)	4.43 (4.41, 4.44)	8.87 (8.57, 9.07)	17.2 (17.1, 17.3)	15.3 (14.9, 15.7)	31.3 (30.1, 32.4)	11.1 (10.9, 11.2)	5.03 (4.85, 5.20)
OS–SQ[a]	----------	4.60	11.4	17.0	19.7	----------	9.0	3.86
INAA[b]	0.675	4.60	8.96	16.3	15.8	32.0	11.4	4.78
XRF[c]	----------	4.75	11.3	20.2	19.0	28.0	19.3	≈10
Others	----------	----------	----------	----------	----------	27.5 (INAA)[d] 31.2 (OS)[d]	----------	----------
Co (^{60}Co; 1173.2, 1332.4 keV; C)								
ENAA (this work)	1.10 (1.09, 1.11)	2.36 (2.29, 2.43)	7.8 (7.8, 7.7)	22.9 (22.7, 23.1)	17.5 (17.1, 17.9)	45.1 (43.4, 46.8)	11.7 (11.4, 12.0)	12.8 (12.8, 12.8)
OS–SQ[a]	----------	1.76	7.31	21.6	20.3	47.4	9.30	9.96
INAA[b]	0.325	1.88	6.92	18.8	16.6	42.1	9.66	10.3
Others	----------	----------	----------	----------	----------	45.5, 44.8 (OS)[d]	11.3 (OS)[e]	13.2 (OS)[e]
Ni (^{58}Co; 811.1 keV; C)								
ENAA (this work)	<40 (N, N)	<40 (N, N)	<40 (N, N)	53 (53, N)	35 (35, N)	92 (89, 95)	<40 (N, N)	34 (30, 38)
OS–SQ[a]	1.65	1.99	1.99	70.2	56.3	140	28.1	32.3
XRF[c]	6	14.0	9.2	53.8	40.7	121.5	28.5	39.2
Others	----------	6 (AA)[f]	----------	----------	----------	114.4 (OS)[d]	29.8 (OS)[e]	31.4 (OS)[e]
Se (^{75}Se; 136.0 keV; LEPD)								
ENAA (this work)	<1 (N, N)	<1 (N, N)	<1 (N, N)	1.0 (1.0, N)	<1 (N, N)	<1 (N, N)	<1 (N, N)	3.3 (3.1, 3.4)
SpFl[g]	----------	----------	----------	1.308	----------	----------	0.907	3.69
Rb (^{86}Rb; 1,078.8 keV; C)								
ENAA (this work)	120 (118, 121)	154 (157, 150)	74 (72, 76)	155 (157, 150)	125 (126, 124)	11 (11, N)	114 (111, 116)	82 (80, 84)
INAA[b]	56.0	193	34.7	84.3	67.9	0.147	68.9	66.5
XRF[c]	112.8	154.2	67.8	186.3	129.0	8.7	122.2	92.2
Others	----------	----------	----------	----------	----------	7.96 (OS)[d]	----------	----------
Sr (^{85}Sr; 514.0 keV; C)								
ENAA (this work)	735 (748, 722)	128 (137, 118)	353 (363, 342)	166 (152, 180)	224 (212, 236)	487 (469, 504)	179 (192, 166)	437 (412, 456)
OS–SQ[a]	843	132	436	185	239	473	215	558
AA[h]	717	112	354	150	183	----------	129	433
XRF[h]	673	96.3	326	128	121	----------	156	417
XRF[c]	711.3	116.5	329.3	167.5	200.3	374.2	193.3	445
AA[i]	609.4	100.1	381.8	173.4	107.5	438.5	152.9	332.2
Others	----------	----------	----------	----------	----------	326.2 (OS)[d]	223.6 (OS)[e]	315.8 (OS)[e]
Mo (^{99m}Tc; 140.4 keV; LEPD)								
ENAA (this work)	5.2 (5.7, 4.2)	1.5 (1.4, 1.6)	2.6 (2.5, 2.6)	<1 (N, N)	<1 (N, N)	1.0 (N, 1.0)	1.4 (1.3, 1.4)	35.7 (36.2, 35.1)
RID[j]	4.4	----------	2.3	----------	----------	0.92	----------	----------
OS–SQ[a]	7.9	2.87	3.40	2.80	1.90	0.58	2.79	36.1
Sb (^{124}Sb; 1691 keV; C)								
ENAA (this work)	1.66 (1.52, 1.80)	1.18 (1.20, 1.16)	1.76 (1.66, 1.86)	1.00 (0.98, 1.02)	0.54 (0.45, 0.62)	0.170 (0.168, 0.172)	2.52 (2.65, 2.38)	3.00 (3.25, 2.74)
INAA[b]	1.88	1.52	2.84	0.83	0.36	0.43	2.40	3.05
INAA[k]	1.67	1.30	2.03	0.88	0.53	0.16	2.51	3.70
Ba (^{131}Ba; 496.3 keV; C)								
ENAA (this work)	597 (577, 616)	854 (881, 827)	1424 (1384, 1464)	536 (503, 568)	649 (639, 658)	161 (167, 155)	595 (597, 592)	323 (347, 298)
OS–SQ[a]	771	752	1173	426	526	117	416	361

IDMS[1]	584	822	1401	476	641	132.5	570	286
XRF[c]	611.7	826.7	1391	513	675	126.5	621.7	328.3
INAA[b]	551	807	1360	311	530	----------	474	225
Others	----------	----------	----------	----------	----------	132.0 SSMS[d] 171.7 OS[d]	----------	----------
Cs (^{134}Cs; 794.0 keV; C)								
ENAA (this work)	1.48 (1.48, 1.47)	9.56 (9.76, 9.35)	1.61 (1.68, 1.54)	8.60 (8.23, 8.96)	3.82 (3.69, 3.95)	<0.2 (N, N)	7.57 (7.47, 7.66)	5.33 (5.47, 5.18)
INAA[b]	1.47	10.3	1.76	7.53	3.85	0.088	6.82	4.61
Ce (^{141}Ce; 145.5 keV; LEPD, C)								
ENAA (this work)	293 (289, 297)	56 (58.0, 53.6)	59 (57.3, 65.8)	95 (95.1, 95.3)	103 (101.4, 105.2)	46 (44.6, 47.5)	67 (65.8, 67.2)	42 (44.8, 39.8)
OS–SQ[a]	354	60.4	75.5	104	124	----------	71.0	58.1
INAA[b]	73.1	46.3	59.8	95.3	106	39.0	62.1	31.9
Others	214 RCNA[m]	----------	----------	----------	----------	33.4 SSMS[d]	54.4 RCNA[m]	----------
Nd (^{142}Nd; 91.1 keV, LEPD)								
ENAA (this work)	86.8 (86.6, 87.1)	18.9 (19.2, 18.6)	27.1 (26.2, 28.0)	46.6 (44.8, 48.3)	45.4 (43.6, 47.1)	31.8 (30.8, 32.8)	26.9 (26.1, 27.7)	16.3 (16.6, 15.9)
OS–SQ[a]	55.7	18.8	35.3	26.8	33.8	----------	23.8	37.0
Others	75.5 RCNA[m]	----------	----------	----------	----------	22.4 SSMS[d]	27.3 RCNA[m]	----------
Sm (^{153}Sm; 40.9, 41.5, 69.7, 103.2; LEPD)								
ENAA (this work)	14.2 (13.7, 14.6)	4.33 (4.32, 4.34)	5.25 (5.29, 5.20)	8.21 (8.11, 8.30)	9.00 (8.83, 9.17)	6.84 (6.60, 7.07)	5.59 (5.50, 5.68)	2.81 (2.85, 2.72)
Others	15.8 OS–SQ[a] 11.6 RCNA[m]	----------	----------	----------	5.18 OS–SQ[a]	5.30 OS[d]	5.13 RCNA[m]	----------
Eu (^{152}Eu, ^{154}Eu; 121.8, 123.1 keV; LEPD)								
ENAA (this work)	3.74 (3.71, 3.77)	0.84 (0.76, 0.92)*	1.64 (1.61, 1.67)	1.71 (1.65, 1.77)	1.86 (1.84, 1.88)	2.34 (2.26, 2.42)	1.24 (1.27, 1.21)	0.64 (0.61, 0.67)*
OS–SQ[a]	3.86	----------	1.15	1.30	1.68	1.59	----------	----------
INAA[b]	4.03	0.725	1.53	1.04	1.86	2.36	1.24	0.52
Others	3.00 RCNA[m]	----------	----------	----------	----------	1.66 SSMS[d]	1.02 RCNA[m]	----------
Gd (^{161}Tb; 74.6 keV; LEPD)								
ENAA (this work)	13.9 (14.5, 13.2)	<5 (N, N)	6.1 (5.7, 6.4)	9.0 (8.4, 9.6)	9.9 (10.7, 9.0)	8.6 (9.5, 8.8)	6.2 (6.4, 6.0)	<5 (N, N)
Others	----------	----------	----------	----------	----------	7.1 OS–SQ[a] 5.6 SSMS[d]	----------	----------
Tb (^{160}Tb; 879.3, 1178.1 1271.9 keV; C)								
ENAA (this work)	1.57 (1.57, 1.57)	0.73 (0.74, 0.72)	0.75 (0.72, 0.78)	1.06 (1.05, 1.06)	1.21 (1.16, 1.26)	1.02 (0.99, 1.05)	0.76 (0.71, 0.81)	0.35 (0.37, 0.33)
INAA[b]	2.10	----------	0.92	0.95	1.35	1.41	0.78	0.34
Others	1.38 RCNA[m]	----------	----------	----------	----------	0.75 SSMS[d]	0.70 RCNA[m]	----------
Tm (^{170}Tm; 84.3 keV; LEPD)								
ENAA (this work)	<1 (N, N)	0.37 (0.33, 0.41)	0.39 (0.41, 0.37)	0.45 (0.42, 0.47)	0.71 (0.69, 0.73	0.34 (0.32, 0.36)	0.35 (0.36, 0.34)	0.19 (0.14, 0.23)
Others	----------	----------	----------	----------	----------	0.289 SSMS[d]	----------	----------
Yb (^{169}Yb; 50.7, 63.5 keV; LEPD)								
ENAA (this work)	4.90 (4.79, 5.00)	3.14 (3.15, 3.13)	3.07 (3.07, 3.06)	2.97 (2.97, 2.97)	5.34 (5.28, 5.40)	2.42 (2.47, 2.37)	2.77 (2.89, 2.65)	1.24 (1.16, 1.31)
OS–SQ[a]	6.67	2.83	3.29	2.68	5.13	4.24	2.21	1.17
Others	4.26 RCNA[m]	----------	----------	----------	----------	2.81 SSMS[d]	2.33 RCNA[m]	----------
Hf (^{181}Hf; 482.2 keV; C)								
ENAA (this work)	27.2 (27.1, 27.4)	6.58 (6.43, 6.72)	4.20 (4.05, 4.35)	4.36 (4.18, 4.54)	8.03 (7.99, 8.06)	4.38 (4.43, 4.33)	4.22 (4.00, 4.54)	1.34 (1.32, 1.36)
INAA[b]	26.4	5.97	4.47	3.15	8.14	3.77	4.38	1.31
INAA[k]	28.87	5.93	4.68	3.52	8.30	4.33	4.73	1.41
Others	----------	----------	----------	----------	----------	3.98 SSMS[d]	----------	----------

See footnotes at end of table.

TABLE 1.—*Comparison of data from the present work with data found in the literature*—Continued

Sample	STM–1	RGM–1	QLO–1	MAG–1	SDC–1	BHVO–1	SCo–1	SGR–1
			Ta (^{182}Ta; 152.4, 222.1, 1189.0, 1221.3, 1230.9 keV; C)					
ENAA (this work)	20.5 (20.4, 20.6)	1.09 (1.10, 1.07)	0.92 (0.91, 0.93)	1.30 (1.32, 1.28)	1.41 (1.33, 1.49)	1.34 (1.32, 1.35)	0.99 (0.98, 1.00)	0.52 (0.55, 0.49)
INAA[b]	18.0	0.87	0.70	0.74	0.90	0.86	0.56	0.22
INAA[k]	17.26	0.90	0.81	1.00	1.15	1.10	0.82	0.57
			Th (^{233}Pa; 311.9 keV; C)					
ENAA (this work)	31.1 (30.8, 31.3)	15.3 (15.4, 15.1)	4.86 (4.88, 4.84)	12.6 (12.5, 12.7)	12.0 (11.6, 12.3)	1.29 (1.23, 1.35)	9.65 (9.66, 9.63)	4.91 (5.05, 4.77)
INAA[b]	38.8	18.6	6.20	13.0	14.2	3.19	10.5	4.86
DNAA[n]	26.6	13.1	3.24	12.2	11.4	0.90	9.52	7.66
Others	----------	----------	----------	----------	----------	0.783 INAA[d] 0.871 SSMS[d]	----------	----------
			U (^{239}Np; 106.4 keV; LEPD)					
ENAA (this work)	9.04 (8.76, 9.32)	5.77 (5.76, 5.77)	1.97 (1.96, 1.98)	2.86 (2.79, 2.94)	2.98 (2.87, 3.08)	0.487 (0.456, 0.488)	3.10 (3.12, 3.09)	5.41 (5.46, 5.36)
DNAA[n]	9.10	5.85	2.01	2.82	3.12	0.48	3.15	5.60
Others	----------	----------	----------	----------	----------	0.36 Fluor[d] 0.34 SSMS[d]	----------	----------

[a] Walthall, Dorrzapf, and Flanagan (1976).
[b] Katz and Grossman (1976).
[c] Fabbi and Espos (1976).
[d] Flanagan, Wright, Taylor, Annell, Christian, and Dinnin (1976).
[e] Brenner and Harel (1976).
[f] Smith and Walsh (1976).
[g] Schnepfe and Flanagan (1973).
[h] Machaček, Rubeška, Sixta, and Šulcek (1976).
[i] Thomas, Mountjoy, and Huffman (1976).
[j] Lillie and Greenland (1976).
[k] Schwarz and Rowe (1976).
[l] de Laeter, Date, and Abercrombie (1976).
[m] Kosiewicz, Schomberg, and Haskin (1974).
[n] Millard (1976).
[o] Values based on 39.5 and 40.1 keV X-rays.

reproducibility of the present work. Except for Sc, Ce, and Eu which do not have favorable I/σ_0 (epithermal to thermal cross section) ratios, most of the elements included were more advantageously determined by ENAA than by the usual thermal irradiation. However, we feel that ENAA can yield adequate results with good precision for Sc, Ce, and Eu. The results of each element are discussed below, with special reference to the work by Katz and Grossman (1976) using INAA. Several points of significant disagreement between the two sets of data are evident. This does not necessarily refer only to the difference in irradiation technique, but may also be associated in part with the fact that Katz and Grossman were limited to a counting system with significantly poorer resolution; that is, 4.5 keV (kiloelectron volts) FWHM (full width, half maximum) for ^{60}Co versus 2.0 keV in the present work.

Scandium

Sc is one of the easiest elements to be determined in silicate rocks by INAA. The good agreement with Katz and Grossman's (1976) data thus indicates that this element is also determined with adequate accuracy by ENAA, in spite of the large reduction of ^{46}Sc relative to other activities. Moreover, the agreement between spectrographic and other analytical techniques is remarkably good for most samples.

Cobalt

Here, also, the spectrographic data match fairly well with those from neutron activation. The data of Katz and Grossman (1976) are systematically 10–20 percent lower than those of the present work, which may be in part because of differences in standardization procedures. There seems to be no obvious reason for the disagreement on STM–1.

Nickel

Ni is not readily determinable, even by ENAA. However, where peaks were positively identified, the results are in fair agreement with those of Fabbi and Espos (1976) using X-ray fluorescence.

Selenium

The results for Se, which were detected only in MAG–1 and SCR–1, agree reasonably with those from spectrofluorimetry (Schnepfe and Flanagan, 1973).

Rubidium

Useful results for Rb by INAA are usually difficult to obtain especially if the sample has a high Sc/Rb

ratio. X-ray fluorescence on the other hand is known to produce good results for this element, even at low concentrations. The conditions for Rb determination in rocks by ENAA are generally improved by more than a factor of 10 relative to ordinary INAA. The results from this work, while showing rather large disagreement with those of Katz and Grossman (1976), are in excellent agreement with the values by Fabbi and Espos (1976).

Strontium

Here, different analytical techniques agree fairly well. Whereas Sr determination by INAA is rather difficult even at the 500 parts-per-million level, ENAA gives results in general agreement with techniques more commonly used for this element.

Molybdenum

The present results agree well with those of Lillie and Greenland (1976), using a radioisotope dilution method, where a comparison is possible. The semiquantitative spectrographic method usually seems to produce good results, but may occasionally appear to be less successful.

Antimony

For Sb the only available data for comparison were obtained by neutron activation. Given the conditions used in the present work, no appreciable difference is found between the INAA and ENAA measurements, except that the ENAA measurements can be made soon after the irradiation. Except for SGR–1, the results reported here agree well with those of Schwarz and Rowe (1976), whereas they differ somewhat from those of Katz and Grossman (1976).

Cesium

Determinations for this element agree well with the INAA results of Katz and Grossman (1976).

Barium

INAA is not sufficiently sensitive, whereas the ENAA seems to yield adequate results. Except for a slight disagreement on BHVO–1, the present set of data compares well with those from isotope dilution mass spectrometry and X-ray fluorescence.

Rare-earth elements

Complete data sets for eight rare-earth elements are presented in this paper. Kosiewicz, Schomberg, and Haskin (1974) analyzed STM–1 and SCo–1 for seven of the eight elements studied in the present work, using a neutron-activation method involving a radiochemical group separation of the rare-earth elements. Their results are systematically lower than ours by about 15 percent. The difference is over 30 percent for Ce. We do not see any obvious explanation for this.

Our results for cerium agree reasonably with the INAA data of Katz and Grossman (1976) except for STM–1 where their value is obviously erroneous. The ENAA data also compare fairly well with the semiquantitative spectrographic values. For Nd, Sm, Gd, and Tm, very few other data exist so far. Our Eu values agree with those from INAA except for MAG–1. For Tb, which should be favorably determined by ENAA, the agreement is somewhat less satisfactory. For Yb, spectrographic values agree fairly well except for STM–1 and BHVO–1.

Hafnium and tantalum

Only neutron-activation values are available for both of these elements. Hf values agree well with both of the previous INAA sets of data. For Ta a difference between our values and the values of the previous investigations is evident for some samples. For those samples the epithermal results confirm the data by Schwarz and Rowe (1976).

Thorium

The Th data from the ENAA agree well with the delayed-neutron data of Millard (1976) and the INAA data of Katz and Grossman (1976) except for BHVO–1 where the high Cr/Th ratio causes spectral difficulty.

Uranium

ENAA yields very satisfactory results for U which agree closely with the delayed-neutron data of Millard (1976), the difference being no greater than 5 percent.

We believe this work has demonstrated that ENAA is a dependable, useful multielement neutron-activation technique in rock analysis which can be applied to a wide variety of matrices. In a laboratory doing instrumental neutron-activation analysis, a routine setup for epithermal work can be established easily. Repeated measurements after longer decay times would have improved the precision and sensitivity for some elements, but would not be consistent with a rational scheme for routine multielement analysis.

REFERENCES CITED

Brenner, I. B., and Harel, A., 1976, Titanium and trace element data in USGS standard rocks SCo–1 and SGR–1, *in*

Flanagan, F. J., editor and compiler, Descriptions and analyses of eight new USGS rock standards: U.S. Geol. Survey Prof. Paper 840, p. 95–98.

Brunfelt, A. O., and Steinnes, E., 1969, Instrumental activation analysis of silicate rocks with ephermal neutrons: Anal. Chim. Acta, v. 48, p. 13–24.

Fabbi, B. P., and Espos, L. F., 1976, X-ray fluorescence analysis of 21 selected major, minor, and trace elements in eight new USGS standard rocks, *in* Flanagan, F. J., editor and compiler, Descriptions and analyses of eight new USGS rock standards: U.S. Geol. Survey Prof. Paper 840, p. 89? 93.

Flanagan, F. J., editor and compiler, 1976, Descriptions and analyses of eight new USGS rock standards: U.S. Geol. Survey Prof. Paper 840, 192 p.

Flanagan, F. J., Wright, T. L., Taylor, S. R., Annell, C. S., Christian, R. C., and Dinnin, J. I., 1976, Basalt, BHVO–1, from Kilaeau Crater, Hawaii, *in* Flanagan, F. J., editor and compiler, Descriptions and analyses of eight new USGS rock standards: U.S. Geol. Survey Prof. Paper 840, p. 33–39.

Gordon, G. E., Rondle, K., Goles, G. G., Corliss, J. B., Beeson, M. H., Oxley, S. S., 1968, Instrumental activation analysis of standard rocks with high resolution X-ray detectors: Geochim. et Cosmochim. Acta, v. 32, p. 369–396.

Katz, A., and Grossman, L., 1976, Intercalibration of 17 standard silicates for 14 elements by instrumental neutron activation analysis, *in* Flanagan, F. J., editor and and compiler, Descriptions and analyses of eight new USGS rock standards: U.S. Geol. Survey Prof. Paper 840, p. 49–57.

Kosiewicz, S. T., Schomberg, P. J., and Haskin, L. A., 1974, Rare earth analyses of USGS rocks SCo–1 and STM–1: Jour. Radioanal. Chemistry, v. 20, p. 619–626.

de Laeter, J. R., Date, R., and Abercrombie, I. D., 1976, Mass spectrometric isotope dilution determinations of barium, *in* Flanagan, F. J., editor and compiler, Descriptions and analyses of eight new USGS rock standards: U.S. Geol. Survey Prof. Paper 840, p. 41–43.

Lillie, E. G., and Greenland, L. P., 1976, Molybdenum in USGS standard rocks, *in* Flanagan, F. J., editor and compiler, Descriptions and analyses of eight new USGS rock standards: U.S. Geol. Survey Prof. Paper 840, p. 47–48.

Machàček, V., Rubešká, I., Sixta, V., and Šulek, Z., 1976, The beryllium, fluorine, lithium, copper, zinc, and strontium content of USGS standard rock samples STM–1, RGM–1, QLO–1, SCo–1, MAG–1, SDC–1, and SGR–1, *in* Flanagan, F. J., editor and compiler, Descriptions and analyses of eight new USGS rock standards: U.S. Geol. Survey Prof. Paper 840, p. 73–77.

Millard, H. T., Jr., 1976, Determination of uranium and thorium in standard rocks by the delayed neutron technique, *in* Flanagan, F. J., editor and compiler, 1976, Descriptions and analyses of eight new USGS standards: U.S. Geol. Survey Prof. Paper 840, p. 61–65.

Schnepfe, M. M., and Flanagan, F. J., 1973, The selenium content of U.S.G.S. standard rocks: Chem. Geology, v. 12, p. 77–80.

Schwarz, L. J., and Rowe, J. J., 1976, The determination of antimony, hafnium, and tantalum in the new USGS standard rocks, *in* Flanagan, F. J., editor and compiler, Descriptions and analyses of eight new USGS rock standards: U.S. Geol. Survey Prof. Paper 840, p. 67–69.

Smith, A. C. S., and Walsh, J. N., 1976, The determination of selected elements in the USGS standard rocks STM–1 and RGM–1, *in* Flanagan, F. J., editor and compiler, Descriptions and analyses of eight new USGS rock standards: U.S. Geol. Survey Prof. Paper 840, p. 83–86.

Steinnes, E., 1971, Epithermal neutron activation analysis of geological material, *in* Brunfelt, A. O., and Steinnes, E., eds., Activation analysis in geochemistry and cosmochemistry: Oslo, Universitetsforlaget, p. 113–128.

Thomas, J. A., Mountjoy, W., and Huffman, C., 1976, Copper, lithium, manganese, strontium, zinc, sodium, potassium, and magnesium contents of eight new USGS rock samples, *in* Flanagan, F. J., editor and compiler, Descriptions and analylses of eight new USGS rock standards: U.S. Geol. Survey Prof. Paper 840, p. 119–122.

Walthall, F. G., Dorrzapf, A. F., Jr., and Flanagan, F. J., 1976, Computerized spectrographic data for USGS standards, *in* Flanagan, F. J., editor and compiler, Descriptions and analyses of eight new USGS rock standards: U.S. Geol. Survey Prof. Paper 840, p. 99–115.

RECENT PUBLICATIONS OF THE U.S. GEOLOGICAL SURVEY

(The following books may be ordered from the Branch of Distribution, U.S. Geological Survey, 1200 South Eads Street, Arlington, VA 22202 (an authorized agent of the Superintendent of Documents, Government Printing Office). Prepayment is required. Remittances should be sent by check or money order payable to U.S. Geological Survey. Give series designation and number, such as Bulletin 1368–A, and the full title. Prices of Government publications are subject to change. Increases in costs make it necessary for the Superintendent of Documents to increase the selling prices of many publications offered. As it is not feasible for the Superintendent of Documents to correct the prices manually in all the previous announcements and publications stocked, the prices charged on your order may differ from the prices printed in the announcements and publications)

Professional Papers

P 574–G. *Q*-mode factor analysis of geochemical and petrologic data matrices with constant row-sums, by A. T. Miesch. 1976. p. G1–G47. 95¢.

P 759–B. Physiographic subdivisions of the Chirikov Basin, northern Bering Sea, by D. M. Hopkins, C. H. Nelson, R. B. Perry, and T. R. Alpha. 1976. p. B1–B7; plates in pocket. $2.10.

P 813–G. Summary appraisals of the Nation's ground-water resources—Great Basin Region, by T. E. Eakin, Don Price, and J. R. Harrill. 1976. p. G1–G37; plate in pocket. $2.40.

P 863. Smaller Foraminifera from deep wells on Puerto Rico and St. Croix, by Ruth Todd and Doris Low. 1976. 32 p; 12 plates. $1.65.

P 887. Merumite—A complex assemblage of chromium minerals from Guyana, by Charles Milton, D. E. Appleman, M. H. Appleman, E. C. T. Chao, Frank Cuttitta, J. I. Dinnin, E. J. Dwornik, B. L. Ingram, and H. J. Rose, Jr. 1976. 29 p.; 6 plates. $1.95.

P 907–C. Copper deposits in sedimentary and volcanogenic rocks, by E. B. Tourtelot and J. D. Vine. 1976. p. C1–C34. $1.05. (Reprint.)

P 933. Geology and resources of fluorine in the United States, edited by D. R. Shawe, *with sections by* D. R. Shawe, R. E. Van Alstine, R. G. Worl, A. V. Heyl, R. D. Trace, R. L. Parker, W. R. Griffitts, C. L. Sainsbury, and J. B. Cathcart. 1976. 99 p.; 28 figs. $2.20.

P 957. Lead in the environment, T. G. Lovering, editor. 1976. 90 p. $2.10.

P 959. Geology and resources of titanium. A, Titanium contents and titanium partitioning in rocks, by E. R. Force; B, Metamorphic source rocks of titanium placer deposits—A geochemical cycle, by E. R. Force; C, Rutile and sphene in blueschist and related high-pressure facies rocks, by M. C. Blake, Jr., and B. A. Morgan; D, Titanium deposits in anorthosite massifs, by Norman Herz; E, Titanium deposits in alkalic igneous rocks, by Norman Herz; and F, Titanium minerals in deposits of other minerals, by E. R. Force. p. A1–A10; B1–B16; C1–C6; D1–D6; E1–E6; F1–F5. $1.90.

P 965. The relation of geology to stress changes caused by underground excavation in crystalline rocks at Idaho Springs, Colorado, by F. T. Lee, J. F. Abel, Jr., and T. C. Nichols, Jr. 1976. 47 p.; plate in pocket. $2.55.

P 973. The Roberts Mountains Formation, a regional stratigraphic study with emphasis on rugose coral distribution, by C. W. Merriam and E. H. McKee, *with a section on* Conodonts, by J. W. Huddle. 1976. 51 p.; 12 plates. $1.90.

P 979. Icings along the trans-Alaska pipeline route, by C. E. Sloan, Chester Zenone, and L. R. Mayo. 1976. 31 p. $1.05. (Supersedes Open-File Report 75–87.)

P 981. The Rinconada and related faults in the southern Coast Ranges, California, and their tectonic significance, by T. W. Dibblee, Jr. 1976. 55 p. $1.45.

P 986. East-trending structural lineaments in central Nevada, by E. B. Ekren, R. C. Bucknam, W. J. Carr, G. L. Dixon, and W. D. Quinlivan. 1976. 16 p.; plate in pocket. $1.75.

P 987. Physical, chemical, and biological aspects of subsurface organic waste injection near Wilmington, North Carolina, by J. A. Leenheer, R. L. Malcolm, and W. R. White. 1976. 51 p. $1.35. (Supersedes Open-File Report 75–659.)

P 1001. Numerical simulation analysis of the interaction of lakes and ground water, by T. C. Winter. 1976. 45 p. $1.25.

P 1011. The environment of south Florida, A summary report, by B. F. McPherson, G. Y. Hendrix, Howard Klein, and H. M. Tyus. 1976. 81 p. $3.65.

P 1013. Glass reference standards for the trace-element analysis of geological materials—Compilation of interlaboratory data, by A. T. Myers, R. G. Havens, J. J. Connor, N. M. Conklin, and H. J. Rose, Jr. 1976. 29 p. 85¢.

Bulletins

B 1278–D. Geochemical exploration techniques based on distribution of selected elements in rocks, soils, and plants, Mineral Butte copper deposit, Pinal County, Arizona, by M. A. Chaffee. 1976. p. D1–D55. 85¢.

B 1421–A. Physical properties of the coexisting phases and thermochemical properties of the H_2O component in boiling NaCl solutions, by J. L. Haas, Jr. 1976. p. A1–A73. $1.05.

B 1421–B. Thermodynamic properties of the coexisting phases and thermochemical properties of the NaCl component in boiling NaCl solutions, by J. L. Haas, Jr. 1976. p. B1–B71. $1.05.

B 1426. Bibliography of reports resulting from U.S. Geological Survey technical cooperation with other countries, 1967–74, by W. E. Bergquist. 1976. 68 p. 90¢. (Supersedes Open-File Report 75–435.)

B 1432. The Reinhardt Thiessen coal thin-section slide collection of the U.S. Geological Survey—catalog and notes, by J. M. Schopf and O. G. Oftedahl. 1976. 85¢.

Water-Supply Papers

W 1662–D. Specific yield—Compilation of specific yields for various materials, by A. I. Johnson. 1976. p. D1–D74. 30¢. (Reprint.)

W 2040. Ground water in the Harrisburg-Halsey area, southern Willamette Valley, Oregon, by F. J. Frank. 1976. 45 p.; plate in pocket. $2.05. (Supersedes Open-File Report 76–249.)

W 2043. Water in carbonate rocks of the Madison Group in southeastern Montana—A preliminary evaluation, by W. R. Miller. 1976. 51 p.; plates in pocket. $2.90.

W 2136. Surface-water supply of the United States, 1966–70—Part 15, Alaska. 1976. 428 p. $4.

U.S. GOVERNMENT
PRINTING OFFICE
PUBLIC DOCUMENTS DEPARTMENT
WASHINGTON, D C 20402

OFFICIAL BUSINESS
PENALTY FOR PRIVATE USE $300

POSTAGE AND FEES PAID
U.S. DEPARTMENT OF THE INTERIOR
INT 413

U.S.MAIL

Special
fourth-class
rate books